PHOTODISSOCIATION DYNAMICS OF POLYATOMIC MOLECULES IN GAS-PHASE

By

MONALI NITIN KAWADE

Enrolment Number:CHEM01200704005

Bhabha Atomic Research Center

A thesis submitted to the

Board of Studies in Chemical Science Discipline

In partial fulfillment of requirements

For the Degree of

DOCTOR OF PHILOSOPHY
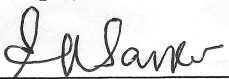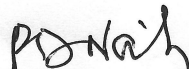
of

HOMI BHABHA NATIONAL INSTITUTE

MAY, 2013

Homi Bhabha National Institute

Recommendations of the Viva Voce Board

As members of the Viva Voce Board, we certify that we have read the dissertation prepared by **Monali Nitin Kawade** entitled "**Photodissociation Dynamics of Polyatomic Molecule in Gas-Phase**" and recommend that it may be accepted as fulfilling the dissertation requirement for the Degree of Doctor of Philosophy.

_____ Date: 13/12/13

Chairman: **Dr. S. K. Sarkar**
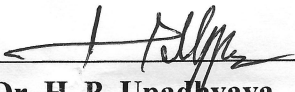
_____ Date: 13/12/13

Guide/Convener: **Dr. P. D. Naik**

_____ Date: 13-12-13

Co-guide: **Dr. Awadhesh Kumar**

_____ Date: 13/12/2013

External Examiner: **Prof. Tapas Chakraborty**

_____ Date: 13/12/2013

Member 1: **Dr. P. N. Bajaj**

_____ Date: 13/12/2013

Member 2: **Dr. R. K. Vatsa**

_____ Date: 13/12/2013

Member 3: **Dr. H. P. Upadhyaya**

Final approval and acceptance of this dissertation is contingent upon the candidate's submission of the final copies of the dissertation to HBNI. I hereby certify that I have read this dissertation prepared under my direction and recommend that it may be accepted as fulfilling the dissertation requirement.

Date: 13-12-2013

Place: Mumbai

STATEMENT BY AUTHOR

This dissertation has been submitted in partial fulfillment of requirements for an advanced degree at Homi Bhabha National Institute (HBNI) and is deposited in the Library to be made available to borrowers under rules of the HBNI.

Brief quotations from this dissertation are allowable without special permission, provided that accurate acknowledgement of source is made. Requests for permission for extended quotation from or reproduction of this manuscript in whole or in part may be granted by the Competent Authority of HBNI when in his or her judgment the proposed use of the material is in the interests of scholarship. In all other instances, however, permission must be obtained from the author.

Monali Kawade

DECLARATION

I, hereby declare that the investigation presented in the thesis has been carried out by me. The work is original and has not been submitted earlier as a whole or in part for a degree / diploma at this or any other Institution / University.

Monali Kawade

This thesis is dedicated to…….

My Three N's, Nitin, Nilay and Nihira!!

Also to the spirit of Science

Acknowledgement

I have saved the most important thank you's for last. These go to my family. Each one of you have played a critical role in my success and survival. Thank you for all of your love and encouragement. To my Mother and Father especially, you have played an important role in shaping me into the person I am today. You taught me by your example to put faith and family above everything else, and for that I am eternally grateful. A huge thank goes to my sister, Ms. Vrushali Pande for constantly sustaining me with courage and perseverance.

I am so fortunate to have two wonderful families. I don't think it is especially common to find someone you want to marry that comes with a family that you love so much, too. Thank you for making me feel so welcome and loved.

And above all I want to express my gratefulness to Nitin, who have been a huge factor in enabling me to achieve my goals so far and has provided more love, more support that one man can bestow. I love you for each and everything that you do and for all that you mean to me. My words here can never be enough.

CONTENTS

SYNOPSIS

INTRODUCTION:

Photodissociation is the formation of two (or more) fragments following absorption of light by a molecule. The microscopic studies of a photodissociation process provides the information on primary photochemical channels, branching ratios, fragment state distributions, and internal energy partitioning among the fragments, which help to explain the dynamics of the process itself. In a photodissociation, the dynamics underlying the process is probed by measuring the formation time of the fragments and the distribution of the available energy into various products states. The photodissociation dynamics is a subset of the chemical dynamics, which deals with the investigation of microscopic details of the chemical reactions, at the molecular level. This arena has developed very fast with its current state-of-the-art ability to look at the details of an elementary act that occurs during the course of chemical change both at spectral and temporal level. The fundamental level understanding of photodissociation process is of an immense importance in chemistry.

The photodissociation processes involve the breaking of a bond leading to the formation of fragments. These radical fragments are quickly transformed into other species and even the stable molecules may result from secondary reactions, in particular, that of radical recombination. So, we can say the stable products may or may not be the fragments produced by photodissociation. When a molecule is excited to an energy level, above the threshold energies for two different product channels, it can, in principle, dissociate in two different ways. The higher the photon energy, the more dissociation channels are open and various fragments can be formed. Dissociation of polyatomic molecules can give rise to chemically different channels, whose branching ratios are often strongly energy-dependent. Typically, at the lowest

energy, the mechanism of dissociation is a simple bond cleavage, a two-centre process. As the photon energy increases, dissociation can take place by three- and four-centre mechanisms and atomic migration also can take place over an internal barrier, producing molecular fragments.

The complete characterization of the products resulting from photodissociation is essential, as it demonstrates how the initial photoexcitation of the reactant molecule is channelled into the multitude of product degrees of freedom. A general way to study photodissociation is to use one laser (known as pump) to dissociate a molecule and a second laser (known as probe) to detect the fragment state-selectively, within a short time after its formation. The typical pressure of compound (P) and the pump-probe delay time (Δt) are in such a combination ($P \cdot \Delta t \leq 2 \times 10^{-9}$ Torr-sec.) that most of the nascent fragments have not undergone any collisions. Thus for all practical purpose, we can assume that the probed species are the nascent primary products of photodissociation. Such laser-based detection is achieved by various experimental techniques, such as laser induced fluorescence (LIF) and resonance enhanced multiphoton ionization (REMPI). These pump-probe techniques are extensively employed in this thesis for investigation of dynamics of a photodissociation process.

LIF is an emission-based spectroscopic technique, where the species to be detected is electronically excited in an emissive state by absorption of light emitted by a laser. Thus, this technique is suitable for only fluorescent molecular species. Molecules that absorb laser light make transition into excited electronic states, and eventually return to the ground electronic state via radiative means (i.e. by emission of light). In LIF, the use of a laser as an excitation source offers the advantage of greater selectivity and sensitivity in detection. The excitation, using specific light wavelengths within the absorption spectrum, of a particular species allows the

identification of the species, with high certainty. Laser sources also offer the possibility of high-resolution measurements, useful for the detection of small traces of compounds within a matrix of other compounds.

In LIF, the emission takes place in a short interval after the initial light absorption event (in around 10^{-15} s). The time needed for fluorescence intensity to decrease to 1/e of its original value, is known as the 'fluorescence lifetime', which is usually of the order of few ns to μs. The temporal characteristics, the intensity of the emission and its spectral features, together provide data for unambiguous identification of the species.

REMPI of internally cooled molecules, prepared in a supersonic expansion, has proven to be a useful technique for studying the spectroscopy of the complex chemical species. The combination of supersonic molecular beam, REMPI and time-of-flight (TOF) mass spectrometer (MB-REMPI-TOFMS) has potential of detecting the chemical species state and mass selectively. This is in contrast to LIF techniques, which provide the same spectroscopic information but lack the mass selectivity. In photodissociation dynamics studies, the molecular beam of cooled molecules, prepared by supersonic expansion of reactant molecules seeded in the buffer gas, is photolysed and the nascent fragments are measured state-selectively by REMPI-TOFMS technique. The non-resonant multiphoton ionizations were avoided to preserve the species selectivity by using the low energy laser pulses, while performing the REMPI.

The thesis presents the photodissociation dynamics studies of organic compounds with different functional groups. The dissociation is induced by a monochromatic laser and the photofragments were probed state-selectively by employing either LIF or (2+1) REMPI technique. All the experiments were performed

at few mTorr compound pressure and very short pump-probe delay time is maintained to ascertain that most of the probed photofragments are in their nascent state. In Chapters 3, 4 and 5 dissociation dynamics studies on oximes, diketone and nitro-compounds, respectively, have been presented. In these studies, the nascent OH photofragment is probed by employing the LP-LIF technique. The Chapters 6 and 7, cover the dissociation dynamics studies on fumaryl chloride and halogenated thiophenes at 234 nm, respectively. In these investigations, REMPI-TOFMS was employed for probing halogen atom photofragments. The thesis consists of eight chapters for a clear presentation of the work carried out. Brief overview of these chapters is given in the following paragraphs.

CHAPTER 1

This is an introductory chapter giving a brief account of the general overview of photodissociation dynamics and importance of its study. A remarkable development in these studies after the advent of lasers in sixties is highlighted. Various aspects of a photodissociation process, which help in understanding the dynamics of the event, are discussed. The general methods for preparing the electronically excited states of molecule, which leads to its dissociation, either from the prepared state or some other coupled states, are also described. All the investigations presented in the thesis are carried out in the gas phase, where one of the three different experimental conditions, (i) static or bulbs, (ii) flow, and (iii) molecular beam, was employed. The essential features of all the three conditions are described.

The various sensitive physical techniques were employed in the literature for probing a photodissociation event, like photofragment translational energy, laser-induced fluorescence, resonance enhanced multiphoton ionization, etc. These

techniques are described briefly. Basic concepts, like potential energy surfaces of reactants and products, partitioning of the available energy into internal states of the nascent products, and the models available for explaining this distribution, have been presented, in the context to the work of the thesis. As the computational chemistry is a vital adjunct to experimental studies, an *ab initio* molecular orbital calculations and semiempirical calculations employing Gaussian programme[1] are discussed. These theoretical calculations are used for supporting the experimental results in this thesis. The geometry and the relative potential energies of the molecules, as well as the transition states of the reactions, are optimized at different levels of theory, using suitable basis sets, to define the molecular parameters.

To show the relevance of photodissociation dynamics in bond selective chemistry, a brief description of the latter is included in this chapter. This has been done to give the due importance to laser based reaction control methodology, which has been an everlasting challenge to chemists and chemical physicists. Coherence control in time and frequency domain, with the help of intense lasers, is a promising tool to realize such a dream.

CHAPTER 2

The second chapter deals with experimental techniques and instrumentation employed to execute the experimental part of the thesis. Two very sensitive and selective, Laser Photolysis-Laser Induced Fluorescence (LP-LIF) technique and Molecular Beam-Resonance Enhanced Multiphoton Ionisation-Time of Flight Mass Spectrometry (MB-REMPI-TOFMS) have been used to detect transient species and to obtain the dynamical information on a dissociation process. The photodissociation was carried out under a collision-free condition of either a flow system or molecular beam environment, and dynamics investigated by LP-LIF and REMPI.

LIF is a very sensitive detection technique, with the level of detection being as low as 10^9 molecules cm^{-3}. A flow system with very low dynamic pressure, together with very short (50-100 ns) pump-probe delay. is used to ascertain a collision-less condition[2,3]. In this set-up, the unimolecular dissociation of a compound is induced by absorption of high power monochromatic pulsed laser (excimer laser), and the nascent products are detected and monitored by recording their fluorescence excitation spectra, employing a tunable laser. The OH fragment is probed by exciting the $A^2\Sigma \leftarrow X^2\Pi$ system, using the frequency doubled output (306-309 nm) of a dye laser, pumped by a seeded Nd:YAG laser, and monitoring the subsequent $A \rightarrow X$ fluorescence. Suitable optics were used to collect the fluorescence and illuminate a photomultiplier tube (PMT), the signal output of which was fed into a boxcar for gate integration and digitization. The scanning of the dye laser and the data acquisition were controlled by a Pentium personal computer (PC).

In REMPI, a single laser beam was employed for photodissociation of parent molecules as well as ionization of the photoproducts Cl/Br ($^2P_{3/2}$) and Cl*/Br* ($^2P_{1/2}$) atoms. The required wavelengths of the laser beam were generated by a Quantel dye laser with frequency doubling and mixing modules, pumped by a seeded Nd:YAG laser, using Rhodamin 101 dye. The generated atomic and molecular ions are detected using a detector system, consisting of a two-stage Wiley–McLaren[4] TOF mass spectrometer, with an extraction and an acceleration region, and 18 mm dual MCP. The TOF profiles were obtained by feeding the detector output to a digital storage oscilloscope for digitization and averaging. The REMPI spectra of Cl/Br ($^2P_{3/2}$) and Cl*/Br* ($^2P_{1/2}$) were measured by scanning the laser frequencies through their absorption transitions, and feeding the signal to a gated boxcar integrator, which after digitization passed on to the PC via GPIB interface, for data acquisition and analysis.

CHAPTER 3

In chapter 3, the dynamics of the N-OH bond scission of cyclohexanone oxime (CHO) and cyclopentanone oxime (CPO) to produce OH, on excitation at 193 nm, is presented. The oximes are molecules with a C=N─OH functional group and have many important applications in synthesis[5], medicine[6], and industries[7]; hence, these compounds are produced in relatively large quantities. The CHO and its lower homologue CPO are employed extensively for synthesis purpose[7]. In this work, the OH photofragment formed after photodissociation was detected state-selectively employing the LP-LIF technique. The partitioning of the available energy in the relative translation, rotation, and vibration of the photoproducts was measured. The *ab initio* calculations were carried out to identify the excited states as well as the transition states involved in the N─OH bond dissociation. These calculations suggested that both CHO and CPO molecules at 193 nm are excited to the S_2 state, which relaxes fast to the T_2 state. Subsequently, the N─OH bond dissociates from the T_2 state to produce OH (v'', J''). In both CHO and CPO, this dissociation channel has an exit barrier, since the corresponding transition state for OH formation could be located. Except for some differences in the values of energy partitioned to different degrees of freedom of products in CHO and CPO, the overall dissociation dynamics for the OH producing channel remains similar. Thus, the effect of the ring size of CHO and CPO is not pronounced on the dynamics of the N─OH bond dissociation. These results on the dynamics of the N─OH bond dissociation in the cyclic oximes, CHO and CPO, were compared with that in non-cyclic acetoxime.

CHAPTER 4

In this chapter, we report the dynamics of generation of the transient OH radical, detected by LIF, on photoexcitation of 1,2-cyclohexanedione (CHD) at 266,

248, and 193 nm in the gas phase. The CHD belongs to the α,β–enone class of compound, whose detailed photochemistry has been studied in recent years[8-10]. The photodissociation dynamics studies of acetylacetone[10], a α,β-enone and β–diketone, at 266, 248, and 193 nm and detection of the OH photoproduct have been previously done in our laboratory. The dissociation dynamics of CHD, a α–diketone, can be different from that of acetylacetone, α,β–diketone. However, the enolic form of CHD is also a α,β–enone, similar to enolic acetylacetone. The only structural difference between the two enone systems is the position of the OH group. Thus, it will be interesting to investigate the dissociation dynamics of CHD, and compare it with that of acetylacetone.

In the above context we have measured the partitioning of the available energy among translational, rotational, and vibrational degrees of freedom of the photoproduct, OH. Based on experimental results, coupled with *ab initio* molecular orbital calculations, we have proposed a plausible mechanism of OH formation. At 266 nm, the rotational population of the OH fragment is characterized by two types of Boltzmann-like distributions, while at 248 nm by a single distribution. At 266 nm photodissociation, the OH formation with higher rotational temperature is attributed to an H–bonded excited state, characterized by H-bonded T_1 state. While at 248 nm and 266 nm, OH formation with lower rotational temperature, is assigned to be formed from a mixture of S_1/T_2, where the H–bonding is not effective. The exit barrier for the OH dissociation channel is estimated to be ~14 kcal/mol. At 193 nm excitation, the initially prepared Rydberg state can cross over to a nearby π^* repulsive state along the C–O bond, from where the dissociation can take place. The existence of a dynamical constraint due to strong hydrogen bond in the ground state is effectively present in the dissociation process at 266, and somewhat minimized at 248

nm photolysis. We have compared the results with the enolic acetylacetone photodissociation, to get a better insight of the dissociative pathway leading to OH formation.

CHAPTER 5

We have observed OH formation on photodissociation of o-nitrotoluene[11] (o-NT), which is assigned to the transformation from the parent (o-NT) to the suitable isomer containing OH. The present work on photodissociation of 2-chloro-5-nitrotoluene (ClNT) was undertaken to determine the influence of Cl atom on OH formation dynamics. We have also investigated OH formation dynamics from electronically excited nitrocyclopentane (NCP), to compare it with our previous work on aliphatic nitro compounds[12,13], and deduce the effect of ring on OH formation dynamics. Thus, the work presented in this chapter, on halogenated aromatic nitro compound and cyclic nitroalkane, is an extension to the earlier work.

In the present investigation, the OH radical is detected on photolysis of ClNT at 193, 248 and 266 nm and NCP at 193 nm, using LIF technique. The complete set of 30 measured OH radical Doppler profiles was evaluated to determine the average energy released into the product translation in the laboratory system. A dissociation mechanism is proposed based on thermo-chemical data obtained from the *ab initio* calculations.

CHAPTER 6

This chapter provides the details of the investigation on photodissociation dynamics of fumaryl chloride (ClCO—CH=CH—COCl), a molecule with two C=O groups and a C=C group in conjugation, in a supersonic molecular beam at around 235 nm. Fumaryl chloride is a planar molecule with three stable isomers, out of which two isomers belong to the C_{2h} point group and the third belongs to the C_s point

group[14-17]. The relative abundances of trans-trans, cis-cis and trans-cis isomers are found to be 30%, 24%, and 46%, respectively, at 480 K[17]. It has a symmetric structure with both carbonyl groups associated with an identical functionality. Fumaryl chloride has variety of synthetic[18-20] applications. The chlorine atom product in both the ground state ($^2P_{3/2}$) and the spin-orbit excited state ($^2P_{1/2}$) has been detected using the REMPI-TOF technique. The translational energy distributions for both types of chlorine atoms and relative quantum yield of Cl* have been measured. The anisotropy parameter (β) is evaluated from polarization dependent studies to gain further insights. The energy partitioning into the translational mode having the fast and slow components is interpreted with the help of an impulsive model and a statistical model, respectively. The measured fraction of available energy going to relative translation (f_T value) for a slow chlorine atom is nicely described with the statistical model and that for the fast Cl atom channel is slightly higher than the predicted value of 0.32, by the impulsive model. Apart from the chlorine atom elimination channel, the molecular HCl elimination is also observed in the photodissociation of fumaryl chloride. Finally, it is proposed that in fumaryl chloride the initially prepared $S_2(^1\pi\text{-}\pi^*)$ state crosses over to various states, namely, $S_1(^1n\text{-}\pi^*)$, (n-σ^*), and the ground state, and the Cl atom can be formed from all these states, with different values of f_T.

CHAPTER 7

In Chapter 7 the photodissociation dynamics of two halogen-substituted thiophenes, namely, 2–chlorothiophene and 2–bromo–5–chlorothiophene, is studied. The halogen-substituted thiophenes are the most studied thiophenes from the viewpoint of photochemistry and applications[21-23]. The dynamics of halogen atom (X/X*) formation, around 235 nm, in a supersonic molecular beam is investigated, using the REMPI-TOF technique. The anisotropy parameters for both Cl(Cl*) and

Br(Br*) are the same, and characterized by values of 0.0±0.05. In the translational energy distribution for the chlorine atom elimination channel in the case of 2−chlorothiophene, we have observed two components for Cl, but only one component for the Cl*. The average translational energies for the fast and the slow components of the Cl channel are 3.0±1.0 and 1.0±0.5 kcal/mol, respectively. For Cl*, the average translational energy is 3.5±1.0 kcal/mol. However, for 2–bromo–5–chlorothiophene, we have observed only one component for all the halogen atom channels in translational energy distribution. The average translational energies for the Cl and Cl* channels are 3.5±1.0 and 5.0±1.0 kcal/mol, respectively. Similarly, the average translational energies for the Br and Br* channels are 2.0±1.0 and 3.5±1.0 kcal/mol, respectively. The partitioning of the available energy into the translational modes is interpreted with the help of impulsive and statistical models. Further, theoretical calculations have been carried out to understand the dissociation dynamics of these molecules.

CHAPTER 8

This chapter provides a summary to the work carried out in this thesis and a future direction in regard to this work to acquire an assistive knowledge. The thesis presents investigations on the dynamics of OH formation using LP-LIF technique at 193/248/266 nm and that of Cl/Br formation around 234 nm, using REMPI technique, in selected organic molecules. The photodissociation dynamics of cyclohexanone and cyclopentanone oximes, 1,2-cyclohexanedione, 2-chloro-5-nitrotoluene and nitrocyclopentane are studied using LP-LIF technique, while that of fumaryl chloride and halogenated thiophenes have been investigated employing REMPI technique. Partitioning of the available energy in different modes of the photoproducts has been discussed. Angular distributions of the products were estimated by performing the

polarization experiments in the REMPI measurements. The mechanism of the photodissociation reactions has been proposed using experimental results and theoretical supports.

FUTURE DIRECTIONS

The better insight of OH formation dynamics in photodissociation of polyatomic molecules, carried out in the present work, can be obtained by performing polarization experiments for the OH fragment. From the angular distributions information obtained from these studies, the vector quantities associated with the photodissociation process can be estimated. In all the work reported in the thesis employing REMPI technique, the photolysis as well as ionization was carried out by single laser beam (same wavelength, single colour experiments). The better information about excited PESs and their interaction can be deduced by accessing various excited PESs. This will be possible by performing two colour experiments by employing different frequencies for pump and probe. The resolution in translational energy distribution measurement can be improved (better than 1%) by employing the velocity map imaging (VMI) techniques. Using both LP-LIF and REMPI techniques, the available energy partitioning in various states of OH/Cl or Br was obtained. However, the energy partitioning in the co-fragment was not measured. The measurement of energy distribution in co-fragment of OH/Cl will provide more dynamical information about the system and thus the predicted nature of dissociative PES will be more accurate.

Because of computation resource constraints we have used lower level of theoretical calculations to support the experimental results. This invariably has higher error level, which can be reduced to a greater extent by performing calculations at higher level using Linux system. This, in particular, will be useful in deducing the

dynamics of dissociation process occurring on the dissociative surfaces having strong interaction with other nearby PESs. Thus, high level of theoretical calculation is required to obtain more refined results in regard to the dynamics of the dissociation process.

References

[1]   M. J. Frisch, G. W. Trucks, H. B. Schlegel, G. E. Scuseria, M. A. Robb, J. R. Cheeseman, J. A. Montgomery, T. V. Jr., K. N. Kudin, J. C. Burant, J. M. Millam, S. S. Iyengar, J. Tomasi, V. Barone, B. Mennucci, M. Cossi, G. Scalmani, N. Rega, G. A. Petersson, H. Nakatsuji, M. Hada, M. Ehara, K. Toyota, R. Fukuda, J. Hasegawa, M. Ishida, T. Nakajima, Y. Honda, O. Kitao, H. Nakai, M. Klene, X. Li, J. E. Knox, H. P. Hratchian, J. B. Cross, C. Adamo, J. Jaramillo, R. Gomperts, R. E. Stratmann, O. Yazyev, A. J. Austin, R. Cammi, C. Pomelli, J. W. Ochterski, P. Y. Ayala, K. Morokuma, G. A. Voth, P. Salvador, J. J. Dannenberg, V. G. Zakrzewski, S. Dapprich, A. D. Daniels, M. C. Strain, O. Farkas, D. K. Malick, A. D. Rabuck, K. Raghavachari, J. B. Foresman, J. V. Ortiz, Q. Cui, A. G. Baboul, S. Clifford, J. Cioslowski, B. B. Stefanov, A. L. G. Liu, P. Piskorz, I. Komaromi, R. L. Martin, D. J. Fox, T. Keith, M. A. Al-Laham, C. Y. Peng, A. Nanayakkara, M. Challacombe, P. M. W. Gill, B. Johnson, W. Chen, M. W. Wong, C. Gonzalez, and J. A. Pople, Gaussian 03 (Gaussian, Inc., Pittsburgh, PA, , 2003).

[2]   P. D. Naik, H. P. Upadhyaya, A. Kumar, A. Sapre, and J. P. Mittal, Chem. Phys. Letters 340, 116 (2001).

[3]   P. D. Naik, H. P. Upadhyaya, A. Kumar, A. V. Sapre, and J. P. Mittal, Journal of Photochemistry and Photobiology C: Photochemistry Reviews 3, 165 (2003).

[4]   W. C. Wiley and I. H. McLaren, Rev. Sci. Instrum. 26, 1150 (1955).

[5]   I. C. Choong and J. A. Ellaman, J. Org. Chem. 64, 6528 (1999).

[6]   K. Rose, J. Am. Chem. Soc. 116, 30 (1994).

[7]   H. Kath, R. Glaser, and J. Weitkamp, Chem. Eng. Technol. 24, 150 (2001).

8 A. Trivella, T. N. Wassermann, J. M. Mestdagh, C. T. Manca, F. Marinelli, P. Roubin, and S. Coussan, Phy. Chem. Chem. Phys. 12, 8300 (2010).

9 W. M. Horspool, Photochemistry 35, 17 (2005).

10 H. P. Upadhyaya, A. Kumar, and P. D. Naik, J. Chem. Phys. 118, 2590 (2003).

11 S. SenGupta, H. P. Upadhyaya, A. Kumar, S. Dhanya, P. D. Naik, and P. Bajaj, Chem. Phy. Lett. 452, 239 (2008).

12 S. Sengupta, Y. Indulkar, A. Kumar, S. Dhanya, P. D. Naik, and P. N. Bajaj, J. Phys. Chem. A 112, 12572 (2008).

13 A. Saha, M. Kawade, H. P. Upadhyaya, A. Kumar, and P. D. Naik, J. Chem. Phys. 134, 044316 (2011).

14 J. E. Katon and J. W. R. Feairheller, J. Chem. Phys. 47, 1248 (1967).

15 D. F. Koster and T. P. Vasiloff, Spectrochim. Acta 27, 1633 (1971).

16 N. Pietri, B. Jurca, M. Monnier, M. Hillebrand, and J. P. Aycard, Spectrochimica Acta Part A 56, 157 (1999).

17 K. Hagen, J. Mol. Struct. 128, 139 (1985).

18 E. Jabbari, J. A. Gruetzmacher, L. Lu, B. L. Currier, and M. J. Yaszemski, Proc. of the 25th Annu. Inter. Confer. of the IEEE EMBS, Cancun, Mexico., 2003.

19 M. Mahmoudi, A. Simchi, M. Imani, and U. O. Hafeli, J. Phys. Chem. C 113, 8124 (2009).

20 S. Maaref, Z. Roz, S.-S. Sun, K. Seo, K. Winston, and C. E. Bonner, J. Appl. Poly. Science 92, 317 (2004).

21 J. W. Rabalais, L. O. Werme, T. Bergmark, L. Karlsson, and K. Siegbahn, Int. J. Mass Spectrom. Ion Phys. 9, 185 (1972).

22 A. W. Potts, A. B. Trofimov, J. Schimer, D. M. P. Holland, and L. Karlsson, Chem. Phys. 271, 337 (2001).

23 A. B. Trofimov, J. Schirmer, D. M. P. Holland, L. Karlsson, R. Maripuu, K. Siegbahn, and A. W. Potts, Chem. Phys. 263, 167 (2001).

LIST OF FIGURES

induced photodissociation of CHO (a) and CPO (b) at 193 nm.

LIST OF TABLES

CHAPTER 1

INTRODUCTION

The chemistry is the science that deals with or investigates the composition, properties, and transformations of substances and various elementary forms of matter. Chemical transformation is the central theme of chemistry and the term photochemistry stands for all kinds of transformations initiated by light. Sunlight, which is coming from the surface at approximately 5800 K, is a rich source of "visible" photons. Many of chemical processes occurring in nature are usually initiated by light. Thus, photochemical investigation has great significance in those studies, which include a broad range of issues of fundamental importance, such as the interaction of light with matter, the quantum mechanical behavior of molecular systems, and the theoretical description of chemical reactions. The first photoinduced experiments were carried out in a glass reactor/cell, in which the gas or the gases under study were photolysed with light from a flash source, like a sodium or mercury lamp. These initial experiments were mainly concerned with the determination of the chemical nature of the fragments themselves or their reactive products[1]. These experiments were devised to understand the elementary chemical reactions in as much

detail as possible.

The fundamental level understanding of chemical reactions is of immense importance in chemistry. The investigation, which deals with the study of microscopic details of the chemical reactions, at the molecular level, comes under the branch of chemistry called *chemical dynamics*. It is concerned with both intramolecular motion and intermolecular collisions[2]. The spectroscopic studies furnish the information about the microscopic details of reactants and products states. The *spectroscopy* is the study of the dependence of physical quantities on frequency. It is the primary tool for remote sensing of physical conditions of molecules. The detailed information about structure and intramolecular dynamics of the molecules can be deduced from the emission or absorption spectra. If all of the relevant molecular processes are understood, the observed rotational/vibrational/electronic excitation can provide valuable information about the density, kinetic temperature, and the intensity of the radiation field in the probed volume. The structural and dynamical information is not only of fundamental interest, but is also valuable in many branches of chemistry. It gives insight of the chemical processes occurring in the probe, by providing molecular level information on the composition of the matter. Owing to experimental and theoretical developments, it is possible to design experiments to address the fundamental issues of a prototypical reaction. The results can be compared with quantum mechanical and classical dynamical calculations on multidimensional potential energy surfaces (PES). In this regard, the gas-phase reactions are more appropriate, as they devoid of solvent interaction. Gas-phase reaction dynamics, which is a branch of physical chemistry/chemical physics, is concerned with this issue and has an increasingly strong impact in many other areas of chemistry[3,4]. Reaction dynamics helps in understanding the molecular level mechanism of elementary

chemical and physical processes. It attempts to understand what actually takes place at that level when a chemical or physical change occurs. The experimentally and theoretically simple reaction, which furnishes the dynamical insight of the reaction system, is *photodissociation reaction*. The photodissociation process provides the simplistic view of unimolecular reaction and correlation between the dynamical information and features of PES. Many of the correlation are valid for a bimolecular process as well. The microscopic signature of photodissociation process is embedded in the population of individual states of photofragment.

In studying the dynamics of photodissociation reaction, main question needs to be answered, are: What is the nature of potential energy surfaces formed during excitations? How does the dissociation depend on the initial state or the temperature of the parent molecule? How is the available energy after dissociation is distributed and partition among the various degrees of freedom of the photoproducts? Which are the probable dissociation pathways that excited molecule can follow and what is the information that we get from the PES from which fragments fly apart?

In this thesis, an attempt is made to correlate the partitioning of the available energy in photodissociation process to the features of initially prepared excited state, its interaction with other states and PES of the state on which dissociation takes place, by studying the photodissociation dynamics of a few organic molecules with the help of experimental techniques and theoretical assistance. In the experiments, the partitioning of the available energy in the product states, formed from the photoexcited reactant molecules, is probed by employing state selective and sensitive techniques, such as laser induced fluorescence (LIF) and resonance enhanced multi-photon ionization (REMPI). The aim in studying the reaction dynamics of the molecules is to understand the mechanism of the various possible photodissociation

pathways, the effect of different functional groups on reaction mechanism and to correlate the features of PES with the dissociation dynamics.

1.1 TYPES OF ELECTRONIC TRANSITIONS IN ORGANIC MOLECULES

A molecule is excited to an electronic state on absorption of a UV-visible photon. There are different types of electronic transitions depending on the nature of molecular orbitals (MO) involved. Kasha[5] had evolved a convenient notation for expressing various electronic transitions in organic molecules in terms of initial and final orbitals involved in the transition. In general, three types of orbitals σ, π or n, are involved in the transition. An electron from any occupied orbital can be promoted to one of the higher unoccupied levels (σ* or π*) on absorption of radiation of appropriate wavelength[6]. A clear picture of all these different types of transition is shown in FIG. 1.1, for a typical carbonyl molecule, formaldehyde, $H_2C=O$.
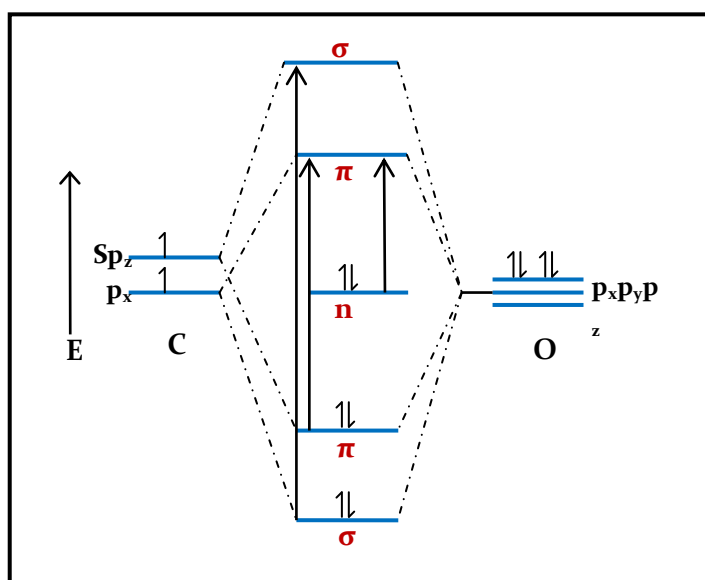
FIG. 1.1: Molecular orbitals, their approximate energy levels and type of transitions in formaldehyde molecule. In the formation of >C=O bond, the six electrons, four from oxygen and two from carbon, are accommodated in the three lower energy levels of σ, π and n[8].

The representation considering the overall symmetry of the corresponding MO

is the most useful way to designate an electronic energy state of a molecule. But for polyatomic molecules, where the details of the electronic structures are not known, the above mapping is difficult. The most common method for such complex molecules is to denote the energy states simply by their spin multiplicity, defined as $2S+1$, where S is the spin quantum number. Thus, an electronic state with all its electrons spin-paired has $S = 0$, multiplicity is 1. Such electronic states are referred as the singlet states and denoted by the symbol 'S'. States having a total electron spin quantum number of 1, and thus having multiciplicity of 3, are called triplet states and represented by 'T'. Each one of these electronic levels has a number of vibrational levels and each vibrational level in turn has a set of rotational levels. In FIG. 1.2, S_0, S_1, S_2 denote, respectively, the ground, first and second excited singlet electronic states of a molecule and T_1, T_2 etc. the states in the triplet manifold. In the condensed phase, the Jablonski diagram (FIG. 1.2) best illustrates the photophysical process of electronically excited molecules that has been prepared by UV or visible light irradiation. Molecules excited to electronic states return to ground state through a variety of deactivation mechanisms. If a molecule gets excited to higher electronic states S_2, S_3 etc. or higher vibrational states in the S_1 state, it returns to the lowest vibrational states in S_1 rapidly through the process known as internal conversion (IC). Molecules can undergo a conversion to the first triplet state T_1 through the process known as inter system crossing (ISC). Molecules can also make a direct transition to the ground electronic state through luminescence. The luminescence from the S_1 state to S_0 state is referred to as fluorescence and from T_1 state to S_0 state is known as phosphorescence. However, transitions from T_1 state to the ground state are forbidden and hence phosphorescence emissive rates are several orders of magnitude slower than those of fluorescence. It may be noted that in the gas phase, the collision-induced

processes are less efficient and hence Jablonski diagram depicted in FIG. 1.2 is not fully applicable to understand the fate of an excited molecule in the gas phase.
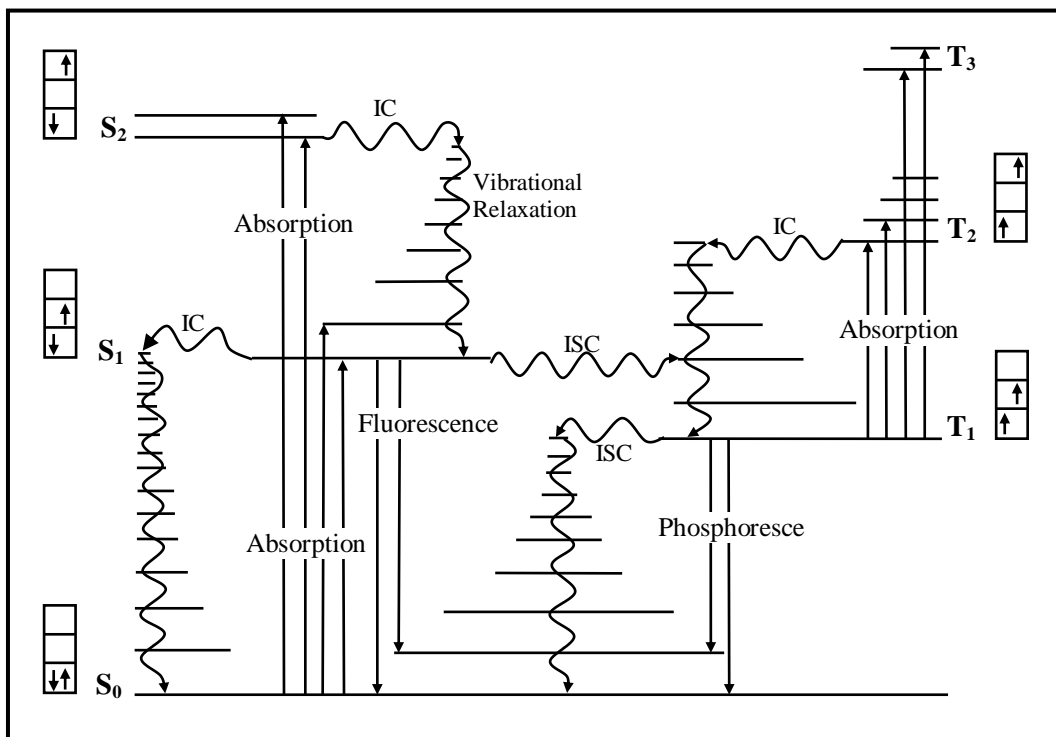
FIG. 1.2: The Jablonski diagram, showing different photo-physical processes undergone by an excited state molecule in condensed phase. Straight and wavy arrows represent radiative and non-radiative processes respectively. The spin of electrons in each of the singlet states (paired spin) compared to the triplet state (unpaired spin).

The photophysical processes, which an excited state may undergo in, gas phase, are similar to that of condensed phase. But the non-radiative relaxation of upper vibrational level of excited electronic state to zero vibrational level of first electronic excited state; by losing the excess energy to surrounding does not take place in gas-phase, as the rate of collisional deactivation is very low compared to other physical and chemical processes. The fluorescence occurs from the same ro-vibronic level of higher state to which the molecule was initially excited. The photophysical process for gas-phase is shown in FIG. 1.3.
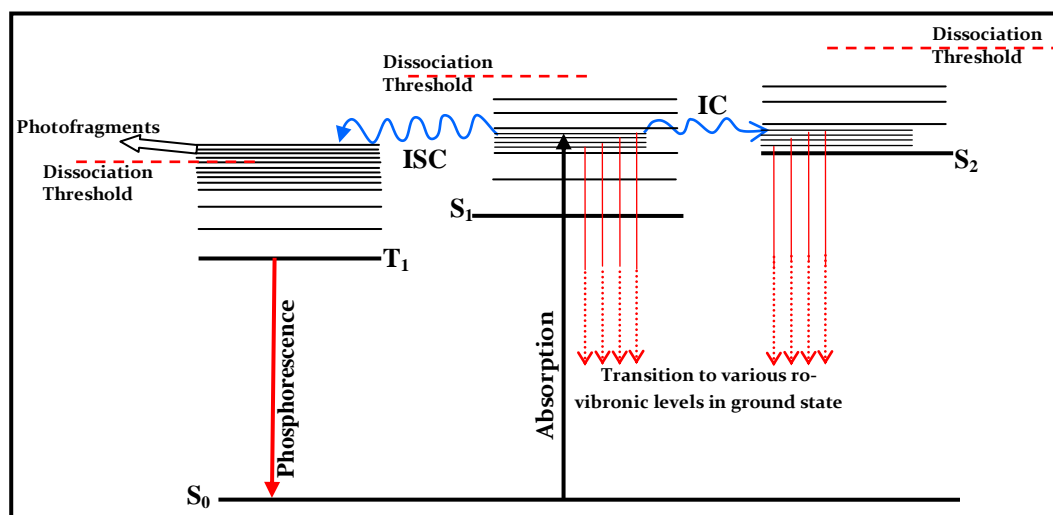
FIG. 1.3: Energy levels of molecular excited states and transitions between them. Figure also depicts a pathway for dissociation of electronically excited species. Here population prepared in S1 state is transferred to T1 state, which is well above its dissociation threshold and thus dissociates to form photofragments.

When a molecule is excited to an upper state, its energy and electron wave function differ from the ground state. The excited molecule undergoes photophysical processes such as radiative and non-radiative relaxations for returning to the ground state, unless it gets involved in a photochemical reaction and loses its identity. On excitation, the reactivity of molecule is altered and it can undergo various photochemical processes, such as photodissociation, photo-isomerism or photo-rearrangement, photo-oxidation etc. In the next section, the photodissociation process is discussed in detail, as the work in this thesis is based on the photodissociation of molecules and dynamics resulting from that.

1.2   PHOTODISSOCIATION DYNAMICS

The fragmentation of a bound molecule through absorption of one or more photons is called ***photodissociation***. The electromagnetic energy of the light beam is converted into internal energy of a molecule and if that energy exceeds the binding energy of the weakest bond then that bond will break apart. Photodissociation reactions occur under the constraint of energy and total angular momentum conservation. On photodissociation, the available energy is distributed to various

degrees of freedom, both translational and internal (electronic, vibrational, and rotational). Vector correlations reveal the interrelations between many directional properties relevant to the photodissociation reaction. Photodissociation dynamics have now become a new form of molecular spectroscopy, providing the detailed information on the nature of chemical bonding both in static and dynamic contexts. The nature of various intramolecular interactions can also be unraveled through the study of the dynamics of photodissociation process.

1.2.1   ROLE OF LASERS IN PHOTODISSOCIATION

Photodissociation process is studied for a long time as a part of photochemistry. However, dynamics studies of photodissociation process have made great progress in the last three to four decades (1970-onwards). The advent of lasers, together with the development of highly sensitive and fast response detection methods, gave a large driving force to the investigation of photodissociation reaction dynamics. The year 1970 in which LASER application were invented corresponds to the dawn of a new era and a magic door to the secrets of photodissociation was opened. Lasers represent intense light sources with spectral energy densities of magnitude several orders higher than that of other incoherent sources. The extremely small bandwidth of single mode lasers allows a greater spectral resolution. Many experiments, which could not be done before the application of lasers, because of lack of intensity or insufficient resolution, are readily performed with lasers. The high intensity and spectral monochromaticity of lasers have opened a new class of spectroscopic techniques, which allow the investigation of the structure of atoms and molecules in much detail. Besides these applications, lasers have been very important to the studies of photodissociation dynamics for a variety of reasons.

(1) The very narrow energy spread of laser light can be exploited in order to prepare

parent molecules in a particular vibronic and even ro-vibronic level. The fate of these molecules can be followed in a very clean way in the studies carried out in the gas phase where low collision frequency is responsible for a very negligible energy exchange with other coexistent species, in a short time window.

(2) The information on the distribution of photofragments among various internal states, including electronic, spin-fine structure, vibrational, rotational, and Λ-type doubling can be acquired by State-selective and highly sensitive detection of photofragments by laser-induced fluorescence (LIF), resonance enhanced multiphoton ionization (REMPI), etc.

(3) The time evolution of the course of reaction can be followed by working in the of pico/femtosecond time domain, using very short laser pulses.

(4) The vectorial characteristics of photodissociation mechanisms can be obtained by employing polarized laser light.

1.2.2   DIFFERENT METHODS OF PREPARING EXCITED STATE

The excited state can be prepared by various methods. Some of them are discussed below:

1.2.2.1 ONE PHOTON EXCITATION

In one photon excitation, a single photon of light is used to excite a molecule from its ground state to an upper energy state. One-photon excitation has a linear dependence on the intensity of the excitation light. A number of selection rules govern the transition between the states. These rules which are concerned with changes in angular momentum are

$$\Delta\Lambda = 0, \pm1 \quad \Delta S = 0 \quad \Delta\Sigma = 0 \quad \Delta\Omega = 0, \pm1$$

$$\text{where } \Delta\Omega = \Lambda + \Sigma$$

and Ω is the quantum number for the component of total angular momentum (orbital

and spin) around the internuclear axis. Λ is component of total orbital angular momentum about the internuclearar axis. S is total spin angular momentum number. Σ is component of total angular spin momentum about internuclear axis. There are two selection rules concerned with changes in symmetry given as follows,

(i) For Σ terms $\Sigma^+ \leftrightarrow \Sigma^+$ and $\Sigma^- \leftrightarrow \Sigma^-$ transitions are allowed, and

(ii) $u \rightarrow g$ and $g \rightarrow u$ transitions are allowed, but $u \rightarrow u$ and $g \rightarrow g$ transitions are forbidden, i.e., the transitions accompanied by a change of parity are only allowed.

1.2.2.2 MULTIPHOTON EXCITATION

In multiphoton excitation, two or more photons are used to excite a molecule. The interaction probability for single-photon absorption is more than multiphoton absorption but if two or more lower energy (longer wavelength) photons arrive simultaneously, there is some probability that they can excite the molecule as long as

$$(E_1 - E_0) = hc \left(\frac{1}{\lambda_1} + \frac{1}{\lambda_2} + \dots + \frac{1}{\lambda_n}\right) \tag{1.1}$$

where $\lambda_1 \dots \lambda_n$ are the wavelengths of individual photons, E_1 and E_0 are the energies of upper state and ground state, respectively. The absorption probability for photons is nonlinear and it increases with the nth power of intensity for n photon absorption.

The electronic excited states, which are not accessible by the conventional one photon absorption, are able to be identified and assigned by the multiphoton excitation. Here the overall transition can occur with no change in parity. Hence $g \rightarrow g$ and $u \rightarrow u$ transitions are observed. Therefore, the multiphoton excitation overcomes the symmetry barrier imposed by selection rule for angular momenta in the one-photon process. By multiphoton excitations, the transitions corresponding to vacuum UV region can be accessed by using visible photon.

The infrared multiphoton excitation (IRMPE) is very well known process because of its potential application to isotope separation. In this process, a polyatomic molecule can absorb number of photons through its vibrational ladder to reach sufficiently high energy levels in the ground electronic state from which it can undergo chemical reactions, isomerization, dissociation, etc.

1.2.2.3 VIBRATIONALLY MEDIATED PHOTOEXCITATION

Vibrationally mediated photoexcitation (VMP) is another method for preparing the excited state. The steps involved in this method are preparation of an initial ro-vibrational state in the ground state and subsequent excitation to an electronically excited state to evolve into the products. Here the molecule in the ground state absorbs one photon, which excites to a vibration in the ground electronic state[7]. The second photon promotes the vibrationally excited molecule to the repulsive electronically excited state FIG.1.4 [a] or to an energy level above the dissociation level (FIG. 1.4[b]) from which it dissociates to form products as shown in FIG. 1.4.
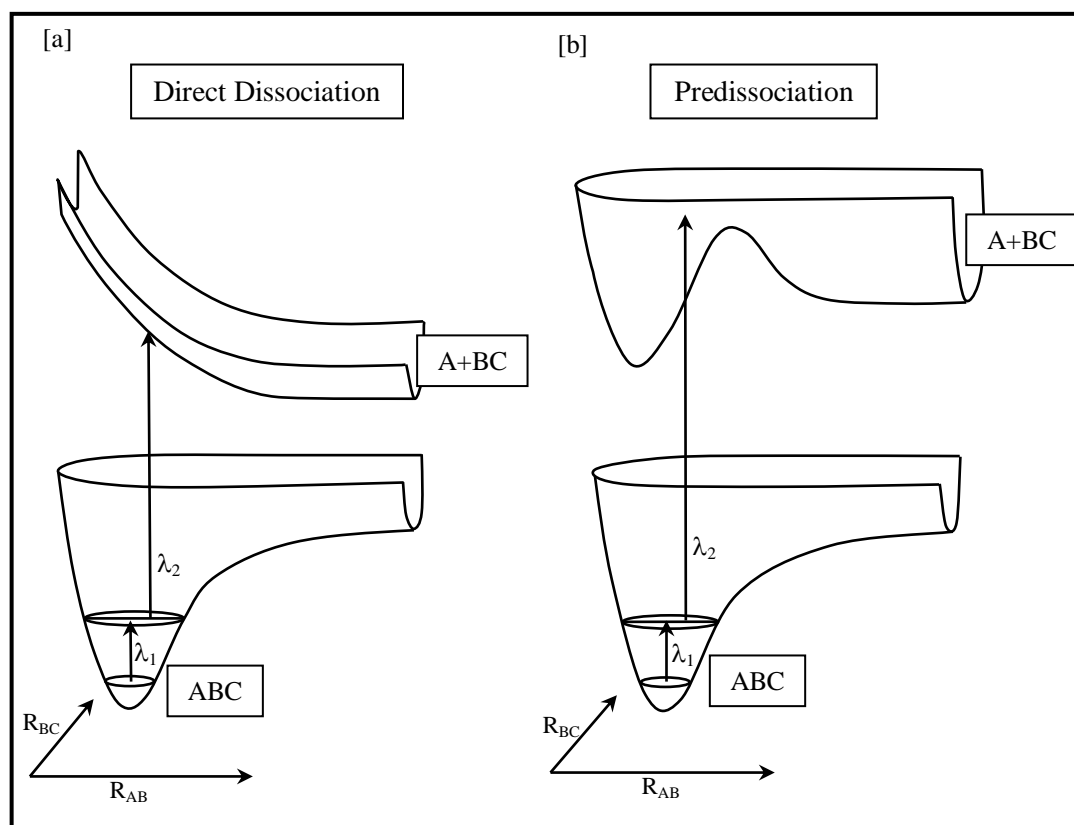
FIG. 1.4: Schematic drawings of ground and electronically excited potential energy surfaces illustrating VMP [a] directly dissociative excited states; [b] predissociative excited state[9].

1.2.3   TYPES OF PHOTODISSOCIATION

Photodissociation can be roughly classified as either ***direct*** or ***indirect dissociation***. The ***direct dissociation*** (FIG. 1.5[a]) is the simplest process in which a molecule absorbs a photon and gets excited to a repulsive state with respect to the nuclear co-ordinate. Since the spontaneous emission back to the ground state is a comparatively slow process (typical Einstein's coefficient of 10^9 s^{-1}), virtually all of the absorptions lead to dissociation of the molecule. In ***indirect photodissociation*** (FIG. 1.5[b], [c] and [d]) a potential barrier or some other dynamical constraint obstructs the immediate dissociation of the molecule. In an indirect process, the initial absorption generates a bound excited electronic state that subsequently interacts non-radiatively with a nearby repulsive electronic state. ***Predissociation*** (FIG. 1.5[b]) is the process, in which the interaction depends sensitively on the type of coupling and

on the energy level involved. The predissociation rates are typically comparable to or larger than the rates of spontaneous emission. In other type of ***predissociation*** (FIG. 1.5[c]) there is a potential well and a barrier at a close distance that blocks the dissociation channel. The barrier might be considered to be the result of an avoided
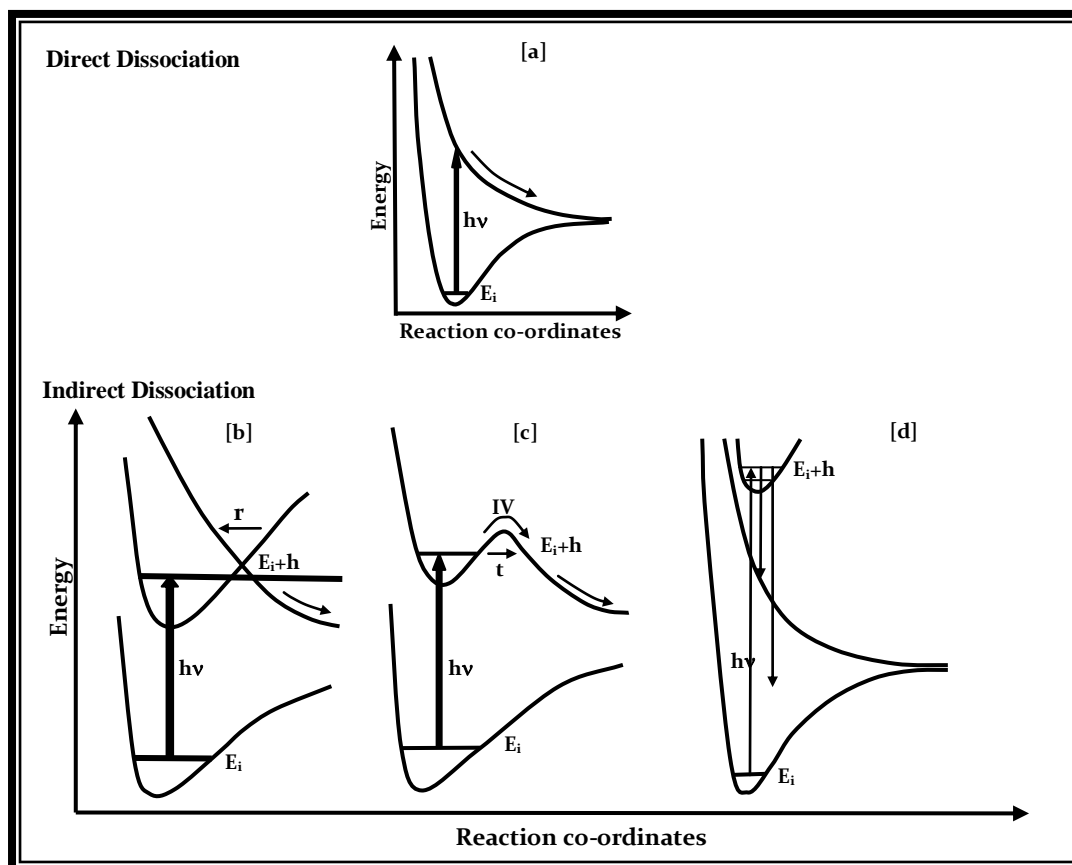
FIG 1.5: Photodissociation processes of diatomic molecules with initial internal energy. [a] Direct dissociation. [b] Electronic predissociation in which molecule undergoes radiationless transition (rt) from bound to the repulsive state and subsequently decays. [c] Vibrational predissociation in which the photon creates a quasi-bound state in the potential well which decays either by tunneling (tn) or by intramolecular vibrational energy redistribution (IVR). [d] Spontaneous radiative dissociation. E_i is the energy of the parent molecule.

crossing with a higher electronic state. In this case, the molecules are excited to quasi-stable (so called "resonance") states inside the well, and are prevented from immediate dissociation by the potential barrier. They can decay either by tunneling through the barrier or by intramolecular vibrational energy redistribution (IVR) between the various nuclear degrees of freedom, if more than two atoms are involved.

Apart from above mentioned predissociation, the excited bound states can dissociate through the *spontaneous radiative dissociation* (FIG. 1.5[d]), in which the emission of photons populates the continuum of a low-lying repulsive state or the vibrational continuum of ground electronic state. The efficiency of the above process is determined by the competition with spontaneous emission into low-lying bound states[8,9].

1.3   EXPERIMENTAL SYSTEMS

The gas-phase experiments can be carried out in different conditions, static, flow and molecular beam, depending on information to be accessed. Each of these experimental conditions is explained briefly as follows:

1.3.1   STATIC SYSTEM

A static system is a system comprising of suitable closed, constant volume container, to hold reacting species at a desired pressure. The reaction vessel is either jacketed to flow temperature controlled fluid or kept in a temperature-controlled environment, for carrying out gas-phase reactions at desired temperature. During the experiments, a finite time is required for the reactants to fill the vessel, mix with the other reagents and reach an equilibrated temperature. Hence, these types of systems are suitable for reaction with very low rate constant. A sample is drawn from the vessel periodically to measure product concentration or it is measured in situ. A major disadvantage of the static system is accumulation of the stable product, which interferes with the reaction of interest. This system was used in the present thesis for the stable product characterization. However, it was ensured that the extent of dissociation was less than 10%.

1.3.2 FLOW SYSTEM

A flow system is an open system, in that reactants continuously enter and product leaves the observation zone. The flow system can be used for moderately faster reactions for which a static system cannot be used. A linear flow velocity of several meter per second can be achieved with roots blower or other high speed pumps. If steady flow conditions are maintained, so that the concentration-distance profile is stable, a series of measurements may be made along the flow tube with sufficient time to afford a good signal-to-noise ratio. The flow reactors are ideal systems for handling the gases, which are toxic or associated with hazards. The detection techniques employed in flow-tube measurements are not simple to move along the flow in the tube; but in these cases, the distance is adjusted by moving the cross-section area of the reaction along the flow direction. Faster reactions can be measured using larger pumps to get faster flow rates and also lower partial pressures.

In the present thesis, flow tube studies are not employed for any research work, however, the gas phase studies on photodissociation dynamics presented in the chapter 3, 4 and 5 by using LP-LIF technique, are carried out in a flow condition to minimize the contribution from secondary reactions, by observing each pulse event on a fresh sample.

The flow experiments are carried out at low pressure of gaseous molecules, one of the reactant is generated in situ from its precursor and the short time window is maintained from the start of the reaction and the product measurements, to ensure collision-free conditions. This may be very difficult to attain in the case of very low sensitivity measurements. This limitation can be overcome by using the supersonic molecular beam experiments, in which collision free conditions are met maintaining a relatively high number density of the reactant.

1.3.3   MOLECULAR BEAM SYSTEMS

A molecular beam (MB) is defined as a well collimated stream of atoms or molecules moving through a high vacuum in a well-defined direction without undergoing collisions. The various advantages of performing MB experiments are single collision condition with reasonable high number density with controlled reactant velocity (translational energy) and internal energy. These also offer the possible measurement of angular, velocity, rotational and vibrational distribution of the products. The most important component in any MB experiment is the vacuum in which the beams are formed and their collisions are studied. Three major requirements of the vacuum techniques in any beam experiment are:

(i)   To provide mean free paths very long in comparison with beam path lengths, thus avoiding significant attenuation and the broadening of the beams.

(ii)   To maintain the density of background material at a much lower figure than the beam density in the collision target.

(iii)   To minimize the background densities in the beam detector chamber, particularly of species that are indistinguishable by the detector from the beam species.

Most thermal energy beam source utilize a flow system in which the beam material flows as a vapour from an oven, through an orifice, into the chamber of lower pressure. Here collimation and differential pumping stages are used to produce a final well defined beam in the experimental chamber. This type of system can be operated under two different regimes− 'molecular effusion' or 'hydrodynamic flow'.

In the molecular flow condition, the molecules move through the slit and beam without undergoing collisions. Their motion is thus mutually independent. Under these conditions the '*Knudsen number*' K_n, where

$$K_n = \frac{Mean\ free\ path\ in\ source}{smallest\ dimension\ of\ orifice\ e.g.slit\ width},\qquad(1.2)$$

is greater than 1. For the reverse condition with $K_n < 1$, hydrodynamic or bulk flow occurs through the orifice and for the some distance downstream. Collisions are frequent and energy transfer from the internal modes of molecules to the beam translational energy occurs. The spread in the speeds is so small that the molecules are effectively in the state of very low translational temperature (FIG.1.6). The translational temperature may reach as low as 1K. Such jets are called as supersonic because the average speed of molecules in the jet is much greater than the speed of sound for the molecules that are not part of the jet.
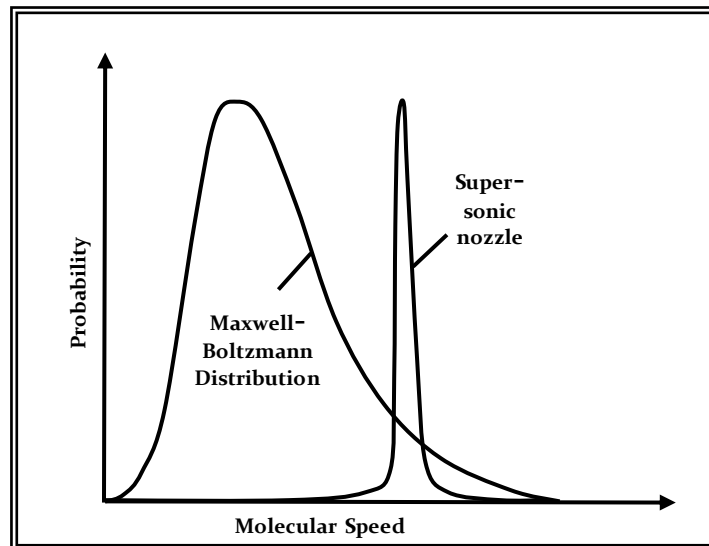
FIG.1.6: The shift in mean speed and the width of the distribution brought about by use of a supersonic nozzle.

A supersonic jet can be converted into a more parallel supersonic beam if it is 'skimmed' in the region of hydrodynamic flow and the excess gas pumped away. A skimmer consists of a conical nozzle, to avoid any supersonic shock wave spreading back into the gas and so increasing the translational temperature (FIG.1.7).
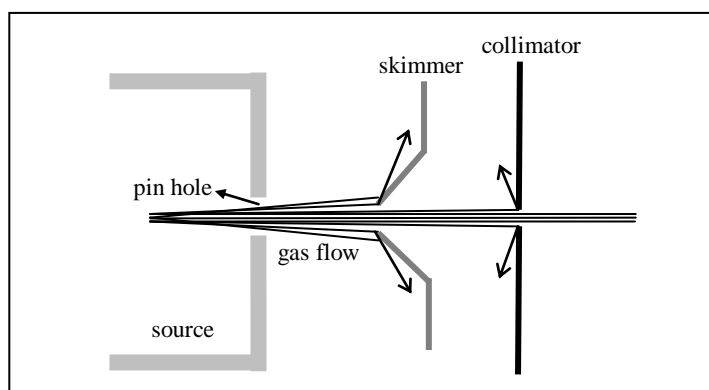
FIG.1.7: A supersonic nozzle skims off some of the molecules of the beam and leads to a beam with well defined velocity.

In 1951 Kantrowitz and Grey[10] suggested the use of hydrodynamic flow for generating high intensity MBs. Since then enormous advances have been made in the design and operation of these beam sources. A well-collimated supersonic MB can be generated by skimming the core of a supersonic flow through a Laval nozzle, or a free-jet, with a hollow truncated cone, and employing additional collimators downstream of the flow. In order to generate MB from a free-jet expansion in high background pressure, skimmer must be placed well before the shock front (Mach disc).

A seeded MB can be created by adding a small mole fraction of species of interest to the lighter buffer gas in the reservoir. Thus, gas mixture consists of a low concentration of a heavy seed gas in a light carrier gas. The flow velocity is governed by the more abundant lighter gas and this enables the acceleration of seed gas to high kinetic energies. Multiple collisions with the lighter carrier gas during the expansion tend to accelerate the heavy gas particles. This results in bending of heavy particles towards the jet axis and hence increases in concentration of heavy species along the axis. This concentration effect can be further enhanced by employing an annular nozzle. This will drive the seed gas towards the centerline of the expansion.

The advantage of seeded MBs are that they allow the seed gas to accelerated

to the beam velocity of carrier gas, and also allow the internal degrees of freedom of the seed gas to be cooled substantially, approaching the translational temperature achieved in the expansion. Thus, using seeded MBs one can accelerate neutral species to high and precisely defined energies which are useful in chemical dynamics investigations[11].

The higher degree of directionality of a supersonic beam, as compared to that of a free-jet, reduces the collision rate. Since the Doppler width of an absorption line is dramatically reduced, supersonic beams are very useful for high resolution spectroscopy, especially of complex molecules. In view of their special characteristics, such as high number density, narrow velocity distribution, low internal temperature for polyatomic molecules, nearly collision-free environment, supersonic free-jets and beams are being increasingly used in a variety of fields, e.g., spectroscopy, chemical dynamics, gas dynamic lasers, isotope separation, cluster science, surface science, etc.

Clusters are the link between properties of an individual molecule and properties of the bulk material. They are weakly bound aggregates of molecules, which can be generated in molecular beams. During the adiabatic cooling of a stream of gas, when it expands into a vacuum from a small nozzle, the density and translational temperature decrease with distance from the nozzle. In this expansion if sufficient collisions occur before the beam becomes too rarefied and cooling stops, the clusters are formed. Clustering can be avoided by warming the source nozzle to prevent the onset of condensation as the beam expands and cools.

1.4 VARIOUS ASPECTS OF PHOTODISSOCIATION PROCESS AND ITS IMPLICATIONS IN UNDERSTANDING DYNAMICS

The aim in studying the photodissociation process is to obtain the clearest picture of the molecular dynamics involved. When a molecule is electronically excited it leaves the Frank Condon region, traverses the 'transition state' and finally reaches the asymptotic channel(s), where the fragments are formed. This whole process can be understood by determining both the scalar and vector properties of the photofragments formed. Following are some aspects of photodissociation process that leave a signature on the photofragments formed, which are helpful in interpreting the molecular dynamics taking place.

1.4.1 ENERGY BALANCE

The rough picture of the photodissociation can be understood by knowing the balance of energy "income" and "outcome" in the process. The "surplus" energy is the input photon energy minus the dissociation energy and generally referred as available energy (E_{avl}). The "energy disposal" is the distribution of E_{avl} among various internal (electronic, vibrational, rotational, spin-fine structure, Λ-type doubling) and "external" (translational) degrees of freedom. The development of ultrasensitive and fast detection methods enables the measurement of photofragments just after they are formed, that is, before any collisions with other species leading to relaxation to a stable state. These fresh photofragments are said to be in the 'nascent' state. When the dissociation event is fast (faster than rotation relaxation), as in the case of dissociation occurring from a repulsive potential energy surface, the available energy distribution of nascent photofragments is very close to impulsive model. If the dissociation event is slow, relaxation to a stable state will compete with the accumulation of photoproducts to a measurable amount. Then the energy distribution of

photofragments is statistical one. For reactions with a considerable energy barrier in the exit channel, a hybrid model, which is combination of both statistical and impulsive model, is usually applicable. In this model, the energy released by the exit barrier is assumed to be distributed impulsively, while the distribution of energy above the barrier is estimated statistically. The partitioning of the available energy and various models for explaining this partitioning among the photofragments is discussed in detail vide infra.

1.4.2 BRANCHING RATIO OF PHOTODISSOCIATION CHANNELS

In the photodissociation of polyatomic molecules, two or more dissociation channels can compete with each other. The branching arises when a molecule is excited to a dissociative excited state's potential energy surface, which correlates with one product and which further interacts with other dissociative excited state surfaces corresponding to another products. The branching ratio can be experimentally calculated by observing the quantum yields of each of the products.

The branching between the chemical reaction pathways can also be calculated theoretically. These calculations are mainly based on predictions of the statistical transition state theories or on exact quantum scattering calculations, in case of smaller system. These theories assume that the change of electronic wave function immediately on excitation follows the nuclear motion, an adiabatic process. However, in some cases non-adiabatic re-crossing between two PESs markedly reduces the rate of crossing the transition state and evolving to one set of products, affecting the branching ratio[12].

1.4.3 VECTOR CORRELATIONS

The energy balance and branching ratios are the scalar quantities associated with photodissociation process, while the electronic transition, vibration, rotation,

spin alignment, fragment recoil directions, etc. are the directional properties which are associated with it. These vector quantities are in combination with scalar quantities, help in elucidating the photodissociation event. By probing the interaction between these directional properties manifested in the photodissociation event, one can have detailed insight into the nature of reaction. The correlation between these quantities influences significantly the molecular dynamics taking place. These vector correlations can be studied by photolysis with a linearly polarized light.

In the photodissociation process the various vector correlations can be observed[13]. A linearly polarized light will preferentially excite those parent molecules whose transition dipole moment **μ** is aligned parallel to the polarization vector **E**. An anisotropic distribution of photofragments can arise due to the vector correlation of **μ** and **v**, where **v** is recoil velocity of photofragment. If the dissociation event is fast enough that the alignment of **μ** is not lost before the moment of fragmentation, then both **μ** and **v** will align in the laboratory frame. Thus the angular correlation between **μ** and **v** will be transformed by the dissociation into an angular correlation between **v** and **E**.

The **E-μ-v** correlation results in an anisotropy of fragment recoil vectors in the laboratory frame. If the bond breaking occurs on the time scale short compared to the rotational motion of the parent, the alignment of **μ** in the laboratory frame by the polarized dissociating light should lead to alignment of **v.** The **E-μ-J** correlation results in an alignment of fragment rotational vectors in the laboratory frame, where **J** is the angular momentum vector. It arises because there is usually an angular correlation between the transition dipole moment and the plane of fragment rotation. Since **μ** is aligned in laboratory frame by **E, J** will also be aligned. If the fragment is born in an excited state, its emission will be polarized, whereas if the fragment is

formed in its ground state, it will preferentially absorb light of a specific polarization.

In **v-J** correlations, the magnitude of anisotropy and alignment does not depend on the relative rates of dissociation and parent rotation like all the correlation does. This is because anisotropy and alignment depend on having μ aligned in the laboratory frame; they tend to be lost if the parent rotates before it dissociates. The **v-J** correlation, however, is not made until the instant of dissociation; it is completely independent of the laboratory frame and so should always be informative. Of course, when the dissociation is rapid, both **v** and **J** will also display a correlation in the laboratory frame. In this case, all three of the vectors μ, **v**, and **J** will be aligned relative to one another and relative to a fixed axis (**E**) in the laboratory frame. The **E-μ-v-J** correlation combines all three effects. Among the above vector correlations, the **E-μ-v** and **v-J** correlations are discussed in this thesis.

A very classical example of vector correlation is given by Y. T. Lee et al.[14] in elimination of H_2 from 1,4-cyclohexadine, in which they have elucidated a *v-J* correlation. They have concluded that H_2 comes from the transition state with a "helicopter" type motion, albeit a wobbly helicopter as shown in FIG. 1.8. Here *v* is parallel to *J* i.e., direction of the photofragment recoil is parallel to the direction of the rotation axis, giving rise to the helicopter type motion.
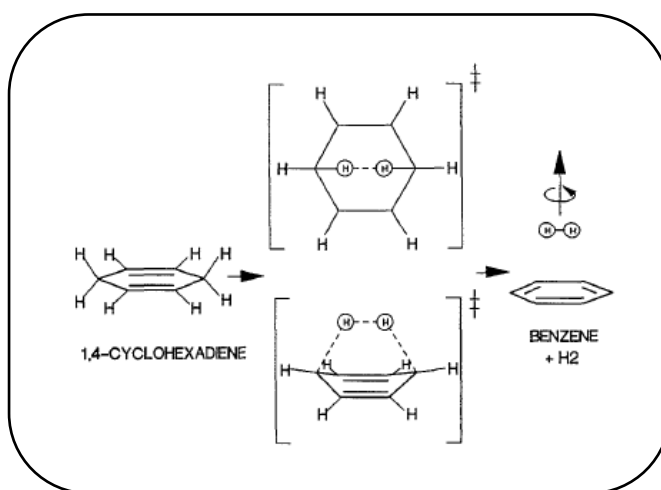
FIG. 1.8: Cartoon of H_2 elimination from 1,4-cyclohexadiene showing a side and a top view of the transition state region and the helicopter motion of H_2 product[17].

1.4.4 EXCITED STATE LIFE-TIMES

Radiative and non-radiative processes limits the maximum lifetimes of an excited state. The population of an excited state decays exponentially with certain decay time. The lifetime of an excited state is the reciprocal of rate constant of all the deactivation processes taking place from that state. The time needed for fluorescence intensity to decrease to 1/e of its original value, is known as the 'fluorescence lifetime', which is usually of the order of few ns to µs. The lifetime of a particular excited state is reflected in the dynamics of photodissociation of a molecule on laser excitation. The time scale of a particular dissociation event can be determined directly from the rise time of the photofragment signal obtained by employing ultrafast (picosecond or femtosecond) pulsed lasers. The pump-probe technique can be employed for measuring the lifetime of an excited state. In this technique, the molecules are excited by a pump laser pulse and a probe laser pulse investigates the time evolution of the population of the excited state formed by the pump laser pulse, by varying the time delay between pump and probe pulse.

1.4.5 TRANSITION STATES

The *transition state(TS) region* separates the reactants from the products. According to 'transition state theory' the transition state of an elementary reaction is that set of states (each characterized by its own geometry and energy) in which an assembly of atoms, when randomly placed there, would have an equal probability of forming the reactants or products of that elementary reaction. The assembly of atoms at the TS has been called an activated complex. The TS is referred to the potential energy maximum at the saddle point for calculated potential energy surfaces. At this point only, the coordinates of the TS may be assumed separately. Theoretically, TS is characterized by geometrical structure having one and only one imaginary frequency.

Several methods have been devised to probe TS by laser based spectroscopic techniques. Many researchers have aided the experimental work of laser based spectroscopic tools along with the theoretical calculations. In modern physical chemistry, the TS encompasses all configurations of intermediate structures that are significantly perturbed from the potential energy of the reagents or the products[15]. Imre, Kinsey, et al.[16] have probed the emission of molecules to enhance the understanding of the transition state in a photodissociation process. While studying the dissociation of O_3 from repulsive surface (Hartley band), they have determined the geometry of the excited state potential energy surface near the saddle point. Zewail and co-workers[17] probed the transition states in the photodissociation reactions of ICN $\rightarrow$ I + CN and IHgI* $\rightarrow$ HgI + I using a femtosecond pump-probe laser technique, which has helped in tracking a real-time dynamics of the transition state. They have defined TS as all the geometric structures with a range of internuclear distances of the breaking bond, for the unbound molecule on the excited surface.

1.5   PROBING TECHNIQUES

The understanding of dynamics in isolated (gas phase) molecules has been greatly aided by the development of several different experimental techniques. These incredible varieties of experimental techniques have been developed over the years to characterize the product state distributions arising from photodissociation. The driving force in the field of chemical dynamics has been to perform increasingly state selective experiments, in which most of the quantum numbers of both the reactant and product are specified. Ideally, such probing techniques should be highly selective and sensitive. An ideal detection scheme should combine three-dimensional spatial resolution with rapid temporal resolution. Even though most of the efforts are made to

improving the probing, none of the techniques developed so far fulfill the above attributes of an ideal detector. The state selective experiments are readily compared to detailed theoretical calculations and, therefore, result in significant advances in our understanding of elementary chemical processes. Photodissociation experiments are exceptionally appealing from this perspective, because in contrast to bimolecular scattering experiments the reactant energy and angular momentum are well defined in photodissociation experiments. In order to take full advantage of this capability, the products resulting from photodissociation should be completely characterized. In this way, the initial photoexcitation of the reactant molecule channeled into the multitude of product degrees of freedom can be identified. Such a characterization is the goal underlying some experimental techniques described in this section. As should be clear from the following consideration, no single technique is ideal for all photodissociation experiments. Each represents a compromise between generality, sensitivity, and resolution. Collectively, they provide a powerful experimental methodology to understand photodissociation dynamics.

1.5.1 PHOTOFRAGMENT TRANSLATIONAL SPECTROSCOPY (PTS)

Molecular beam photofragment translational energy spectroscopy offered the first opportunity to study the dynamics of photodissociation reactions in a collision-free regime. These experiments seek to measure two observables:

(1) The time required for a photofragment, produced by a pulsed, usually narrow-band, photolysis laser, to travel from the interaction region of the laser and molecular beam to the detector to obtain photofragment velocity distribution.

(2) The angular distribution[18] of the photofragments with respect to the electric vector of the photolysis laser. The rotatable detector in this type of instruments is employed to obtain the photofragment velocity and angular

distributions.

The detector consists of an electron-bombardment ionizer followed by a mass spectrometer. This detector configuration can detect any neutral photofragment, whether stable molecule or reactive radical, irrespective of its internal energy or other quantum state. Thus, the main limitation of these types of experiments is that they don't have sufficient energy resolution to yield the information on the rotational distribution of the photofragment[19].

1.5.2   LASER INDUCED FLUORESCENCE (LIF)

In photodissociation, when the fragments are formed in the ground state and hence do not emit, they can be probed by laser induced fluorescence (LIF), by bringing them into an emitting state by excitation using another laser (a probe laser). The excitation wavelength is scanned to transfer population from a particular ro-vibrational ground state to the well defined excited state and the resulting total fluorescence is measured without dispersion. The schematic of laser photolysis-LIF is shown in FIG. 1.9. Photodissociation laser (hv_1) forms a fragment, which is in different ro-vibrational states. By scanning the probe laser (hv_2), photofragments in a particular ro-vibrational level (v'', J'') are excited to a particular ro-vibrational level (v', J') in the electronic excited state, when the energy of the laser light coincides with the energy separation between the two levels. All the fluorescence from the excited level to various ground state levels (hv_f) is collected without energy dispersion. This technique is employed extensively for my work, which is described in the subsequent chapters of the thesis.
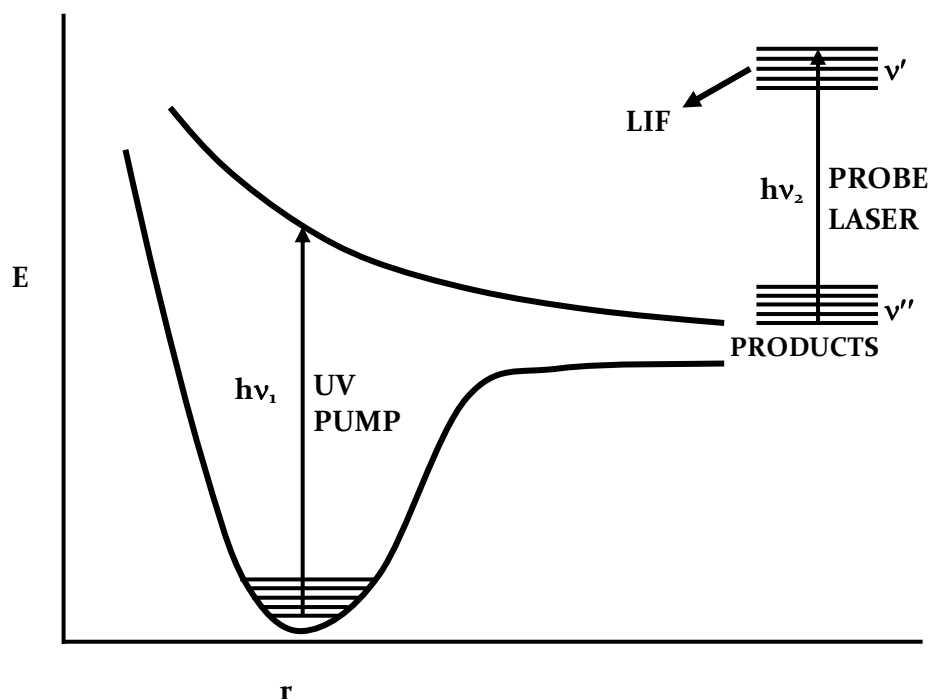
FIGURE 1.9: Schematic diagram of Laser Photolysis-Laser Induced Fluorescence technique.

The fluorescence spectra are mostly red shifted with respect to the absorption spectra. This is advantageous as measurement of the shifted emission is associated with less interference from the scattered photons. The measurement of the fluorescence excitation spectrum (which is usually called laser-induced fluorescence (LIF) spectrum) corresponds to that of the absorption spectrum[20]. In principle, the technique can be used for detecting single molecular species, in practice, for most of the systems; one may obtain sensitivity of 10^6 particles cm^{-3}. The limitation of the LIF technique is that one cannot study those molecules that do not fluoresce or have fluorescence with low quantum yield.

1.5.3 RESONANCE ENHANCED MULTIPHOTON IONIZATION (REMPI)

The possibility of simultaneous two-photon absorption for ionization was pointed out in 1931 by Göppert-Mayer[21]. The arrival of lasers, as an intense incident light source[22], made possible to carry out experimental observation for multiphoton ionization, in the optical region. When a resonant step is involved in the multiphoton

ionization (MPI) the process becomes selective and more sensitive; and the scheme is known as resonance enhanced multiphoton ionization (REMPI). In most of the chemical species, two-photon (UV-visible) resonantly prepared electronically excited state is just one-photon transition below the ionization continuum. REMPI designation is based on the number of photons employed resonantly to prepare the excited state. The REMPI process, in which one photon is used for resonant formation of the excited state, and the other for pumping the prepared state into the ionization continuum, is designated as (1+1)REMPI. This process occurs when the excited state prepared by mono-photonic absorption has energy more than half of the molecular ionization energy. The above ionization process requires relatively low laser intensities, and thus leads to the minimal fragmentation of the parent ion. The other variants commonly employed are (2+1) and (3+1) REMPI, where two and three photons, respectively are resonant with the electronic transitions (FIG. 1.10). In the above processes, the second-step transition i.e. ionization is saturated at the typical intensity of about 10^{26} photons cm^2/s obtained from nanosecond pulsed laser system.
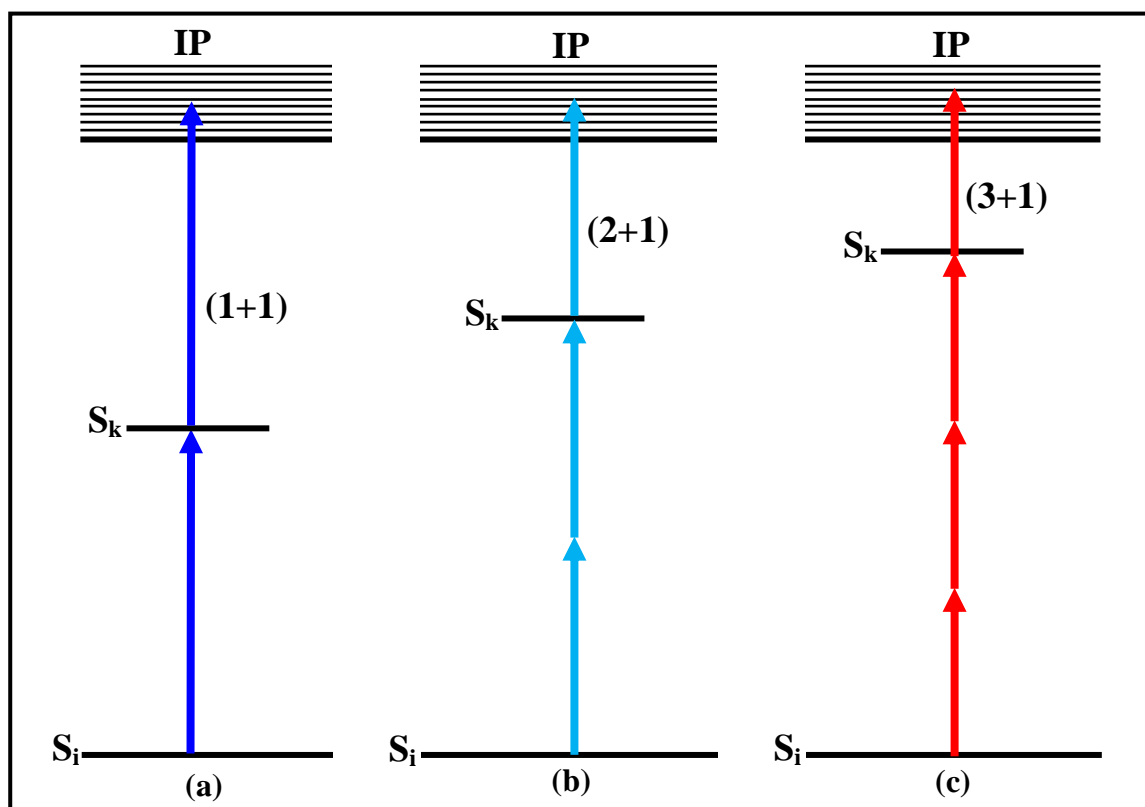
FIG 1.10: Schematic of some MPI schemes: a) (1+1)REMPI; b) (2+1)REMPI; and c) (3+1)REMPI. Other schemes are also possible. S_i denotes ground state; S_k denotes resonant excited state; **IP** denotes ionization continuum.

The REMPI is very convenient, because visible light from a wavelength tunable dye laser can be utilized for ionization. It provides the highly sensitive detection of photofragments as ionized formed can be mass analyzed with suitable technique. The investigation of photofragment state distributions using REMPI offers several advantages over LIF detection. REMPI technique is generally more sensitive than the LIF technique, as detection of the ion-current is much easier than the measurement of fluorescence-light photons. Unlike in LIF, in the REMPI process, molecule or atom is induced to absorb two or more photons simultaneously and to compensate for the very small cross-section a sufficiently high intensity of light is employed. REMPI is easily adaptable with a mass spectrometer and thus mass-selective. This eliminates any uncertainty concerning the identity of the photofragment. In addition, since a large fraction of the ions produced by the probe

pulse are collected in a typical experiment, the sensitivity of this method is extremely high. The first investigation[23] of photodissociation using REMPI detection of the photofragments was conducted just shortly after the first photodissociation/LIF experiments, and since then it has been used extensively as a probe technique. In brief, REMPI utilizes laser radiation to prepare a molecule in an excited state via multiphoton absorption and ionize this state before it can decay. A reactant or product to be studied is selectively ionized by tuning the laser frequency to the electronic absorption band. The technique is described in detail in the subsequent chapters.

1.5.4 PHOTOFRAGMENT IMAGING

The experiments based on photofragment imaging technique were first time carried out by Chandler, Houston, and co-workers[24] in 1987. This method is a combination of REMPI and two-dimensional imaging of fragment ions. Two counter propagating pulsed laser beams are employed in the experiment, one photodissociate molecules in a molecular beam, and other ionize the resultant fragments by REMPI. Fragment ions generated in a small volume are extracted by an electric field towards the two-dimensional position sensitive detector. The REMPI process ionizes only fragments in the preselected state. Directional (with respect to the polarization of the dissociation light pulse) and velocity information of the fragments are projected on the two-dimensional screen. Chandler and co-workers[25,26] showed that information containing anisotropy (β) parameter, branching ratio, Doppler profile, and vector correlations can be extracted from the two-dimensional image. This method was illustrated by carrying out the photodissociation of CD_3I at 266 nm and H_2S at 243 nm[25]. FIG. 1.11 depicts the schematic view of photofragment imaging technique used in CD_3I experiment. A velocity mapping of multiphoton excited states for two diatomic molecules, D_2 and O_2, is described by Chandler and Parker[27]. As these

experiences are very convenient, various groups have employed the technique with modifications which are reviewed by Houston[28].
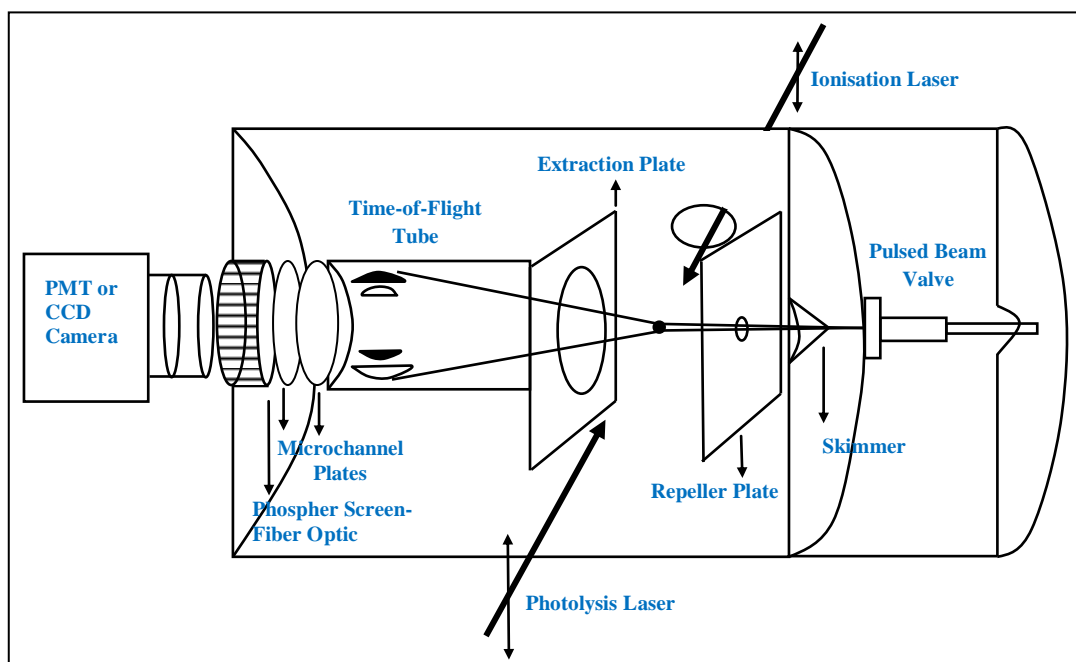
FIG.1.11: Schematic of the photofragment imaging apparatus. A pulsed molecular beam enters the photodissociation region of the apparatus through a hole in a repeller plate of a time of flight mass spectrometer. A photolysis laser beam intersects the molecular beam and causes photodissociation. A few nanoseconds later a tunable UV laser beam intersects the fragments and resonantly ionizes them. A few microseconds later the ion impacts a position sensitive ion detector creating a two-dimensional projection of the ion distribution. The image is recorded in CCD camera. In order to obtain REMPI spectra a photomultiplier is used to monitor the detector[23].

1.5.5   COHERENT ANTI-STOKES RAMAN SPECTROSCOPY (CARS)

CARS technique does not require a suitable excited state (which is the limiting condition for LIF and REMPI studies). It is sensitive to the same vibrational signatures of molecules as seen in Raman spectroscopy, the nuclear vibrations of chemical bonds. It is more sensitive (stronger signals) than spontaneous Raman microscopy. As generated CARS signal is of high frequency (lower wavelength) than the pump frequency, it has minimal fluorescence interference. This technique employs multiple photons to address the molecular vibrations, and produces a signal in which the emitted waves are coherent with one another. CARS is a third-order nonlinear

optical process involving three laser beams: a pump beam of frequency ω_p, a Stokes beam of frequency ω_s and a probe beam at frequency ω_{pr}, as shown in FIG.1.12. These beams interact with the sample and generate a coherent optical signal at the anti-Stokes frequency ($\omega_{pr}+\omega_p-\omega_s$). The latter is resonantly enhanced when the frequency difference between the pump and the Stokes beams ($\omega_p-\omega_s$) coincides with the frequency of a Raman resonance[29].
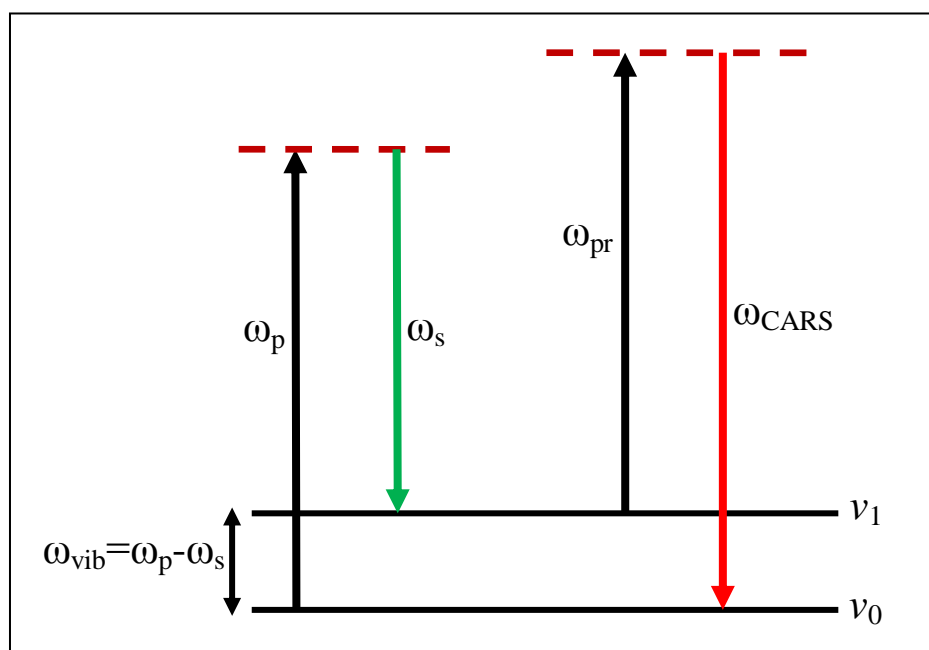
FIG. 1.12: CARS energy scheme. v_1 and v_0 are ground state vibrational levels. ω_p, ω_s, ω_{pr} and ω_{CARS} are frequencies of pump, stokes, probe and CARS signal beams.

1.5.6   CAVITY RING-DOWN SPECTROSCOPY (CRDS)

Cavity ring-down (laser absorption) spectroscopy was invented in the late 1980s, and since then it is being widely used for measuring electronic and vibrational absorption spectra of trace species in gas-phase environments[30]. The technique is capable of making ultrasensitive direct absorption measurements ($<<1x10^{-6}$ fractional absorption) on time-scales as short as microseconds. CRDS is based on measuring the intensity decay rate of a light pulse trapped in an optical cavity, formed by two high-reflectivity mirrors ($R \geq 0.999$). A light pulse, physically shorter in time than the

cavity round-trip time, is directed onto the input mirror of the cavity; most of the laser light is reflected straight back off the mirror, but a small percentage (<0.1 per cent) is transmitted. The small amount of light transmitted into the cavity through the high-reflectivity entrance mirror is trapped for some period of time and is reflected back and forth between the two mirrors. The intensity of the pulse slowly decays, due to the finite losses (primarily the minute mirror transmission). A sensitive photodetector monitors this leakage of light out of the cavity at each reflection. Because the light intensity decreases by a constant percentage on each round trip, the detector sees an exponential decay of light, i.e. ringing down, as shown in FIG.1.13. A very fast detector will respond to the individual events in the train of pulses, within an exponential decay envelope. However, the time response of associated detection electronics usually means that the pulses are smoothed out into a single exponential decay.
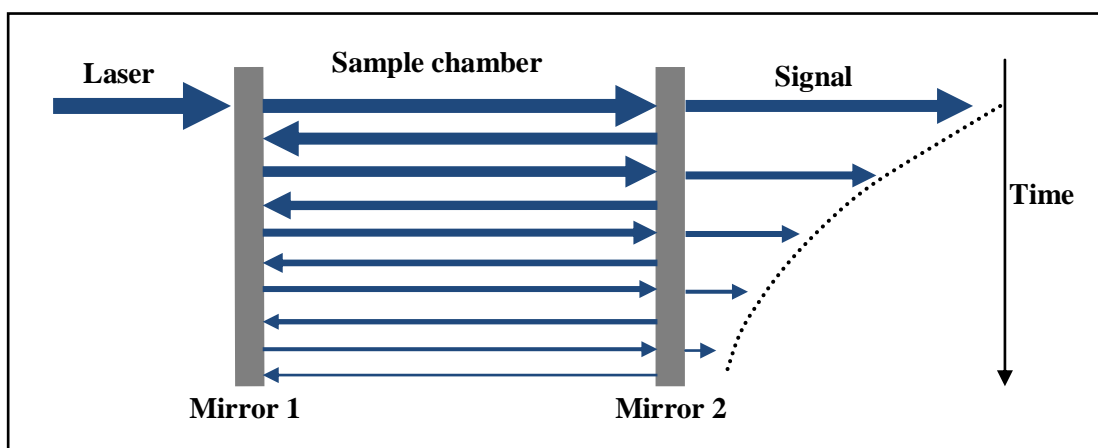
FIG.1.13: The Scematic of the operating principle of Cavity Ring-Down Spectrocsopy

The effective path length of each laser pulse between the high-reflectivity mirrors is about few kilometers due to enormous number of passes. This makes the sensitivity of CRDS stems far higher than for conventional multipass arrangements. In addition, by measuring the ring-down *decay rate* rather than *absolute intensity* of the laser pulse, pulse-to-pulse variations in laser output are removed from the final

spectrum. These two aspects allow the detection of absorptions smaller than ~10^{-7} per pass. Though the sensitivity of LIF spectroscopy is better than CRDS, the ability to record *quantitative* absorption spectra makes the ring-down technique superior in situations where the measurement of absolute values is required, or where fluorescence yields are poor (e.g. as in pre-dissociating systems). The apparatus required for CRDS is compact and inexpensive.

All the above techniques can be employed for measuring population of various states of photofragment and thus the distribution of available energy in the photofragment states can be estimated. The next section deals with the principle governing the partitioning of the available energy among the products.

1.6   AVAILABLE ENERGY PARTITIONING IN THE PRODUCT STATE

In a molecular dissociation process induced by photon absorption, with a wavelength shorter than that required to rupture the chemical bond, the question arises about the distribution of excess energy among the fragments. In the photodissociation of diatomic molecules, all energy above the dissociation threshold is transformed into kinetic energy of the recoiling atoms. However, for a polyatomic molecule the excess energy need not appear solely as translational energy, and may produce a high level of rotational or vibrational excitation of a molecular fragment. This available energy distribution is mainly governed by the features of potential energy surfaces for a given chemical reaction. Eyring[31], Polanyi and Evans[32] have approximated the thumb rule for the energy partitioning and the type of energy needed for the reaction to overcome the activation barrier[33].

There is a correlation between the position of the barrier on the reaction path and the energy partitioning. In an exothermic reaction A+BC→AB + C, with an

attractive PES (early barrier), the most of the exoergicity is converted into the product vibration. For an endothermic reaction, with a repulsive PES (late barrier), the most of the energy is converted into the product relative translation. There is also a good correlation between the location of the barrier on the reaction path and initial energy most conductive to the reaction (FIG. 1.14). Translational energy is most effective for passage across an early barrier, whereas vibrational energy of the reactant molecules is more effective for surmounting a late barrier. These requirements can be interpreted by availability of kinetic energy along the proper co-ordinate. For an early barrier, one requires momentum along R_{A-B}, whereas to overcome a late barrier, energy is required along R_{B-C} co-ordinate. The energy requirements of the reaction becomes less restrictive at higher collisional energies, where an efficient interchange of vibrational and translational energy along the reaction path is more likely[34]. This correlation holds good for simple molecular system. However, for a large polyatomic molecule, it is difficult to predict energy disposal and the energy requirement for overcoming a reaction barrier. The nascent internal energy state distribution of product has capability to provide the above information and hence these studies are of great important and form a major area of experimental research in chemical dynamics. Vibrational and rotational energy distributions are usually obtained in LIF experiments, whereas the translational energy distribution is obtained from TOFMS and Doppler shift studies. Since a measurement of product energy distribution is the focus of the present work, it is described in detail.

Early Barrier:

    Kinetic energy effective in overcoming the barrier $E_T >> E_V = 0$ **(left)**

    Vibrational energy ineffective $E_V >> E_T$ **(right)**

Late Barrier:

    Vibrational energy effective in overcoming the barrier $E_V >> E_T$ **(left)**

    Kinetic energy ineffective $E_T >> E_V = 0$ **(right)**
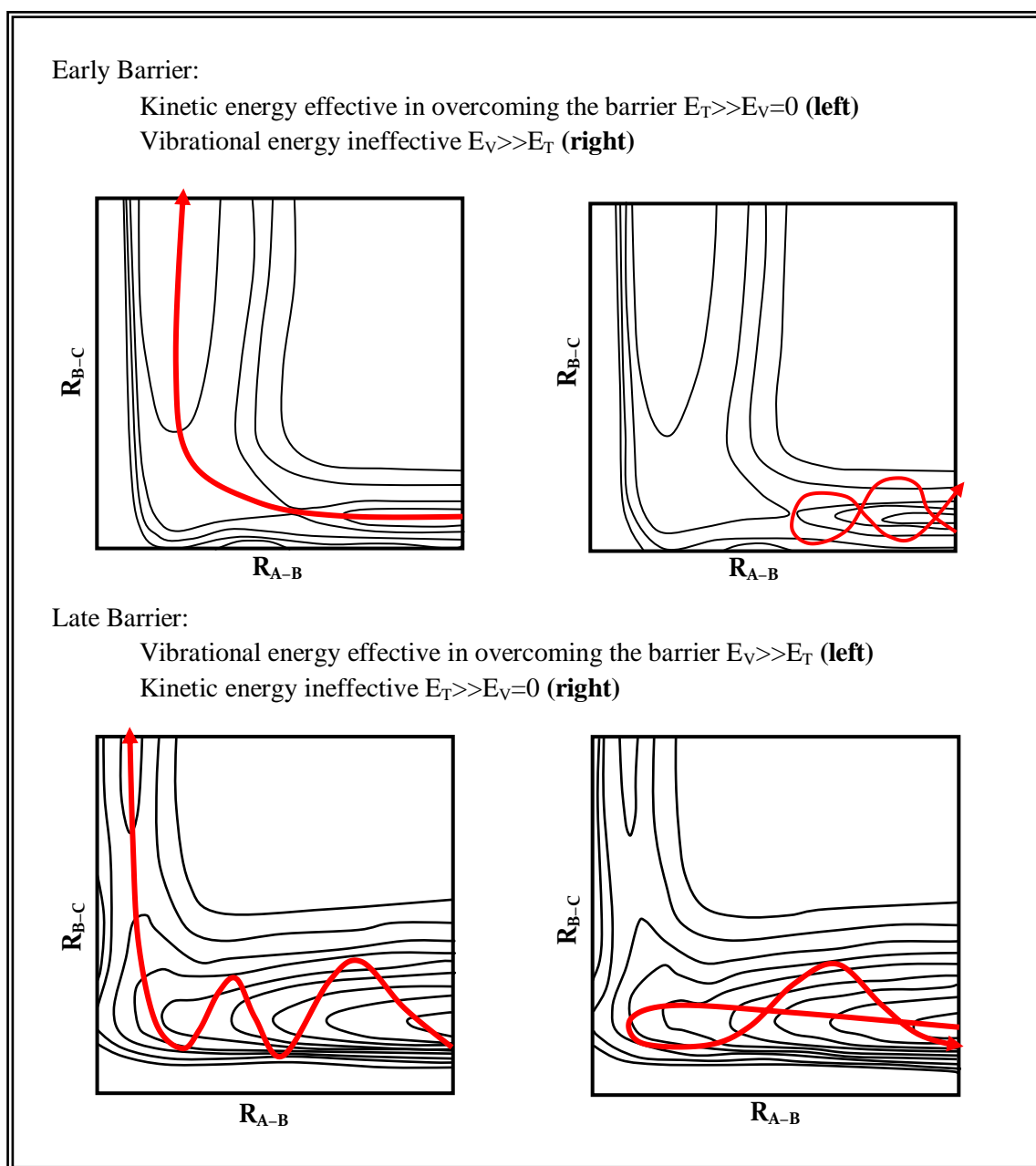
FIG. 1.14: The position of the barrier controls what type of energy is deposited into product degrees of freedom as well as what type of reactant energy is required.

1.6.1   VIBRATIONAL AND ROTATIONAL DISTRIBUTION

      The translational energy and the angular distribution of the products can be used to deduce the rotational and vibrational energy distributions. The vibrational and rotational distributions can more directly be obtained by LIF technique, as described earlier.

The rotational excitation arises primarily from the torque impart to the fragments at the time of bond rupture. The magnitude of torque depends on the force applied, the length of the lever arm connecting the axis to the *sine* of the angle between the force vector and the lever arm. Hence, if the reaction occurs principally through the bent configuration, then repulsion between the fragments produces substantial rotational excitation. However, if the reaction occurs through the collinear geometry, only translational and vibrational excitation takes place with little excitation of rotation.

The vibrational state distribution in the products depends on the location of saddle point on the PES where the initial bond breaks during the course of reaction. If it occurs within the entrance channel (attractive surface), vibrational excitation is produced. However if it lies in the exit channel (repulsive surface), little vibrational excitation is produced. In other words, if the bond to be broken is immensely extended in the TS, significant vibrational excitation in products is expected. In the reactions, if the products are formed in the vibrational or electronic excited state in substantial population, in the favorable cases IR or UV fluorescence method can be employed to determine the vibrational or electronic energy distribution of the products.

1.6.2 DOPPLER SHIFT AND TRANSLATIONAL ENERGY MEASUREMENT

When a source emitting radiation of wavelength λ and moves away from an observer with velocity v, the wavelength of radiation which observer detects is

$$\left(1 + \frac{v}{c}\right)\lambda, \tag{1.3}$$

where c is the velocity of radiation. Similarly, when the emitting source approaches

the observer, wavelength of radiation appears to be

$$\left(1 - \frac{v}{c}\right)\lambda. \tag{1.4}$$

Molecules in gas-phase have a wide range of velocity distribution, so depending upon the velocity of the particle it absorbs a wide range of wavelengths i.e., there will be a broadening of its absorption or emission profile. This profile reflects the velocity distribution of the particle in the gas-phase. The linear Doppler shift

$$\Delta v = v - v_0 = v_z \frac{v_0}{c}, \tag{1.5}$$

directly reflects the distribution $f(v_z)$ of the velocity component v_z of the absorbing species along the propagation direction of the probe laser beam. For an isotropic velocity distribution,

$$f(v_x) = f(v_y) = f(v_z), \tag{1.6}$$

the average translational energy in the laboratory frame is given by

$$E_T^{lab}(m) = \frac{3}{2}m\langle v_z^2\rangle, \tag{1.7}$$

where $\langle v_z^2\rangle$ represent the second moment of the laboratory velocity distribution of the atom of mass m and is given by

$$\langle v_z^2\rangle = \int_{-\infty}^{+\infty} v_z^2 f(v_z)dv_z = c^2 \int_{-\infty}^{+\infty} \left[\left(\frac{v-v_0}{v_0}\right)\right]^2 g(v)dv, \tag{1.8}$$

with c being the speed of light and g(v) is the normalized Doppler profile of the absorbing or emitting species. For a Maxwell-Boltzmann velocity of the particle the above integration simply gives

$$\langle v_z^2\rangle = \frac{1}{2ln2}\left[\frac{\Delta v_D}{2v_0}\right]^2 c^2, \tag{1.9}$$

where v_0 is the line-centre of the profile and Δv_D is the full-width at half-maximum (FWHM) of the profile. This method gives an average value of the translational energy released into the photoproducts; however, it does not give the

velocity distribution function. To obtain the velocity distribution function for the products, the distribution obtained by forward convoluting the adjustable empirical function with instrument response function is compared with the observed instrumental function.

The experimentally measured partitioning of available energy among the photoproducts is compared with theoretical models for better understanding of the dynamics of dissociation. The next section is based on formulations for distribution of available energy among the various degrees of freedoms of photoproducts.

1.7 MODELS FOR DISTRIBUTION OF AVAILABLE ENERGY AMONG THE PRODUCTS

The total energy E of the colliding molecules for any chemical reaction is a conserved quantity and remains constant throughout the collision. The total available energy E_{avl} is usually defined considering to the lowest possible energy state of the reactants and the products. For a particular initial reactant state, the total available energy (E_{avl}) in photodissociation process is the sum of photon energy, the internal energy of the reactants (E_R^{int}), minus D_0^0, dissociation energy from the ground state parent to the ground state fragments.

$$E_{avl} = E_R^{int} + h\nu - D_0^0, \tag{1.10}$$

The total available energy released after the bond has broken is partitioned as the translational and internal energy (consisting of electronic, vibrational and rotational energy) of products. For photodissociation reaction, the partitioning of this available energy is mainly governed by the nature of the transition state on the dissociative potential energy surface. It can be examined quantitatively in terms of two limiting models, the Impulsive Model[35] and the Statistical Model[36-38]. Apart from

these two, a third model developed from the combination of the above mentioned two models is Hybrid Model. We have employed these models, to estimate the partitioning of the available energy among the various degrees of freedom of the photofragments and compared the results with the observed experimental partitioning. All these three models are briefly discussed below.

1.7.1 STATISTICAL MODEL

From the fundaments of prior distribution[39], Phase Space Theory (PST) [40], or Separate Statistical Ensembles theory (SSE),[41] the statistical model for distribution of the available energy is developed. The prior distribution and PST solely rely on the information about the product states for partitioning the energy, fully ignoring the vibrational modes of parent molecule, while the SSE attempts to correct these deficiencies by using some of the information about energy partitioning in the parent molecule[42]. It assumes that vibrations become adiabatic prior to rotations and uses different ensembles to calculate the vibrational and rotational distributions. However, SSE and PST do not differ below the vibrational threshold.

The statistical model predicts the energy distribution among the fragments statistically at the transition state. The vibrational degree of freedom at the transition state is grouped into three ensembles, T, V, R, which correlate with translational, vibrational and rotational degrees of freedom for fragment[43]. All vibrational modes of transition state go into ensemble V. The skeletal stretch mode, torsional and skeletal bend, of transition state goes into ensemble T and ensemble R, respectively.

According to this model the average energy partitioning to the translational (E_T), vibrational (E_V) and rotational (E_R) degrees of freedom is given in the following manner

$$\langle E_M^{stat} \rangle = \frac{\int_0^{E^{stat}} dE_V \int_0^{E^{stat}-E_V} dE_T \int_0^{E^{stat}-E_V-E_T} dE_R \rho_V(E_V)\rho_R(E_R)\rho_T(E_T)\delta(E^{stat}-E_V-E_T-E_R)E_M}{\int_0^{E^{stat}} dE_V \int_0^{E^{stat}-E_V} dE_t \int_0^{E^{stat}-E_V-E_T} dE_R \rho_V(E_V)\rho_R(E_R)\rho_T(E_T)\delta(E^{stat}-E_V-E_T-E_R)}$$

(1.11)

where M=T, V, R and ρ_T, ρ_V, and ρ_R are the densities of states of ensemble T, V, and R, respectively. Partitioning of the available energy is made with a number of important assumptions. Both the fragments are assumed as symmetric tops and their vibrational densities of states are calculated by using the rigid rotor harmonic oscillator (RRHO) approximation. In the harmonic approximation, the densities of states can be easily computed using the Beyer-Swinehart algorithm[44]. By conservation of linear momentum, average translational energies of fragments, say A and B, owing to E^{stat} are

$$\langle E_T^{stat}(A) \rangle = \frac{m_B}{m_A + m_B} E^{stat} \tag{1.12}$$

$$\langle E_T^{stat}(B) \rangle = \frac{m_A}{m_A + m_B} E^{stat} \tag{1.13}$$

Similarly $\langle E_R^{stat} \rangle$ i.e., average rotational energies for fragments A and B are partitioned using conservation of angular momentum as

$$\langle E_R^{stat}(A) \rangle = \frac{I_B}{I_A + I_B} E^{stat} \tag{1.14}$$

$$\langle E_R^{stat}(B) \rangle = \frac{I_A}{I_A + I_B} E^{stat} \tag{1.15}$$

As it is assumed that both fragments are symmetric tops the moments of inertia, I_A and I_B, are calculated accordingly. In an additional approximation, it is assumed that the parent has no rotational motion prior to the dissociation.

The vibrational energy from the statistical reservoir has to be divided between the two fragments. The energy in the modes that develop into fragment vibrations should then be assigned to the appropriate fragment. Identifying these modes and obtaining their frequencies seems to be impossible. By approximating the frequencies of these modes by the frequencies of the fragment modes themselves, one obtains the following expression for the vibrational energy partitioned into fragments A and B

from the statistical model as,

$$\langle E_V^{stat}(A) \rangle = \frac{\int_0^{E_V^{stat}} dE_V \int_0^{E_V^{stat}-E_A} dE_B \rho_A(E_A)\rho_B(E_B)\delta(E_V^{stat}-E_A-E_B)E_A}{\int_0^{E_V^{stat}} dE_V \int_0^{E_V^{stat}-E_A} dE_B \rho_A(E_A)\rho_B(E_B)\delta(E_V^{stat}-E_A-E_B)} \qquad (1.16)$$

where ρ_A and ρ_B are the vibrational densities of states of fragments A and B, respectively. A significant problem with this method is that it tends to overestimate product rotational excitation above the vibrational threshold[45], while underestimating product vibrations[46].

1.7.2 IMPULSIVE MODEL

In the impulsive model, the dissociation event governs the distribution of the available energy among the product states. The soft radical model of A.F. Tuck[35] can be used for calculating the impulsive energy for the photofragments. In this model, it is assumed that excitation of a molecule creates a stiff repulsive potential between the two atoms in a molecule. At the moment of dissociation they are assumed to be independent of the other atoms present in the structure. Due to this repulsive potential, the bond between the concerned atoms breaks rapidly. All the available energy E_{avl} goes initially to the kinetic energy of the recoiling atoms, because of the suddenness of the rupture. The impulse is not along the centre of mass of the photofragments, and hence imparts rotational angular momentum to them. Once cleaved, the recoiling atoms collide with the other atoms in the respective photofragments, and their initial translational energies get partitioned into translational, rotational and vibrational energies of the respective photofragments. The translational energy of the individual photofragments can be calculated, applying the conservation of momentum, as the recoiling atom in each is slowed down by the remainder of the fragment. Similarly, rotational energy can be calculated from the rotational angular momentum, using conservation of angular momentum in the whole process. No assumptions are made

about the stiffness of any of the vibrations, which means no restrictions are placed on the amount of energy, which may appear as fragment vibrational excitation. From the conservation of energy, the remaining available energy is assumed to be partitioned in the vibrational mode.
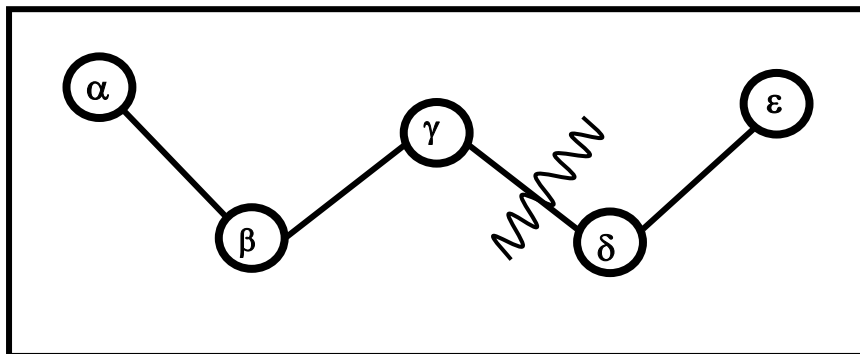
FIG. 1.15: A hypothetical model of a molecule, where the γ—δ bond breaks impulsively.

The partitioning of the available energy employing impulsive model is illustrated below, considering the above assumption for a hypothetical pentatomic molecule αβγδε (as in FIG. 1.15) for cleavage of bond between atom γ and atom δ. The initial translational energy of the recoiling atoms, using the conservation of linear momentum, can be calculated as:

$$E_T^\delta = \frac{m_\gamma}{m_\gamma + m_\delta} E_{avl} \tag{1.17}$$

$$E_T^\gamma = \frac{m_\delta}{m_\gamma + m_\delta} E_{avl}, \tag{1.18}$$

where m_i denotes the mass of the identity i. Conservation of linear momentum applied to the fragments gives the relations:

$$E_T^{\delta\varepsilon} = \frac{m_{\alpha\beta\gamma}}{M} \frac{\mu_a}{\mu_f} E_{avl} \tag{1.19}$$

$$E_T^{\alpha\beta\gamma} = \frac{m_{\delta\varepsilon}}{M} \frac{\mu_a}{\mu_f} E_{avl} \tag{1.20}$$

Here, E_T^i is the translational energy of the fragment i, m_i is the mass of the fragment i, μ_a is the reduced mass of atoms γ and δ, μ_f is the reduced mass of the

fragments and M is the mass of the parent molecule. The angular momenta of atoms γ and δ about the centre of mass of $\delta\varepsilon$ and $\alpha\beta\gamma$ are given by,

$$J_\gamma = \left(2m_\gamma E_T^\gamma\right)^{1/2} r_\gamma \sin\chi_{frag}^\gamma \tag{1.21}$$

$$J_\delta = \left(2m_\delta E_T^\delta\right)^{1/2} r_\delta \sin\chi_{frag}^\delta \tag{1.22}$$

where r_i is the distance between the centre of mass of the fragment i from atom i, and χ_{frag}^i is the angle between the cleaved and the line joining c.m. of fragment of the i atom and atom i. If we assume that the angular momenta J_γ and J_δ are conserved, the energies of rotation $E_T^{\alpha\beta\gamma}$ and $E_T^{\delta\varepsilon}$ may be calculated from the formulae,

$$E_T^{\delta\varepsilon} = \frac{J_\delta^2}{2I_{\delta\varepsilon}} = \frac{m_\delta m_\gamma}{m_\delta + m_\gamma} \frac{r_\delta^2 \sin^2\chi_{frag}^\gamma}{I_{\delta\varepsilon}} E_{avl} \tag{1.23}$$

$$E_T^{\delta\varepsilon} = \frac{J_\gamma^2}{2I_{\alpha\beta\gamma}} = \frac{m_\delta m_\gamma}{m_\delta + m_\gamma} \frac{r_\delta^2 \sin^2\chi_{frag}^\delta}{I_{\alpha\beta\gamma}} E_{avl}, \tag{1.24}$$

where I_i is the moment of inertia of the fragment i.

The fragment vibrational excitation can be calculated by applying the conservation of energy to the fragment. With computed translational and rotational energies and assuming that there is no electronic excitation of either fragment, the fragment vibrational energy can be calculated as,

$$E_V^{\delta\varepsilon} = E_T^\delta - E_T^{\delta\varepsilon} - E_R^{\delta\varepsilon} \tag{1.25}$$

$$E_V^{\alpha\beta\gamma} = E_T^\gamma - E_T^{\alpha\beta\gamma} - E_R^{\alpha\beta\gamma} \tag{1.26}$$

1.7.3 HYBRID MODEL

It is observed that, for the reactions with considerable energy barrier in the exit channel, neither statistical nor impulsive model is appropriate to calculate the energy partitioning, and the hybrid model, a combination of statistical and impulsive model is usually applicable. In this model[38,43], which is known as "barrier impulsive model",

the total E_{avl} of the products is divided into two energy reservoirs. One is the statistical energy reservoir consisting of excess energy above the transition state, E^{stat}(total), and the other is the impulsive energy reservoir consisting of energy released by exit barrier, E^{imp}(total). These energy reservoirs are shown in FIG. 1.16. The total available energy can be expressed as,

$$E_{avl} \text{ (total)} = E^{stat} \text{ (total)} + E^{imp} \text{ (total)}, \tag{1.27}$$

E^{imp}(total) is distributed impulsively among the rotational, vibrational, and translational degrees of freedom of each fragment, following the laws of energy and angular momentum conservation, and E^{stat}(total) is partitioned into the same modes according to simple statistical calculations. The total energy partitioned into all the
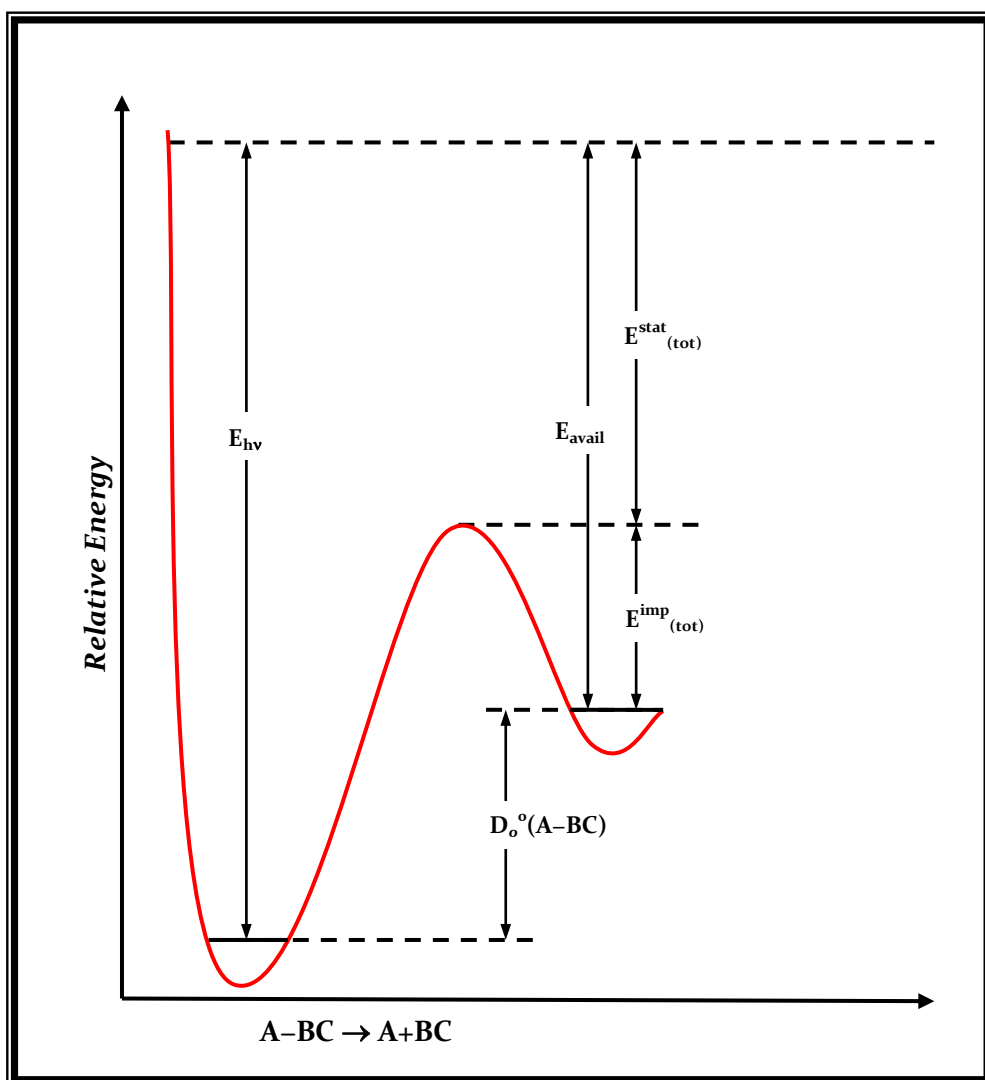
FIG.1.16: Schematic diagram illustrating the relations between various energetic quantities in the hybrid model (barrier impulsive model).

individual degrees of freedom of each fragment is obtained by adding contributions from each of these two models, each applicable to a specific proportion of the available energy.

The experimental technique provides us the knowledge of partitioning of available energy among the photoproducts and comparing the experimental results with various models helps in formulating the mechanism for reaction. The results obtained with various models can be elucidated by theoretical and computational methods. A variety of theoretical calculations can be helpful in explaining not only the experimental results, but also predicting the outcome of photodissociation reactions. Some of the methods of theoretical calculations, which are used to support the experimental work carried out in this thesis, are explained below.

1.8   THEORETICAL AND COMPUTATIONAL CHEMISTRY

The term **theoretical chemistry** may be defined as the mathematical description of chemistry. The term **computational chemistry** is usually used when a mathematical method is sufficiently well developed that it can be automated for implementation on a computer. Very few aspects of chemistry can be computed exactly, but almost every aspect of chemistry has been described in a qualitative or approximate quantitative computational scheme. With the help of computational chemistry, we can predict chemical structures and reactions. These are based fully or partly on the fundamental law of physics. These techniques allow chemists to study chemical phenomena by running calculations on computers rather than by examining the reaction and compounds experimentally. Some methods can be used to model not only stable molecules, but also short-lived, unstable intermediates and even transition states. In this way information about molecules and reactions, which is impossible to

obtain through observations, can be obtained. Computational chemistry is a vital adjunct to experimental studies. Depending on the complexities of the molecular system and the accuracy of the calculations required, *ab initio* or Semiempirical method of calculation is carried out.

1.8.1 *AB INITIO* METHOD

"*Ab Initio*" is Latin term for "from the beginning". This name is given to computations, which are derived directly from theoretical principles, with no inclusion of experimental data. Most of the time this type of calculation is referred to as approximate quantum mechanical calculation. These are solely based on the laws of quantum mechanics and the values of small number of physical constants: the speed of light, the masses and charges of electrons and nuclei, and Planck's constant.

1.8.1.1 HARTREE FOCK CALCULATION (HF)

The most common type of *ab initio* calculation is called a Hartree Fock (HF) calculation in which the primary approximation is called the central field approximation. This means that the coulombic electron-electron repulsion is not specifically taken into account. However, its net effect is included in the calculation. This is a variational calculation, meaning that the approximate energies calculated are all equal to or greater than the exact energy. The energies calculated are usually in units called Hartrees (1 H = 27.2114 eV).

The second approximation in HF calculations is that the wave function must be described by some functional form, which is only known exactly for a few one electron systems. Here the basis functions are usually taken as atomic orbitals (AO). Each AO can be represented as a Linear Combination (LC) of one or more Slater Type Orbitals (STO). For polyatomic molecules, LC-STOs are used as centred on each atom. For simplification in the evaluation of molecular integral, Gaussian type

functions are used instead of STOs. The wave function is formed from linear combinations of atomic orbitals or more often from linear combinations of basis functions. The exact set of basis functions used is often specified by an abbreviation, such as STO-3G or 6-311++g**.

1.8.1.2 DENSITY FUNCTIONAL THEORY (DFT)

Another *ab initio* method is Density Functional Theory, in which the total energy is expressed in terms of the total electron density, rather than the wavefunction. In this type of calculation, there is an approximate Hamiltonian and an approximate expression for the total electron density. By this method, we can eventually converge to the exact solution, once all of the approximations are made sufficiently small in magnitude. However, these methods are expensive and often take enormous amounts of computer CPU time, memory and disk space. In practice, extremely accurate solutions are only obtainable when the molecule contains half a dozen electrons or less.

In general, *ab initio* calculations give very good qualitative results and can give increasingly accurate quantitative results as the molecules in question become smaller.

1.8.2   SEMIEMPIRICAL CALCULATIONS

Semiempirical calculations are set up with the same general structure as a HF calculation. Within this framework, certain pieces of information, such as two electron integrals, are approximated or completely omitted. In order to correct for the errors introduced by omitting part of the calculation, the method is parameterized, by curve fitting in a few parameters or numbers, in order to give the best possible agreement with experimental data. They are much faster than the *ab initio* calculations. However, the results obtained by these methods can be erratic. If the

molecule being computed is similar to molecules in the database used to parameterize the method, then the results may be very good. If the molecule being computed is significantly different from anything in the parameterization set, the answers may be very poor.

Semiempirical calculations have been very successful in the description of organic chemistry, where there are only a few elements used extensively and the molecules are of moderate size. Semi-empirical Methods, such as AM1, MINDO/3 and PM3, are implemented in programs like MOPAC, AMPAC, HyperChem, and GAUSSIAN series.

1.8.3   GAUSSIAN PROGRAMME

Various commercial programs are now available for *ab initio* or Semiempirical calculations. Among all these, GAUSSIAN PROGRAM is very versatile and user friendly, hence used extensively. Gaussian is a computational chemistry program. Using this program, computation can be carried out on systems in the gas phase or in solution, and in their ground state or in an excited state. It can serve as a powerful tool for exploring areas of chemical interest like reaction mechanisms, potential energy surfaces and excitation energies. Gaussian is characterized by the combination of theoretical procedure and the basis set.

1.8.3.1 METHODS

Gaussian contains the hierarchy of procedures corresponding to different approximation methods. Some of the keywords for the methods, which are used in this work, are listed in TABLE 1.1. More accurate method becomes correspondingly more expensive computationally.

Table 1.1: Commonly used methods in Gaussian calculation.

Keyword	Methods
HF	Hartree-Fock Self-Consistent Field
MP2	2nd Order Møller-Plesset Perturbation Theory
QCISD	Quadratic Configuration Interaction (Singles and Doubles)
CIS	Configuration Interaction (Singles)
MP3	3nd Order Møller-Plesset Perturbation Theory
MP4	4nd Order Møller-Plesset Perturbation Theory
QCISD(T)	Quadratic CI (Singles, Doubles and Triples)

1.8.3.2 BASIS SET

A basis set is a mathematical representation of the molecular orbitals within a molecule. It can be interpreted as restricting each electron to a particular region of space. It is a key factor in the accuracy of any *ab initio* calculation. Ideally, one can systematically increase the size of the basis set until the results converge to within some desired limits of accuracy. Larger basis sets impose fewer constraints on electrons and more accurately approximate exact molecular orbitals. Table 1.2 lists commonly used basis sets with some relevant descriptions.

Table 1.2: Commonly used basis functions with their basis criteria and field of usefulness.

* Lithium through Neon.

Basis set	Description	No. of basis function	
		heavy atom*	hydrogen
STO-3G	Minimal basis set: Used for more qualitative results for big systems	5	1
3-21G	2 sets of functions in the valance region: Used when 6-31G is too expensive	9	2
6-31G(d)	Adds polarization functions to heavy atoms: Used for most jobs up to medium size systems	15	2
6-31G(d,p)	Adds polarization functions to hydrogen as well: Used when hydrogens are the site of interest	15	5
6-31+G(d)	Adds diffuse functions: Most important for systems with lone pairs, anions, excited states	19	2
6-31+G(d,p)	Adds p functions to hydrogen as well: Used when diffuse functions are needed over 6-31G(d,p)	19	5
6-311+G(d,p)	Adds extra valance functions (3 sizes of s and p functions) to 6-31+G(d,p)	22	6
6-311+G(2d,2p)	Puts 2d and 1f functions (and diffuse functions) on heavy atoms and 2p functions on hydrogens.	27	9
6-311++G(2df,2pd)	Puts 2d and 1f functions (and diffuse functions) on heavy atoms and 2p and 1d functions on hydrogens	34	14
6-311++G(3df,3pd)	Puts 3d and 1f functions (and diffuse functions) on heavy atoms and 3p and 1d functions on hydrogens	39	18

1.8.3.3 OPTIMIZATION OF THE MOLECULAR GEOMETRY

The GAUSSIAN calculation starts by specifying an approximate molecular geometry, either in terms of bond length, bond angles and dihedral angles or in Cartesian coordinates. The former is generally more convenient and better suited for molecular structure optimization. Once the coordinates of a molecule are read, the program determines the point group of the molecule. A basis set is now specified. Mostly they are pre-stored in the library. At this point, the one-electron overlap, kinetic energy, and the potential energy integrals and the two-electron repulsion integral are calculated. A flow-chart for such type of calculation is given in FIG.1.13. Once the self-consistency is achieved, the wave function can be printed out with the population analysis. A common practice has been to employ the molecular geometry obtained by optimization at the low level of theory for a single computation at a higher level for the energy accuracy. We have used the GAUSSIAN 92 program for theoretical calculations, in collaboration with Pune University.
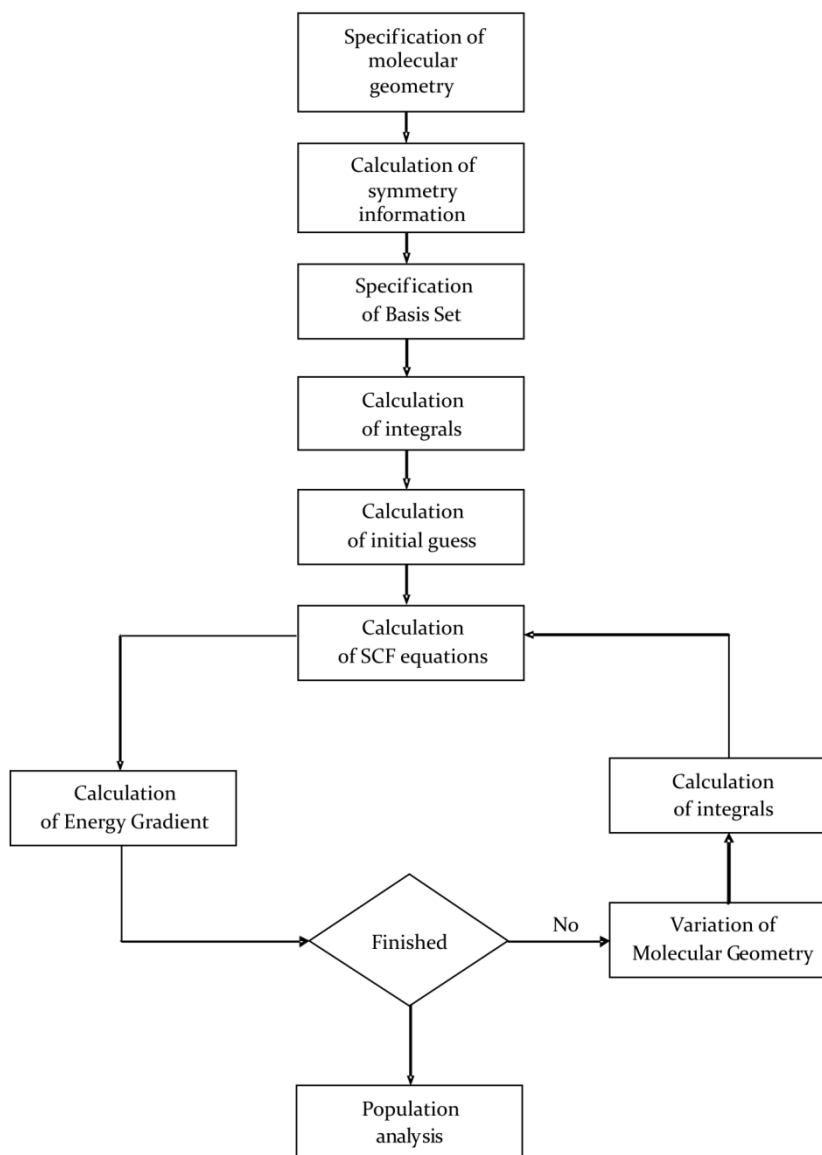
FIG. 1.13: Sequence of execution of program modules resulting in the optimization of the molecular geometry for a particular basis set.

1.9   BOND-SELECTIVE   CHEMISTRY   AND   PHOTODISSOCIATION DYNAMICS

The control over the route of chemical reactions by driving them in the desired directions has been an everlasting challenge to chemists and chemical physicists. In principle, one can excite a specific bond of a molecule, and cleave the same selectively. However, generally, the excitation energy is redistributed among various bonds of the molecule (known as intramolecular vibrational energy redistribution, IVR) and the weakest bond cleaves. Now, it is possible to defeat the IVR and

selectively dissociate a bond in specific cases, employing some exotic methodology.

The requirement for controlling the outcome of some photodissociation reactions is that the original phase of the electronic wave packet should survive during the photodissociation event. As discussed above there can be many mechanisms for the coherence to be lost, it is kept in some favourable cases. In his review[15] Zewail had explained the ultrafast photodissociation dynamics of HgI_2. In this case, HgI is born vibrationally excited state and its initial wave-packet is a coherent state and propagates out in the exit valley just as a classical trajectory will. It means that it undergoes oscillatory motion along the symmetric stretch coordinate and the nascent products are not simply vibrationally excited but are coherently excited.

In principle in the absence of environmental perturbations, the coherence will revive. The revival time is expected to be much longer than a vibrational period. This aspect has direct relevance to "coherent control" on the outcome of chemical reactions.

Vibrationally mediated photodissociation (VMP) is one of the methods for implementation of bond-selective chemistry. The vibrational motion changes the positions of nuclei therefore, the vibrational excitation is suitable for controlling the chemical reactions. The vibration excitation of reaction coordinate, whose motion of nuclei carries the arrangement of atoms of reactants to the products, facilitates the reaction. So far, this approach is used to study the photodissociation and bimolecular atom transfer reactions. In photodissociation reaction, the carefully prepared vibrational state predetermines the outcome of the reaction. A properly chosen bound vibration in a ground electronic state is excited with light from a laser for becoming the reaction co-ordinates for dissociation[7,47].

VMP technique is suitable for molecules with very short excited-state

lifetimes and has no spectral structure that allows the selective excitation of particular vibrational motions in the excited state. The vibrational motion is generated before excitation to the dissociative state. VMP can create excited state molecules with vibrations other than those that are active in the one-photon excitation spectra. From VMP experiments, we can get "action spectra", which is generated by monitoring the yield of a specific reaction product, while scanning the frequency of the vibrational excitation laser. The analysis of the action spectra is used to gather information about the intramolecular vibrational relaxation (IVR).

The VMP technique has two variant, a single-colour and two-colour excitations. In single-colour VMP, one photon excites $v=0$ of the ground electronic state to a vibrational overtone state, lying below the ground state dissociation threshold, followed by absorption of a second photon of the same colour within the few ns duration of laser pulse. The second photon excites the vibrationally excited molecule to a dissociative electronic state to produce a radical fragment, which is detected using LIF. Since the fragmentation requires that the first photon should be in resonance with a vibrational overtone state, the variation of the yield of a product with the wavelength of laser radiation reflects the vibrational overtone-excitation spectrum. In two-colour VMP, the vibrational overtone excitation and the subsequent photodissociation use different laser wavelengths, for selective vibrational excitation and subsequent pumping to dissociative electronic state. The two-colour scheme does not require the presence of a dissociative electronic state at twice the energy of vibrational overtone. The use of second photon with different colour provides the detailed quantum-state-resolved information concerning the photodissociation dynamics of vibrationally excited molecules. Crim's group[48] applied the VMP technique to the OH-containing molecules such as H_2O_2, $HONO_2$, and t-C_4H_9OOH.

These molecules were excited in the region of $4\nu_{OH}$ (the third overtone of O-H stretching vibration) at 740-765 nm. A time-delayed second photon, either of the same or different energy than the first one, dissociates the molecule. The dynamics in the VMP were substantially different from those observed for dissociation by single photons of comparable energy. In the case of H_2O_2, more than 11% of the OH fragments were vibrationally excited ($v = 1$) as compared to almost none in the single-photon UV dissociation. Sinha et. al[49]. investigated VMD of HOD by exciting third overtone, ($4\nu_{OH}$) and subsequent dissociation of the prepared state by 266 nm photon and observed OD/OH $\geq$ 15, clearly, demonstrating selectivity with initial vibrational state.

1.10 SCOPE OF THIS THESIS

The first part of this thesis comprises the study of photodissociation dynamics of polyatomic organic molecule, with emphasis on formation dynamics of the OH radical. The OH radical is an important radical in the chemistry of the atmosphere and is a key reactive species in the interstellar medium. The LIF technique, which is quite selective and sensitive to probe the OH radical, was employed to probe the nascent OH fragment formed on photolysis, state selectively. As a part of the thesis work, photodissociation dynamics of a few cyclic organic compounds, such as cyclohexanone oxime (CHO), cyclopentanone oxime (CPO), 1,2-cyclohexanedione (CHD), 2-chloro-6-nitrotoluene (2Cl6NT) and nitrocyclopentane (NCP) were investigated by mapping partitioning of the available energy in the OH fragment.

Photodissociation dynamics of halogenated organic molecules in the ultraviolet region are important from the point of view of stratospheric ozone depletion, since the UV light induced C−X bond fission is one of the well-known

processes generating halogen atoms in the stratosphere that initiate and propagate ozone-depleting reactions. The second part of this thesis includes the experimental studies on the C−X (X=Cl and Br) bond dissociation dynamics and probing of halogen atom using the REMPI technique. This study is focused particularly on the mechanism of X atoms formation in their ground ($^2P_{3/2}$) and excited ($^2P_{1/2}$) spin-orbit states.

The outline of the thesis is as follows. In Chapter 1, topics essential for effortless reading of the thesis is covered. The Chapter 2 includes the description of experimental techniques used in the research work. The general overviews of Laser Photolysis-Laser Induced Fluorescence (LP-LIF) spectroscopy and Resonance Enhanced Multiphoton Ionization-Time of Flight-Mass Spectrometry (REMPI-TOF-MS) techniques are discussed, which include principles, experimental set-up, and application in spectroscopy and the present work.

The Chapter 3 covers the study of photodissociation dynamics of CHO and CPO in the vapour phase at 193 nm, wherein the OH fragment has been probed state-selectively employing LIF. The partitioning of the available energy in the relative translation, rotation, and vibration of the photoproducts has been measured. *Ab initio* calculations were carried out to identify the excited states as well as the transition states involved in the N-OH bond cleavage. The results on the dynamics of the N-OH bond dissociation in the cyclic oximes CHO and CPO were compared with that in non-cyclic acetoxime and the effect of the ring size on the dynamics of OH formation are also addressed.

Chapter 4 covers the studies on the formation dynamics of the transient OH radical, by LIF method, on photoexcitation of CHD in the gas phase at 266, 248, and 193 nm. CHD is a α-diketone and formation of OH on UV excitation of this

compound has not been reported in literature. In present work, OH formation was observed, and measured the partitioning of the available energy among translational, rotational, and vibrational degrees of freedom of the photoproducts, by employing LIF technique. Based on experimental results, coupled with *ab initio* molecular orbital calculations, we have proposed a plausible mechanism of OH formation from dione, which are devoid of any OH group.

The Chapter 5 deals with the detection of the OH radical from cyclic nitrocompounds on UV laser excitation. Like dione, these compounds are also lack of any OH group, but rearrange and form OH on UV excitation. We have investigated dissociation of 2-chloro-6-nitrotoluene (ClNT) and nitrocyclopentane (NCP) under collision-free condition. The OH radicals were detected using LIF technique on photolysis of ClNT at 193, 248 and 266 nm, and that of NCP at only 193 nm. The photolysis was carried out at three different wavelengths for ClNT and investigated the influence of excitation wavelengths on the dissociation channel. *Ab initio* theoretical calculations were also carried out to find out the probable channels that lead to OH formation. Based on both experimental and the theoretical results, a possible mechanism of ClNT and NCP photodissociation leading to OH formation of is proposed.

The Chapter 6 discusses the work undertaken to investigate the dynamics of the C-Cl bond dissociation on UV excitation of fumaryl chloride, a molecule with two C=O groups and a C=C group in conjugation, in a supersonic molecular beam at around 235 nm. The chlorine atom product in both the ground state Cl ($^2P_{3/2}$) and the spin-orbit excited state Cl* ($^2P_{1/2}$) has been detected using the REMPI-TOF technique. The translational energy distributions for both types of chlorine atoms and the relative quantum yield of Cl* were measured. To gain further insights, the anisotropy

parameter (β) was estimated for both the channel. The TOF profiles for both Cl and Cl* were found to be independent of laser polarization; i.e., β is well characterized by a value of 0.0, within the experimental uncertainties. The measured polarization-dependent and state-specific TOF profiles were converted into kinetic energy distributions, using a least-squares fitting method, taking into account the fragment recoil anisotropies. Two components, were observed in the translational energy distribution, P(E_T), of Cl and Cl* atoms, and assigned to be formed from different potential energy surfaces.

The Chapter 7 elaborates on the UV photodissociation of two halogen substituted thiophenes. We studied 2-chlorothiophene and 2-bromo-5-chlorothiophene to investigate the halogen atom (X/X*) formation dynamics, in a supersonic molecular beam, around 235 nm using REMPI technique. The translational energy distribution for both spin-orbit states of chlorine and bromine atoms was determined. Besides, the relative quantum yields of Cl* and Br* and ratio for chlorine and bromine channel in 2-bromo-5-chlorothiophene were measured. The recoil anisotropy parameter, β was also estimated for chlorine and bromine atom elimination channels. For both Cl and Br atoms formed from 2-chlorothiophene and 2-bromo-5-chlorothiophene, the β parameter was well characterized by a value of ~0.0, within the experimental uncertainties. For 2-chlorothiophene, in the translational energy distribution, two components were observed for Cl, and only one component for Cl* atom elimination channel. However, for 2-bromo-5-chlorothiophene, only one component was observed for Cl, Cl*, Br and Br* in the translational energy distributions. The energy partitioning into the translational modes is compared with the values obtained from various models, such as impulsive and statistical models.

Finally, Chapter 8 presents a summary of the thesis as well as future

directions, which can provide a further understanding of the molecular systems investigated in particular, and photodissociation dynamics of polyatomic molecules, in general.

CHAPTER 2

EXPERIMENTAL METHODS

2.1   OVERVIEW

This chapter is an introduction to the experimental methods employed to obtain the results presented in this thesis. Two types of experimental set-ups were used for studying the photodissociation dynamics of selected molecules. Experimental results described in chapters 3, 4, and 5 have been carried out using the Laser Photolysis-Laser Induced Fluorescence (LP-LIF) technique and those in chapters 6 and 7 using Molecular Beam-Resonance Enhanced Multiphoton Ionization-Time of Flight-Mass Spectrometry (MB-REMPI-TOF-MS) technique. All the experimental works carried out in this thesis were performed in gas-phase. The investigation of dynamics of a reaction system in gas-phase needs collision-free environment and hence a vacuum system plays an important role during the actual work. By performing the experiments using the above two set-ups in a collision-free condition, the available energy partitioning in the nascent photofragments, formed on photoexcitation of the selected molecules, has been deduced to investigate the dynamics of dissociation. In this chapter at first, these two techniques are discussed in

details along with the analysis of the experimental data obtained, and then components that are used during the experiments are briefly discussed. In later chapters, we will refer back to the present chapter for descriptions of employed experimental techniques and set-ups. Schematic of the apparatus used in photodissociation experiments are depicted in the figures 2.1 and 2.2.
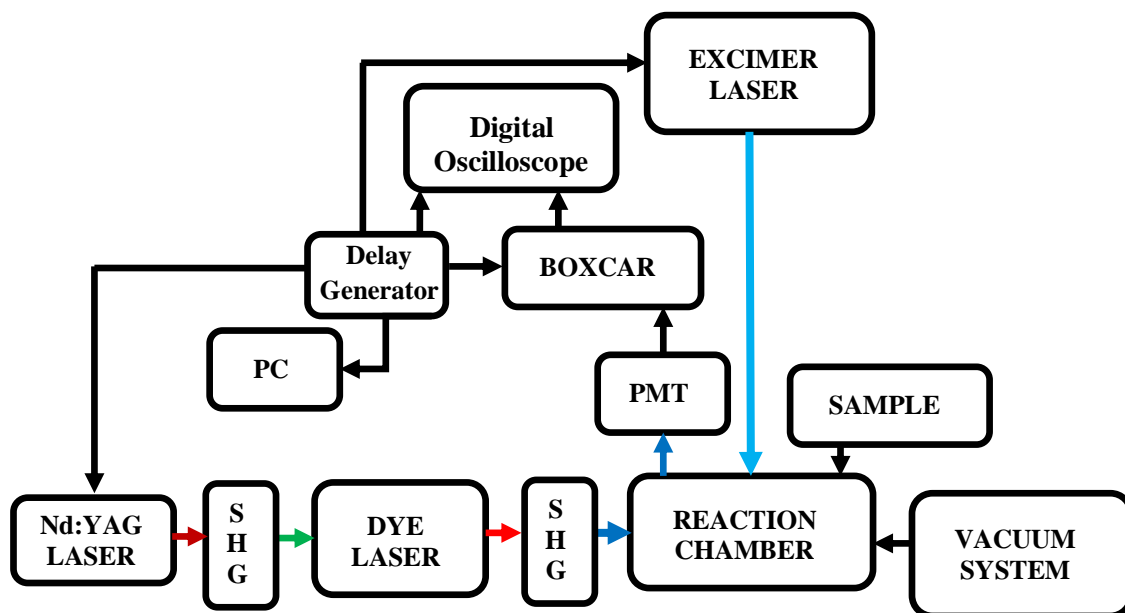
FIG. 2.1: Schematic diagram of LP-LIF set-up.

FIG. 2.1 depicts the schematic of the basic components employed in LP-LIF technique. The photolysis and probe lasers intersect each other at the right angles in a reaction chamber. The photolysis laser is an excimer laser, and the probe laser is a Nd:YAG pumped dye laser, where second harmonic generator (SHG) is used for frequency doubling. The observed fluorescence from the probe laser excited OH fragment is collected by an appropriate optical system and measured by a photomultiplier tube (PMT), which is mounted perpendicular to the crossing of two laser beams. The analogue signal is converted into digital data through the data acquisition system and stored in the computer (PC) for analysis. A digital delay

generator (DG) maintains the time delay between photolysis laser, probe laser and data acquisition system.

FIG. 2.2: Schematic diagram of MB-REMPI-TOF-MS technique.

The schematic in Fig. 2.2 shows the basic components employed in MB-REMPI-TOF-MS technique. In all the experiments reported using this technique, the same laser beam is employed as a pump as well as a probe, i.e., for both photodissociation of the parent molecule and ionization of photoproducts. A supersonic molecular beam (MB) of a sample with 1000 Torr helium gas is formed using a pulsed solenoid valve (PSV) with nozzle and skimmed by nozzle, and shined by a laser beam at right angle. The halogen atoms formed on photolysis is probed (ionized) using (2+1) REMPI transitions. The resulting ions are collected and detected using a traditional two-stage Wiley-McLaren Time-of-flight (TOF)-MS coupled with

a set of dual Chevron microchannel plates (MCP). The MCP output is fed to a digital oscilloscope, analyzed, and archived on a PC. The REMPI signals are gate integrated and averaged by boxcar integrator/average, as a function of wavelength. The digital delay generator is employed as a master to trigger all the instruments for time synchronization.

2.2.   LASER INDUCED FLUORESCENCE

The layout of LIF set-up has been already discussed in the previous section. The detailed experimental features, which are used in chapters 3, 4 and 5, are discussed in this section. In experiments, a pump laser is used for the photodissociation of reactant molecule. The photofragment population in various ro-vibrational states in the ground state is transferred to a ro-vibrational state in the excited electronic state, using a laser tuned to the requisite wavelength. In gaseous medium, it is possible to excite species from a particular ro-vibrational state in the ground state to a particular ro-vibrational state in the excited state, provided the spectral bandwidth of the laser employed is less than the rotational state spacing. The fluorescence intensity from this excited state is related to the laser intensity and population density of absorbing nascent photofragment formed.

To understand the working principle of LIF, let us consider a system with two energy levels. Let n_1 be the number density of the species in the ground state. A very small fraction of it on laser irradiation is excited to the higher energy state. Let the number density of the excited state species is n_2, then n_2 can be expressed in terms of n_1

$$n_2 = n_1\, I_{ex} \times \sigma_{species} \times \tau \qquad\qquad (2.1)$$

where I_{ex} is intensity of excitation laser, $\sigma_{species}$ is cross section of species at excitation wavelength, and τ is pulse width of the excitation laser. The excited state species will emit fluorescence. If fluorescence is the sole deactivation process for excited state species then the fluorescence signal, S_f is related to the number density, n_2, of the excited state species by the relation,

$$S_f = (n_2 \times A_{21} \times V_{fl})\,(\Omega_c/4\pi)\,\eta_c\,(\eta_p \times G_e) \qquad\qquad (2.2)$$

where, A_{21} is Einstein coefficient of spontaneous emission. Ω_c is solid angle subtended by collection optics. η_c is transmission efficiency of the optical collection system and η_p is quantum efficiency of photodetector. G_e is gain of detector electronics and V_{fl} is the fluorescence volume generated by the excitation laser, and it is assumed that the excited molecules/atoms are uniformly distributed in the fluorescence volume.

The sensitivity of LIF system depends on many factors, like absorption cross section of the species at the wavelength of excitation, intensity of excitation source (provided the intensity is not saturating the transition), quantum efficiency of fluorescence, A_{21} and efficiency of detection system, together with the collection optics. Thus, the selectivity of LIF system depends on types of chemical species present, its absorption spectra, whether their spectra overlap or well separated. If absorption bands are closely spaced then the spectral width of the exciting source plays an important role in selectivity.

Although, LIF is a very sensitive, selective and accurate diagnostic method of measurement, various uncertainties are associated with the measurement of LIF signal. Some of them are listed below:

1. The fluctuations in the intensity of the excitation laser propagate into the measured signal.

2. In detection system, the signal precision is affected by shot noise, which arises if the number of detected photons is small.

3. The most common uncertainty in gaseous system at high pressure is from collision quenching.

4. The competing fluorescence from other species can cause degradation of the measurement.

In the present thesis, Laser Photolysis-Laser Induced Fluorescence (LP-LIF) technique is employed for understanding the dynamics of photodissociation, where the LIF of the OH radical is used to probe the nature of a dissociative surface in a polyatomic molecule, in general, and strained cyclic molecule, in particular. Since the work is based on the LIF detection of OH formed, the electronic transitions involved in OH are described below.

2.2.1 SPECTROSCOPY OF OH

The notations for electronic states of diatomic molecules are similar to that for atoms, with $^{2S+1}\Lambda_\Omega$ used in place of $^{2S+1}L_J$, where

$$\Lambda = |M_L| \tag{2.3}$$

$$\Omega = |\Lambda + \Sigma| \tag{2.4}$$

M_L is the projection of electronic orbital angular momentum on internuclear axis. The total electronic angular momentum about the internuclear axis, Ω is given by the algebraic addition of Λ, the orbital angular momentum along the internuclear axis, and Σ, the electronic spin angular momentum along the internuclear axis.

According to the international nomenclature, $\Lambda = 0, 1, 2, 3, \ldots$ are designated as Σ, Π, Δ, Φ, . . . states, respectively. The spins of the individual electrons in the molecule give the resultant spin S. For $\Lambda = 0$ (Σ state), the resultant spin is oriented in a fixed space along the internuclear axis, as long as the molecule does not rotate, while for $\Lambda \neq 0$ the internal magnetic field in the internal nuclear axis resultant from the orbital angular motion causes the precession of S about it. It is designated as Σ (should not be confused with above Σ state), and quantum theory allows $2S + 1$ different values for it. The electronic states of diatomic molecules are also labeled with letters: X is reserved for the ground state, while A, B, C, and so on, are used for excited states of the same multiplicity (2S+1) as the ground state, in order of increasing energy. The states with a multiplicity different from that of the ground state are labeled with lowercase letters a, b, c, and so on, in order of increasing energy.

Being diatomic molecule, OH can rotate as whole about the axis passing through the centre of gravity and perpendicular to the line joining the nuclei (internuclear axis), and its atoms can vibrate relative to each other along the internuclear axis. Thus in case of OH, there is only axial symmetry about the internuclear axis; the motion of the electron takes place in a reduced symmetry of the field. The ground state configuration of the OH radical with nine electrons, in the united atom picture, is given by: $(1s\sigma)^2 (2s\sigma)^2 (2p\sigma)^2 (2p\pi)^3$. For this configuration the projection of the electron orbital angular momentum, M_L on the internuclear axis is $\Lambda = \pm 1$ and the projection of the electron spin angular momentum, S, on the internuclear axis is $\Sigma = \pm\frac{1}{2}$ i.e., the ground state term symbol, $^2\Pi$. The interaction of electron spin and orbital angular momentum splits each rotation state with $\Lambda \neq 0$ into two spin-orbit states.
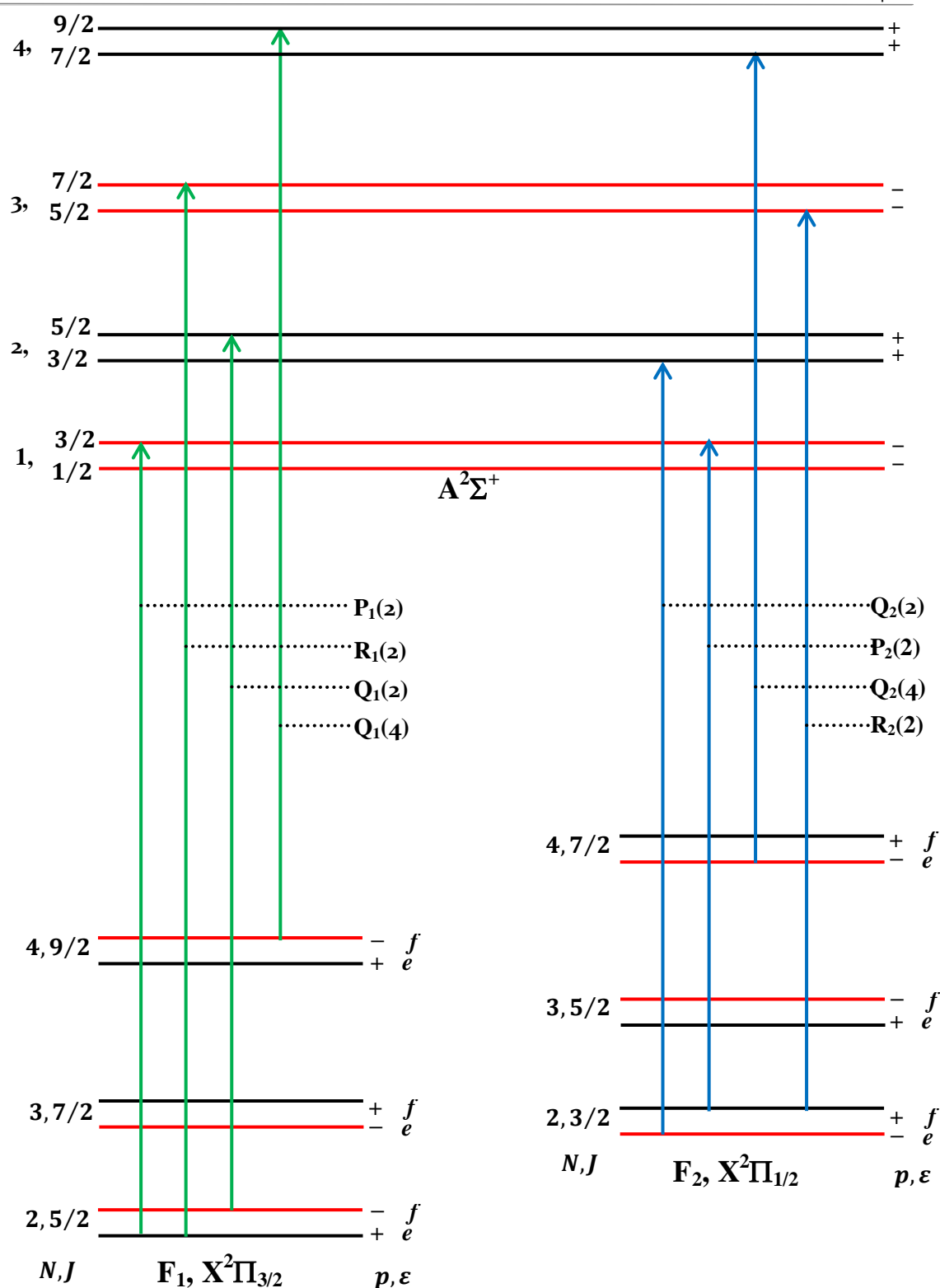
FIG. 2.3: A partial rotational energy level diagram of the ground X $^2\Pi$ (v''=0) and first excited $A^2\Sigma^+$ (v'=0) electronic states of OH including some dipole allowed transitions. The energy levels are labeled by both quantum numbers N and J, parity p and Λ-doubling symmetry e/f. The energy splitting of the Λ-doublet and ρ-doublet components is exaggerated for reasons of clarity.

Thus, for the ground state of OH (X $^2\Pi$), the two spin-orbit states are $^2\Pi_{1/2}$ and $^2\Pi_{3/2}$. At high rotational quantum number, the rotational angular momentum interacts strongly with the electronic angular momentum and lifts the degeneracy of the $\Lambda \neq 0$ states, which are doubly degenerate and gives the two Λ-doublet components $\Lambda^+(A')$ and $\Lambda^-(A'')$.

The first excited state of OH has the term symbol, $^2\Sigma^+$. The spectral features of the $A^2\Sigma^+ \leftarrow X$ $^2\Pi$ band system of OH at 308 nm have been very well studied. Therefore, LIF detection of OH is very convenient at 308 nm. The non-zero angular momenta of the fundamental electronic state of OH radicals shows fine structure and the effects of the coupling between rotation and electronic motion, such as Λ-doubling in the $^2\Pi$ and ρ-doubling in the $A^2\Sigma^+$ state. FIG.2.3 shows a partial energy level diagram for the $A^2\Sigma^+ \leftarrow X^2\Pi$ system of OH.

2.2.2   EXPERIMENTAL SET-UP

The schematic of the set-up for LP-LIF, used in the studies is shown in FIG.2.4. The probe laser employed here is a Quantel dye laser, with frequency doubling and mixing modules (TDL90), pumped by a seeded Nd:YAG laser (Quantel model YAG980 E-20). The dye laser, operated with DCM (4-dicyanomethylene-2-methyl-6-(p(dimethylamino)styryl)-4H-pyran) special dye pumped by a 532 nm laser beam from the second harmonic of the Nd:YAG laser, provides the fundamental wavelength tuning range of 600-640 nm. The fundamental dye laser output is frequency doubled in a KDP crystal to obtain the laser output in the range 300-320 nm and used for probing the OH radical. The pulse width of the laser is ≤ 8 ns and the fluence used is < 20 μJ cm^{-2}.
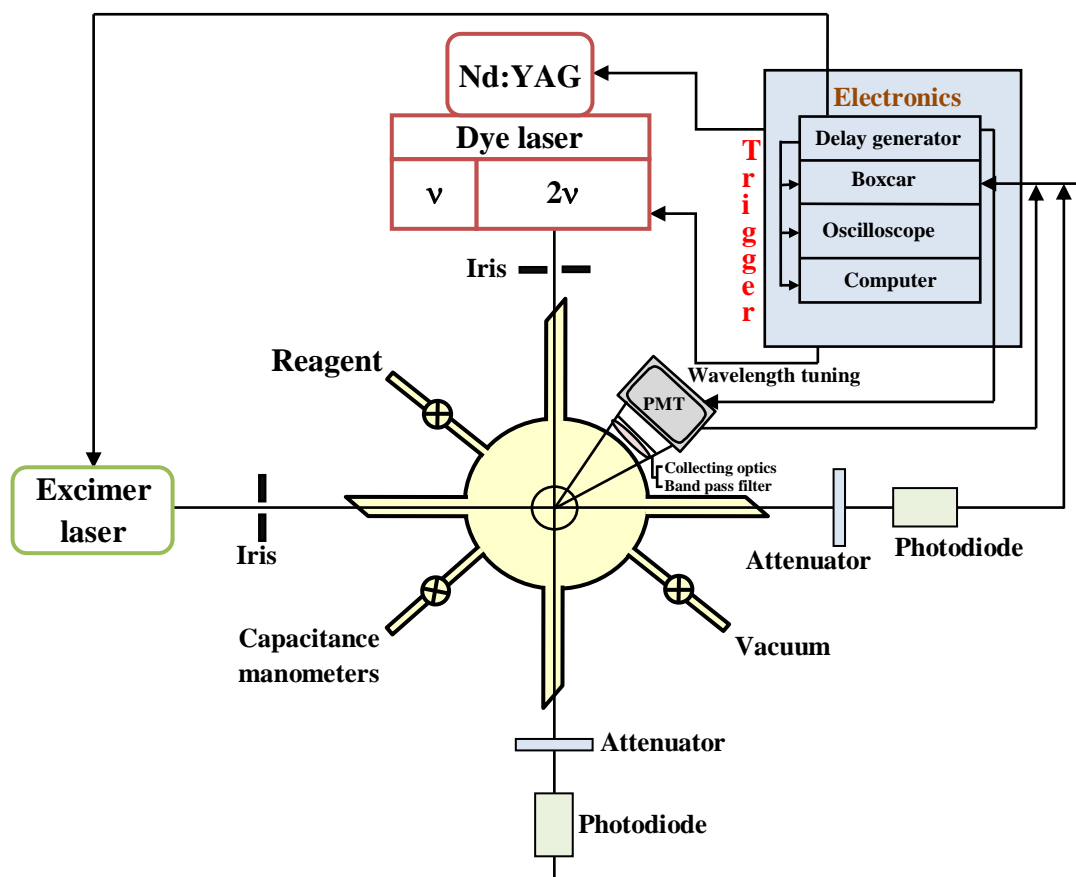
FIG. 2.4: An experimental set-up for laser photolysis-laser induced fluorescence technique.

The glass reactor has crossed arms at right angles with suitable windows, allowing the photolysis and the probe laser beams to intersect at the centre of the reaction chamber. The crossed arms are provided with MgF_2 and quartz windows at the Brewster angle to facilitate transmission with reduced scattering of the photolysis and the probe beams, respectively. The reactor is also equipped with three ports for the pressure transducer, gas inlet and the vacuum pump. The bottom arm that views the intersection volume of the photolysis and probe lasers is attached to a detector. The fluorescence is collected by 38-mm diameter lens of focal length 50 mm, and detected by a photomultiplier tube (PMT, Hamamatsu, model R 928P). A band-pass filter (λ_{centre} = 310 nm, FWHM = ±10 nm, Transmission at 310 nm = 10%) is placed between the collecting lens and the PMT to cut-off the scattering from the photolysis

laser. The laser intensity fluctuations are corrected by monitoring both the pump and the probe lasers by photodiodes, and normalizing the fluorescence intensities during the analysis. The laser frequency is calibrated, using an optogalvanic cell (Fe-Ne), with an accuracy of ± 0.3 cm^{-1}. The spectral resolution of the probe laser is 0.06 cm^{-1}. The fluorescence signal from the PMT is sampled with a boxcar integrator (SRS250). During the LIF experiments, the gate width of the boxcar integrator was $\sim$100 ns, and the signal is averaged over 30 laser shots for a good S/N ratio and fed to an interface (SRS245) for A/D conversion.

Table 2.1: Specifications of delay generator employed in experimental set-up.

S.No.	Feature	Parameters	Specifications
1.	Delays	Channels	Four independent delay outputs: A,B,C and D
		Range	0 to 999.999,999,999,995 s
		Resolution	5 ps
		Accuracy	1500 + timebase error x delay
		RMS Jitter	60 ps + delay x 10^{-8}
2.	Frequency	Repetition rate	0.001 Hz to 1.000 MHZ
3.	Inputs	External trigger	Impedance : 1 MΩ or 50 Ω
			Threshold : $\pm$ 2.56 Vdc
4.	Outputs	Channels	T0, A, B, C, D, AB, -AB, CD and –CD
		Load	50 Ω or high impedance
		Rise time	3 ns
		Type	TTL, ECL, NIM, VAR
5.	Interface	Computer interface	IEEE 488 Standard GPIB

A Pentium IV PC is used to control the scan of the dye laser via a RS232 interface and to collect data through a GPIB interface using a control and data acquisition program. A digital delay/pulse generator, with pulse resolution of 20 ps, was employed as the master to trigger all the instruments for time synchronization. The detailed specifications of the digital delay/pulse generator employed are given in Table 2.1.

The set-up in FIG. 2.4 is routinely used for LIF measurement of gaseous samples. It is modified for solid samples by introducing a special arrangement, which is devised to flow the vapour from solid sample through the reaction chamber. A capillary tube (internal diameter = 1.5 mm), with an open top end for admitting the vapour and the other end tapered as a nozzle, was fused inside a ¼ inch glass tube with the nozzle protruding out, as shown in FIG. 2.5. The solid sample can be loaded in the ¼ in. glass tube, around the capillary tube, and the vapour at the room temperature entered through the open top end of the capillary tube and exited through the protruded nozzle. After loading the sample, the sample holder along with the reaction chamber can be degassed thoroughly by an oil diffusion pump, which is backed with a rotary pump. It is possible to translate the 1/4 in. tube in the reaction chamber under vacuum, since this tube is mounted on a linear motion feed through. Both laser beams spatially overlapped just below the nozzle from which the sample vapour effused out. The height of the sample holder with respect to the laser beams can be adjusted to optimize the LIF intensity.
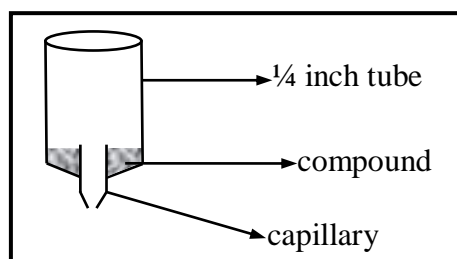
FIG. 2.5: The schematic for solid samples.

The OH fragment is probed state-selectively by exciting the $A^2\Sigma^+ \leftarrow X^2\Pi$ (0, 0) transition of OH (306-309 nm) and monitoring the subsequent A→X fluorescence. During the experiments, both the laser beams are unfocused and attenuated to prevent saturation and multiphoton events. This is verified by plotting LIF signal versus laser intensity. Those plots have found to be linear, for both photolysis and probe lasers. To examine whether a transition is saturated, we measured the line intensities of main and satellite branches of OH. Since a main branch and the adjacent satellite branch lines probe the population of the same state, and if there is no saturation in the LIF intensities, the ratio of their LIF intensities should be equal to the ratio of their Einstein coefficients. The Einstein coefficients for the main branches are around 10 times higher than those of their satellite branches. Hence, the saturation in LIF intensities can be estimated from the ratio of their intensities, which is found to be negligible in the present work. The compound vapour flowed through the reaction chamber at a flow velocity of approximately 10 cm/s. The pressure is maintained at less than 100 mTorr, which is measured using a capacitance gauge (Pfeiffer vacuum model). The LIF spectra are measured at pump-probe delays of 50 and 100 ns, and found to be identical, thereby ensuring negligible collision relaxation of the nascent OH radical. The LIF intensities are measured as a function of the substrate pressure, and found to be linear within the pressure range used. During a few experiments, the windows of the photolysis laser developed a thick coating (from the deposits of some photoproducts), which is cleared regularly to avoid the attenuation of the laser energy. Each liquid samples are used as supplied but after degassing through several freeze-pump-thaw cycles, while the solid samples are thoroughly degassed before use.

The data obtained by LP-LIF are used for extracting important dynamic information of the photolysis reaction. The rotationally resolved electronic spectra

collected under collisionless condition gives a reliable picture of the energy state distribution among the product species at their nascent states. The intensity of the different rotational lines is directly proportional to the population of the product in the different rotational levels. If higher vibrational states of the product molecules are found to be populated, the ratio of intensity of the same rotational line for transitions from two different vibrational states can give an idea about the vibrational temperature, too, i.e., vibrational energy of the products. Each of the rotational lines has some finite width due to Doppler effect. A Doppler broadened rotational line would have contributions from the different line broadening factors, like molecular velocity of the fragments, thermal motion of the parent molecule, and the spectral width of the probe laser. Hence, after correcting for the probe laser line width (0.07 cm^{-1} in the present work, measured by de-convolution of the line width of thermalized OH at high pressure and a longer pump-probe delay time of ~100 μs), the Doppler profile of a line in the spectrum shows the distribution of velocity component v_z of the absorbing species, i.e., the OH radical along the propagation direction of the probe laser beam. Thus, the LIF spectrum can be analyzed, and distribution of the energy among nascent products can be obtained.

The transition width between the two energy levels of the probed species is reflected in LIF line width. The width of the rotational line is due to the contribution from the natural, Doppler and pressure broadenings. The natural width arises from the Heisenberg uncertainty principle and is related to the lifetime of the excited state. The Doppler broadening is due to the thermal motion of the probed species. The distribution of velocities at a thermodynamic temperature T can be evaluated from the Maxwell-Boltzmann expression. Different velocity component arises from the projection of velocity of probed species on the propagation direction of probing light.

Hence, each of these probed species has slightly different transition frequency. The corresponding line shape function g(ν) is given by the expression,

$$g(\nu) = \frac{c}{\nu_0} \sqrt{\frac{m}{2\pi kT}} \, exp\left[-4ln2 \frac{(\nu-\nu_0)^2}{\Delta\nu_D^2}\right] \tag{2.5}$$

Where, ν_0 is the center frequency of transition and $\Delta\nu_D$ is the transition width (FWHM) which is given by

$$\Delta\nu_D = \frac{2\alpha\nu_0}{c} \sqrt{2ln2} \tag{2.6}$$

Here, α is most probable velocity of the molecule Doppler broadening is caused by the random thermal motion and is inhomogeneous, so it is having a Gaussian line shape. In a flowing system at temperature T, the Doppler width is same as given by the Eqn. (2.6), however, the center frequency of transition is shifted, which is given by the expression

$$\nu - \nu_0 = \frac{\vec{v}.\vec{k}}{2\pi} \tag{2.7}$$

where $\vec{k}$ is the wave propagation vector of probing light and $|\vec{k}| = 2\pi/\lambda$ (λ being the wavelength of the probing light). The collisional broadening is homogeneous in nature and hence generally results in a Lorentzian line shape, while the Doppler broadening, due to random thermal motion of the absorbing species, is inhomogeneous, resulting in a Gaussian line shape. The transition line broadening in LIF spectra contains information about the temperature, flow velocity and pressure, which can be extracted by suitable deconvolution method.

If the velocity distribution f(v) is isotropic, i.e., $f(v_x)=f(v_y)=f(v_z)$, for a Gaussian Doppler profile, the one-dimensional distribution of velocity along any co-ordinate is given by,

$$f(v_z) = \frac{1}{\alpha\sqrt{\pi}} e^{\frac{-v^2}{\alpha^2}} \tag{2.8}$$

Hence, $<v_z^2>_{OH}$, which represents the second moment of the laboratory velocity distribution of the OH radical in the direction of laser propagation, is given as,

$$\langle v_Z^2 \rangle_{OH} = \int_{-\infty}^{\infty} v_z^2 f(v_z) dv = \frac{1}{\alpha\sqrt{\pi}} \int_{-\infty}^{\infty} v_z^2 e^{\frac{-v^2}{\alpha^2}} dv \tag{2.9}$$

By putting the value of the standard integral, and substituting the value of α from eqn. (2.6).in eqn. (2.9), we get,

$$\langle v_Z^2 \rangle_{OH} = \left(\frac{\Delta \nu_D}{2\nu_0}\right)^2 \frac{c^2}{2\ln 2} \tag{2.10}$$

ν_0 and $\Delta\nu_D$ are the position of the peak and width of the profile, respectively. The average translational energy in the laboratory frame is given by,

$$E_T^{lab}(OH) = \frac{3}{2} m_{OH} \langle v_Z^2 \rangle_{OH} \tag{2.11}$$

About 15 rotational line widths were estimated for each of $P_1(2)$ and $Q_1(4)$ lines, and using the above two equations, the kinetic energy of the OH fragment in laboratory frame, $E_T^{lab}(OH)$, was determined. The average translational energy in the centre-of-mass frame, E_{CM}, was calculated from $E_T^{lab}(OH)$, neglecting the translational energy of the parent molecule, by the use of the equation,

$$E_T^{CM} = E_T^{lab}(OH)\left[1 + \frac{m_{OH}}{m_{other\ fragment}}\right] \tag{2.12}$$

The line shape function corresponding to the collision or pressure broadening is given by the expression

$$g(\nu) = \frac{\Delta\nu_C}{2\pi} \frac{1}{(\nu-\nu_0)^2 + (\Delta\nu_C/2)^2} \tag{2.13}$$

The transition line broadening in LIF spectra contains the information about the temperature, flow velocity and pressure, which can be extracted by suitable de-convolution methods. The temperature of the system in thermodynamic equilibrium can be estimated from the population distribution of the rotational levels, as populations of different levels are related to the temperature by Boltzmann equation.

$$\frac{N_{J=m}}{N_{J=n}} = \frac{LIF_{signal\ at\ J=m}/2m+1}{LIF_{signal\ at\ J=n}/2n+1} = \exp\left(-\left[\frac{E^R_{J=m}-E^R_{J=n}}{kT}\right]\right) \tag{2.14}$$

Where, $N_{J=m}$ and $N_{J=n}$ are the population of rotational levels *m* and *n*, respectively. Hence, from the relative populations of different rotational levels i.e., from the normalized relative LIF intensities, the temperature of the system can be estimated. Positions of all the rotational lines in the spectrum of the OH radical were marked, following the assignments made by Dieke and Crosswhite[50].

The respective LIF intensities were normalized with respect to the photolysis and the probe laser intensities, pressure of the sample in the cell, and Einstein's absorption coefficients B_{ij} (taken from the work of Chidsey and Crossley[51]), to calculate the relative population of each rotational level. The populations P(J), obtained in this fashion, of the nascent OH fragment generated by photodissociation, were plotted against energy of rotational levels (ε), to construct a Boltzmann plot given by the equation

$$\ln\frac{P(J'')}{(2J''+1)} = \frac{-\varepsilon hc}{kT_R} + \text{constant} \tag{2.15}$$

Here T_R is the rotational temperature of the OH. The vibrational temperature T_V can also be obtained by assuming a Boltzmann distribution of vibrational populations of OH. The ratio of the LIF intensities of the same rotational line of the (0, 0) and (1, 1) transitions is expressed by the relation,

$$\frac{I(R_{1,2}(N'');v''=1)}{I(R_{1,2}(N'');v''=0)} = \exp\left(\frac{-\Delta\varepsilon_v hc}{kT_v}\right) \qquad (2.16)$$

where ε_v is the energy difference between $v''=1$ and $v''=0$ for a given spin-orbit state and N''. The constants h, c, and k have their usual meaning.

2.3   RESONANCE ENHANCED MULTIPHOTON IONIZATION

Resonance ionization is a photo-physical process in which electromagnetic radiation is used to ionize atoms, or molecules, via an excited state, prepared resonantly. In this process, the atomic or molecular system serves as a summing device for storing the energy of the resonantly absorbed photons, and when the stored energy exceeds the ionization energy, this leads to spontaneous ionization. In the REMPI detection of a chemical species in gas phase at the room temperature, only a small fraction of the total available molecules is accessible to the excitation process. This is due to a broad population distribution in the ro-vibrational states, expressed by the Boltzmann equation. The sensitivity of REMPI can be improved and the transitions can be made sharp by enhancing the population in the ground state and minimizing the collisions between gas molecules themselves, as well as with the background gas molecules. Both these objectives can be achieved by employing supersonic beams. The molecular beam (MB) systems are ideal for studying the reaction under collision-free conditions, which enable us to extract the microscopic parameters of the reaction. Supersonic MBs are realistic in improving the sensitivity of a detector. They can provide an intense source of molecules traveling with a fixed velocity in a given direction in vacuum, having an extremely narrow velocity distribution, isolated from each other, and cooled to such an extent that the excited rotational and vibrational levels are almost depopulated. Thus, they enable to prepare

molecular reactants in well-defined quantum states, with known translational energy. Thus, supersonic beams are employed for carrying out quantum state selective chemistry, as well as to investigate the effect of translational energy on the reaction cross-sections. The importance and utility of using supersonic beams have been already discussed in Chapter 1.

The REMPI transitions are state-selective hence; fragments in only a specific quantum state are detected. This means that not only the mass of the photofragment can be selected using the microchannel plate (MCP) gating and time-of-flight tube, but fragments of a specific internal energy can be selectively ionized as well by simply tuning the wavelength of the ionization laser to the desired electronic state. This method allows us to obtain correlated information about the photodissociation process. Because of the state selectivity of (2+1) REMPI detection, the electronic state of the detected fragment is known. In addition, the internal energy of the unseen fragment is also measured because of the measured speed distribution of the detected fragment. The work reported in this thesis is based on the REMPI detection of Cl and Br atom formed. The (2+1) REMPI transitions of atomic species studied in this work are given in Table 2.2.

Table 2.2: (2+1) REMPI transitions of atomic species of chlorine and bromine.

Atomic Species	Electronic State	Intermediate State	Wavelength
Cl	3p $^2P_{3/2}$	4p $^2D_{3/2}$	235.336 nm
			(42719.3 cm^{-1})
Cl*	3p $^2P_{1/2}$	4p $^2P_{1/2}$	235.205 nm
			(42516.1 cm^{-1})
Br	4p $^2P_{3/2}$	6p $^4P_{3/2}$	233.700 nm
			(42789.9 cm^{-1})
Br*	4p $^2P_{1/2}$	6p $^2S_{1/2}$	234.040 nm
			(42727.7 cm^{-1})

Both chlorine and bromine atoms are having one unpaired electron in p orbital in their ground state leading to the term symbol, ^2P, and due to the spin-orbit interaction, it splits into $^2P_{3/2}$ and $^2P_{1/2}$. A typical (2+1) REMPI scheme for the chlorine atom and bromine atom is given in FIG. 2.6 and FIG. 2.7. In case of chlorine atom, the two spin-orbit states are separated by 882 cm^{-1}. The ionization limit for chlorine atom is 104591.0 cm^{-1}. The chlorine atom requires two photons of frequency 42719.3 cm^{-1} (235.336 nm) for excitation to an intermediate state. It is then followed by one photon absorption to ionize the excited chlorine atom. Similarly, in bromine atom the two spin-orbit states are separated by 3685.24 cm^{-1}. The ionization limit for bromine atom is 95172.9 cm^{-1}. The bromine atom requires two photons of frequency 42789.9 cm^{-1} (233.7 nm) for excitation to an intermediate state. It is then followed by one photon absorption to ionize the excited bromine atom.
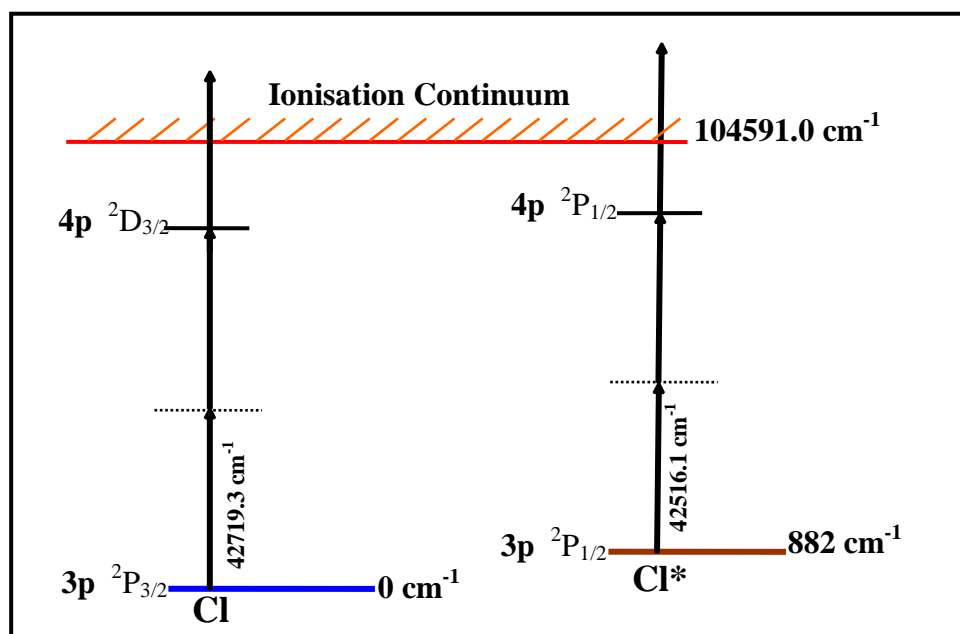
FIG. 2.6: REMPI scheme for the chlorine atom for the two spin orbit states.
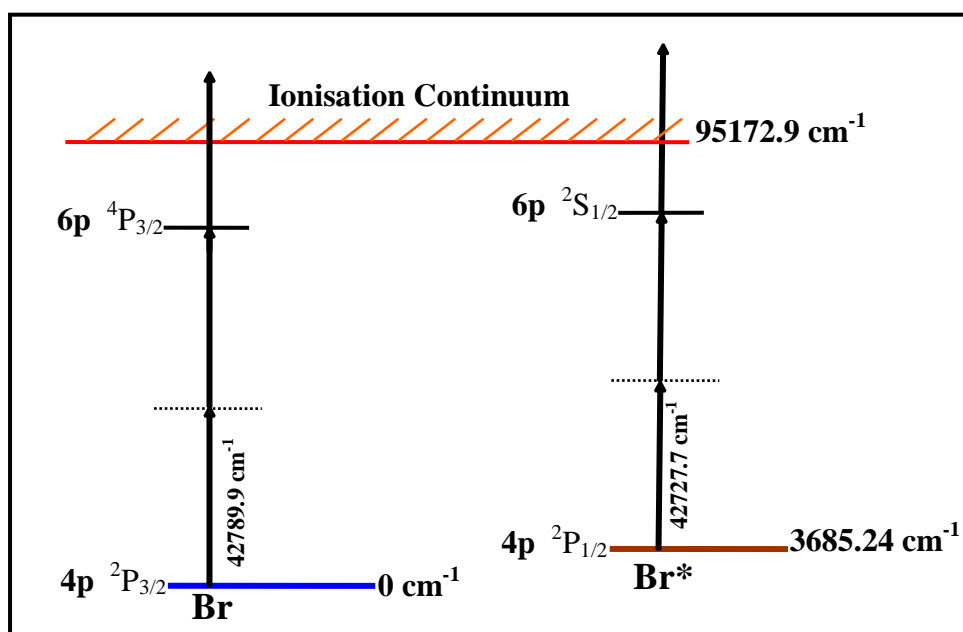
FIG. 2.7: REMPI scheme for the bromine atom for the two spin orbit states.

Along with MB-REMPI, a TOF-MS is employed to analyze ions of different m/z, on the basis of their flight times to the detector, at a fixed accelerating electric potential. The detailed experimental set-up and analysis of acquired data are explained below.

2.3.1   EXPERIMENTAL SET-UP

The experiments are performed using a molecular beam time-of-flight mass spectrometer system (MB-TOF-MS), consisting of a supersonic beam source and an ionization (beam-laser interaction) region. The system is differentially pumped, using two similar 9 inch. turbomolecular pumps (TMP), backed by rotary pumps. An additional 4 inch. TMP is used to pump the TOF tube located at the end, near the detector. A schematic diagram of the system is shown in FIG.2.8 and the picture of the assembled setup is shown in photograph 2.1.

1.	Expansion Chamber	7.	Gas/reagent inlet
2.	Ionisation Chamber	8.	Pulsed valve
3.	TOF Tube	9.	Skimmer
4.	MCP Detector	10.	Molecular Beam
5.	HV supply for MCP	11.	Interaction Zone
6.	Turbomolecular pumps backed by rotary pumps	12.	Repeller Plate
		13.	Extraction Grid
		14.	Acceleration Grid
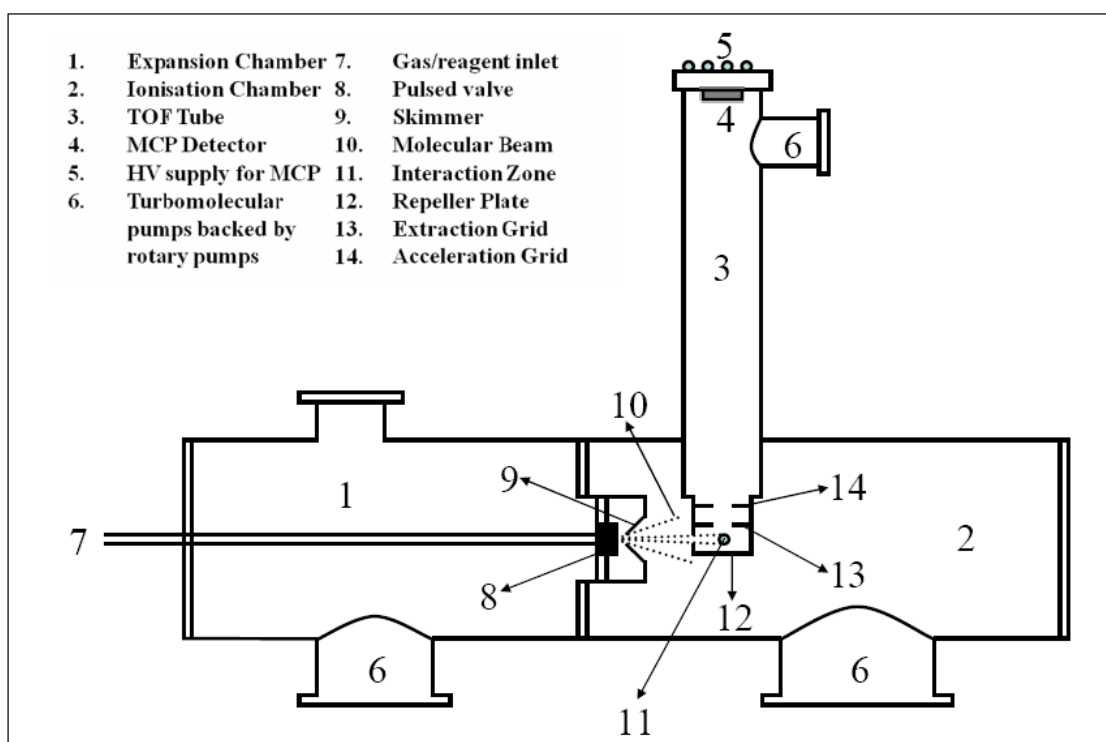
FIG. 2.8: A schematic diagram of MB-REMPI-TOF-MS system.

Photograph 2.1: A picture of the MB-REMPI-TOF setup.

Typical operating pressures in the source and the ionization regions are 5×10^{-5} and 8×10^{-7} Torr, respectively. A pulsed supersonic molecular beam is generated using a solenoid valve, with a 0.8 mm nozzle and 500 μs opening time. The molecular beam is skimmed off through a 1.9 mm diameter conical skimmer to the interaction region. The MB pulse profile and the number density are characterized using a fast ion gauge (FIG) located beyond the ion optics, which has a provision for movement along the MB axis. The pulsed valve was located $\sim$2 cm from the skimmer, and 7.5 cm from the interaction region. The specification of the nozzle-skimmer assembly is outlined in table 2.3.

Table 2.3: Specifications of nozzle-skimmer assembly employed in experimental set-up.

Nozzle-Skimmer Assembly	Characteristics
1. Pulsed valve type	Solenoid
2. Nozzle diameter	800 μm
3. Pulse width	500 μs
4. Skimmer diameter	1.9 mm
5. Distance between nozzle to skimmer	20 mm
6. Distance between nozzle to laser beam interaction region	75 mm

During the experiment, helium is bubbled through the sample maintained at room temperature, and the mixture is expanded through the nozzle at a stagnation pressure of 1500 Torr of He. It is ensured that any interference to the measurements due to cluster photofragmentation is absent or negligible by operating at a low stagnation pressure, and using only the rising part of the molecular beam pulse. The detector system consists of a two-stage Wiley-McLaren[52] time-of-flight mass spectrometer (TOF-MS), with an extraction and an acceleration region. The system is mounted vertically, perpendicular to the horizontal MB.

The extraction region consists of a repeller electrode (5 cm ✕ 5 cm), which is a solid stainless steel plate, and an extraction grid, mounted 10 mm above the repeller electrode. The acceleration region is defined by the extractor electrode and a grid held at the ground potential, separated from each other by 10 mm. Both these grids (5 cm ✕ 5 cm) are constructed from stainless steel mesh, with 90% transmission. To collect the total ion signal, the extraction region was held at ∼300 V/cm, and the acceleration region was held at ∼3900 V/cm. After passing through the acceleration region, the ion

packet passed through a 1035 mm long field-free flight tube to the detector. Two deflector plates, placed perpendicular to the detector axis (z axis) allowed the ion packet to be translated in the (x, y) plane to center the ion packet on the detector. The typical field strength for the deflector plates is 2-6 V/cm. The ions are detected by a set of 18 mm dual microchannel plates. A single compact voltage generator, having multiple output voltage ports, is employed to power the TOF ion optics, the deflection plates and the MCP detector. Before applying any voltage to the MCP, it is pumped at a dynamic vacuum of $< 10^{-6}$ Torr for 2-3 days. The grid of the MCP is grounded, while the MCP plates are powered, using a divider box. The applied voltage to the voltage divider box is divided, to provide the requisite voltages to the dual channel MCP detector.

The laser system comprises a dye laser (TDL 90, Quantel), pumped by a Nd:YAG laser (YG-981-C, Quantel). The chlorine and bromine atoms are probed, using (2+1) REMPI transitions in the region of 234-236 nm and 230-235 nm, respectively. The laser pulses are generated by a dye laser, using rhodamine 101 dye. The dye laser (TDL 90, Quantel) is pumped by a 532 nm laser beam, the second harmonic of a Nd:YAG laser, YG-981-C, Quantel, operating at 20 Hz. For obtaining the required wavelength, in the region around 235 nm, in the first stage, the fundamental output of the dye laser (598-608 nm) is doubled in a KDP crystal, to obtain laser radiation in the range 299-304 nm. The doubled output is separated from the fundamental using Pellin-Broca prisms and mixed in a BBO crystal, with the fundamental frequency of the Nd:YAG laser (1064 nm), to obtain the required range of 230-236 nm output wavelength. A schematic of the procedure used to generate required wavelength is shown in FIG.2.9. The resultant light has a bandwidth of ~ 0.14 cm^{-1}, and is calibrated, using a Fe/Ne optogalvanic (OG) cell and a wavemeter.

The above laser output is separated from the rest of laser beams, using four Pellin-Broca prisms.
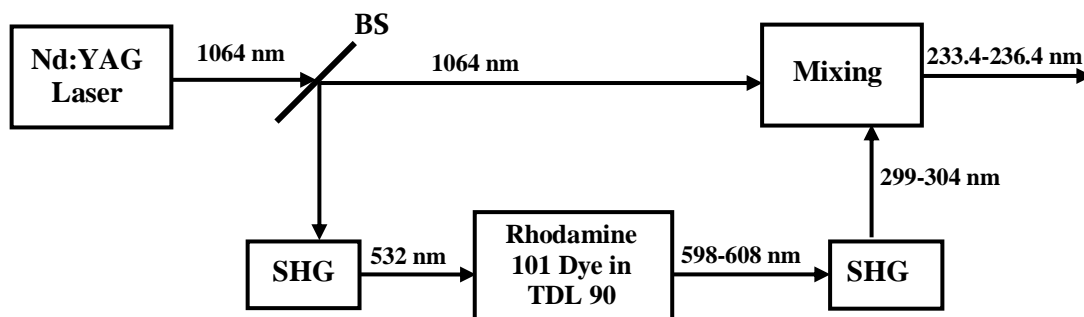
FIG. 2.9: The resultant output wavelength around 235 nm from Quantel dye laser with frequency doubling and mixing modules pumped by Nd:YAG laser.

In all the experiments reported in this work, the same laser beam is employed as a pump as well as a probe, i.e., for both photodissociation of the parent molecule and ionization of the photoproducts, X/X*. The laser beam is focused by a 200 mm focal length lens, and the distance of the lens from the center of the molecular beam axis was varied, to obtain the best ratio of on- and off-resonant signals. The spin-orbit ratio can be calculated from the ion intensities for different corresponding transitions, after correction due to their two-photon oscillator strengths. For this purpose, two lines of each Cl and Br are chosen. For chlorine atom peaks at 42 492.5 cm^{-1} and 42 516.1 cm^{-1}, corresponding to 4p $^2D_{3/2} \leftarrow$ 3p $^2P_{3/2}$ and 4p $^2P_{1/2} \leftarrow$ 3p $^2P_{1/2}$ transitions, respectively, and for bromine atom peaks at 42789.9 cm^{-1} and 42727.7 cm^{-1}, corresponding to 6p $^4P_{3/2} \leftarrow$ 4p $^2P_{3/2}$ and 6p $^2S_{1/2} \leftarrow$ 4p $^2P_{1/2}$, respectively, were selected. The branching ratios of Cl (^2P_j) are obtained by observing the 4p $^2D_{3/2} \leftarrow$3p $^2P_{3/2}$ transition around 235.336 nm and the 4p $^2D_{3/2} \leftarrow$3p $^2P_{1/2}$ transition around 237.808 nm. The magnitude of the REMPI signal is proportional to the square of the probe laser intensity. The two-photon absorption is the bottleneck in this MPI process. The relative two-photon absorption cross sections for $^2D_{3/2} \leftarrow^2P_{3/2}$, $^2P_{1/2}$ were previously calculated using the *L-S* coupling approximation and the ratio was found to

be unity[53]. Hence, the intensity ratio experimentally obtained is the same as the relative formation ratio of the Cl atoms in each J level.

The polarization of the resultant light is rotated using a double Fresnel rhomb, and a polarizer ensured 99% polarization of the light entering the chamber. The laser power is monitored, using a power meter, and is typically maintained at 50-100 μJ/pulse. To obtain the TOF spectrum, the signal is sent to a 500 MHz digital oscilloscope (LeCroy 9350A), which is interfaced to a Pentium PC. Subtracting the off-resonant signals from the on-resonant signals effectively removed the minor pump-oil related background contribution to the TOF spectra, and the contribution from a multiphotonic process.

A delay generator with pulse resolution of 20 *ps* maintained the time delay between photolysis laser, probe laser and data acquisition system. The time delay between the trigger pulse applied to the pulsed valve and the valve opening was obtained by measuring the delay between the trigger pulse and the fast ionization gauge (FIG) signal, employing a digital oscilloscope. The flow velocity of the molecular beam can be estimated by measuring time delays for different FIG positions with respect to the skimmer. The time required for the molecular beam to reach the extraction region is obtained. This delay is the sum of the time required to open the pulsed valve from its trigger input and that for the molecular pulse to reach FIG from its position of generation, i.e., the nozzle exit.

Fast photodiodes (Becker-Hickl Model PDM-400) are used to measure the time delays between the external-trigger inputs and the laser outputs at ~235 nm from Nd:YAG pumped dye laser after doubling the fundamental beam and mixing with 1064 nm (fundamental of Nd:YAG laser). Based on the above measured delays, the

trigger pulses of different instruments are adjusted. All the experiments were carried out with single colour laser, i.e., the same laser beam is used for both photolysis and probing. The laser pulse and the rising part of molecular beam pulse are temporarily and spatially overlap in the ionization/extraction region of TOF system. The ion signal was gate integrated by a boxcar, averaged for 30 laser pulses, and fed into an interface (SRS 245), for A/D conversion. A PC is used to control the scan of the dye laser via an RS232 interface and collect data from SRS 245, through a GPIB interface, using a control and data acquisition program. The power dependence measurements are performed by measuring the integrated chlorine atom REMPI signal, i.e., measuring boxcar gated on the m/z 35 and m/z 37 peaks in the TOF spectrum. The laser powers were varied, and the signal outputs were recorded at various laser intensities to obtain REMPI signal as a function of laser intensity. The REMPI spectra and survey scans were taken, by recording the boxcar signal output as a function of the laser wavelength and archiving the spectra on a PC interfaced to the dye laser controller. TOF profiles are taken for three different experimental configurations, v*ertical* (laser polarization | detection axis), *horizontal* (laser polarization ⊥ detection axis), and *magic angle* (laser polarization at 54.7° to detection axis). Doppler broadening of the transitions in all experiments are always well within the laser bandwidth.

2.3.2   ANALYSIS OF DATA ACQUIRED FROM REMPI EXPERIMENTS

The flight distribution of Cl, Cl*, Br and Br* were obtained in the above experiments. These flight distributions contain the information about the photofragment speed distribution, and thus, the translational energy distribution. To extract these information, a commonly used forward convolution (FC) technique[54] was employed to fit our experimental TOF profiles.

The measured TOF profile is a convoluted output of flight distribution with instrumental response function. The instrumental response function has been characterized by studying the REMPI of aniline beam. The REMPI spectrum of aniline recorded at 34029 cm^{-1} (293.77 nm) matches well with the reported value in the literature[55]. The aniline molecular ion signal was measured as a function of laser intensity at resonance wavelength, and found to be quadratic dependent. This shows that at 293.77, the REMPI is 1+1 type due to one photon, $^1A_1 \rightarrow {}^1B_2$, resonant transition, followed by pumping to the ionization continuum with absorption of the second photon. Since the v_z for aniline molecule in the beam is almost zero, measurement on single ro-vibrational state of aniline molecule is used to determine the instrument response function. Such measurement showed the instrumental response function to be well described by a fixed Gaussian function in the time domain, with FWHM 27 ns, at aniline mass. Under space focusing conditions, this leads to a convolution function in the velocity domain, which is linearly dependent on the extractor voltage V_{ex}.

The forward convolution method[56] employed in fitting the experimental data is being outlined briefly. In a dissociation process of isotropically oriented sample, using linearly polarized light, the angular distribution of a photofragment is given by[57]

$$f(\theta_s, \Phi_s) = \frac{\sigma}{4\pi} [1 + \beta P_2(\cos\theta_s)] \tag{2.17}$$

where σ is the total cross-section, θ_s and Φ_s are the lab frame polar and azimuthal angles about the axis defined by the laser polarization, P_2 is the second order Legendre polynomial and β is a parameter that describes the degree of anisotropy ($-1 \leq \beta \leq 2$) and

$$\beta = 2\langle P_2(\cos\theta_m)\rangle = 3\cos^2\theta_m - 1 \tag{2.18}$$

where θ_m is the molecular frame angle between the molecular transition dipole moment μ and photofragment recoil direction v.

In the REMPI-TOF technique, the component of the photofragment that speeds along the TOF-MS axis, which defines the lab frame Z-axis, is measured. This speed component results from averaging of the angular distribution in Eq. (2.17) over the photofragment speed distribution $g(v)$, and it is given as[56,58]

$$f(v_z,\chi) = \int_{|v_z|}^{\infty} \frac{g(v)}{2v} \left[1 + \beta P_2(\cos\chi) P_2\left(\frac{v_z}{v}\right) \right] dv \qquad (2.19)$$

where v_Z is the velocity component along the Z axis and v is the recoil speed of the fragments, $P_2(\cos\chi)$ is the second Legendre polynomial. $\cos\chi = \hat{E}\cdot\hat{z}$, used in above equation is the projection of the pump laser electric field, $\hat{E}$, on the detector axis, $\hat{z}$ and χ is also defined as the angle between the dissociation laser polarization and the Z axis.

One can predict the angular recoil velocity distribution and TOF profiles, based on Eqns (2.17)-(2.19)[59]. For that, we consider two cases

Case I: $\mu \parallel v$

If detector axis is along the $\hat{E}$, then $\chi=0$, $\beta=2$, and distribution is $f(\theta_s,\phi_s)=\cos^2\theta$, which is the dumbbell-shaped angular distribution, and if detector axis is perpendicular to $\hat{E}$, then $\chi=90$, $\beta=-1$, and distribution is $f(\theta_s,\phi_s)=\sin^2\theta$, which is the toroidal probability distribution. (FIG. 2.12 right panel).

Case II: $\mu \perp v$

If detector axis is along the $\hat{E}$, then $\chi=0$, $\beta=-1$, and distribution is $f(\theta_s,\phi_s)=\sin^2\theta$, which is the toroidal probability distribution, and if detector axis is perpendicular to

Ê, then χ=90, β = 2, and distribution is $f(\theta_s,\phi_s)= \cos^2\theta$, which is the dumbbell-shaped angular distribution (FIG. 2.12 right panel).
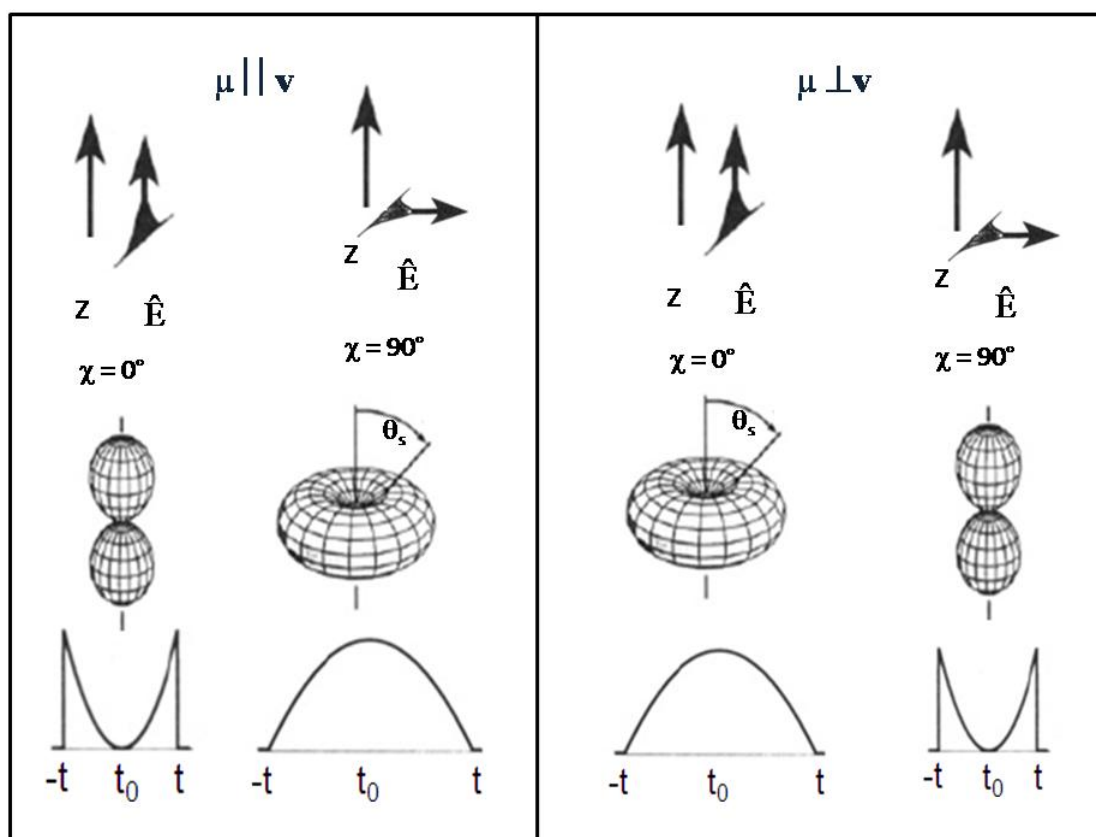
FIG. 2.10: Illustrates change in time of flight profile (at the bottom of the panel) by the correlation of the polarization of dissociating laser light when the molecular transition dipole moment is aligning either parallel (left panel) or perpendicular (right panel) to the recoil velocity of photofragment.

In the present work, we have used a procedure of non-core sampling data, in which it is assumed that measurement of angular distributions of the chlorine or bromine photofragment is independent of probe polarization. In general, this assumption holds good, but the presence of atomic **v.j** correlation might make this assumption only approximate. However, these correlations are weak[60] enough to be neglected. In the case of several contributing channels, Eq. (2.19) must be summed over the photofragment speed distribution $g_i(v)$ and anisotropy β_i of each channel i. The dependence of f (v_z, χ) on β can be eliminated by either measuring data with magic angle of χ=54.7°, where $P_2(\cos\chi)$ is zero or by co-adding normalized profiles

with χ=90° and χ=0°, giving a 2:1 weightage. Both the approaches yield isotropic f(v_z, χ) profiles, the total center of mass (c.m.) speed distribution is obtained by differentiation of equation (2.19) at χ=54.7°

$$g(v_z) = -2v\frac{d}{dv_z}f(v, 54.7°)\Big|_{v_z=v} \tag{2.20}$$

We have recorded TOF profiles of photofragment ion signal in time domain, $I(t,χ)$. The first part of analysis is to transfer this time domain signal into velocity domain, v_Z. Under space focusing conditions, a simple linear transformation gives the signal in the velocity domain $I(v_Z,χ)$ according to[61]

$$v_Z = \frac{qV_{ex}(t-t_0)}{m} \tag{2.21}$$

where *q* and *m* are the charge and mass of the photofragment, V_{ex} is the electric field in the extraction region, and t_0 is the mean time-of-flight. The observed velocity domain TOF signal $I(v_Z,χ)$ is the result of convolution of the function $f(v_Z,χ)$ above with an instrumental response function, which consists of a number of experimental factors, including the duration of the laser pulse, the finite time response of the detector, diffraction from the ion optics grids and inhomogeneities of the electric fields. Other factors, such as space-charge distortions and the finite dimensions of the ionization region, coupled with deviations from space focusing, may also give rise to a minor contribution.

The major task of the analysis procedure is to extract the photofragment speed distribution $g_i(v)$ and anisotropy $β_i$ of each decay channel i, active in the photodissociation, and hence contributing to the experimental TOF profiles $I(v_Z,χ)$. In principle, this might be achieved by first deconvoluting the function $f(v_Z,χ)$ from

$I(v_Z, \chi)$ with a Fourier transform method. However, this procedure requires an exact knowledge of the convolution function as well as the use of numerical filters to suppress the effects of high frequency noise. In the present case, we have used an intrinsically numerically stable forward convolution method. Here, an initial c.m. photofragment speed distribution $g_i(v)$ is assumed for each active decay channel i. Application of Eq. (2.19) on the magic angle TOF profile $I(v_Z, 54.7°)$ yields an estimate of the total c.m. speed distribution $g(v)$ and in turn some indication of the form of the individual speed distributions $g_i(v)$. These are usually modeled with the empirical functional form[62]

$$g_i(v_z) = (f_T)_i^{a_i}(1 - (f_T)_i)^{b_i} \tag{2.22}$$

where $(f_T)_i$ is the fraction of the available energy channeled into translation, E_T^i/E_{avl}^i, and a_i and b_i are adjustable parameters. This equation has the advantage of being able to represent many symmetric and asymmetric single peaked functions, while obeying energy conservation. By taking into account an adjustable anisotropy parameter β_i and weightage for each decay channel, $f(v_Z, \chi)$ is simultaneously calculated for the geometries $\chi=0°$, $54.7°$ and $90°$. The convolution with the instrument response function yields simulated TOF profiles, which can be compared with the experimental TOF profiles. The parameters are then adjusted until a satisfactory agreement of simulated TOF profiles with the experimental profile is achieved. Once the photofragment speed distributions have been determined, these are used to obtain the corresponding translational energy distributions.

In summary, we have used a forward convolution analysis procedure, which has the capability to include all the contributions active in the photodissociation. This procedure provides the weightage of the individual decay processes, as well as their

c.m. speed distributions and anisotropy parameters. A translational energy distribution is deduced from the photofragment speed distributions.

Various components employed in the above two techniques are discussed in detail in following sections.

2.4   LASER SYSTEM

A laser is a coherent, collimated monochromatic light source. In natural light source, an excited medium is brought back to its fundamental state by emitting photons (light waves), in a spontaneous and non-coherent manner. In LASER (**L**ight **A**mplification by **S**timulated **E**mission of **R**adiation), an incident photon on active excited atom creates a similar photon in the terms of wavelength and phase when depleting the atom to its fundamental energy state. In this work, an excimer laser was employed for photolysis, and a tunable nano-second laser light was generated using Nd:YAG pumped dye lasers. All the laser systems were operated at a repetition rate of 20 Hz.

2.4.1   Nd:YAG LASER
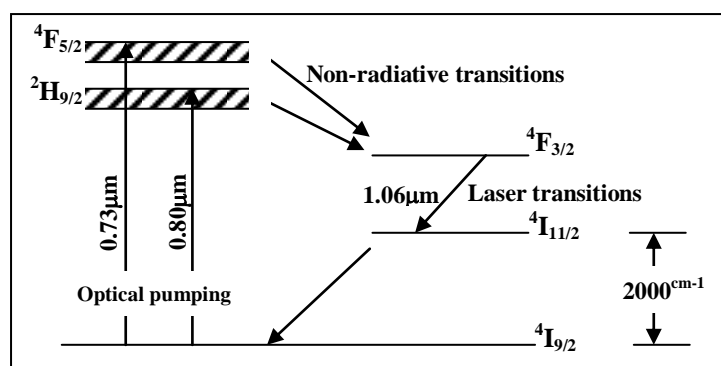
FIG. 2.11: Energy levels of Nd^{3+}:YAG

Nd:YAG (Neodymium: Yttrium Aluminium Garnet) laser is a four level laser system using the rare-earth neodymium ion. The trivalent Nd^{3+} is incorporated in the $Y_3Al_5O_{12}$ lattice. This crystal is represented by the symbol YAG. The simplified

energy level scheme[63] for Nd:YAG is presented in FIG. 2.11. In our commercially supplied system from Quantel (Model: YG980), the optical pumping is carried out by using flash lamps. The laser emission characteristics of the Nd:YAG laser are given in table 2.4.

Table 2.4: Laser emission characteristics of Nd:YAG Laser employed.

Features	Specified Value
Wavelength	1064, 532, 355, 266 nm
Pulse width	8 ns
Energy per pulse	1000 mJ at 1064 nm
Repetition rate	20 Hz
Beam divergence	0.5 mrad
Temporal jitter	2 ns
Line width	0.003 cm^{-1}

The 1064 nm is the fundamental wavelength generated by Nd:YAG laser. Its second, third and fourth harmonic (532, 355 and 266 nm, respectively) are achieved with Second, Third and Fourth harmonic Generation crystals, respectively, with appropriate input laser beams. All these harmonic generators are made from KDP crystal cut at the proper angle for the required wavelength. The second harmonic output (532 nm) from Nd:YAG laser is used to pump the dye laser. In the next section we will see a brief working of a dye laser.

2.4.2   DYE LASER

Dye laser is used for excitations of atomic and molecular transitions in LIF and REMPI techniques. Since experiments are carried out in gas phase, it is essential to have a laser with a narrow line-width and wavelength tunability. Dye lasers in their various modifications are the most widely employed tunable laser source, particularly in the UV and visible range[64]. The active media of dye lasers are organic dye molecules dissolved in solvents, and these dyes show strong broadband fluorescence spectra under excitation by UV or visible light. With different dyes, the overall spectral range extends from 300 nm to 1.2 μm, and by using frequency doubling or mixing techniques, the wavelength range of tunable devices can be extended from the VUV at 100 nm to the infrared at about 4 μm. When dye molecules in a liquid solvent are irradiated with UV or visible light, higher vibrational levels of the first excited
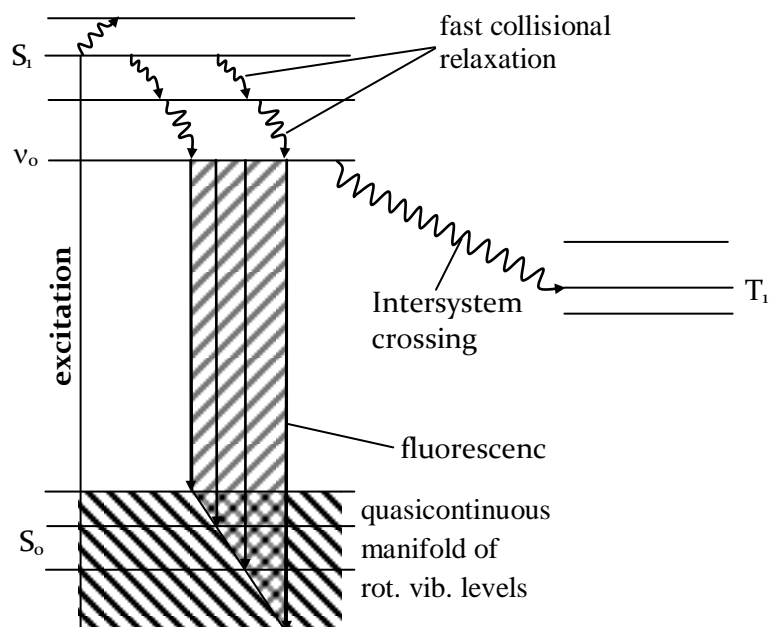
FIG. 2.12: Schematic energy level scheme and pumping cycle in dye molecules.

singlet state, S_1, are populated by optical pumping from thermally populated ro-vibronic levels in the S_0 ground state (FIG. 2.12). The collisions induced with solvent molecules, the excited dye molecules undergo very fast radiationless transitions into

the lowest vibrational level υ_0 of S_1 with relaxation times of 10^{-11} to 10^{-12} s. This level

is depopulated either by spontaneous emission into different ro-vibronic levels of S_0,

or by radiationless transitions (intersystem crossing) into a lower triplet state T_1. Since

the levels populated by optical pumping are generally above υ_0 and since many

fluorescence transitions terminate at higher ro-vibronic levels of S_0, the fluorescence

spectrum of a dye molecule is red shifted against its absorption spectrum. At

sufficiently high pump intensity, population inversion may be achieved between the

level υ_0 in S_1 and higher ro-vibronic levels υ_k in S_0, which have a negligible

population at room temperature, due to the small Boltzmann factor, $\exp[-E(\upsilon_k)/kT]$.

As soon as the gain on the transition $\upsilon_0(S_1) \rightarrow \upsilon_k(S_0)$ exceeds the total losses, laser

oscillation starts. The lower level υ_k (S_0), which now becomes populated by

stimulated emission, is depleted very rapidly by collisions with the solvent

molecules[65]. Table 2.2 shows the parameters of Seeded Nd:YAG pumped dye laser

(probe laser) employed for the studies.

Table 2.5: Specifications of second harmonic of Seeded Nd:YAG and the dye laser systems employed.

Laser	Features	Specified value
Pump Laser:	Energy	≤ 500 mJ
(Second harmonic, 532 nm)	Pulse width	≤ 8 ns
Seeded Nd:YAG Laser	Line width	~ 0.003 cm^{-1}
	Rep rate	20 Hz
Dye laser	Temporal jitter	≤ 2 ns
	Wavelength range	216-850 nm
	Beam divergence	≤ 0.5 mrad
	Line width	≤ 0.06 cm^{-1}
	Fundamental output energy	10-25% of pump energy
	Doubling energy	10-15% of fundamental output
	Mixing after doubling	15-20% of Doubling output

2.4.3   EXCIMER LASER

Excimers (that is, excited dimers) are molecules that are bound in excited states but are unstable in their electronic ground states (FIG. 2.13). These molecules have mainly a repulsive potential in the ground state with a very shallow van der Waal minimum. The well depth ε of this minimum is small compared to the thermal energy kT at room temperature, which prevents the stable formation of ground state molecules.

Excimer laser contains a gaseous mixture of helium, fluorine, and one of the rare gases argon, Krypton, or xenon. The rare gas is electronically excited by an

electron produced in discharge followed by reaction with fluorine to form excited species such as *XeF**, *KrF**, *ArF**, which are called excimers because they are stable only in excited state. The excitation reactions for ArF excimer laser are as follows:

(i)   Metastable formation $Ar + e^- \rightarrow Ar^* + e^-$

(ii)   Reaction with Fluorine $Ar^* + F_2 \rightarrow ArF^* + F$

(iii)   Radiation $ArF^* \rightarrow Ar + F + h\nu$
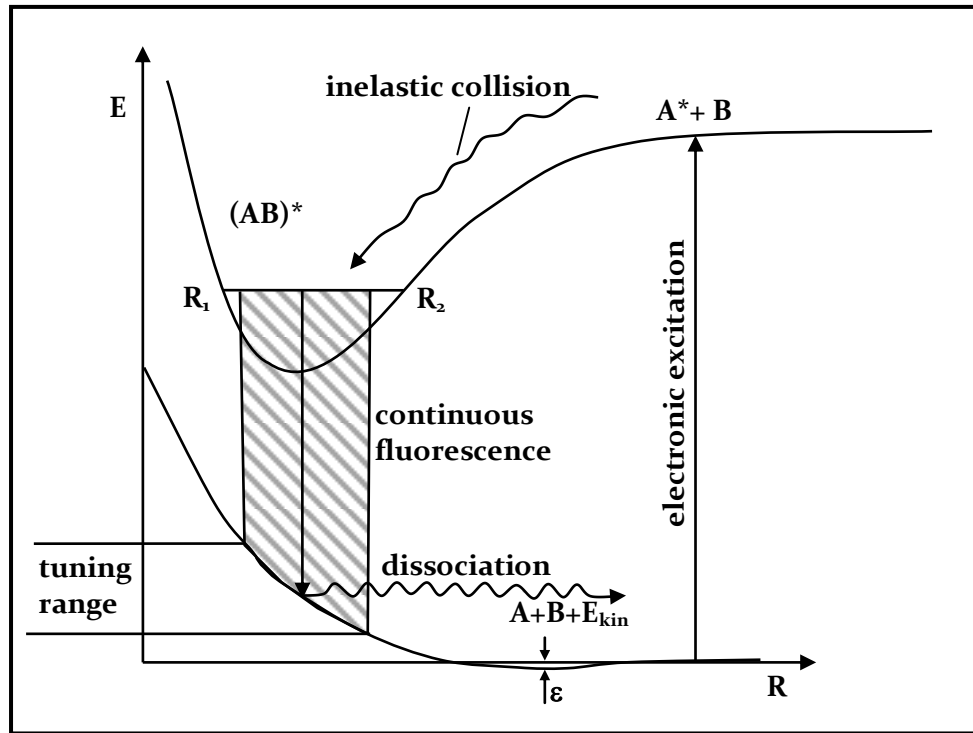
FIG. 2.13: Schematic potential energy diagram of an excimer laser.

For excimer laser used in our experiments, the pumping sources are provided by high-voltage, high-current electron beam sources, such as the FEBETRON discharges. The primary step is the excitation of rare gas atoms by electron impact. Since the formation of the upper excimer states needs collisions between these excited atoms and ground-state halogen molecule (there are no ground-state excimer molecules). High atom densities are required to form a sufficient number N^* of excimers in the upper state. A typical gas mixture of a ArF laser is: Ar: 160 mbar, 5%

F in He: 100 mbar, Ne: 2340 mbar, He: 400 mbar and KrF laser is: Kr: 100 mbar, 5% F in He: 80 mbar, Ne: 3120 mbar. These high pressures obstruct a uniform discharge along the whole active zone in the channel. In order to obtain a controlled, spark-free discharge, the laser gas has to be pre-ionized, i.e. a sufficiently high density of free charged molecules has to be created between the electrodes. This is achieved by fast electrons or by ultraviolet radiation; in our model this is achieved by pre-ionization pins arranged along the main electrode. Fast switches, such as magnetically confined thyratrons have been developed, and the inductances of the discharge circuits matched to the discharge time. Inversion is reached sufficiently fast and large population increase of the upper laser level is achieved. This is obtained through a chain of different collision processes, which are still not completely understood.

The photolysis laser employed in LP-LIF is an excimer laser (Lambda Physik Model Compex-102, fluorine version). The photodissociation dynamics studies at 193 nm (using ArF laser) and 248 nm (KrF laser) are presented in chapters 3, 4 and 5. The pulse width of the laser is 10 ns and its optimum energy is 200 mJ per pulse (ArF) and 350 mJ per pulse (KrF). The photolysis laser flux of < 5 mJ cm^{-2} is used for experiments and it is achieved by using an aperture, filters and by changing the high voltage to the laser system. Specifications of excimer lasers used for the photolysis studies are shown in Table 2.6.

Table 2.6: Specifications of excimer laser employed.

Features	Specified Value
Energy per pulse	
ArF Laser(193 nm)	210 mJ
KrF Laser(248 nm)	380 mJ
Pulse Energy Stability	$\leq \pm 2\%$
Pulse Width	≤ 30 ns
Temporal jitter	$\leq \pm 5$ns
Repetition rate	Maximum 50 Hz
Beam divergence	3 x 1 mrad^2
Trigger	Internal and external (TTL)

2.5   VACUUM SYSTEM

Vacuum may be defined as the condition of a gas under less than atmospheric pressure. This is achieved by removal of air from a system to some acceptable sub-atmospheric pressure by the use of vacuum pumping equipment. The removal of gases from a container will reduce the number of gas atoms that are available to interact with materials in the container. The rate at which materials vapourise under vacuum is a function of the pressure in the system and the vapour pressure of the material. There are a few basic ways to remove air (or another gas) from the space of a vacuum chamber.

1. Gas can be removed by an action of positive displacement devices, such as reciprocating pistons, rotary pistons, rotary vanes, gears, cams, meshed screws, orbiting scrolls, and so on.

2. Another way is by partial displacement or momentum transfer, such as fast moving blades (fan or turbine), or a high-velocity jet stream of a vapour or other motive fluid (ejector).

Pumps based on these methods are often known as *throughput* pumps, because usually the gas evacuated from the vacuum chamber is compressed and exhausted to the atmosphere. Generally, it is not easy to design a single pumping device that would function effectively under all conditions. All pumping devices have pressure or density ranges in which they have reasonable performance. Typically, at least two different pumping devices are used to obtain high vacuum. They can be conveniently designated as coarse vacuum pumps (range 25-10^{-3} Torr) and high- (or fine) vacuum pumps (range 10^{-3}-10^{-6} Torr). Coarse pumps are used to remove the bulk of the gas from a chamber (the gas that was in the space or volume), and high-vacuum pumps are used for maintaining vacuum by removing the gas evolving from the surfaces. In following part a brief working of the pumps used in experiments reported in this thesis is discussed.

2.5.1 ROTARY PUMP

Rotary pump is a mechanical vacuum pump, which work on positive gas displacement principle. The pump periodically creates increasing and decreasing volumes to remove gases from the system. The vacuum can be achieved using rotary pump is of the order $\sim 10^{-3}$ Torr. The rotary vane pump consists of vanes mounted to a rotor that rotates inside the cavity. The vane-length can be varied to maintain the

contact with the walls as pump rotates. The vanes are metallic in oil-sealed pumps. The oil in an oil-sealed pump acts as lubricant along with providing a vacuum seal at the pump exhaust and cooling for the pump.

2.5.2 DIFFUSION PUMP

Diffusion pumps are vapour jet pumps that work on the principle of momentum transfer. This occurs when a heavy, high-speed vapour molecule collides with a gas molecule and moves it in a preferred direction through the pump[66]. The bottom of the pump contains an electric heater, which is used to heat the pumping fluid to its boiling point, thus, producing the vapour. This must be done at a reduced pressure. Before the diffusion pump is started, it must be "rough pumped" down to an acceptable pressure, typically 100 mTorr, otherwise will result in no pumping action and possible damage to the pumping fluid. Once boiling of the fluid has begun, the vapour is forced up the central columns of the jet assembly. It then exits at each downward directed jet in the form of a molecular curtain that impacts the pump body. The pump body is externally cooled so that the fluid will condense on its inside surface and run back down into the boiler. Pump bodies are typically water-cooled, but some are air-cooled. As gas molecules from the system randomly enter the pump (molecular flow conditions), they encounter the top jet. Some of them are impacted and driven on to the next jet. Subsequently, they reach the fore-line where they are exhausted to the atmosphere by the mechanical backing pump.

2.5.3 TURBOMOLECULAR PUMP

The turbomolecular pump (TMP) is a bladed turbine that compresses gases by momentum transfer from the rapidly rotating blades of the rotor disks to the gas molecules. The rotor impulse is transmitted to the particles by the superposition of the

thermal velocity of colliding particles with the velocity component of the moving rotor surface. The non-directed motion of the particles is changed to a directed motion, creating the pumping process[67]. When the mean free path of the particles is larger than the spacing between rotor and stator blades (molecular flow range, typically $<10^{-3}$ Torr), particles collide primarily with the rotor, resulting in an efficient pumping process, and there is no interacting influence of the different gases. In the laminar flow range (typically $>10^{-3}$ Torr), the action of the rotor is diminished by the frequent collisions between the particles. Therefore, normally, a TMP is not capable of pumping gases against atmospheric pressure and must be backed by an adequate roughing pump.

The photodissociation study carried out in this thesis using the LP-LIF and REMPI set-up, have been performed under low pressure (high vacuum condition). The vacuum system, which we have used, consists of two different pumping devices. In LIF experiments, we need a vacuum better than 10^{-3} Torr. In this set-up, a reaction cell is evacuated through an oil diffusion pump backed by a rotary vane pump to attain a high vacuum, shown in FIG. 2.14.
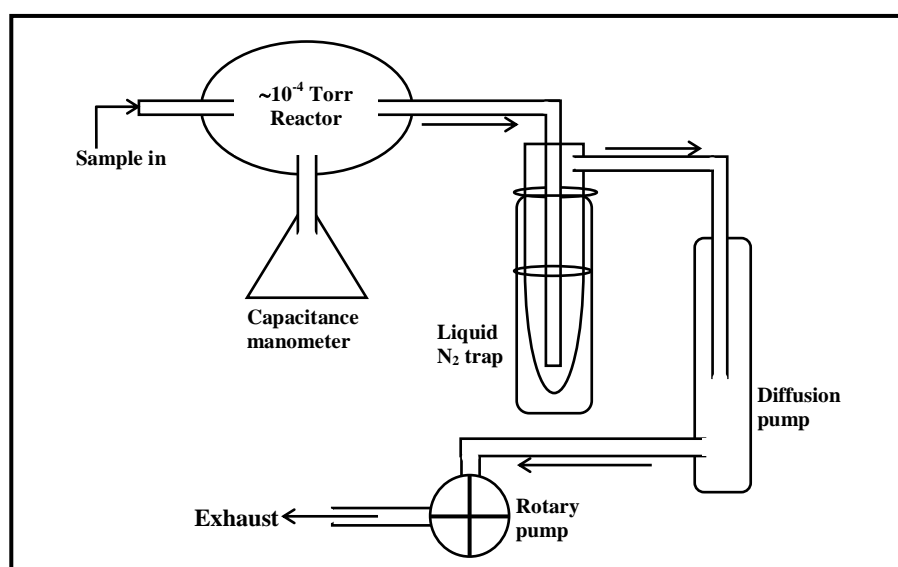
FIG. 2.14: Schematic of the vacuum system employed for LP-LIF setup.

In REMPI experiments vacuum better than 10^{-6} Torr is required. This set-up consists of three different vacuum regions, expansion chamber, ionization chamber, and TOF tube (FIG. 2.15). All the three regions are pumped by turbomolecular pumps backed by rotary pumps. The expansion chamber is pumped by 900 l/s, Alcatel turbomolecular pump, ionization chamber by 400 l/s Electrovalta and TOF tube by 250 l/s Peiffiffer turbomolecular pump.
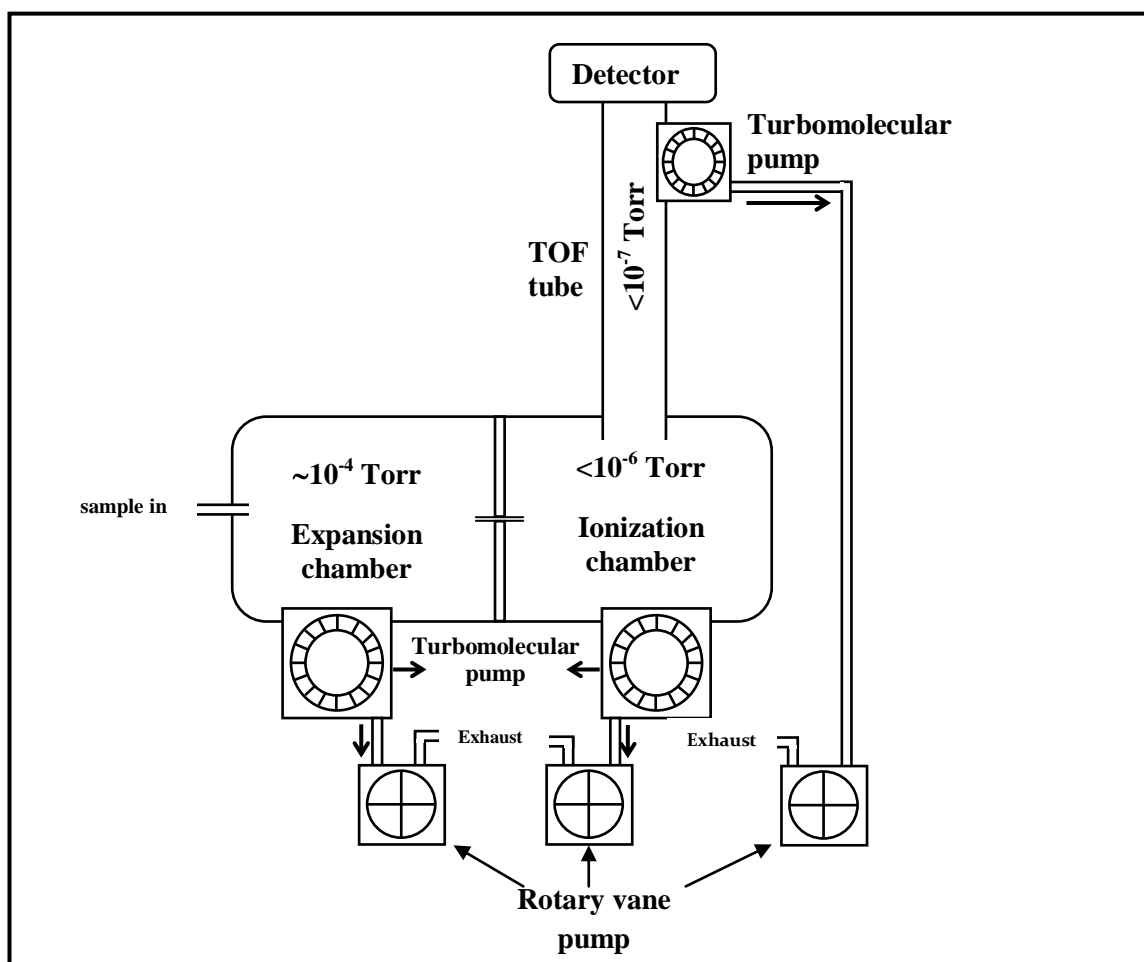
FIG. 2.15: Schematic of the vacuum system employed for REMPI setup.

2.6   PHOTOMULTIPLIER TUBE

A typical photomultiplier tube consists of a photoemissive cathode (photocathode) followed by focusing electrodes, an electron multiplier and an electron collector (anode) in a vacuum tube. When light enters the photocathode, the

photocathode emits photoelectrons into the vacuum. The focusing electrode voltage directs these photoelectrons towards the electron multiplier, where electrons are multiplied by the process of secondary emission. The multiplied electrons are collected by the anode as an output signal. The FIG. 2.16 shows the photomultiplier tube, which is having the sensitive photocathode element on the side (**Side-on**) of the vacuum tube. In this type, the incident light is detected through a window at the curved side of photomultipliers. It contains an opaque and relatively thick reflection-mode photocathode surrounded by a circular cage-like dynode element chain. The incident photoelectrons do not pass through the photocathode in a side-on photomultiplier, but are ejected from the front face and are angled toward the first dynode element.
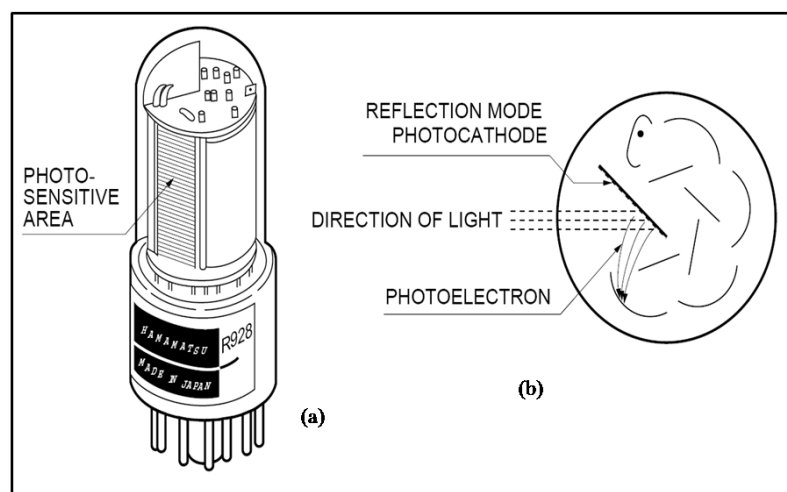
FIG. 2.16: The external appearance of (a) Side-on Type and (b) Schematic of working of photocathode with reflection mode.

In LIF set-up, the PMT model R 928P, a side-on type PMT with multialkali photocathode having high, wide spectral response from the ultraviolet to near infrared region (185-900 nm)[65,68], is used, and the photograph of the same is shown in Photograph 2.2.

Photograph 2.2: A picture of model R 928 PMT used in LIF experiments

2.7   BOXCAR AVERAGE

A Boxcar averaging is a procedure for smoothing irregularities and enhancing the signal-to-noise ratio in a waveform, assuming that the analog analytical signal varies only slowly with time and the average of a small number of adjacent points is a better measure of signal, than any of the individual points. Boxcar integrator uses a fast electronic switch to sample a repetitive waveform at a programmed time interval from the origin of the waveform. The advantage of acquisition of signal by means of integrator is that the averaging time of the units may be increased to provide S/N enhancement[69]. The detailed specifications of the Boxcar used are given in Table 2.7.

Table 2.7: Specifications of boxcar employed in experimental set-up.

S. No.	Feature	Properties	Specifications
1.	Trigger	Internal trigger	0.5 Hz to 20 kHz
		External trigger	1 MΩ input impedance. Trigger threshold adjustable from 0.5 to 2 V
2.	Delay	Delay scale	1 ns to 10 ms
		Insertion delay	25 ns
		Jitter	<20 ps or 0.01 % of full-scale delay, whichever is larger
3.	Gate	Gate Width	1 ns to 15 μs
		Width accuracy	2 ns or 20 % of full scale, whichever is greater
		Minimum width	2 ns, FWHM
4.	Signal	Sensitivity (V_{out}/V_{in})	1V/V to 1V/5 mV
		Offset control	±0.4 VDC
5.	Averaging	Type	Exponential moving average
		Number of samples	Max. 10,000

2.8   TIME-OF-FLIGHT MASS SPECTROMETRY

TOF-MS is a simple and efficient mass spectrometer having almost unity ion transmission. It consists of three distinct parts, an ion source, an analyzer and a detector. In the first part, the ions are produced, extracted, accelerated and directed into analyzer. A bunch of ions of the species to be analyzed/detected is produced by photoionization, using a pulsed laser beam, at the region between the repeller plate and the extraction plate. The ions are accelerated to very high energy, and thus reducing the spread in the initial energy of the ions. This is achieved by applying appropriate potential to the acceleration grid with respect to the extraction plate. The kinetic energy of all the ions in a given ion pulse coming out of the ion source is

almost the same, and, therefore, the velocity of each ion depends on its mass to charge ratio (m/z). The ions are then injected into the analyzer. The analyzer is a field-free drift tube, also called flight tube, wherein the ions travel under field-free conditions, with the velocity obtained in the acceleration region. Here, the ions are spatially dispersed, depending on their m/z. Lastly, the ions are detected by a dual micro-channel plate (MCP). In the present experimental work described in this thesis, the TOF-MS assembly, similar to Lubman and Jordan design[70], is used.

In TOF-MS, identification of the ions is made on the basis of their flight time from the region of generation to the detector. If the length of the field-free flight tube is very much larger than the acceleration region, then m/z of the ion is related to its flight time 't' by an expression of type,

$$^m/_z = at^2 + b \tag{2.23}$$

where a and b are fitting parameters. The above expression is used for calibrating m/z of ions with respect to their flight times. This method of calibration is most general and widely used. In our research activity, the calibration was done in a different way. First, we took a multiphoton ionization (MPI) time-of-flight spectrum of tetrachloroethylene (TCE) and confirmed the REMPI lines for ^{35}Cl and ^{37}Cl in this spectrum by scanning the probe laser. We compare this spectrum with mass spectrum of TCE reported by NIST and confirmed few other lines according to fragmentation pattern. A calibration curve was then drawn for m/z against time (t) shown in FIG. 2.17.
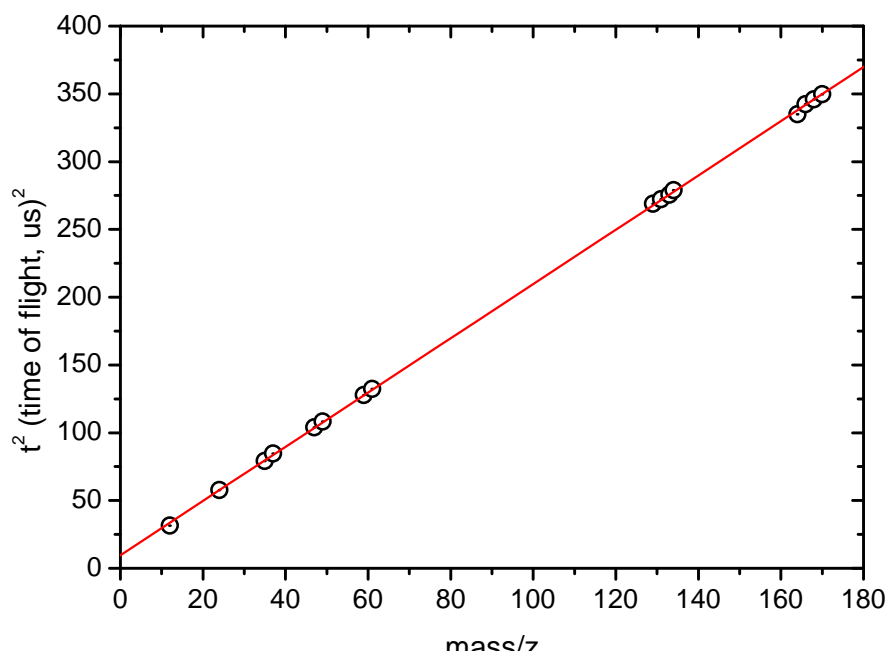
FIG. 2.17: Plot of arrival time (µs) for various fragments (m/z) for TCE for mass calibration.

2.9 MICROCHANNEL PLATES

The **Microchannel Plates** (MCP) consists of a photocathode layer on a thin semiconductive glass plate (0.5-1.5 mm) that is perforated by millions of small holes with diameters in the range 10-25 µm and is coated with a secondary electron emissive materials, thus each channel becomes an independent electron multiplier. This channel matrix allows charge replenishment from an external voltage source. Each channel can be considered as continuous dynode structure, which acts its own dynode resistor chain. The amplification factor is about 10^3 at an electric field of 500V/mm. The advantage of MCP detector is the short rise time (<1 ns) of the electron avalanche generated by a single photon, the small size and the possibility of spatial resolution. Placing two microchannel plates in series allows an amplification of 10^6, which is comparable to that of photomultipliers.
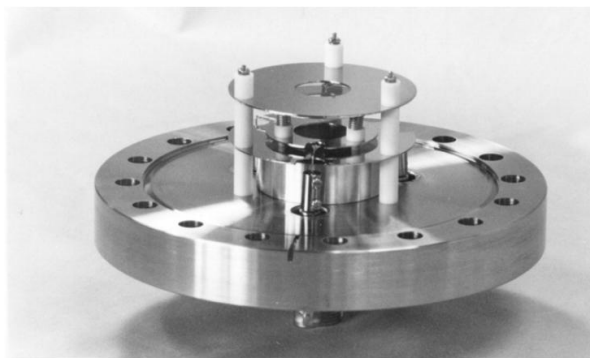
Photograph 1.3: A picture of 18 mm dual channel MCP used for detection in REMPI experiments

MCP is sensitive to charged particles, UV radiations and X-rays. In our REMPI work, a dual MCP is used to detect ions and it has sub-nanosecond rise time, high spatial resolution, high gain, small size and immunity to magnetic fields (Photograph 2.3).

In this thesis, the dissociation dynamics of organic compounds with different functional groups, induced by monochromatic laser photon, were investigated by employing either laser-induced fluorescence (LIF) or (2+1) Resonance enhanced multiphoton ionization (REMPI) along with time of flight (TOF). All the experiments were performed in high vacuum conditions. In Chapter 3, 4 and 5 dissociation dynamics of oximes, diketone and nitrocompound studied by probing OH photofragment state selectively, employing the LP-LIF technique, are presented, while in Chapter 6 and 7, the dissociation dynamics studies of fumaryl chloride and halogenated thiophenes at 234 nm are presented, where REMPI technique was employed for probing halogen atom photofragments. In LP-LIF experiments the photolysis wavelength used are 193 nm, 248 nm and 266 nm, while the probe wavelength is in the range 306-309 nm. For REMPI experiments, the pump and probe laser is same with wavelength around 235 nm.

Although the general principles and the techniques used for the experiments are given in chapter 1 and this chapter, some essential details of the techniques and analysis for each experimental study will be given at appropriate places in respective chapters.

CHAPTER 3

N−OH BOND DISSOCIATION DYNAMICS IN OXIMES: A LASER PHOTOLYSIS-LASER INDUCED FLUORESCENCE STUDY

3.1 INTRODUCTION

Bond dissociation is an important fundamental process and provides rich information, especially when induced by a laser, on a bond cleavage process. Therefore, there exists a tremendous interest in the field of photodissociation dynamics, mainly because its understanding can help us in directing a reaction to produce the desired, unconventional products or products with particular final state distributions. Photodissociation dynamics of polyatomic molecules have been studied extensively and yielded a wealth of information[3,8]. However, not much work has been reported on photodissociation dynamics of oximes, particularly in the vapour phase. Oxime is a class of molecules with a functional group C=N−OH, having many important applications in synthesis[71], medicine[72], and industries[73]; hence, these

compounds are produced in relatively large quantities. Among these cyclic oximes, cyclohexanone oxime (CHO) and its lower homologue cyclopentanone oxime (CPO) are employed extensively for synthesis purpose. CHO is used primarily as a captive intermediate in the synthesis of caprolactum for production of polycaprolactum (Nylon-6) fibres and plastics[73]. Because of the huge production volume of CHO-derived products, a large population is potentially exposed to this chemical. Hematological disorders have been reported in humans exposed to CHO, and even dermatitis and skin sensitization are suspected[74]. However, no exposure limit has been set for CHO. In biological studies, Conaway et al. have demonstrated that CPO can cause damage to liver DNA and RNA in rats and may also be hepatocarcinogenic[75].

The importance of oximes has attracted numerous studies on their photochemistry, particularly photodissociation and isomerization. Several theoretical calculations are reported as well[76]. Photochemistry of oximes in solution phase is well documented[76-80], the most commonly studied reaction being the photo-Beckmann reaction[77], generating lactum. In addition, the photochemical rearrangement of oximes to amides, the syn-anti isomerization[78] about the C=N bond, and photohydrolysis[79] of the C=N bond are also extensively studied. On photolysis, CHO is reported[81] to undergo three main dissociation processes, generating caprolactum, amide (hexanamide), and cyclohexanone. Relative yields of these channels are strongly dependent on the nature of a solvent and duration of irradiation. Although, the photochemistry of oximes has been studied in detail in the solution phase, not much work has been carried out in the vapour phase. Photodissociation dynamics studies on a few non-cyclic oximes in the vapour phase have been reported[82-85]. Unlike in the solution phase, the predominant primary dissociation channel in the vapour phase of the oximes is the N−OH bond cleavage, producing OH. Dagdigian et al.[82] detected

OH and CN on photodissociation of formaldoxime [H_2CNOH] and its methylated homologues, acetaldoxime [$H_3CCHNOH$] and acetoxime [$(H_3C)_2CNOH$] at 193 and 248 nm. In a similar work on photodissociation of acetaldoxime[83] at 193 nm, the dynamics of the N－OH bond dissociation is reported. No direct evidence for the counter fragment of OH could be obtained in all these studies. In a subsequent work, the H_2CN fragment was detected in the photodissociation of formaldoxime by cavity ring down spectroscopy[84]. In our laboratory, the dynamics of the N－OH bond dissociation on photoexcitation of acetoxime at 193 and 248 nm has been investigated, and measured partitioning of the available energy in the nascent fragments[85]. Based on both the experimental and the theoretical calculations, it was proposed that acetoxime dissociates from the T_2 state, and the dissociation channel has an exit barrier. Emission was also observed between 300 and 550 nm with a peak at 430 nm.

In the present work, we have undertaken studies on the photodissociation dynamics of cyclic oximes, CHO and CPO, to investigate whether the N－OH dissociation channel operates even in the cyclic oximes at 193 nm. If the above channel operates in the cyclic oximes, it is interesting to compare their dynamics vis-à-vis simple non-cyclic oximes and to address the effect of the ring size on the dynamics of OH formation. In this chapter, we report the studies on the photodissociation dynamics of CHO and CPO at 193 nm, wherein the OH fragment has been probed state-selectively employing laser induced fluorescence. The partitioning of the available energy in the relative translation, rotation, and vibration of the photoproducts has been measured. We have also carried out ab initio calculations to identify the excited states as well as the transition states involved in the N－OH bond dissociation. We have compared the results on the dynamics of the

N−OH bond dissociation in the cyclic oximes CHO and CPO, and also with that in non-cyclic acetoxime.

3.2   EXPERIMENTAL SECTION

In the present work, the LP-LIF set-up was used to study the photodissociation dynamics of CHO and CPO. The set-up of LP-LIF remains similar as described in detail in Chapter 2, section 2.2.2. The CHO and CPO being solid compounds, in experimental set-up, a special experimental arrangement was devised to flow its vapour through the reaction chamber. The schematic of special arrangement, which is devised to flow the vapour from solid sample through the reaction chamber, is shown in Chapter 2, FIG. 2.5. The CHO and the CPO samples with purity >97% were used as supplied by Aldrich. However, these samples were thoroughly degassed before their use.

3.3   THEORETICAL METHODS

The structures of the molecular species along with the transition states were optimized using the IBM PC compatible Gaussian 03 software[86] for a better understanding of the dynamics of OH formation on photodissociation of CHO and CPO at 193 nm. All the ground electronic state geometries have been optimized employing density functional theory (DFT) at the B3LYP level, using 6-311++G(d,p) basis sets. Besides the B3LYP energy, the energies of the optimized structures were also calculated at the Moller-Plesset [MP4(SDQ)] level of theory, using the same basis sets. The harmonic vibrational frequencies and the force constants were calculated to ensure that the stationary points on the potential energy surfaces are true saddle points. The calculated energies include corrections for the zero point energies, with unscaled vibrational frequencies. All the transition state (TS) structures were characterized by only one imaginary frequency and one negative eigenvalue of the

force constant matrix. We also carried out the excited electronic state calculations at the configuration interaction with the single electronic excitation (CIS) level to understand the dynamics of the N−OH bond cleavage leading to OH formation. The time-dependent density functional theory (TD-DFT) with 6-311++G(d,p) basis sets was employed to calculate the vertical excitation energies of the low-lying electronic states, and MOs were analyzed to assign each electronic transition. The excited state geometries were then optimized following the CIS method with 3-21G basis sets, and the TS structure for the OH formation was searched on these surfaces. The calculated structures and energies for the ground state geometries are reasonably accurate. But, the excited state calculations for the TS structure for OH formation could be carried out at only low basis sets, mainly because of our resource limitation in calculations for relatively large molecules. Although these energies are not having the sufficient accuracy, the qualitative prediction on the presence of an exit barrier is quite reliable to support our experimental results.

3.4   RESULTS AND ANALYSIS

3.4.1 DETECTION OF OH ON EXCITATION OF CHO AND CPO AT 193 nm

A transient OH radical was detected by LIF technique among the products formed on photolysis of CHO and CPO at 193 nm. The state distribution of the nascent OH radical was probed by measuring fluorescence of the $A^2\Sigma^+{\rightarrow}X^2\Pi$ system, after exciting the same system with the frequency doubled tunable dye laser (~ 308 nm). Both the (0, 0) and (1, 1) vibronic bands were studied, and the rotationally resolved lines were measured. In the case of CHO, strong LIF intensities were obtained in the (0, 0) vibronic transition; with no signal obtained in the (1, 1), whereas for CPO the LIF signals were obtained from both the transitions. This indicates that

for CHO the OH radicals are generated mainly in the ground vibrational level; the yields of other higher vibrational levels are negligible. But in the photodissociation of CPO at 193 nm, OH is produced both in $v''=0$ and 1. Several rotational lines were measured for the (0, 0) transition, shown in FIG. 3.1, with 50 ns time delay between the photolysis and the probe lasers. Analyzing the profiles of the rotational lines of the excitation spectrum, we extracted the information on the dynamics of OH radical formation. All line positions in FIG. 3.1 are marked as per assignments of Dieke and Crosswhite[87]. The relative populations of the OH fragment in different vibrational and rotational states are calculated from the normalized LIF intensities of the transition with respect to the photolysis intensity, the probe intensity and the Einstein absorption coefficient, *Bij*. The *Bij* coefficient values are taken from the work of Chidsey and Crosley[88]. These normalized LIF intensities are also used for determining the rotational distribution in the $v''=0$ state, the ratio of population in two spin-orbit $\Pi_{3/2}$ and $\Pi_{1/2}$ states, and the ratio of population in Λ-doublet states, whereas the LIF line width is used to estimate the translation energy released in the OH fragment.
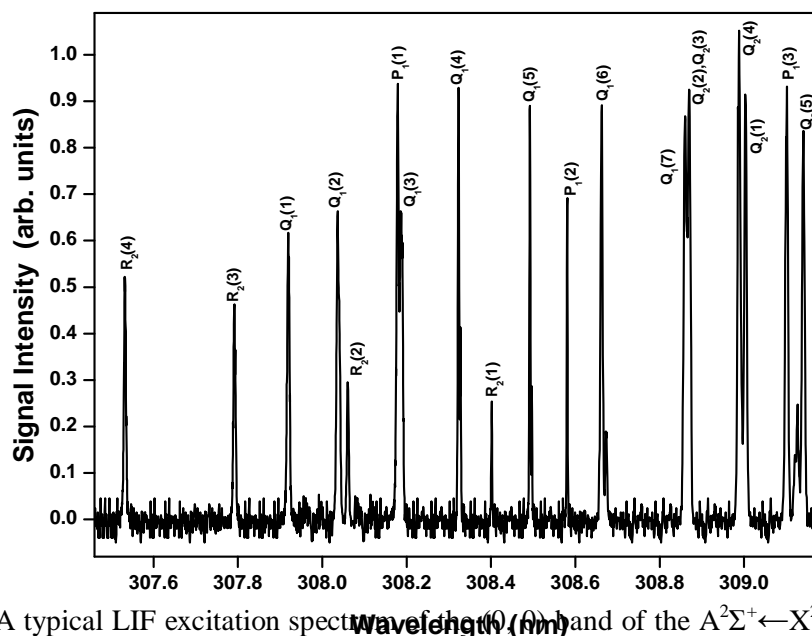
FIG.3.1 A typical LIF excitation spectrum of the (0, 0) band of the $A^2\Sigma^+ \leftarrow X^2\Pi$ system of the nascent OH radical formed in photodissociation of cyclohexanone oxime (50 mTorr) at 193 nm. The time delay between pump and a probe laser was 50 ns. The rotational lines are assigned in the figure.

3.4.2 VIBRATIONAL AND ROTATIONAL STATE DISTRIBUTION OF OH

Photoexcitation of CHO at 193 nm produces OH, mostly in (v''=0, J''), that is, vibrationally cold, whereas CPO yields OH in (v''=0 or 1, J''), that is, vibrationally hot OH are also formed. The normalized populations, P(v''=0 or 1, J'') of the nascent OH fragment generated on photodissociation, were plotted against their corresponding energy of the rotational levels (ε), to construct a Boltzmann plot as per Eqn. 2.15 (Chapter 2). From the slope of the plot (FIG. 3.2), the rotational temperature (T_R) of OH(v''=0) for CHO was estimated to be 1440±80 K, whereas in the case of CPO it was estimated as 1360±90 K for v''=0 and 930±170 K for v''=1, assuming the statistical rotational population distribution. The inconsistency with the above assumption in the data is reflected as error bars in the estimated rotational temperature. The vibrational temperature T_V can also be obtained by assuming a Boltzmann distribution of vibrational populations of OH. The ratio of the LIF

intensities of the same rotational line e. g., $R_{1,2}(N)$, of the (0, 0) and (1, 1) transitions is expressed by the relation

$$I(R_{1,2}(N); \upsilon = 1)/I(R_{1,2}(N); \upsilon = 0) = \exp(-\Delta\varepsilon_v hc/kT_v) \qquad (3.1)$$

where ε_v is the energy difference between $v''=1$ and $v''=0$ for a given spin-orbit state and N''. The constants h, c, and k have their usual meaning. Intensities of a few rotational lines $P_1(1)$, $P_1(2)$, $Q_1(5)$, and $Q_1(6)$ were used to estimate the T_V, and its average value is 1030±80 K.
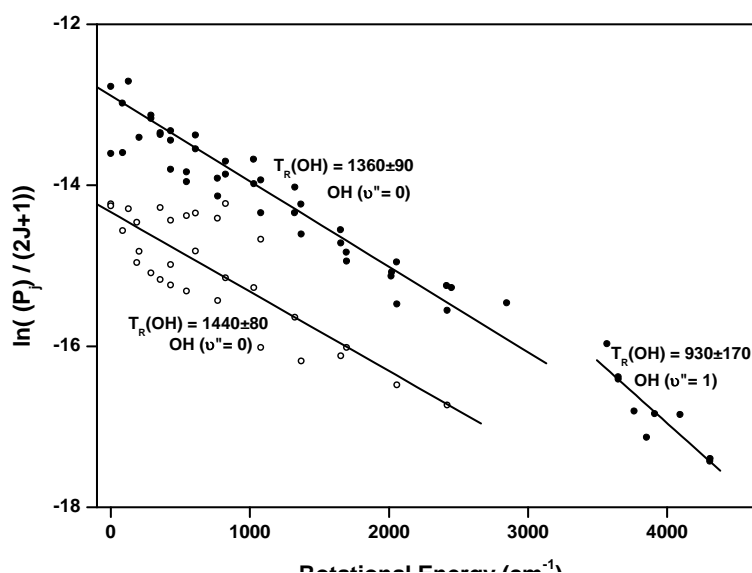
FIG. 3.2: Boltzmann plots of rotational state population against energy of rotational states of OH ($v''= 0$) generated in dissociation of CHO (open circles) and CPO (solid circles) with 193 nm laser.

3.4.3 AVERAGE TRANSLATION ENERGY OF OH

Several factors, such as molecular velocity of the fragments, thermal motion of the parent molecule, the finite probe laser width, and vector correlations, contribute to the broadening of LIF lines, out of which the molecular velocity of the fragments contributes significantly to the Doppler broadening. The average translation energy of the photoproduct OH can be estimated from the widths of Doppler broadened rotational lines. The Doppler profiles of the $P_1(2)$ line of OH($v''=0$) from CHO and CPO are shown in FIG. 3.3. All the rotational lines measured were found to have

similar line widths, within the range of the experimental error. The Doppler profiles of the rotational lines were corrected for the probe laser line width. The average translational energy in OH, E_T(OH), is given by the Eqn. 2.11 (Chapter 2). Doppler profiles of ten each of the $P_1(2)$ and $P_1(5)$ lines were measured, and from their corrected line widths, the translation energy of the OH fragment was determined. For a completely isotropic distribution of the OH fragment, deconvolution of the peak profiles with the instrumental functions gives the average width of 0.45 ± 0.03 cm^{-1} for CHO. This corresponds to E_T(OH) of 18.5 ± 2.2 kcal/mol, and the total translation energy released in the fragments to be 21.8 ± 3.0 kcal/mol. A similar analysis in the case of CPO results in E_T(OH) of 17.0 ± 2.0 kcal/mol, and the total translation energy release of 21.0 ± 2.5 kcal/mol.
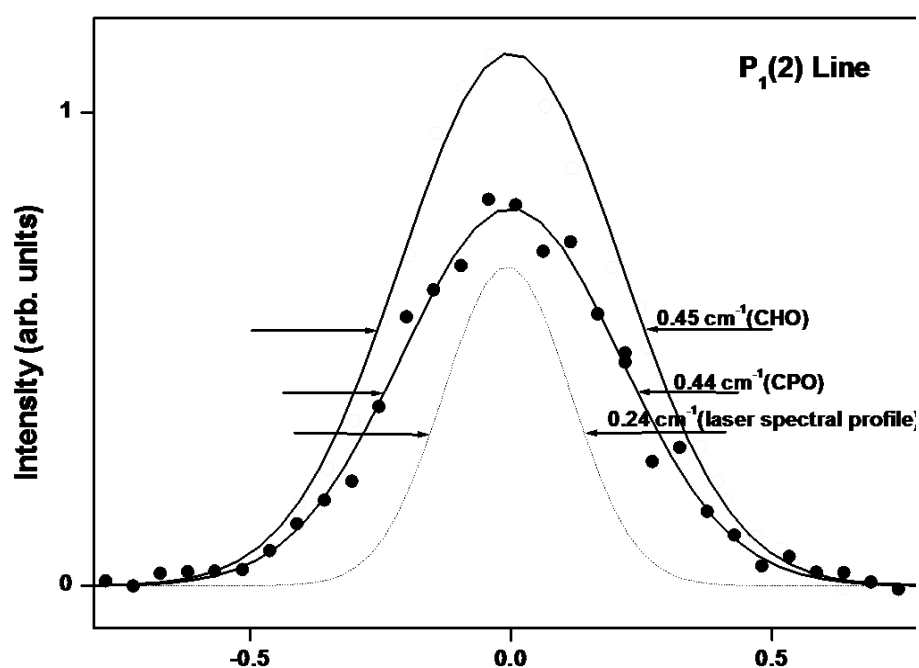
FIG. 3.3: Doppler profile of $P_1(2)$ line of the $A^2\Sigma^+ \leftarrow X^2\Pi$ (0,0) system of the OH radical produced in dissociation of CHO (open circles) and CPO (solid circles) with 193 nm laser. The dotted line shows the laser spectral profile.

3.4.4   DISTRIBUTION IN THE Λ-DOUBLETS AND SPIN-ORBIT STATES

The Λ-doublet states arise from the orientation of the π lobes of OH with respect to the plane of rotation. In the Π^+ state, the π lobe lies in the plane of rotation and the intensities of P and R lines correspond to the population of OH in this state. In the Π^- state, the π lobe lies perpendicular to the plane of rotation and the intensity of Q lines corresponds to the population of OH in this state. The ratio of LIF intensities of Q lines with P or R lines gives the population distribution ratio of OH in Λ-doublets. The relative population, $[\Pi^-(A'')/\Pi^+(A')]$ provides information about the exit channel dynamics during the breaking of the chemical bond. In the case of CHO, the Λ-doublet states of the nascent OH radical are populated almost equally for lower N'', while for higher N'' there is a preference for the $\Pi^+(A')$ state, as shown in FIG. 3.4(a). In the case of CPO, shown in FIG. 3.4(b), OH has been equally populated in both the doublet states for all N''. The spin-orbit state distribution gives the relative population of OH in $\Pi_{3/2}$ (F_1) and $\Pi_{1/2}$ (F_2) states, measured by the relative intensities of the rotational branches, that is, P_1 (N'')/P_2 (N''), Q_1 (N'')/Q_2 (N''). For F_1 (N'') and F_2 (N'') lines, the J'' values are not the same, and therefore the population was normalized over the statistical weight factor $2J''+1$. The ratios of the corrected intensities of $P_1(N'')$ to $P_2(N'')$ and $Q_1(N'')$ to $Q_2(N'')$ lines were plotted against N'', shown in FIG. 3.4(a) and (b), for CHO and CPO, respectively.
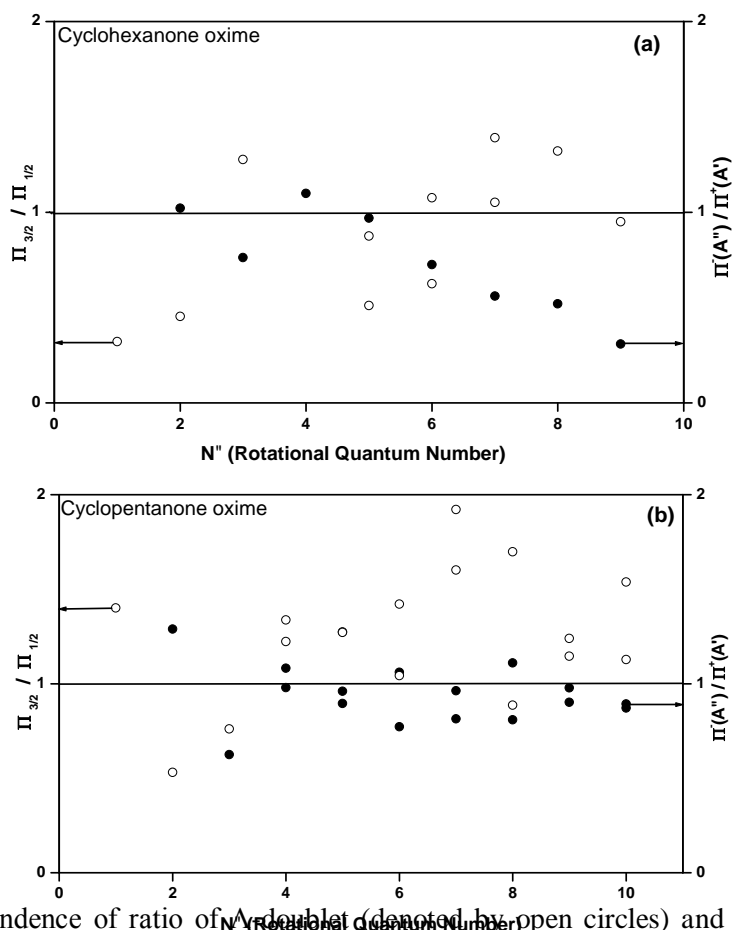
FIG. 3.4: Dependence of ratio of Λ-doublet (denoted by open circles) and spin-orbit state (denoted by filled circles) populations against rotational quantum number N'' for the nascent OH formed in laser-induced photodissociation of CHO (a) and CPO (b) at 193 nm.

For CHO the states are almost equally populated for all the rotational levels, suggesting that no preference exists for either of the two spin-orbit states of OH. Unlike in CHO, in CPO the spin-orbit population is mostly distributed in the $\Pi_{3/2}$ state, implying a strong interaction between the initially excited states with the nearby triplet states.

3.4.5 FORMATION TIME OF OH RADICAL

The formation time of the OH ($v''=0$, J'') radical was measured by scanning the time delay between the photolysis and the probe lasers, after selecting the excitation wavelength of a particular ro-vibronic line of OH. The measured time

evolutions of OH (v''=0, J'') in different rotational levels are shown in FIG. 3.5. The figure shows that the formation time of OH has a strong dependence on N''. For N''=2-4, the initial fast formation followed by slow formation, even up to 600 ns, could be observed. This slow formation of OH in the lower rotational levels, that is, N''=2-4 is due to the complications arising from the rotational relaxation of OH formed in the higher rotational levels. Thus, the relaxation of higher levels to the lower levels delays the actual formation time of OH. Hence, these lines show much slower formation of OH as compared to that shown by lines of higher N''=5 and N''=6. The line with the highest value of N'' provides the correct value of the OH formation time. The value obtained from the $P_1(6)$ line in the case of CHO is less than 50 ns. Employing similar time delay scans, the formation time of OH produced from CPO upon excitation at 193 nm is measured to be similar. Since the measured formation time is close to the rise time (~35 ns) of the experimental set-up, we cannot provide accurate information on the rate of the primary dissociation process in both CPO and CHO.
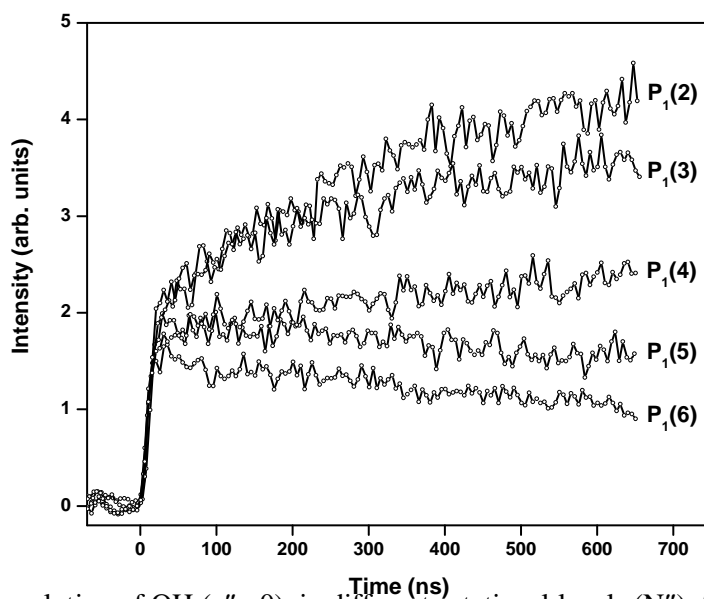
FIG. 3.5: Time evolution of OH (v''= 0), in different rotational levels (N''), from CHO on excitation at 193 nm. The plot shows the LIF signal for N''=2, 3, 4, 5 and 6 with time delay.

3.4.6   UV/VISIBLE AND IR FLUORESCENCE

The UV-vis emission was measured using experimental set-up consisting of a Bausch & Lomb monochromator, a PMT (Hamamatsu model R928), and a digital oscilloscope (Tektronics). The sample was allowed to flow in a stainless steel cell, equipped with four perpendicular MgF_2 windows, at a pressure of ~20 mTorr, and monitored by a capacitance gauge. During the measurement of the emission at wavelengths greater than 350 nm, suitable cut off filters were used. As well, to measure the IR fluorescence from the vibrationally excited products, a liquid nitrogen cooled InSb IR detector was used. On excitation of CHO and CPO at 193 nm, we could detect small UV/visible emission from excited parent molecule, whereas a strong emission was observed in the case of acetoxime[85] having λ_{max} at 430 nm under similar experimental conditions.

3.5   DISCUSSION

3.5.1   OH GENERATION CHANNEL

Photoexcitation of oximes, in general, and UV/visible absorption spectra, in particular, are well studied. UV absorption spectra of oximes in the gas phase show two features, at ~210 nm (weak and diffuse) and ~190 nm (intense)[89], assigned to ^{1}(n-π*) and ^{1}(π-π*) transitions, respectively. Thus, excitation of CHO and CPO at 193 nm is assigned to the S_2 state. The molecules prepared in the S_2 state can dissociate to produce OH, or can relax to some other state(s) before dissociation. Both CHO and CPO undergo the N−OH bond dissociation at 193 nm, generating the observed OH radical, in addition to other channels. This OH channel can involve either the simple N−OH bond cleavage, or may proceed via a transition state (TS). The latter mechanism implies the presence of an exit barrier for OH formation. Our

measurements on partitioning of the available energy for both the oximes suggest that a significant fraction of the available energy is released as the relative translation of the products, indicating that either the dissociative states of CHO and CPO are repulsive in nature, or the N−OH dissociation channel has an exit barrier. Since, potential energy surfaces of the initially excited states and the dissociating states of both CHO and CPO are not repulsive in nature (*vide infra*), OH formation, upon excitation of CHO and CPO at 193 nm, from a repulsive state can be ruled out. Alternatively, if the N−OH dissociation channel has an exit barrier, the parent molecule should dissociate from an excited electronic state, because the dissociation from the ground electronic state is generally barrier-less[90], except for the dissociation and the isomerization of some radical species[91]. Thus, our experimental results suggest that OH should operate from an excited electronic state of CHO and CPO, and it should have an exit barrier. Therefore, we performed *ab initio* molecular orbital (MO) calculations for both the oximes, using the Gaussian program, to locate a TS structure on PES for the OH channel.

3.5.2   GROUND ELECTRONIC STATE OF CHO AND CPO

We carried out molecular orbital (MO) calculations, to investigate the potential energy surface (PES) for the OH dissociation channel from CHO and CPO, upon excitation at 193 nm. For all the radical channels studied, the projected MP2 (PMP2) energies, wherein spin contamination has been taken care of, were generally found to be lower as compared to the MP2 energies. The optimized structure of the ground electronic state of CHO suggest the presence of two chair conformers, differing in orientation of O−H with respect to C=N. The dihedral angle HONC in these two syn and anti conformers is 2.3° and 179.3°, respectively. Thus, O−H and C=N in both the syn and anti conformers lie almost in the same plane. Even the other

two C atoms (C2 and C6) attached to C=N lie in this plane. Between these two, the syn and anti forms, the latter is calculated to be more stable by about 6.7 kcal/mol (6.8 and 6.6 kcal/mol at B3LYP and MP2 level, respectively) and depicted as CHO in FIG. 3.6.
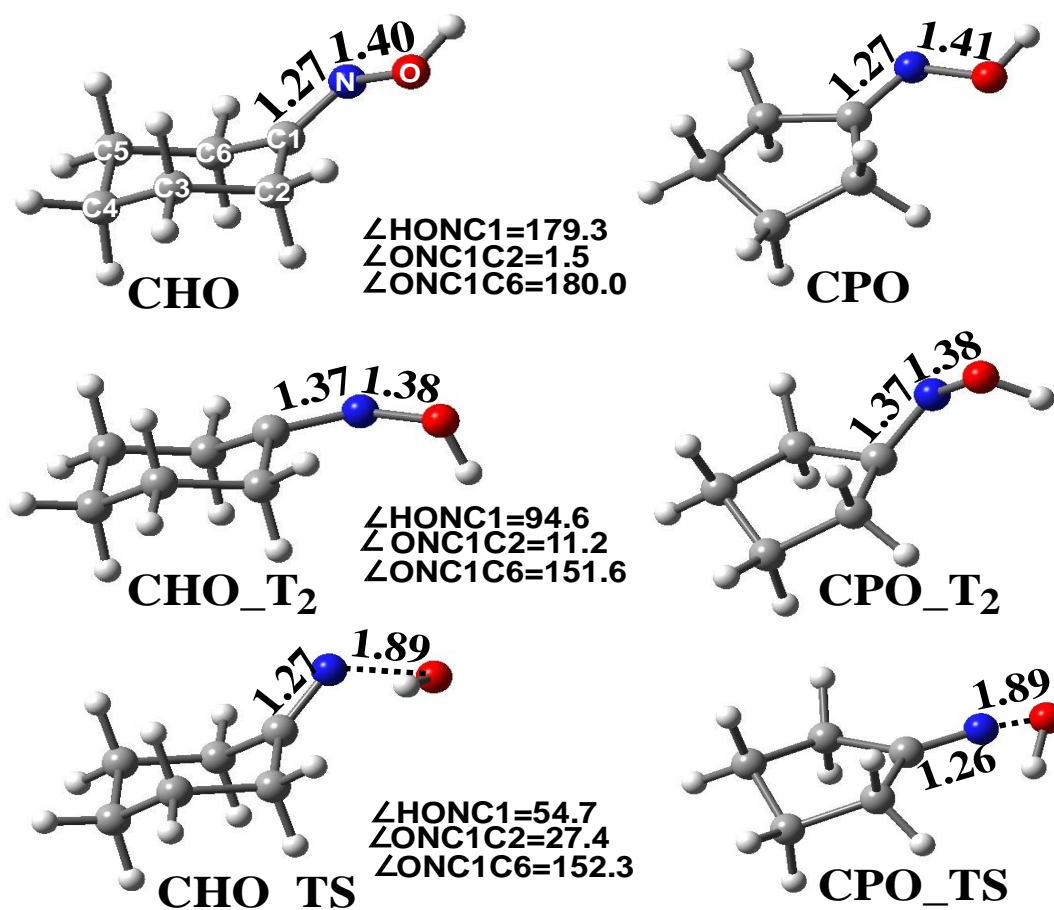
FIG. 3.6: The optimized structures of the ground electronic state (most stable anti conformers depicted as CHO and CPO), the T_2 state (marked as CHO_T_2 and CPO_T_2) and the transition states (marked as CHO_TS and CPO_TS) from the T_2 state for OH formation from CHO (shown in the left column) and CPO (shown in the right column). A few important bond distances (in Å) and dihedral angles (only for CHO, in degrees) are given in the figure. The ground and the excited electronic state structures are optimized at the B3LYP/6-311++G(d,p) and CIS/3-21G level of theory, respectively.

We located the corresponding TS structure, and calculated the rotational barrier for the conversion of the anti conformer to the syn conformer of CHO to be 8.0 kcal/mol (8.2 and 7.8 kcal/mol at B3LYP and MP2 level, respectively). Similar energy calculations at MP4(SDQ)/6-311++G(d,p) level on CPO also show that its anti

form (shown as CPO in FIG. 3.6) is more stable than the syn form by 6.2 kcal/mol, and the rotational barrier for the conversion of the anti conformer to the syn conformer is 7.1 kcal/mol. However, we could not locate the TS structure for the N−OH bond cleavage producing OH from the ground electronic state of either CHO or CPO. We carried out the excited state calculations to understand the excited state of CHO and CPO responsible for the OH formation.

3.5.3   TRANSITION STATE FOR OH CHANNEL FROM CHO AND CPO

Using theoretical calculations, we could locate the TS (shown as CHO_TS in FIG. 3.6) for the N−OH bond cleavage in CHO only on an excited triplet state, the T_2 state (depicted as CHO_T_2 in FIG. 3.6) having $^3(n\,\pi^*)$ character. Similar to CHO, in CPO as well the TS structure (shown in FIG. 3.6 as CPO_TS) for the N−OH bond cleavage could be found from only the T_2 state (the structure is depicted as CPO_T_2), with almost similar structural parameters as the TS in CHO. We could characterize the TS at the basis sets 3-21G and could not do so with larger basis sets, mainly because of our resource limitation in calculations for relatively large molecules (as mentioned earlier). The TS obtained at smaller basis sets is well-characterized, satisfying all the conditions. Moreover, we could characterize the TS for the OH channel at higher basis sets from the T_2 state of relatively smaller acetoxime molecule[85]. Hence, we think that our calculated TS structures for OH formation in both CHO and CPO represent real transition states. For the relative energies of the T_2 state and the TS, we have used the MP2/3-21G energies of the ground states of CPO and CHO. Since we could characterize the TS only from the T_2 state, it implies that both CPO and CHO dissociate from the T_2 state to produce OH. However, we cannot rule out the possibility of OH formation from another excited state of CPO and CHO. An experimental evidence for the dissociative state to be triplet in CPO comes from

the measured spin-orbit ratio of OH, which shows a preference to the $\Pi_{3/2}$ state. This evidence is not obvious in CHO, wherein the spin-orbit ratio of the OH product is almost statistical. The TS structure (CHO_TS) has the angle HON and the dihedral angle HONC1 as 99.1° and 54.7°, respectively. The TS structure in CPO has the angle HON and the dihedral angle HONC1 as 99.2° and 48.0°, respectively, with the N−OH bond extended by 37% from 1.38 to 1.89 Å. One significant structural change is observed in the orientation of OH with respect to NC1 when CHO undergoes transformation from the ground state to its T_2 state through the TS for the OH channel. The dihedral angle HONC1 in CHO changes from 179.3° in S0 to 94.6° in T_2 to 54.7° in TS. Similar change in the dihedral angle of HONC1 is observed in CPO, but with a value of 48.0° in TS. This implies that OH is rotated to a larger extent with respect to C1N, implying higher torsional energy in the TS for the OH channel in CPO than that in CHO. Thus, it is expected that the nascent OH from CPO should have higher rotational energy than that from CHO, assuming that the torsional energy mainly contributes to the rotational excitation of the OH fragment. But in both cases, CHO and CPO, almost similar rotational energy goes to OH; implying torsion is not an important factor for rotational energy in the OH product. Along with the N−OH bond dissociation channel producing OH, other channels are possible from both CHO and CPO. We have theoretically investigated the H_2O elimination channel from CHO, which is accompanied by a biradical (triplet) cofragment with an activation and exit barriers of 66.1 and 36.4 kcal/mol, respectively.

3.5.4 MECHANISM OF OH-FORMATION FROM CHO AND CPO ON EXCITATION AT 193 nm

Based on theoretical and experimental results, we come to a conclusion that although CHO and CPO are excited to a higher electronic state (the S_2 state) at 193

nm, these molecules do not dissociate from this initially excited state to produce OH. The excited CHO and CPO molecules relax to a triplet state (the T_2 state), either directly involving intersystem crossing or indirectly involving internal conversion to the S_1 state, followed by intersystem crossing. Subsequently, CHO and CPO in the T_2 state undergo the N−OH bond dissociation to produce OH with an exit barrier. The relaxation process from the S_2 to the T_2 state appears to be quite efficient in both CHO and CPO, since we observed negligibly small fluorescence upon excitation of these compounds at 193 nm. This implies that the emission process does not compete with the non-radiative relaxation of these molecules from the S_2 state. In contrast, emission was observed between 300 and 550 nm upon excitation of acetoxime at 193 and 248 nm[85]. Although a higher emission yield is expected from rigid cyclic oximes, CHO and CPO, upon excitation at 193 nm, negligibly small emission was observed. The lower emission quantum yields of CHO and CPO may be due to efficient non-radiative relaxation rates, which are enhanced by curve crossing of the excited states.

3.2.5 PARTITIONING OF THE AVAILABLE ENERGY

The partitioning of the available energy in different degrees of freedom of the products formed upon excitation of CHO and CPO at 193 nm was measured by employing LIF. The available energy, E_{avl}, is the energy remaining after the dissociation, and it is partitioned between primary photoproducts. The E_{avl} of the primary photoproducts, OH and its cofragment, E_{avl} (OH + cofragment), can be expressed as

$$E_{avl} \text{ (OH + co − fragment, RN)} = h\nu(193 \text{ nm}) + E_{int} \text{ (RNOH)} − D_0^0 \text{(RN − OH)} \qquad (3.2)$$

The bond dissociation energies (RN−OH) of CHO and CPO are not known. We estimated theoretically, the change in energy for the reaction generating OH and its cofragment RN, D_0(RN−OH), to be 64.1 and 55.3 kcal/mol in CHO and CPO,

respectively. This dissociation energy for the N−OH bond in CHO is in good agreement with the reported values[82,83] of 63.6 and 66.6 kcal/mol for that in formaldoxime and acetaldoxime, respectively. However, the bond dissociation energy value in CPO is lower than that in other oximes, probably because of a strain in the 5-membered ring of CPO. With energy of the photon hν (193 nm) being 147.8 kcal/mol, and after adding the internal energy of the parent molecules (4.8 and 4.3 kcal/ mol for CHO and CPO, respectively), the values of E_{avl} for CHO and CPO are estimated to be 88.5 and 96.8 kcal/mol, respectively. This energy is partitioned among various degrees of freedom of the photofragments with $E_{avl} = E_{int}$ (OH) + E_{int} (co-fragment) + E_T (OH + co-fragment), where E_{int} consists of both the rotational and vibrational excitations. We estimated the average rotational energy of OH, E_R, in CHO and CPO to be ∼2.9 kcal/mol and ∼2.5 kcal/mol, respectively, after summing over the rotational excitation in the vibrational state populated (ν″=0 and 1),

$$\langle E_R \rangle_v = \sum P_v (J'') E_R (J''), \tag{3.3}$$

where, $P(J'')$ is the fractional population of the rotational state distribution, and $E_R(J'')$ is the energy of a rotational state J'' in the chosen vibrational manifold. The average translational energy of OH from CHO is estimated from the Doppler profile to be 18.5 kcal/mol, from which the relative translational energy of the fragment pair, E_T(OH + cofragment), is determined using conservation of the linear momentum to be 21.8 kcal /mol. The remaining available energy (63.8 kcal/mol), which is 72% of the total available energy, is channelled into the internal energy of the co-product. In CPO also, a major fraction (0.22) of the available energy of 96.8 kcal/mol is partitioned to the relative translation of the products, with a moderate rotational excitation of 2.5 kcal/mol and a small vibrational excitation of ∼0.2 kcal/mol in the OH product. Thus, ∼2.7 kcal/mol of energy goes into the internal energy of the OH fragment. The

remaining 73.1 kcal/mol, which is about 75% of the total available energy, is channelled into the internal energy of the co-product. The measured values of the energy channelled to the relative translation, rotation, and vibration can be understood qualitatively through two simple theoretical limiting models, statistical[37] and impulsive[35]. The impulsive model is applicable for dissociation from a repulsive surface and estimates the f_T values of 0.52 and 0.53 thus 46.0 and 51.3 kcal/mol of energy, be released as the relative translation in the OH channel of CHO and CPO, respectively. The comparison with the experimental values indicates that the impulsive model overestimates the relative translational energy release and precludes dissociation from a repulsive surface. The other limiting model is the statistical model[37], which is applicable for reactions without any exit barrier. In this model, the partitioning of the available energy among different degrees of freedom of the fragments is estimated from the simple statistical formulation. Since the N−OH bond cleavage has an exit barrier, this model is also not applicable. A hybrid model[43,92] can explain the experimental energy distribution in this case. In this model, it is assumed that the total available energy is divided between two different energy reservoirs. The energy corresponding to the exit barrier of the reaction is distributed among the products according to the impulsive model, and that above the barrier is distributed according to the statistical model. Thus, the hybrid model of energy partitioning predicts an exit barrier of ~33 and ~32 kcal/mol to explain the measured relative translational energy release of 21.8 and 21.0 kcal/mol in CHO and CPO, respectively. The excited state molecular orbital calculations also predict the exit barrier to be about 29.0 and 36.4 kcal/mol, respectively, for CHO and CPO. Thus, the agreement between theoretically calculated and hybrid model predicted values of the exit barrier in CHO and CPO is quite good. However, not much importance is attached to the

quantitative value of the calculated exit barrier; because of high uncertainties in energies expected at CIS/3-21G level of theory. The origin of a barrier in the exit channel of the N−OH bond cleavage of CHO and CPO is mainly due to non-adiabatic surface-crossing of the excited-state PESs. An efficient non-radiative mechanism responsible for relaxation of the S_2 state to the T_2 state of CHO and CPO before dissociation is possibly aided by this curve crossing, hence emission is not observed upon excitation of these molecules at 193 nm.

3.5.6 COMPARISON ON N−OH BOND DISSOCIATION IN DIFFERENT OXIMES

Although CPO has a strained cyclic structure, the dynamics of the N−OH bond dissociation producing OH in both CHO and CPO remains similar. Both molecules are excited to their S_2 electronic state, from which these relax to the T_2 state before dissociation to yield OH. Both these molecules have an exit barrier for the N−OH bond scission. However, since the dissociation energy is lower for the N−OH bond of CPO, the E_{avl} is higher in this case. This higher energy can be responsible for the observed difference in the amounts of energy partitioned in the relative translation, rotation and vibration of the products in CPO. Unlike in CHO, wherein OH ($v''=0$) is produced, in photodissociation of CPO, OH is produced in $v''=1$ as well. However in both the cases the rotational temperatures, T_R, of OH ($v''=0$) are comparable. Even the overall dissociation dynamics of the N−OH bond in cyclic oximes at 193 nm is similar to that observed in non-cyclic acetoxime[85] (as shown in Table 3.1). Like in cyclic oximes, in acetoxime also the N−OH bond cleavage occurs from the T_2 state, and it has a comparable exit barrier of ∼30.0 kcal/mol. Energies partitioned in translation, rotation and vibration remain qualitatively similar. An appreciable amount of the available energy is released in the relative translation in all

these oximes investigated. However, in acetoxime the N−OH bond is extended to a larger extend by 52% in contrast to 37% in the CHO and CPO, implying the saddle point for the OH channel in acetoxime lies relatively more toward the product side in the exit channel. Thus, higher f_T value (fraction of the E_{avl} partitioned to translation) is expected in acetoxime than in CHO and CPO. As expected, a higher f_T (>0.3) value is reported in acetoxime than that in CHO (0.25) and CPO (0.22). Like in CPO, in acetoxime as well OH($v''=1$) could be detected. Unlike in acetoxime, negligibly small UV/visible fluorescence could be observed in cyclic oximes. Since the absorption cross section of oximes at 248 nm is very small, OH could not be detected from CHO and CPO upon excitation at this wavelength, but its small yield could be detected in acetoxime. Photodissociation dynamics of cyclic oximes at 193 nm being similar to that of acetoxime, implies that the electronic excitation of oximes remains localized on the side chain (oxime group), and the ring remains almost unaffected. This explains why 5- and 6-membered rings in CPO and CHO, respectively, do not influence much the dissociation dynamics of these molecules. However, the dissociation dynamics of lower cyclic oximes can differ from that of larger cyclic (CHO and CPO) and acyclic oximes, due to significantly different ring strain. Lee and co workers[93] found the dissociation dynamics of cyclohexane and higher cyclic alkanes similar to that of acyclic alkanes, but different from that of lower cyclic alkanes. They ascribed this different photolytic behaviour of small cyclic alkanes due to their significantly different electronic structures caused by the large ring strain in these alkanes.

Table 3.1: Comparison of results on photodissociation of oximes at 193 nm. All energies are reported in kcal/mol.

	CHO[a]	CPO[a]	Acetoxime[b]	Acetaldoxime[c]
E_T(OH+cofragment)	21.8	21.0	28.0	20.0
E_R(OH(v''=0))	2.9	2.5	5.1	2.3
E_R(OH(v''=1))	--	1.8	2.5	1.9
E_V(OH(v''=0, 1))	--	1.9	2.8	2.4
Λ-doublet ratio	~1 at low N <1 at higher N	~1	<1	--
Spin-orbit ratio	~1	>1	<1 at low N ~1 at higher N	--
Exit barrier height	~33	~32	~29	~49
Emission	Weak	Weak	Strong (λ_{max} at 430 nm)	Strong (λ_{max} at 310 nm)
Available energy (E_{avl})	88.5	96.8	81.6[d]	81.4[d]

[a]Present work;   [b]Taken from ref. 19;

[c]Taken from ref. 17.   [d]Exclusive of the internal energy

3.5.7   DISSOCIATION DYNAMICS OF N−OH BOND IN OXIMES VERSUS C−OH IN CARBOXYLIC ACIDS

The dissociation of the N−OH bond in oximes producing OH appears to be quite similar to the C−OH bond dissociation in carboxylic acids at 193 nm. The C−OH bond dissociation pathway also has an exit barrier with the dissociation from an excited electronic state. However, most of the saturated carboxylic acids investigated[94] dissociate from the T_1 state, which involves $\pi^*_{C=O} \leftarrow n_{O(C=O)}$ transition, except for thiolactic acid[95], which dissociates from the S_1 state ($\pi^*_{C=O} \leftarrow n_S$), to produce OH upon excitation at 193 nm. Unsaturated propiolic acid[96,97] also dissociates from the T_1 state, which involves $\pi^*_{C\equiv C} \leftarrow \pi_{C\equiv C}$ transition, upon excitation

at 193 nm. However, unsaturated acrylic acid[98] dissociates from both the S_1 and T_2 states, which involve $\pi^* \leftarrow n$ transition, upon excitation at 193 nm.

3.6 CONCLUSIONS

Cyclohexanone oxime (CHO) and cyclopentanone oxime (CPO) in the vapour phase produce OH, as detected by laser induced fluorescence, upon excitation at 193 nm. We measured the state distribution of the nascent OH(v', J'') product, and found that it is produced mostly in the vibrational ground state ($v''=0$) in CHO and in both ($v''=0$) and ($v''=1$) states in CPO. Its rotational population is characterized by a rotational temperature of 1440±80 K in the case of CHO, and 1360±90 K ($v''=0$) and 930±170 K ($v''=1$) in the case of CPO. In both CHO and CPO, a higher fraction (25 and 22%, respectively) of the available energy is partitioned to the relative translation of the fragments, mainly because of the presence of an exit barrier in the dissociation channel producing OH. In the case of CHO, the Λ-doublet states of the nascent OH radical are populated almost equally in lower rotational quantum levels N'', with a preference for Π^+ (A') states for higher N''. However, there is no preference for either of the two spin-orbit states $\Pi_{3/2}$ and $\Pi_{1/2}$ of OH. Unlike in CHO, in CPO the nascent OH product prefers the spin-orbit state $\Pi_{3/2}$ to $\Pi_{1/2}$ and is equally populated in both the Λ-doublet states. Based on our experimental work and molecular orbital calculations, it is suggested that both CHO and CPO molecules at 193 nm are excited to the S_2 state, which relaxes fast to the T_2 state. The electronically excited CHO and CPO molecules undergo the N−OH bond dissociation from the T_2 state to produce OH (v'', J''). In both CHO and CPO, this dissociation channel has an exit barrier, since the corresponding transition state for OH formation could be located. Except for some differences in the values of energy partitioned to different degrees of freedom of products in CHO and CPO, overall dissociation dynamics for the OH producing

channel remains similar. Thus, the effect of the ring size of CHO and CPO is not pronounced on the dynamics of the N−OH bond dissociation. The energy diagram of dissociation channel is shown in FIG. 3.7.
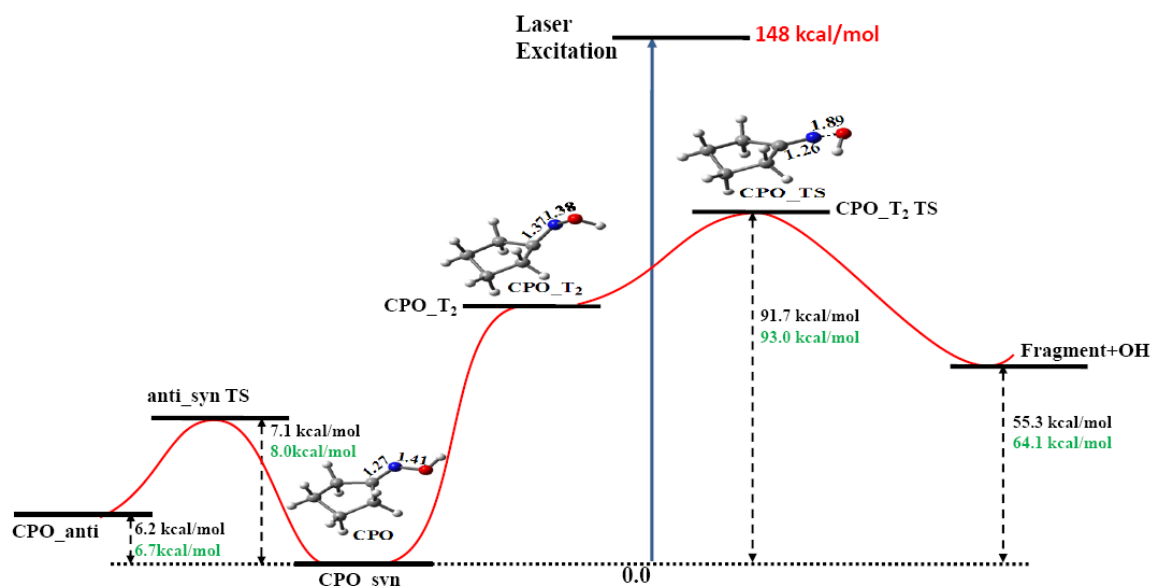
FIG. 3.7: The schematic energy diagram for formation of OH fragment after photodissociation of CPO at 193nm. The figure shows two isomers of CPO, CPO_anti and CPO_syn, and the transition state of conversion of these two forms. The OH fragment formation takes place from T_2 state and the transition state involved in it is also shown. The scheme for CHO is same as that for CPO, the energy values given in green colour are for CHO molecule.

CHAPTER 4

PHOTODISSOCIATION DYNAMICS OF ENOLIC-1, 2-CYCLOHEXANEDIONE AT 266, 248 AND 193 NM: MECHANISM AND NASCENT STATE PRODUCT DISTRIBUTION OF OH

4.1   INTRODUCTION

The α-diketones are the compounds having two keto groups on adjacent carbon atoms in an aliphatic chain or ring. These compounds show the tendency for interconversion between a keto and enol form, widely known as tautomerism. This keto-enol tautomerism plays an important role in many organic reactions, and is exploited by synthetic chemists, as its enol form is responsible for a large number of important reactions, e.g., benzilic acid rearrangement, Michael reaction, Claisen rearrangement and several other photochemical reactions. Though keto-enol transformation is very important, very few studies explore its fundamental nature and reactions associated with it. This is primarily due to the difficulty in isolating these

molecules in an easily characterized form. As a result, experimental work involving tautomerism is mostly limited to the studies in the gas phase.

Spectroscopic and electronic properties of α-diketones have been the subject of an important number of theoretical and experimental studies[99]. In case of aromatic α-diketones, photo-rotamerism, related to the dihedral intercarbonyl bond has a strong influence on the ground state and excited state properties[100]. The 1,2-diketo functional group in a six-membered ring system is an important structural unit found in a number of biologically important molecules and, in addition, it is also important from synthetic viewpoints. The structural unit is considered to be the active site of the anticancer drug Quassinoid Bruceantin[101], and anti-tumor steroid 4-hydroxyandrost-4-ene-3,17-dione[102]. A small member of this family, 3-methyl-1,2-cyclohexanedione, is considered to be responsible for coffee aroma[103]. It has been found that α-diketones undergo facile Strating-Zwanenburg photo-decarbonylation to produce the corresponding poly(acene)[104]. These diketones show a weak fluorescence and phosphorescence, and have a small singlet-triplet energy gap that facilitates rapid intersystem crossing from the singlet to the triplet state. Both of these states of diketones are short-lived, and their decarbonylation is a rapid process, occurring within few nanoseconds.

Monocarbonyl cyclohexanone does not display any enolic characteristics, and exists mainly in keto form in solution (~99%). However, introduction of second carbonyl group in the molecule can have a profound effect on the enolisibility of cyclohexanone. The effect depends on the position of the second carbonyl group on the ring. When the carbonyl group is introduced at the α-position, the diketone shows enolic character in both solution and gas phase. However, when it is at the β-position, enolic character is seen in only solution phase. In contrast, on substitution at the γ-

position, the diketone does not show enolic character, it exists only in keto form. Thus, 1, 3- and 1, 4-cyclohexanedione are expected to exist mainly in keto form in the gas phase, implying a preference for a chair like structure. This was confirmed by the strong spectral similarities between these two compounds[105]. Unlike 1,3- and 1,4-cyclohexanedione, 1,2-cyclohexanedione (CHD) is expected to have dominant enolic character. Several studies have reported on the molecular structure and keto-enol tautomerism in 1,2-cyclohexanedione (CHD)[105-108], and suggested the enol form to be predominant in the gas phase. The theoretical calculations done for this compound show that the enol form with hydrogen bond only is lower in energy than the keto form, and that without hydrogen bond is higher in energy than the keto form[107]. Walzl et al.[109], in their detailed studies on various diketones using electron-impact spectroscopy, have suggested that in CHD molecule, the two carbonyl groups can be twisted away from co-planarity due to constraint imposed by ring. This increases the overlap of highest occupied non-bonding (n) orbital and the lowest unoccupied π^* orbital, resulting in a large value of the n,π^* singlet-triplet splitting.

CHD is synthetically an important compound and has various applications in complex chemistry. The reaction of CHD with specific ω-alkenyl organometallics proceeds readily at both carbonyls and leads to 1,2-diols bonded to terminal olefinic chains in aqueous THF[110]. Schwartz[111] et al. have observed that the reactions of CHD with diamond (001) and Silicon (001) surfaces are quite different. It reacts with diamond (001) through the OH portion of the monoenol species via OH cleavage, while preferentially undergoes a 1,3-H shift with Si (001) and results in a product involving both O atoms. This difference is due to fact that the zwitterionic Si=Si dimer induces an intramolecular 1,3-H shift, suggesting the charge transfer effect, which is an important element of uncatalyzed enol keto transformations.

An another interesting aspect of CHD is that it belongs to the α, β-enone class of compound, whose detailed photochemistry has been studied in recent years[112,113]. We have studied the photodissociation dynamics of acetylacetone[113] a α,β-enone and β-diketone, at 266, 248, and 193 nm and detected the OH photoproduct. The dissociation dynamics of the CHD, a α-diketone, can be different from that of acetylacetone, a,β-diketone. However, the enolic form of CHD is also a α,β-enone, similar to enolic acetylacetone. The only structural difference between the two enone systems is the position of the OH group. Thus, it will be interesting to investigate the dissociation dynamics of CHD, and compare with that of acetylacetone. In this chapter, we report the dynamics of generation of the transient OH radical, detected by laser induced fluorescence (LIF) method, on photoexcitation of CHD at 266, 248, and 193 nm in the gas phase. We have measured the partitioning of the available energy among translational, rotational, and vibrational degrees of freedom of the photoproducts. Based on experimental results, coupled with *ab initio* molecular orbital calculations, we have proposed a plausible mechanism of OH formation. We have compared the results with our earlier work on the enolic acetylacetone photodissociation.

4.2   EXPERIMENTAL SECTION

The present studies on photodissociation dynamics are carried out in a flow reactor, at mTorr level pressure, using the laser photolysis-laser induced fluorescence set-up (LP-LIF). The experimental set-up is discussed in detail in Chapter 2, section 2.3. The CHD sample, with purity >98%, was used as supplied by Alfa Aesar. However, as the sample was semi-solid, it was thoroughly degassed before use. During the experiment, the vapour of the sample is flowed through the reaction

chamber in a pressure range of mTorr level, monitored by a capacitance pressure gauge and photolysed at 266, 248 and 193 nm as required.

4.3 RESULTS AND ANALYSIS

A typical LIF spectrum with appropriate assignments is shown in FIG. 4.1. A detailed description of notation used, can be seen in literature[87]. Briefly, the symbols P, Q, and R denote rotational transitions with $\Delta N = -1$, 0, and 1, respectively. The subscripts 1 and 2 represent the transitions, satisfying selection rules of both ΔJ and ΔN, from $\Pi_{3/2}$ and $\Pi_{1/2}$ spin-orbit states respectively, which form the main branches of the transition. The subscripts 21 and 12 represent the transition where only ΔN is satisfied and are satellite to the main branches represented by subscript 1 and 2. The Q and P/R branches originate respectively from Λ-doublet states Π^- (A") and Π^+ (A') due to the parity selection rule ($+ \leftrightarrow -$). The relative populations of the OH fragments are determined by normalizing the peak areas of the rotational lines with respect to pump and probe laser intensities, pressure change, if any, and the respective Einstein absorption coefficients[88]. The spin-orbit and the Λ-doublet ratios are calculated from the relative populations of different rotational states. The translational energy associated with the OH fragment is calculated from the Doppler profiles of the rotational lines. The detailed results are presented below.
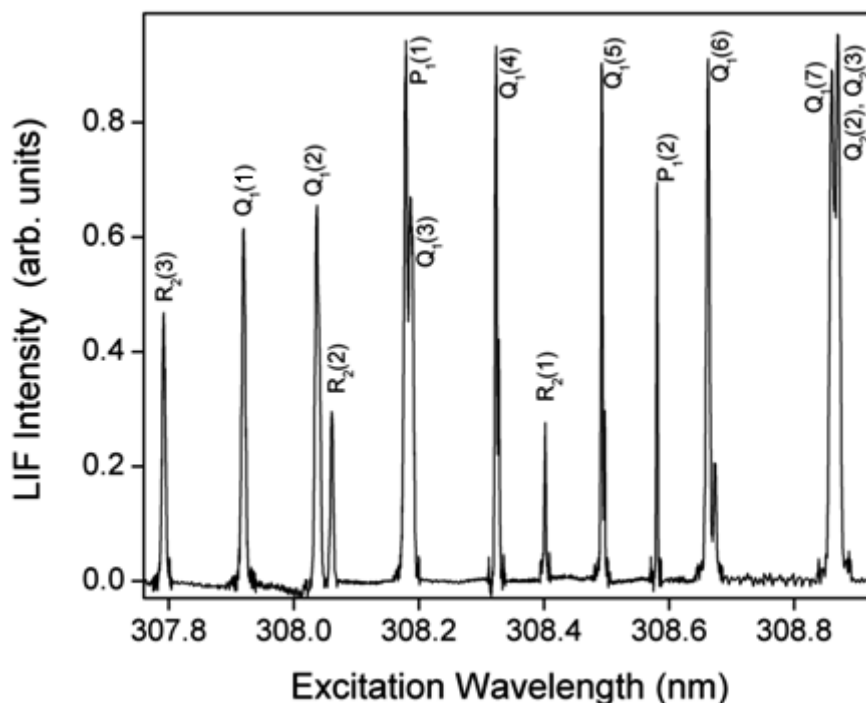
FIG. 4.1: A portion of typical LIF spectrum of OH after photodissociation of CHD (10 mTorr) at 248 nm and the pump-probe delay of ~50 ns.

4.3.1   ROTATIONAL STATE DISTRIBUTION

The nascent rotational state population of OH radicals, generated on photodissociation of CHD at 248 and 266 nm, is used to construct a Boltzmann plot for obtaining the rotational temperature of nascent OH fragments. The rotational state population at 193 nm could not be measured with a good signal-to-noise ratio due to low absorption coefficient of CHD at 193 nm. A typical Boltzmann plot for the photodissociation of CHD at 266 and 248 nm is shown in FIG. 4.2. The rotational temperatures have been obtained by the best fit to all the rotational states. At 266 nm photolysis, the Boltzmann plot is non-linear, showing a curvature. The rotational population of OH is fairly described by two types of Boltzmann-like distributions, which are characterized by rotational temperatures of 3100±100 and 900±80 K. However, at 248 nm photolysis, the rotational distribution is described by a single rotational temperature of 950±80 K. The OH (1, 1) transition is also scanned to determine the population of the OH fragment in $v''=1$, if any, but no LIF signal was

observed. Based on the experimental detection limit and Frank-Condon factors relative to the OH (0, 0) transition, it is estimated that less than 5% of the total OH yield is formed in the v"=1 state.
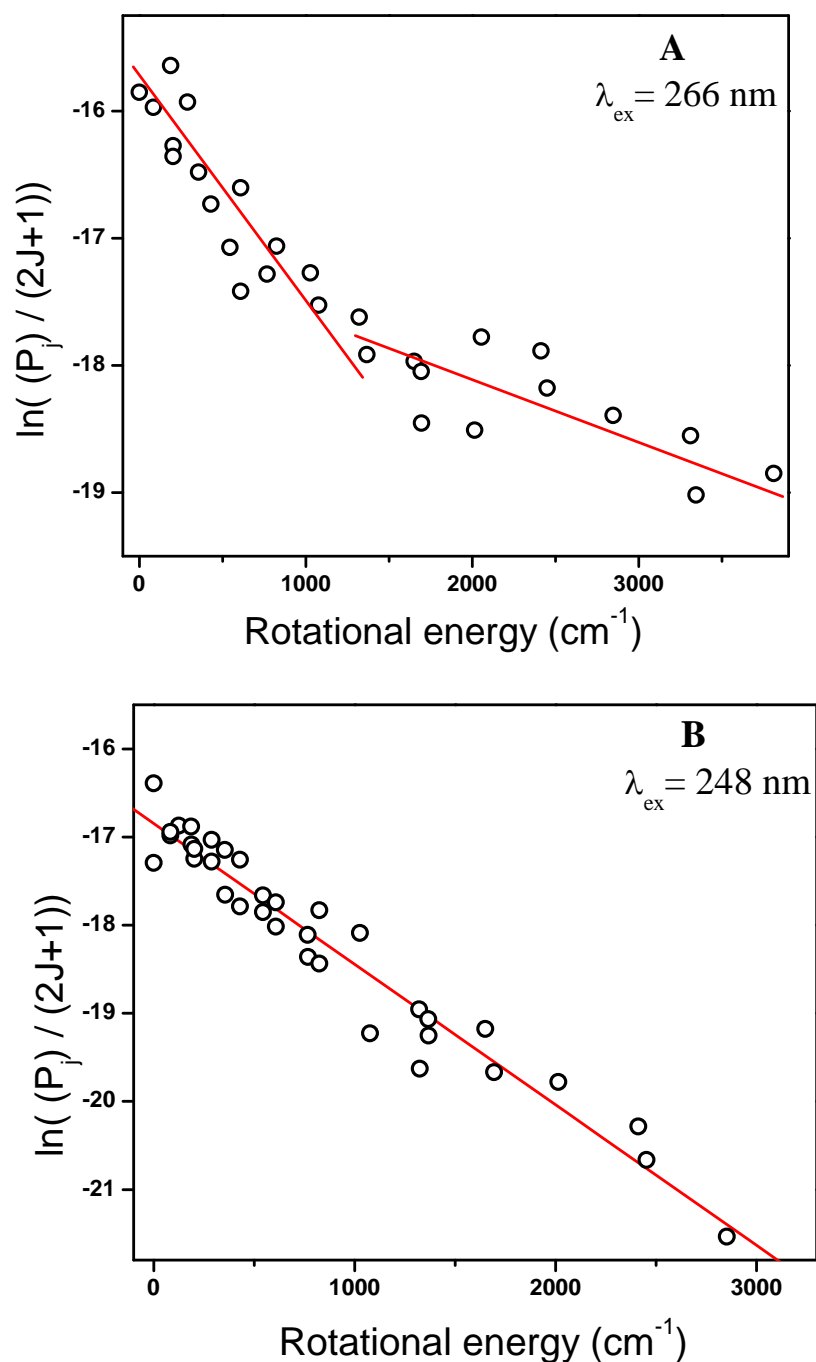
FIG. 4.2: Boltzmann plots of rotational distributions of the nascent OH radical generated on A) 266 nm and B) 248 nm photolysis. The solid lines are the fit to the experimental data points.

4.3.2 SPIN-ORBIT STATE DISTRIBUTION

The ground electronic state of OH being $^2\Pi$, there are two spin-orbit components, $^2\Pi_{3/2}$ and $^2\Pi_{1/2}$. The LIF intensities of only $P_1(N)$ and $P_2(N)$ lines are used to obtain the spin-orbit population. FIG. 4.3 shows the spin-orbit ($\Pi_{3/2}/\Pi_{1/2}$) ratios, multiplied by appropriate statistical weights (2J+1), and plotted versus the OH rotational quantum number (N), for photodissociation at 266 and 248 nm. From the figure, it is evident that the average value is unity within experimental errors, at 248 nm photolysis, thereby indicating a statistical distribution and no preference for either of the spin-orbit states in the dissociation process. However, at 266 nm photolysis the average value seems to be slightly greater than one. Thus, the nature of spin-orbit ratios for 266 and 248 nm photolysis is different. The relative population of spin-orbit states provides a clue on the coupling between the initially prepared excited state with a nearby dissociating state[114]. A statistical distribution suggests that the initially excited state probably does not interact directly with a triplet dissociating state. However, a non-statistical distribution, with preferential population of $^2\Pi_{3/2}$ state, indicates the role of a triplet state in the photodissociation process.
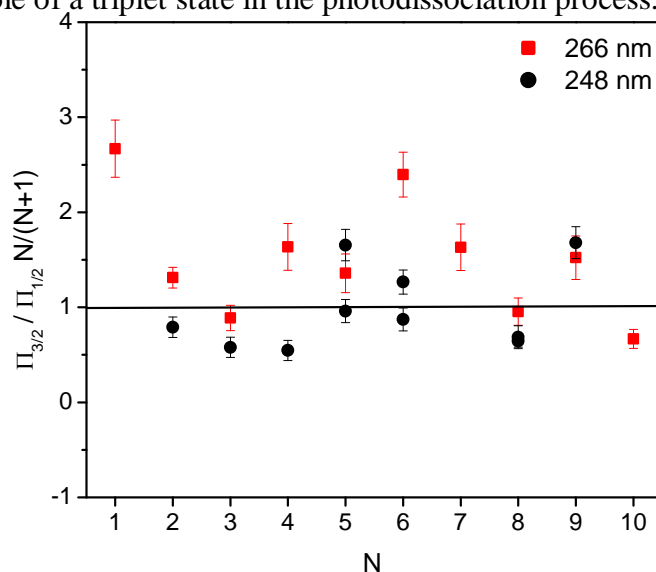
FIG. 4.3: The statistically weighted spin-orbit ratios of nascent OH (v″=0) as a function of the rotational quantum number (N). The red filled squares and the black filled circles denote the ratios at 266 and 248 nm photolysis, respectively.

4.3.3 POPULATION OF THE Λ-DOUBLETS

Each spin-orbit state of OH has two Λ-doublet components, denoted as Π^+ (or A') and Π^- (or A"), depending on the orientation of the π-lobe of the unpaired electron on OH with respect to the plane of rotation. In the high J limit, in the Π^+ (A') state, the π lobe lies in the plane of rotation, while in the Π^- (A") state, the π-lobe is perpendicular to the plane of rotation. The relative populations of the Λ-doublets provide information on the exit channel dynamics during the breaking of a chemical bond. In FIG. 4.4, the Λ-doublet ratio is plotted against the rotational number, N. Both at 248 and 266 nm photodissociation, the Λ-doublet ratio deviates from the statistical value of unity. The deviation is more prominent in the case of 266 nm photolysis. The result implies a role for exit channel interaction in formation of OH.
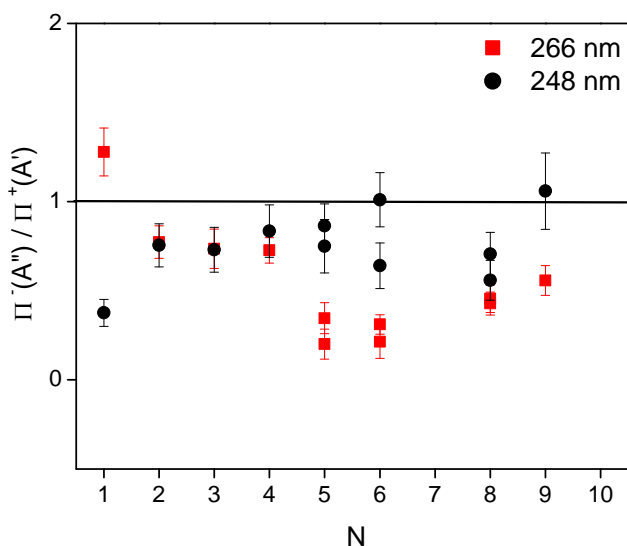
FIG. 4.4: Λ-doublet ratio of nascent OH(v''=0) as a function of the rotational quantum number (N). The red filled squares and the black filled circles denote the ratios at 266 and 248 nm photolysis, respectively.

4.3.4 TRANSLATIONAL ENERGY IN PRODUCTS

From the OH Doppler profiles, the average kinetic energy of the OH radical in the laboratory frame, E_T(OH), can be determined. The Doppler profiles of the rotational lines were corrected for the probe laser line width. All the rotational lines

measured were found to have similar line widths, within the range of the experimental error. The average translational energy in OH, $E_T(OH)$, is given by the Eqn. 2.11 (Chapter 2). In the present case, the Doppler profile is a Gaussian function as depicted in FIG. 4.5 for the $Q_1(4)$ line, which implies that the translational energy follows the Maxwell-Boltzmann distribution. The width and the shape of the Doppler-broadened LIF line include contributions from the fragment molecular velocity, the thermal motion of the parent molecule and the finite probe laser line width. Thus, the actual Doppler width is calculated using a deconvolution procedure using the width (FWHM) of the laser spectral profile of the probe laser beam, which is obtained from the OH Doppler profile measured in a thermalized condition. All the rotational lines exhibit the same width within an experimental error. More than 45 rotational line profiles are evaluated to estimate the average kinetic energy of the OH fragment in the laboratory frame, $E_T(OH)$. The product translational energy in the center of mass frame $E_T^{C.M}(OH)$ is obtained from the $E_T(OH)$, and is found to be 12.5±3.0, 12.7±3.0 and 12.0±3.0 kcal/mol at 266, 248 and 193 nm excitation, respectively. Although the excitation energies in these three cases of photodissociation are very much different, the translational in the fragments is almost similar. This observation suggests the presence of exit barrier. Since an exit barrier is generally not observed in the ground electronic state dissociation for a single bond scission, possibly the OH formation takes place from an excited state. Taking the value of ~90 kcal/mol, as the bond dissociation energy for the OH producing channel, similar as in acetylacetone[115], the f_T values are calculated as 0.73, 0.51, and 0.21 at 266, 248 and 193 nm excitation, respectively.
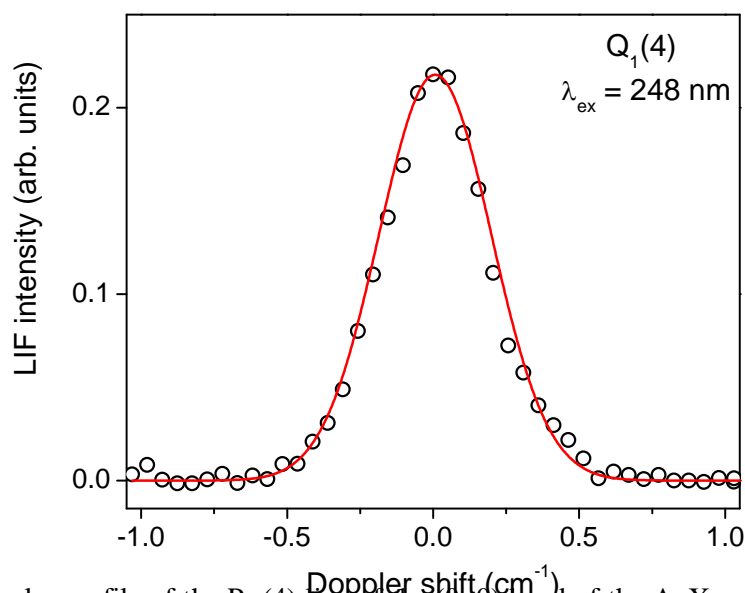
FIG. 4.5: Doppler profile of the P_1 (4) line of the (0, 0) band of the A–X system of OH on 248 nm photodissociation of CHD.

4.4   COMPUTATIONAL DETAILS

Ab initio molecular orbital (MO) calculations are performed to investigate the potential energy surface (PES) of the ground and excited electronic states of various conformers of CHD, using Gaussian[86] suite of program. CHD exists in various conformers shown in FIG. 4.6, namely, the H-bonded enolic form (structure **a**), diketo form (structure **b**) and non-H-bonded enolic form (structure **c**). We optimized geometries of these conformers/isomers at HF level using 6-311++G** basis set and confirmed the nature of stationary state geometries through vibrational frequency calculation. The relative energy is then calculated at the MP2 level using 6-311++G(3df,2p) basis set. Ground state self-consistent field (SCF) wave functions are examined for their stabilities before doing excited state calculations.
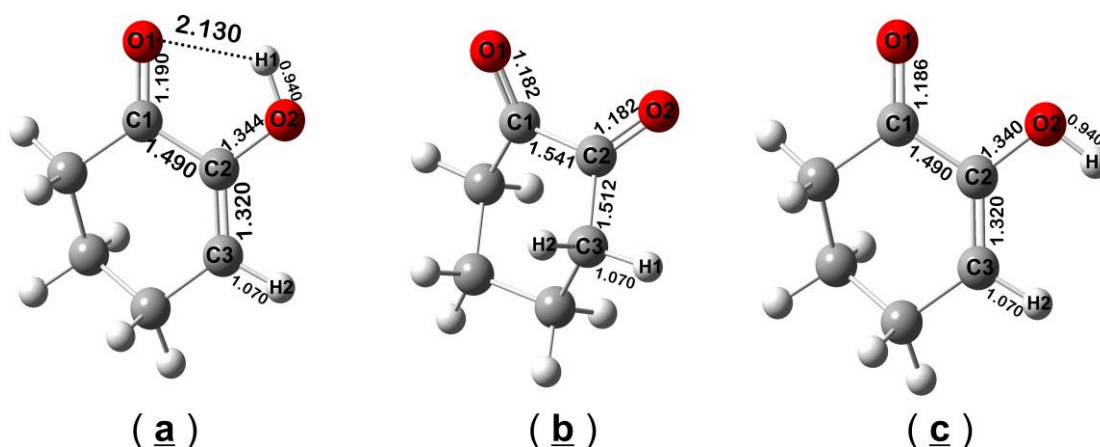
FIG. 4.6: Optimized structures of three conformer of 1,2-cyclohexanedione.

Excited electronic state calculations were performed at the configuration interaction with single electronic excitation (CIS) level, and various excited states of CHD accessible at 266, 248 and at 193 nm excitations are examined. Each of the excited state geometries (T_1, T_2, S_1, and S_2) was then fully optimized following the CIS procedure for both types of enolic form (**a** and **c**). For calculation of stationary point energies of various excited states, a hybrid approach was employed. Once the structure of different excited states, namely, T_1, T_2, S_1, and S_2, were optimized using CIS procedure, the vertical excitation energies (VEE) for these structures were then calculated using time-dependent density functional theory (TD-DFT) to get the total energy for better accuracy. The augmented basis set, with diffuse and triple zeta functions, namely, aug-cc-pVTZ, was used for obtaining the vertical excitation energies for various transitions, using time-dependent density functional theory (TD-DFT). Vibrational frequencies were also calculated with the final optimized geometries to confirm the nature of the stationary state geometries. Orbitals participating in the electronic transitions were assigned for each of the excited states, and these can be seen in FIG. 4.7.

enolic,– 1,2–cyclohexanedione, H–bonded Structure a

H–bonded Structure a   29 (n), HOMO-1   30 (π), HOMO   31 (π^*), LUMO

enolic,– 1,2–cyclohexanedione, non–H–bonded Structure c

non–H–bonded Structure c   29 (n), HOMO-1   30 (π), HOMO   31 (π^*), LUMO
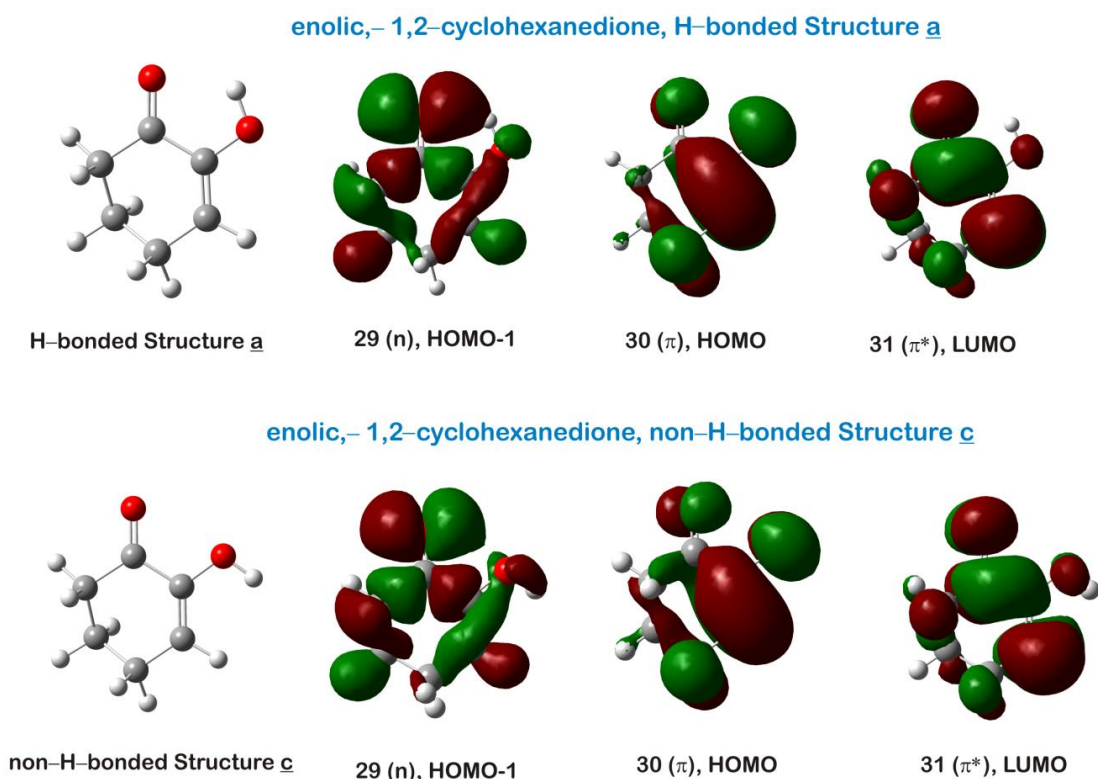
FIG. 4.7: Computed MOs involved in the transition of both the conformers of enolic 1,2–Cyclohexanedione (CHD).

4.4.1 PROFILES OF DIFFERENT POTENTIAL ENERGY SURFACES IN GROUND STATE

Various conformers of CHD in the ground state are optimized using 6-311++G** basis set. The most stable geometry has both the C=O and OH moieties lying in a plane and forming H-bonded 5-member ring structure. These structures can be seen in FIG. 4.6. The hydrogen bonded (**a**) and non-hydrogen bonded structures (**c**) are optimized and the energy of the latter is found to be 6.9 kcal/mol higher than the former. The transition state structure correlating these two structures, is also optimized, and shown in FIG. 4.8 as S_0-TS. This transition state structure lies 11.1 kcal/mol above the structure **a**. The diketo form of CHD, structure (**b**), is also optimized and the relative energy was calculated. The diketo structure (**b**) lies 4.5 kcal/mol above the hydrogen bonded structure (**a**). The non-hydrogen bonded structure (**c**) is least stable among all the structure in the ground state.

Although different reaction channels are possible from the ground state of CHD, in the present study our main aim is to characterize the structure responsible for the OH formation. The measured f_T values indicate an involvement of excited state(s) for the OH formation channel (*vide infra*). Hence, detailed excited state *ab initio* calculations are performed, using CIS procedure to locate the TS structure for OH formation.
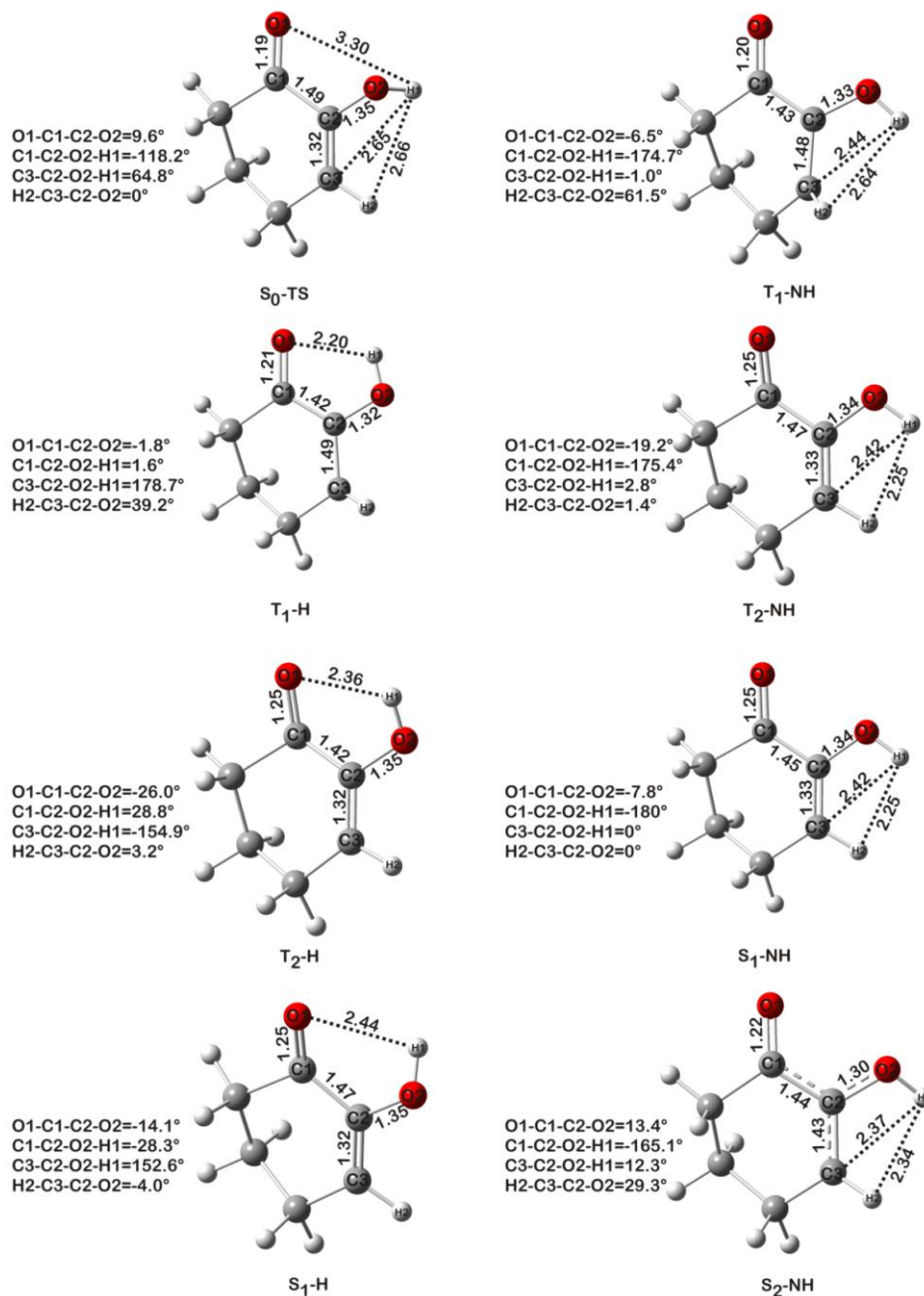
FIG. 4.8: Different optimized structures for various excited states of CHD (for details see the text).

4.4.2 NATURE OF EXCITED STATES

The onset of optical absorption in enolic-CHD occurs at ~286 nm (4.34 eV). Its gas phase UV spectrum shows strong absorption extending up to 218 nm (5.7 eV), with $\lambda_{max} = 256$ nm (4.84 eV). The nature of this band has been attributed to the π-π* transition. To understand the nature of the transitions involved in enolic-CHD in UV region, detailed excited state *ab initio* molecular orbital (MO) calculations were performed. The calculated vertical excitation energies and the respective oscillator strengths of several low-lying triplet and singlet states for enolic-CHD are shown in Table-1. The calculated vertical transition energies slightly differ as compared to the experimental results, but this method predicts accurately the nature of transitions that of the orbitals involved. The orbitals participating in the different electronic transitions were visualized, for better understanding of the process. Total four excited states are considered, two each of triplet and singlet states. These states are primarily due to excitations from either n_{HOMO-1} or π_{HOMO} orbitals to the π^*_{LUMO} orbitals. Besides excitations involving these valance states, excitations involving the Rydberg states to a diffuse 3s orbital are also possible at higher energies. For H-bonded CHD (structure **a**) the T_1 state is due to a π-π* transition at 2.44 eV (508 nm). The second triplet state, T_2, involve an n-π* transition at 3.42 eV (363 nm). The S_1 state is mainly due to an n-π* transition, with very low oscillator strength (0.0006), at 3.98 eV (311 nm). The S_2 state involves mainly a π-π* transition, with considerable oscillator strength (0.1570), at 4.538 eV (274 nm). Similarly, for non-H-bonded CHD (structure **c**) the two lowest triplet states, T_1 and T_2, are at 2.99 eV (414 nm) and 3.33 eV (372 nm), which involve the π-π* and n-π* transitions, respectively. The singlet states, S_1 and S_2, involve mainly the n-π* and π-π* transitions with the oscillator strengths of 0.0003 and 0.1558 at 3.93 eV (316 nm) and 5.03 eV (247 nm), respectively. The

higher singlet states S_3 and S_4 are Rydberg states in both H-bonded and non-H-bonded structures of CHD. For H-bonded CHD (structure **a**) the S_3 and S_4 states are at 5.74 eV (216 nm) and 6.16 eV (202 nm) with oscillator strengths of 0.0068 and 0.0008 respectively. Similarly, for non-H-bonded CHD (structure **c**) the S_3 and S_4 states are at 5.56 eV (223 nm) and 6.02 eV (206 nm) with oscillator strengths of 0.0017 and 0.0084, respectively. Considering the corresponding wavelengths for vertical excitation energies and the respective oscillator strengths of the various transitions, it is evident that at 248 and 266 nm, CHD has a π-π* transition. The excited state with π-π* transition adiabatically correlates only with highly excited photoproducts. Since the formation of excited states of OH is not feasible in a single-photon excitation in the present case, it implies that OH is not produced from the initially excited (ππ*) state. Hence, it is assumed that the initially prepared singlet (ππ*) state of CHD crosses over to the nearby states, mostly either triplet or singlet (nπ*) state, or the triplet (ππ*) state, from where the OH formation may take place. At 193 nm excitation, the molecule is prepared in its Rydberg state from where various other processes may occur, including the formation of the OH radical.

#	Excited State	Transition Type	enolic-1,2-cyclohexanedione (H-bonded, structure **a**)		enolic-1,2-cyclohexanedione (non H-bonded, structure **C**)	
			Vertical excitation energy in eV and in (kcal/mol, nm, oscillator strength)	Relative energy in kcal/mol and in (nm) of the different stationary points	Vertical excitation energy in eV and in (kcal/mol, nm, oscillator strength)	Relative energy in kcal/mol and in (nm) of the different stationary points
1	T_1	$^3(\pi-\pi^*)$	2.4418 (56.30, 508, 0.0)	31.0 (922)	2.9949(69.06, 414, 0.0)	34.0 (841)
2	T_2	$^3(n-\pi^*)$	3.4151 (78.75, 363, 0.0)	76.3 (375)	3.3304(76.80, 372, 0.0)	76.3 (375)
3	S_1	$^1(n-\pi^*)$	3.9817 (91.82, 311, 0.0006)	88.1 (325)	3.9278(90.58, 316,0.0003)	87.3 (328)
4	S_2	$^1(\pi-\pi^*)$	4.5322 (104.51, 274, 0.1570)	-	5.0298(115.99, 247,0.1558)	110.0 (260)

Table 4.1: Different transition type in CHD and their vertical excitation energies in eV and corresponding values in kcal/mol, nm and respective oscillator strength, (given in parentheses) of various excited states of both the conformers of enolic-1,2-cyclohexanedione, namely H-bonded conformer (**a**) and non-H-bonded conformer (**c**). Table also reports the relative energy in units of kcal/mol and nm of different stationary points in the excited states of both the conformers.

4.4.3 PROFILES OF DIFFERENT POTENTIAL ENERGY SURFACES IN EXCITED STATES

4.4.3.1 HYDROGEN BONDED ENOLIC-CHD (STRUCTURE <u>a</u>)

a) *The T_1 State:*

The T_1 minimum at the CIS/6-311++G** level has a non-planar structure, shown in FIG. 4.8 as T_1-H. From the natural orbital analysis of the structure, it is quite reasonable to expect that the lowest triplet structure arises from the π-π* transition of the C=C bond. One electron is initially excited from the π to π* orbital converting the C2=C3 double bond (1.32Å) to almost a single bond (1.49Å) and the C1–C2 single bond (1.49Å) is shortened to 1.42Å. Similarly, the C2–O2 bond length is slightly shortened from 1.34Å to 1.32Å while C1=O1 is lengthened from 1.19Å to 1.21Å. Apart from these changes, the O1····H1 distance is slightly elongated to 2.20Å at the T_1 minimum from the ground state value of 2.13 Å. It seems that the H-bonding is still effectively present in the T_1 structure, because of the near planarity of the O1–C1–C2–O2–H1 backbone. These atoms are also nearly planar with C3, as in the case of the ground state structure. However, the H2 atom, which is on the plane in the ground state, is now out of the plane in the T_1 minimum. These details can be seen in FIG. 4.8. The position of the T_1 minimum is about 31.0 kcal/mol above the S_0 ground state.

b) *The T_2 State:*

The structure for the T_2 minimum is shown in FIG. 4.8 as T_2-H. In this structure, all the atoms (O1–C1–C2–O2–H1 backbone with C3 and H2) are non-planar, making this structure a truly puckered one. Careful examinations of structural parameters and the natural orbital analysis confirmed this structure to be an (nπ*) state. It is quite reasonable to assume that the initial excitation is from the n orbital to

the $\pi^*_{C=O}$ orbital, weakening the C=O bond to a large extent. The T_2 minimum structure shows an increased C=O bond length of 1.25Å as compared to 1.19 Å in the ground state. The O1······H1 distance in the T_2 minimum is 2.36Å, indicating that the H-bonding is less effective in the T_2 state as compared to its ground state. The position of the T_2 minimum is about 76.3 kcal/mol above the ground state.

c) *The S_1 State:*

The structure for the S_1 minimum is non-planar and shown in figure as S_1-H. A comparison shows that the structure is quite similar to the T_2 $^3(n\pi^*)$ in structure. Natural orbital analysis and a close examination of the structure suggest that this structure results from a $^1(n-\pi^*)$ transition. The O1······H1 distance in the S_1 minimum is 2.44Å, indicating that the H-bonding is even less effective in the S_1 state as compared to either T_2 or the ground state. The S_1 state minimum is located about 88.1 kcal/mol above the ground state.

d) *The S_2 State:*

We failed to optimize the structure of the S_2 minimum at the present level of theory for the H-bonded CHD. However, in a recent article by Chakraborty and co-workers[108] the S_2 state, along with the S_1 state, for the H-bonded structure is reported. A careful examination of both their S_1 and S_2 structures and our own calculations reveal that both the structures are equivalent, geometrically as well as energetically. We also repeated the theoretical calculations and confirmed that after a few iterations in CIS calculations, the S_1 and S_2 excited states cross over and finally produce the structure of the S_1 state only. So the reported structure for the S_2 state by Chakraborty and co-workers[108] does not seem to be genuine. Moreover, we tried to optimize the structure of the S_2 minima at various levels of theories but failed. However, the absorption spectra of compound show a very intense peak at around 266 nm,

indicating a bound state of the ($\pi\pi^*$) character in nature, similar to a state that can be termed as S_2. This discrepancy prompted us to search for the local minimum for the ($\pi\pi^*$) singlet state for non-hydrogen bonded CHD, which will be discussed in detail in following section.

4.4.3.2 NON-HYDROGEN BONDED ENOLIC-CHD (STRUCTURE c):

a) *The T_1 State:*

The T_1 minimum at the CIS/6-311++G** level for non-hydrogen bonded enolic CHD ☐ has a non-planar structure, similar to the hydrogen bonded counterpart, except for the O–H orientation shown in FIG. 4.8 as T_1-NH. The C2=C3 double bond (1.32Å) is converted to almost a single bond (1.48Å) and the C1–C2 single bond length (1.49Å) is shortened. Similarly, the C2–O2 bond length is slightly shortened, while the C1=O1 bond is lengthened. The O1–C1–C2–O2–H1 backbone with C3 atom is nearly planar, similar to the ground state. The only difference in structure arises as H2 is in the plane in the ground state but out of the plane (at ~61°) in the T_1 minima. These details can be seen in the FIG. 4.8. The position of the T_1 minimum is about 34.0 kcal/mol above the S_0 ground state of structure **a**.

b) *The T_2 State:*

The structure for the T_2 minimum is shown in FIG. 4.8 as T_2-NH. In this structure, all O1–C1–C2–O2–H1 atoms are non-planar, while the backbone connecting H2–C3–C2–O2–H1 atoms is planar. In this structure, the initial excitation of the n orbital to the $\pi^*_{C=O}$ orbital weakens the C=O bond significantly. The T_2 minimum structure shows an increased C=O bond length of 1.25Å as compared to 1.19Å in the ground state. The position of the T_2 minimum is about 76.3 kcal/mol above the ground state.

c) *The S₁ State:*

As shown in FIG. 4.8 (S_1-NH), the structure for the S_1 minimum is almost planar. A comparison shows that the S_1 minimum is quite similar to the T_2 ^{3}($n\pi$*) state in structure. Natural orbital analysis and a close examination of the structure suggest that this structure results from a ^{1}(n-π*) transition. The position of the S_1 minimum is about 87.3 kcal/mol above the ground state.

d) *The S₂ State:*

We could optimize the structure of the S_2 minimum at the present level of theory, and it is shown in FIG. 4.8 as S_2-NH. From the natural orbital analysis of the structure, it is quite reasonable to expect that this particular structure arises from the π-π* transition of the C=C bond. One electron is initially excited from the π to π* orbital converting the C2=C3 double bond (1.32Å) to almost a single bond (1.43Å) and shortening the C1–C2 single bond length (1.49Å) to 1.42Å. Similarly, the C2–O2 bond length is slightly shortened, while the C1=O1 bond is lengthened. Similar to the structure T_1-NH, and that in the ground state the O1–C1–C2–O2–H1 atoms with C3 atom are nearly planar. The only difference from the T_1-NH structure and the ground state is that the H2, which lies in plane in the ground state, is now out of the plane at ~30° as compared to ~61° in T_1 minima. These details can be seen in the FIG. 4.8. The location of the S_2 minimum is about 110.0 kcal/mol above the S_0 ground state.

Generally in the case of α, β-enones, the S_2 state originates from a π-π* transition centered at the double bond having a mixed character of π*$_{C=O}$/π*$_{C=C}$. For acrylic acid, the S_2 state structure calculated by Arendt et al.[116], shows transfer of a large amount of electron density from the C=C double bond to the COOH group, which can be treated as intramolecular charge transfer. This structure is so different from the ground state that the double bond is actually shifted to the next carbon atom,

and the initial double bond is elongated and behaves as a single bond. Similarly, in enolic-acetylacetone[113] a strong intramolecular H-bonding counterbalances the charge at the O atom and the structure gets stabilized. This stable structure of the S_2 state indeed lowers the transition energy in enolic-acetylacetone with the $^1(\pi\text{-}\pi^*)$ transition showing a peak at 267 nm, compared to that in acrylic acid, which shows a peak at ~198 nm. Similar to enolic-acetylacetone, the $^1(\pi\text{-}\pi^*)$ transition in the CHD, shows an intense absorption peak in the 267 nm region. Like in acrylic acid, the $^1(\pi\pi^*)$ state in CHD is expected to show transfer of a large amount of electron density from the C=C double bond to the adjacent C–C single bond and to the C=O group, which can be treated as intramolecular charge transfer. Contrary to the case in enolic-acetylacetone, where the charges are effectively balanced by the strong H-bonding forming a six-membered ring, the situation is different in CHD because of its ring structure. The ring structure does not allow the enolic H-bonded structure (**a**) to stabilize by balancing the charges effectively. This is the main reason why we failed to optimize the S_2 minimum structure for structure **a**. The only option to stabilize the structure by the H atom of the OH moiety is by rotation of C–OH bond with almost no barrier, and thus giving rise to the S_2 structure minimum. In this process, the H-bond is broken and the geometry changes to non-H-bonded structure (**c**). The above discussion clearly shows why we could get a S_2 structure minimum for the non-H-bonded structure (**c**) and not for the H-bonded structure (**a**).

4.5   DISCUSSION

4.5.1   AVERAGE ENERGIES OF THE FRAGMENTS

The partitioning of the available energy into various degrees of freedom of the fragments is mainly governed by the nature of the transition state and its location on the dissociative potential energy surface. Dissociation of CHD at 266 and 248 nm

occurs with a large fraction of the available energy being imparted into relative translational energy of the fragments. In addition, similar amount the relative translational energy in both the cases indicates the presence of an exit barrier. Since the statistical model predicts well only the energy partitioning of a dissociation process with no barrier, we have employed different models, including the statistical model, to understand the dissociation process at different wavelengths.

Statistical Model:

A statistical prior distribution is often the starting model to understand any dissociating event. In this model, the available energy, E_{avl}, is distributed among all the accessible states with equal probabilities under the constraint of conservation of energy. This model completely ignores angular momentum constraints in the photodissociation process. A statistical dissociation process occurs predominantly, if the photo-excited parent molecule is so long lived that the excess energy is partitioned statistically amongst the available degrees of freedom of the products. This includes a process wherein a rapid internal conversion to the ground electronic state takes place, followed by the subsequent slow dissociation. Under these events, in a large molecule, with many low frequency modes, a relatively small amount of the excess energy is partitioned into translational motion of the products. For this kind of dissociation process, *a priori* calculations[117-119] were adopted, along with a simple analytical expression established by Klots[120], relating the mean translational energy release, E_T, and the E_{avl}, for a statistical barrier-less dissociation process. The density of states were estimated from the vibrational frequencies and the rotational constants of the fragments obtained at the HF/6-311++G(d,p) level of theory. The statistical model puts ~7% of the available energy into the relative translational mode of the photofragments. Thus, the available energy appearing as the relative kinetic energy of

the products is underestimated using statistical model. Hence, the statistical model fails to explain the observed partitioning of the available energy among photofragments at all the wavelengths studied.

Impulsive Model:

In the impulsive model, the distribution of energy among product states is governed by the dissociative event, i.e., by the repulsive force acting during the breaking of the parent molecule into the products. This treatment conserves energy and both linear and angular momenta. The model assumes that all the available energy is stored within the breaking bond. We have employed the method for calculation as given by Crim and co-workers[117] and Tuck[121] to estimate the energy partitioning using impulsive model. The impulsive model estimates ~48% of the available energy into the product translational mode. Like the statistical model, the impulsive model also is unable to explain the experimentally obtained relative translational energy in the fragments for 266 and 193 nm photodissociation processes, which are ~73% and ~21%, respectively. However, the prediction based on the impulsive model is closer to the experimental value, at least, at 248 nm, which is ~51%. However, both statistical and impulsive models allocate low rotational and vibrational energies into the OH radical, as observed at 248 and 266 nm.

The failure of both the statistical and impulsive models in explaining the partitioning of the available energy prompted us to apply the hybrid model, employed by North[92] et al. for a reaction with a barrier. In this model, the E_{avl} for the products is divided into the excess energy above the exit barrier (E_{stat}) and the exit barrier energy (E_{imp}). The partitioning of E_{stat} and E_{imp} is treated respectively by the statistical and modified impulsive models. The energy partitioned into each fragment is then obtained by adding contributions from each of these two models. The measured

energy partitioning into the fragments is reproduced well with an exit barrier of ~14.0 kcal/mol. This model predicts almost no vibrational excitation of OH.

4.5.2 MECHANISM OF THE DISSOCIATION PROCESS

We shall now present the complete picture of the dissociation process in the light of the above discussion in conjunction with the dynamics models for energy partitioning and the structure calculations with the help of *ab initio* method. As discussed earlier, the major fraction of the available energy is channeled into the translational mode of the photofragments, which indicates either the impulsive dissociation of the C–OH bond, or the presence of an exit barrier. As shown earlier, the impulsive dissociation does not account for such a high fraction of the available energy being partitioned into the translational energy of the products, at least, at 266 nm photolysis. In addition, the amount of translational energy is almost constant, irrespective of the excitation wavelength or the available energy. This kind of behavior in translational energy release in any photodissociation process is typically of dissociation process with an exit barrier. Thus, there should be an exit barrier to the C–O bond cleavage. Such an exit barrier is observed for a simple bond cleavage leading to OH in photodissociation of acetic[122] and acrylic acid[123,124] and acetylacetone[113]. The 266 and 248 nm excitation of CHD leads to the same electronic state through $^1(\pi\text{-}\pi^*)$ transition. Dissociation mechanism of CHD at different wavelengths is discussed below.

The absorptions of 266 and 248 nm photons by enolic CHD lead to the allowed $(\pi\text{-}\pi^*)$ transition near the S_2 state origin. Subsequent to excitation, we are unable to get any fluorescence even though the excitation energy is near the origin of the transition. This suggests the importance of fast non-radiative processes in this region of excitation. As discussed earlier, the enolic-CHD exists in two forms namely,

the H-bonded (**a**) and non-H-bonded form (**c**), with an energy difference of about ~7 kcal/mol in favour of H-bonded structure. However, the S_2 structure for the H-bonded structure (**a**) does not exist because of the non-stabilization of the charge separation as discussed earlier. Therefore, in the vicinity of Franck-Condon region, the C–OH bond rotates very fast almost with no barrier and gives rise to the S_2 structure minimum for the non-H-bonded form, depicted in FIG. 4.8 as S_2-NH. This shows that even though the non-H-bonded structure (**c**) is not excited initially from the ground state, the excited state dynamics is totally controlled by its structure. Due to fast non-radiative processes, the S_2-NH state crosses over to various other states, either S_1 or T_1/T_2 of both the structures, and the subsequent dissociation results into the formation of OH. However, we are unable to locate any transition state structure for the OH fragment formation, using CIS method in any of these excited states. However, we observe that similar amount of translational energy released into the photofragments irrespective of the excitation energy or the available energy indicates the presence of an exit barrier for the dissociation process. To further investigate this issue we have mapped the potential energy (PE) curves for various excited states. In FIG. 4.9, we have shown calculated PE curves as a function of the C2–O2 bond length for various excited electronic states, such as T_2, S_1 and S_2 for both the H-bonded (**a**) and non-H-bonded structures (**c**) of CHD. The molecular geometries in the ground state for different discrete values of C2–O2 bond lengths were optimized at HF/6-311++G** level of theory, and the energies of such fully optimized configurations were used to generate the PE curve for the ground state. For excited states, the curves were generated by plotting the calculated vertical transition energies, corresponding to different ground state optimized geometries, using TD-DFT method, employing aug-cc-pvDZ basis

sets. All the excited states presented in FIG. 4.9 are bound states, and the relative energy is with respect to the H-bonded structure (**a**).
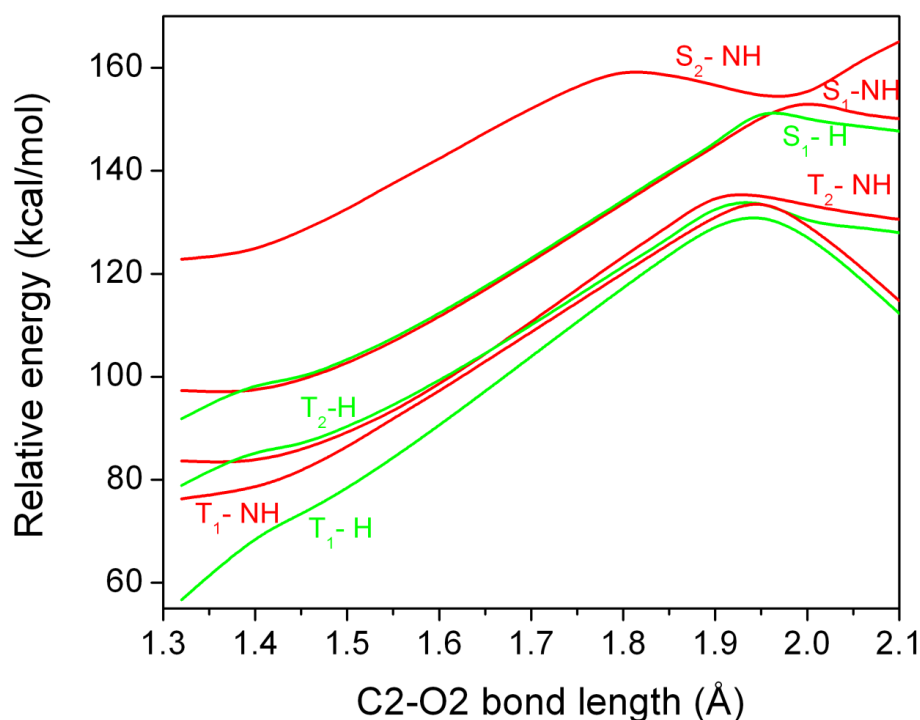
FIG. 4.9: Potential energy curves for various excited electronic states of different CHD structures namely H–bonded (**a**) and non–H–bonded structures (**c**) calculated with the TD-DFT method as a function of the C2–O2 bond length.

The first point in the PE curves belongs to the energy minimum structure for C2–O2 bond length of 1.32Å. At equilibrium geometry, the excited states namely T_2H and S_1H, belonging to the H-bonded structure (**a**) have the minimum energy and are more stable than the corresponding structures for the non-H-bonded entity (**c**). However, as the C2–O2 bond starts elongating, excited states belonging to the non-H-bonded isomer become comparatively more stable and again this tendency is changed at longer C2–O2 bond length. This clearly demonstrates that the crossing-over of an excited state from the H-bonded to the non-H-bonded isomers and vice versa is very efficient. We think that this efficient crossing over may be a reason for not getting an optimized transition state (TS) geometry for the OH elimination channel, using the

present theoretical approach. Possibly, a more accurate method like Complete-Active-Space self-consistent field (CASSCF) can produce an optimized TS geometry for the OH formation. However, at present we are not able to carry out this type of calculation for a medium large molecule, such as CHD. Although we could not optimize the TS structure, our present theoretical calculations in combination with experimental results, unambiguously suggest the presence of an exit barrier for the OH elimination channel.

The large amount of translation energy release in present case is very much similar to the photodissociation dynamics of similar enones, such as enolic acetylacetone. The transition state for the OH elimination channel in enolic acetylacetone was fully optimized at the T_1 ($\pi\pi^*$) excited state[113]. However, a combination of ultrafast electron diffraction (UED) studies and CASSCF calculation indicates the mixing of the S_2 state with the S_1 state in enolic acetylacetone responsible for the OH elimination channel[125]. Similar mixing or crossing of the S_2 and the S_1 states of non-H-bonded structure of CHD is seen in present case also (see FIG. 4.9). Moreover, the T_1 state of both the H-bonded and non-H-bonded structure also has an exit barrier. Thus, the initially prepared S_2 state either crosses to S_1-NH or to T_2-NH/T_2-H or T_1-H and finally dissociates to give the OH radical as a photoproduct with an exit barrier. The different values of the rotational temperature and the nature of rotational distribution at 266 nm and 248 nm photolysis indicate different type of dissociation mechanisms taking place at these two wavelengths. At the 266 nm photolysis, the two types of rotational temperatures and hence the rotational energies were observed, which clearly indicate that there may be two types of molecular geometries responsible for the OH elimination channel. Similar observations were also reported for the rotational state distribution of the nascent OH

radical formed in the photolysis of nitro-benzoic acid[126] and alkyl nitriles[127] by Han and co-workers. They suggested the involvement of more than one structures in the OH formation channel giving rise to non-Boltzmann distribution of OH rotational state. Likewise, we propose that the OH channel with high rotational temperature is originating from an excited state with the H-bonding e.g. T_1-H. The situation can be visualized as follows: the C–OH bond dissociation from an H-bonded structure is expected to generate a large torque generally giving rise to large rotation to the OH radical. Hence, we strongly believe that the dissociation at 266 nm involves the H-bonded structure, such as T_1H, for the large rotational energy distribution and a non-H-bonded structure for the low rotational energy distribution. At 248 nm photolysis, the experimentally determined rotational temperature matches quite well with the lower value of rotational temperature at 266 nm photolysis. This indicates that a similar mechanism is responsible for these two cases, and hence at 248 nm we have attributed the OH formation channel to a non-H-bonded structure.

The value for the barrier height can be obtained experimentally from partitioning of the available energy into the product translational mode, which obeys a modified hybrid model. The translational energy released into the photofragments is in good agreement with the modified impulsive model with an exit barrier of 14.0 kcal/mol. Hence, the transition state on the excited surface for the OH formation channel is located at $\approx$104 kcal/mol, from the ground state structure **a**, using an experimental value of 90.3 kcal/mol for the C–OH bond dissociation energy.

At 193 nm photolysis, we lack sufficient experimental data to discuss unambiguously the mechanism of the OH formation. Absorption of 193 nm light prepares CHD in a Rydberg state and due to fast internal conversion, it can cross over to higher vibrational levels of different lower potential energy surfaces. The

translational energy release into photofragments estimated from the experiment is higher compared to the energy evaluated using the statistical method and somewhat lower compared to the impulsive model. Since we were not able to measure the rotational state distribution and other parameters like spin-orbit and Λ-doublet ratios, it is difficult to suggest any explicit mechanism for 193 nm photolysis. At this point, we can only guess that the dissociation is taking place from a repulsive state, similar to acetylacetone.

4.6   CONCLUSION

In summary, enolic CHD generates the OH radical upon excitation wavelengths of 266, 248, and 193 nm, which prepare the molecule in ($\pi\pi^*$) and Rydberg states. The nascent state of the photofragment OH is probed with the LIF technique. At 266 nm photolysis, the rotational population is fairly described by two types of Boltzmann-like distributions, which are characterized by rotational temperatures of 3100±100, and 900±80 K. While at 248 nm photolysis, the rotational distribution is described by a single rotational temperature of 950±80 K. The average translational energy partitioned into the photofragment pairs in the center-of-mass co-ordinate is determined to be 12.5±3.0, 12.7±3.0 and 12.0±3.0 kcal/mol at 266, 248 and 193 nm excitation, respectively. The high percentage of translational energy partitioned into the products at 266 and 248 nm photolysis is consistent with the hybrid model showing the presence of an exit barrier for the OH formation channel. The spin-orbit and Λ-doublet ratios are also measured to gain insights into dynamics of OH formation. Detailed *ab initio* quantum calculations suggest that at 266 nm photolysis, the OH fragment is formed from two different excited state structures, one with a strong H-bonding and another without effective H-bonding. The lowest planar T_1-H($\pi\pi^*$) excited state, with strong H bond, can be responsible for the OH formation

with higher rotational temperature which is confirmed by preferential population of $\Lambda^+(A')$ state. At 248 nm photodissociation, we suggest that the OH formation occurs mainly from an excited state, which is devoid of any effective H-bonding. At 248 nm and at 266 nm with lower rotational temperature, a mixture of S_1/T_2, where the H-bonding is not effective, has been suggested. At 193 nm excitation, the initially prepared Rydberg state can cross over to a nearby π^* repulsive state along the C–O bond, from where the dissociation can take place. The exit barrier for the OH dissociation channel is estimated to be 14 kcal/mol. The existence of a dynamical constraint due to strong hydrogen bond in the ground state is effectively present in the dissociation process at 266, and somewhat minimized at 248 nm photolysis. The energy diagram of dissociation channel is shown in FIG. 4.10.
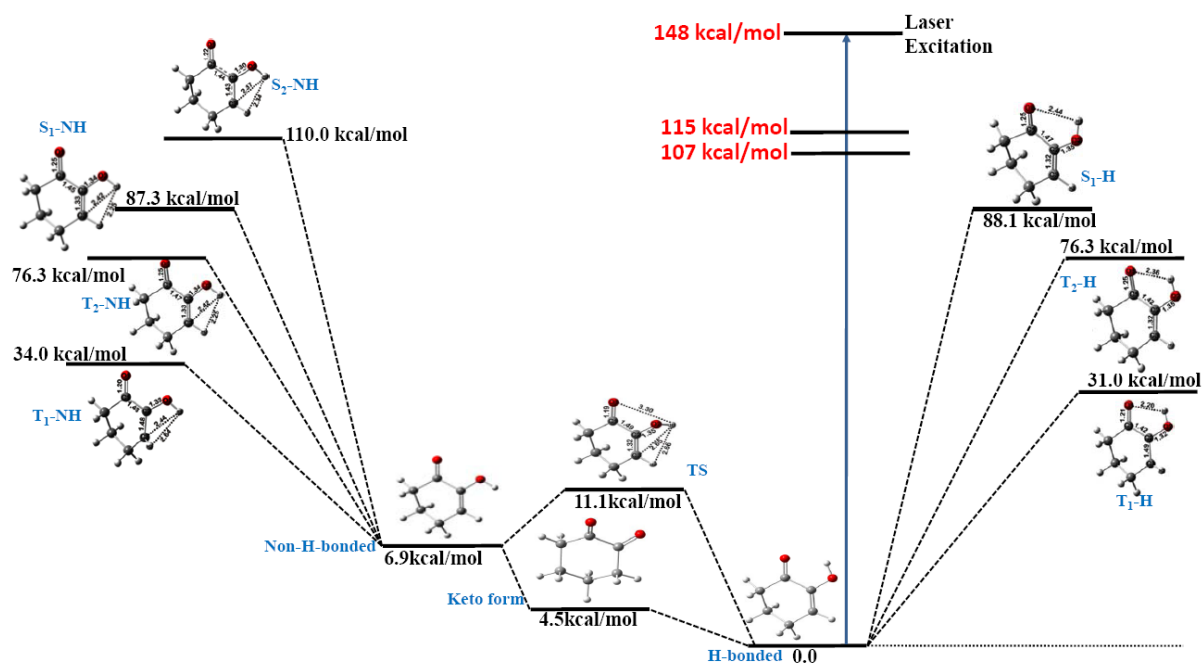
FIG. 4.10: The schematic energy diagram for CHD molecule. The figure shows the three isomers of CHD namely, H-bonded, non-H-bonded and keto-form of CHD and the transition state for conversion from non-H-bonded form to H-bonded form. The energetic of T_1, T_2, S_1 and S_2 states formed after photodissociation of both non-H-bonded and H-bonded CHD at 193, 248 and 266 nm are also shown in the figure.

CHAPTER 5

PHOTODISSOCIATION DYNAMICS OF 2-CHLRO-6-NITROTOLUENE AND NITROCYCLOPENTANE IN GAS PHASE

5.1   INTRODUCTION

The nitroaromatic and nitro cyclic compounds are common industrial chemicals, however some of them are toxic substances, which raise safety and environmental-hazard concerns. They are either directly emitted into the atmosphere due to industrial activities or can be formed in situ by secondary photochemical processes in the atmosphere. The photodissociation dynamics of these compounds is currently an interesting topic due to their relevance to the atmospheric and combustion chemistry. The low barriers for dissociation of these compounds have motivated work on their unimolecular decay as it pertains to combustion. These molecules have NO_2 as a major photodissociation product, which participates in various atmospheric reactions, including ozone generation in the troposphere. Hence,

they are relevant from the point of view of atmospheric chemistry. Recent work on photo-oxidation processes of aromatic hydrocarbon performed in the presence of hydroxyl radical scavengers revealed that OH radicals are generated during the photolysis of nitrophenols[128] and the OH radical has also been directly observed in the photodissociation of o-nitrophenol[129] and nitrotoluene[130]. The OH radical is an important radical in the chemistry of the atmosphere. It is a key reactive species in the interstellar medium and one of the most important oxidants in the troposphere acting as a "detergent", as it reacts with many pollutants. The ability to detect OH by laser-induced fluorescence (LIF) has led to the study of a number of molecules that liberate the OH radical on photolysis. This capacity of the system to produce a well known chain carrier such as OH may be a key to understanding the initial stages of the decomposition of energetic materials in condensed phases. The relative complexities of small nitro compounds, which have several different dissociation pathways at the energies of ultraviolet photons, make their photodissociation dynamics particularly interesting. The dynamical information on the photodissociation process can be obtained by measuring the energy disposal in the photo fragmentation process and the nature of the dissociative state potential energy surface can be deduced. With a powerful support from the advanced theoretical methods, the experimental studies on photodissociation dynamics of polyatomic molecules employing various selective and sensitive techniques have been pursued extensively in the past several decades. Due to its importance in explosive, atmospheric and combustion chemistry, the photochemistry and photodissociation dynamics of nitro compounds have been extensively investigated by many researchers.

Our group has carried out a detailed study on photodissociation dynamics of aliphatic and aromatic nitro compounds by employing LP-LIF technique[130-132]. In

extension to that work, we have carried out the studies on halogenated aromatic nitro compound and cyclic nitroalkane. In our earlier work, it was observed that on UV absorption, among o-, m- and p-nitrotoluenes, only o-nitrotoluene produces OH moiety, while in aliphatic nitro compounds those, which are having methyl group adjacent to the nitro group, produce OH fragments. In the present work, we have selected two interesting molecules, 2-Chloro-6-nitrotoluene (ClNT) an o-nitrotoluene with Cl group adjacent to methyl group, and nitrocyclopentane (NCP) a cyclic nitroalkane. As NCP is not having any methyl group adjacent to nitro group it will be interesting to see whether it will produce OH on UV photodissociation. The photodissociation dynamics studies on ClNT, at 193, 248 and 266 nm, and NCP at 193 nm, were carried out under collision-free condition and the OH radicals observed using LIF technique. A dissociation mechanism was proposed by the assistance from the theoretical calculations.

5.2   EXPERIMENTAL SECTION

The experiments were carried out in a flow reactor, at a typical parent pressure of 20 mTorr, employing laser photolysis-laser induced fluorescence (LP-LIF) pump and probe technique. The set-up is described in details, in Chapter 2, Section 2.3. The 2-chloro-6-nitrotoluene being solid compounds, a special experimental arrangement was devised to flow its vapour through the reaction chamber, as shown in FIG. 2.5, Chapter 2. After loading the sample, the sample holder along with the reaction chamber was degassed thoroughly by an oil diffusion pump, which is backed with a rotary pump. The ClNT vapor pressures in the chamber were maintained at ~20 mTorr, which were measured with the help of a capacitance manometer. The solid ClNT supplied by Aldrich, with 99% purity was used after degassing without further purification. The 99% pure nitrocyclopentane sample was obtained from Aldrich, and

used without further purification, but after 4-5 freeze-pump-thaw cycles. Low pressure (20-40 mTorr) of the sample was maintained in a flow cell, and was measured by a capacitance gauge.

The experimental set-up for measuring time-resolved UV-vis emission consisted of a Bausch & Lomb monochromator, a PMT (Hamamatsu model R928), and a digital oscilloscope (Tektronics). The sample was allowed to flow in a stainless steel cell, equipped with four perpendicular MgF_2 windows, at a pressure of 20-200 mTorr, monitored by a capacitance gauge. Suitable cut-off filters were used, during the measurement of the emission, which is at wavelengths greater than 350 nm.

5.3   RESULTS AND ANALYSIS

The OH radical was observed on photolysis of ClNT at 193, 248 and 266 nm and NCP at 193 nm only. The FIG. 5.1 shows the fluorescence excitation spectra of the (0, 0) band of the $A^2\Sigma^+ - X^2\Pi$ system of OH, formed on photolysis of ClNT at 193 nm. The excitation spectra observed on photolysis at 193 nm are quite similar to that at 248 and 266 nm, and hence not shown. A similar spectrum is recorded for NCP at 193 nm, where OH is formed in both the vibrationally ground state, $v''= 0$, and the excited state, $v''= 1$. The FIG. 5.2 shows the fluorescence excitation spectra of the (1, 1) band of the $A^2\Sigma^+ - X^2\Pi$ system of OH, formed on photolysis of NCP at 193 nm.
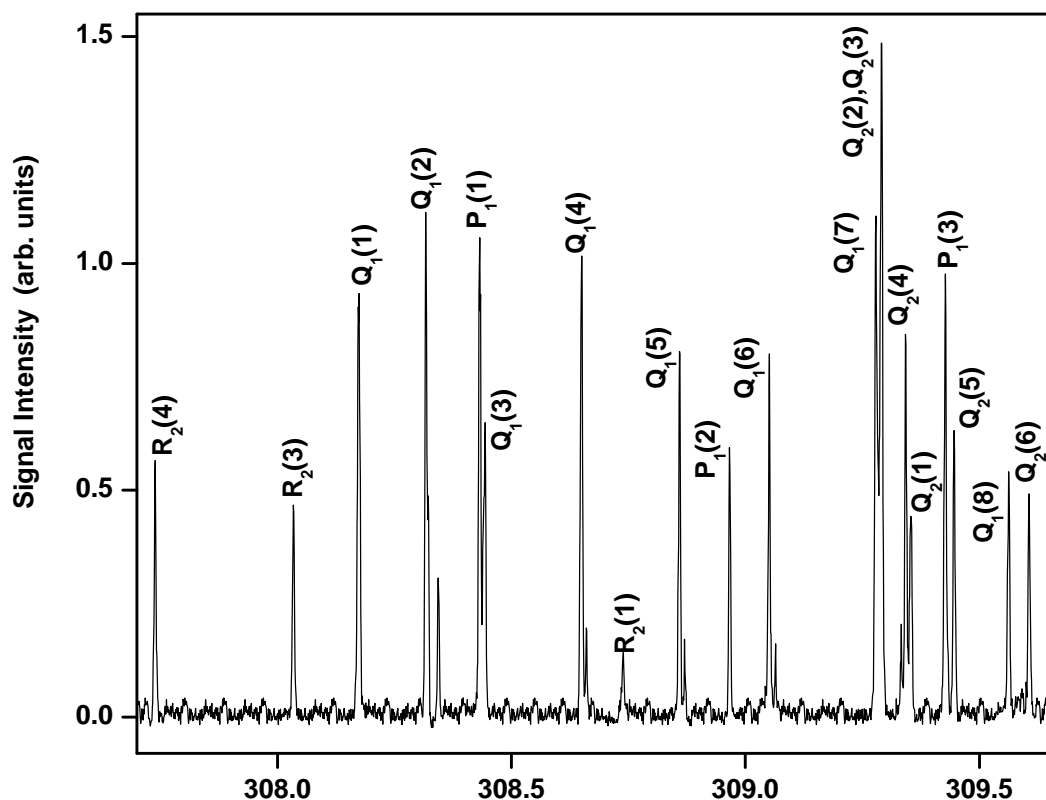
FIG. 5.1: The fluorescence excitation spectra of the (0,0) band of the $A^2\Sigma^+$–$X^2\Pi$ system of OH formed on photolysis of ClNT at 193 nm.

The standard nomenclature is used for designating the observed transitions. The subscripts 1 and 2 represent the transitions $\Sigma_{J=N+1/2} \leftarrow \Pi_{J=N+1/2}$ and $\Sigma_{J=N-1/2} \leftarrow \Pi_{J=N-1/2}$, respectively, whereas the subscripts 21 and 12 represent the transitions $\Sigma_{J=N-1/2} \leftarrow \Pi_{J=N+1/2}$ and $\Sigma_{J=N+\square/2} \leftarrow \Pi_{J=N-1/2}$, respectively. According to the parity selection rule ($+ \leftrightarrow -$), the Q branch arises from the Π^- (A″) state, while the P and R branches originate from the Π^+ (A′) state. The individual lines are broadened due to Doppler effect but are still well separated so that each individual line profile could be fitted by a Gaussian function. The relative populations of the OH fragment were determined by normalizing the respective peak areas of the rotational lines with respect to the pump and probe laser intensities, the pressure change (in case of NCP only, as ClNT is solid compound), if any, and the respective Einstein absorption coefficients[88]. Spin-orbit

and the Λ-doublet ratios were calculated from the relative populations of the different states. The translational energy associated with the OH fragment was calculated from the Doppler profiles of the rotational lines. The detailed results are presented below.
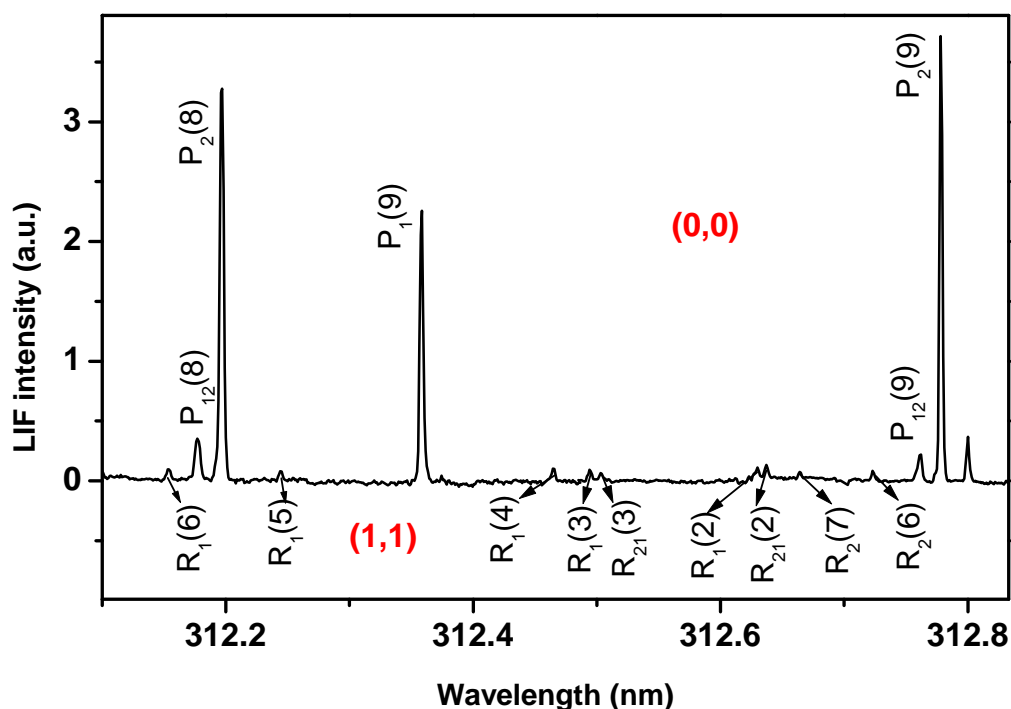
FIG. 5.2: The fluorescence excitation spectra of the (1,1) band of the $A^2\Sigma^+–X^2\Pi$ system of OH formed on photolysis of NCP at 193 nm.

5.3.1 ROTATIONAL AND VIBRATIONAL ENERGY DISTRIBUTIONS

The nascent rotational state population of OH radicals, generated on photodissociation of ClNT at 193, 248 and 266 nm and NCP at 193 nm, is used to construct a Boltzmann plot for obtaining the rotational temperature of nascent OH fragments. Typical Boltzmann plots based on this normalized population distribution are shown in FIG. 5.3 for $v''=0$ states of OH at 193, 248 and 266 nm wavelength for ClNT, while FIG. 5.4 (b) shows the Boltzmann plots for $v''=0$ and $v''=1$ states of OH at 193 nm for NCP. As shown in the FIG. 5.3, the Boltzmann plots for P and Q lines at 193 and 266 nm are having different rotational excitation, while at 248 nm P and Q lines are having comparable rotational excitation. The corresponding rotational

temperatures for P and Q lines at 193, 248 and 266 nm are 1000±60 K and 750±50 K, 700±50 K and 600±40 K and 1200±80 K and 650±50 K, respectively. This disparity arises mainly due to (1) preferential population of $\Lambda(A')$ state, which is probed by P lines, and (2) more pronounced effect of Λ splitting at higher N (rotational quantum number). Hence, the average rotational energy of OH, E_R, in ClNT at all the three excitation wavelengths is estimated after weighted summing over the different rotational quantum number, in the ($v''=0$) vibrational state. The resulting rotational energies are ~1.73, ~1.29 and ~1.83 kcal/mol at 193, 248 and 266 nm, respectively.

In case of NCP, the OH fragment is formed in both $v''=0$ and $v''=1$ vibrational states. The population distribution of OH fragments in ($v''=0$) and ($v''=1$) level are characterized by rotational temperature of 1570±90 K and 650±180 K, respectively. By weighted summing up all the rotational populations in the $v''=1$ and $v''=0$ vibrational states, the ratio of the populations of the two vibrational states can be estimated.
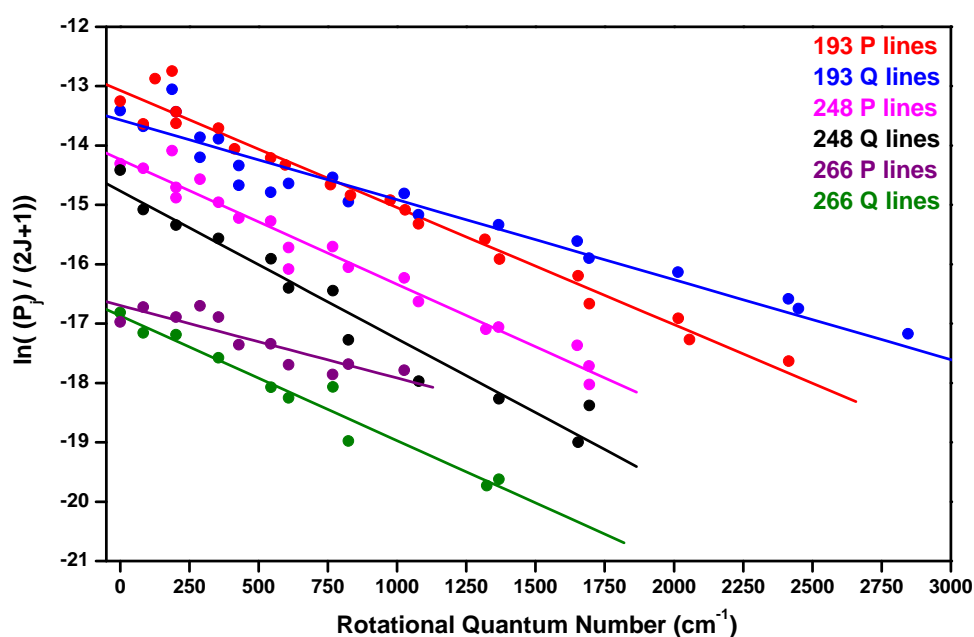
FIG. 5.3: Typical Boltzmann plots of the distribution of rotational energy in the nascent OH from photolysis of ClNT 193, 248 nm, 266 nm in $v''=0$ vibrational level.
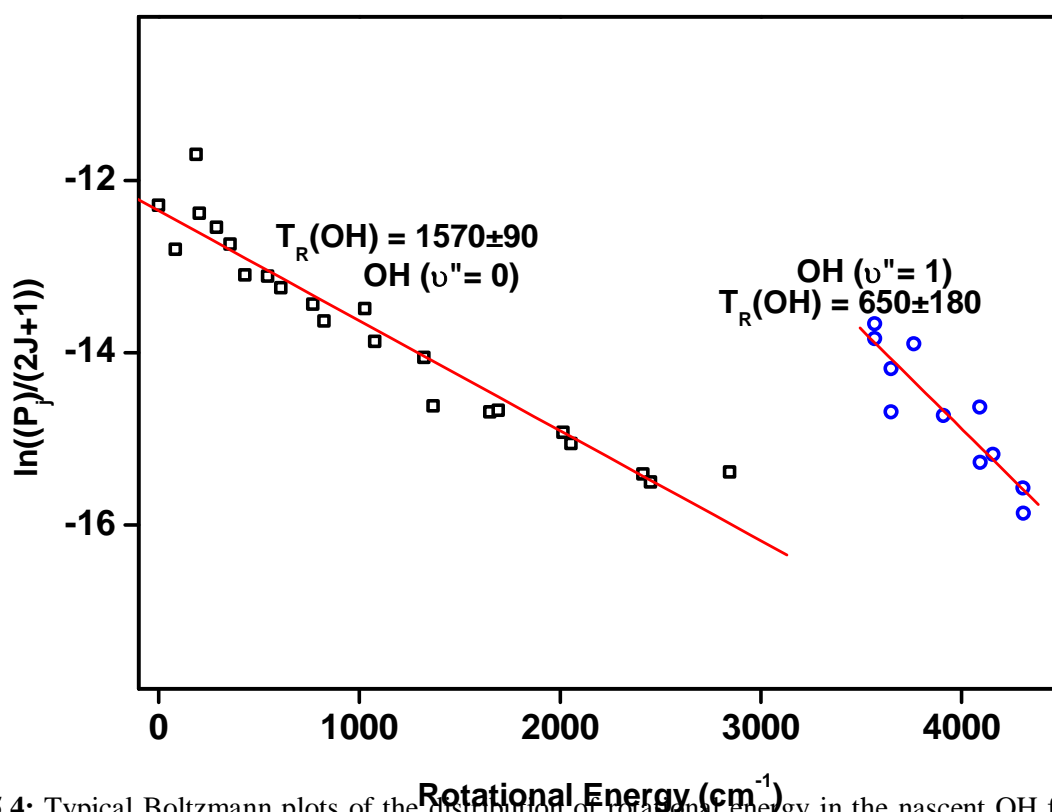
FIG. 5.4: Typical Boltzmann plots of the distribution of rotational energy in the nascent OH from photolysis of NCP in (a) in $v''=0$ vibrational level, and (b) in $v''=1$ vibrational level.

In the present experiments, populations in a few rotational states could not be determined very accurately due to overlapping signals. Within this experimental limitation, the average ratio of population in $v''=1$ to that in $v''=0$ vibrational state was estimated to be 0.12 ± 0.03 from three different sets of rotational spectra. In view of the small fraction of $v''=1$ state, the presence of higher vibrational states are expected to be negligible. From this ratio, the mean vibrational energy of OH fragments is calculated to be 4.9 ± 1.4 kcal/mol. Considering the rotational excitation in both the ground and the first vibrational states, the rotational energy of the OH fragment is 3.5 ± 1.3 kcal/mol. Thus, the total internal energy of the OH fragment is 8.4 ± 1.9 kcal /mol.

5.3.2   TRANSLATIONAL ENERGY OF THE FRAGMENTS

From the OH Doppler profiles, the average kinetic energy of the OH radical in the laboratory frame, $E_T(OH)$, can be determined. All the rotational lines measured were found to have similar line widths, within the range of the experimental error. More than 45 rotational line profiles for each photolysis wavelengths for ClNT and NCP are evaluated to estimate the average kinetic energy of the OH fragment in the laboratory frame, $E_T(OH)$. The Doppler profiles of the rotational lines were corrected for the probe laser line width. The average translational energy in OH, $E_T(OH)$, is given by the Eqn. 2.11 (Chapter 2). In the present case, the Doppler profile is a Gaussian function, as depicted in FIG. 5.5(a) and 5.5(b) for the $P_1(5)$ line for ClNT and NCP respectively, which implies that the translational energy follows the Maxwell-Boltzmann distribution. The width and the shape of the Doppler-broadened LIF line include contributions from the fragment molecular velocity, the thermal motion of the parent molecule and the finite probe laser line width. Thus, the actual Doppler width is calculated using a deconvolution procedure using the width (FWHM) of the laser spectral profile of the probe laser beam, which is obtained from the OH Doppler profile measured in a thermalized condition. The product translational energy in the laboratory frame $E_T^{lab}(OH)$ is obtained, and is found to be 7.2±1.1, 8.7±1.0 and 11.1±1.1 kcal/mol at 266, 248 and 193 nm excitation, respectively. In the case of NCP photodissociation at 193 nm, the similar analysis results in $E_T^{lab}(OH)$ of 19.6±3.3 kcal/mol.
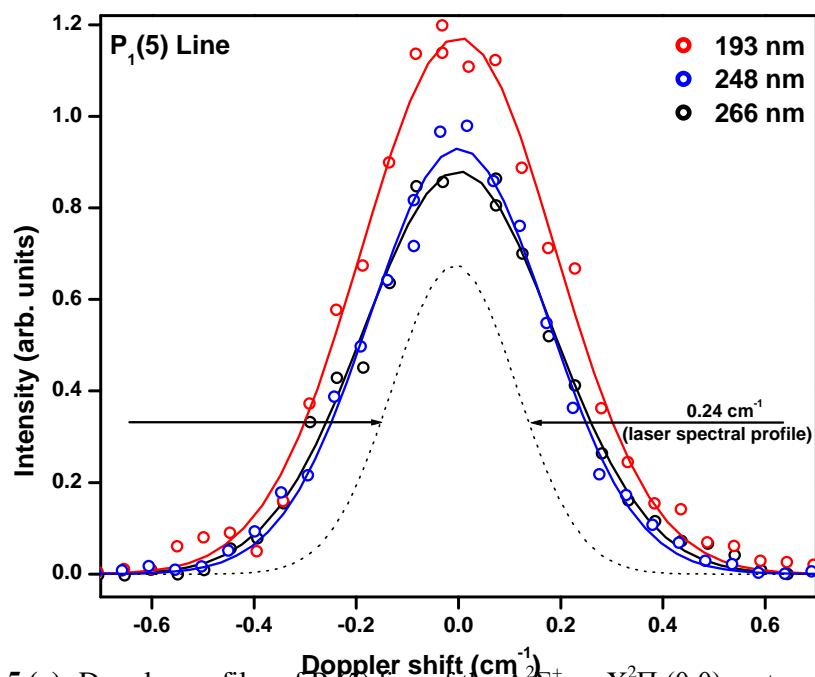
FIG. 5.5 (a): Doppler profiles of $P_1(5)$ line of the $A^2\Sigma^+ \leftarrow X^2\Pi$ (0,0) system of the OH radical produced in dissociation of ClNT at 193, 248 and 266 nm laser.
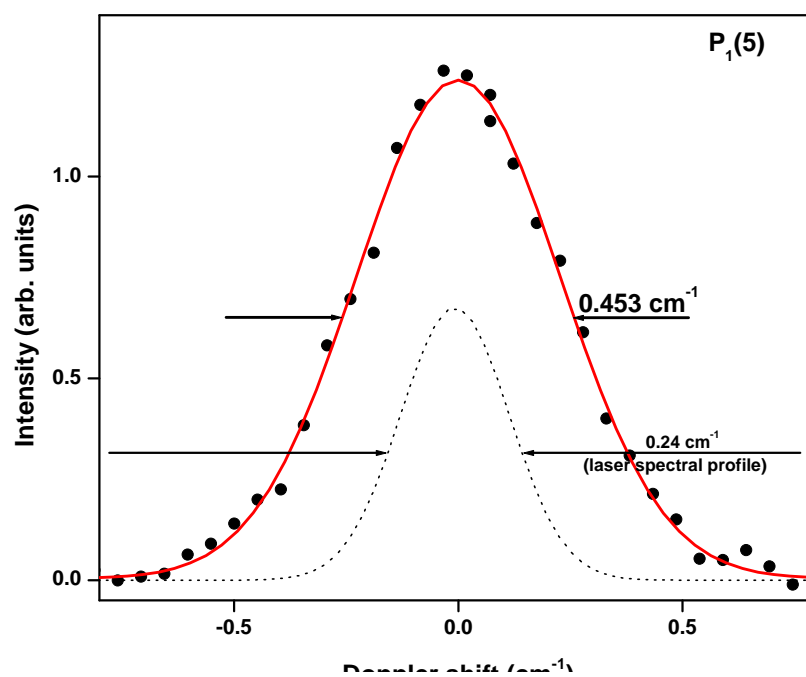
FIG. 5.5 (b): Doppler profile of $P_1(5)$ line of the $A^2\Sigma^+ \leftarrow X^2\Pi$ (0,0) system of the OH radical produced in dissociation of NCP at 193 nm laser.

5.3.3 SPIN-ORBIT STATE DISTRIBUTION

The ground electronic state of OH being $^2\Pi$, there are two spin-orbit components, $^2\Pi_{3/2}$ and $^2\Pi_{1/2}$. The LIF intensities of only $P_1(N)$ and $P_2(N)$ lines are

used to obtain the spin-orbit population, as they are well separated from satellite peak. FIG. 5.5(a) and (b) shows the spin-orbit ($\Pi_{3/2}/\Pi_{1/2}$) ratios multiplied by appropriate statistical weights (2J+1) plotted versus the OH rotational quantum number (N), at 266, 248 and 193 nm for ClNT and at 193 nm for NCP, respectively. From the figure, it is evident that for NCP at 193 nm and for ClNT, at all the photolysis wavelengths studied, the average ratio is more than one.

The relative population of spin-orbit states gives a clue in terms of coupling between the initially prepared excited states with a nearby dissociating state[114]. A statistical distribution suggests that the initially excited state probably does not interact directly with a triplet dissociating state; a non-statistical distribution, with preferential population of $^2\Pi_{3/2}$ state, indicates the role of a triplet state in the photodissociation process.
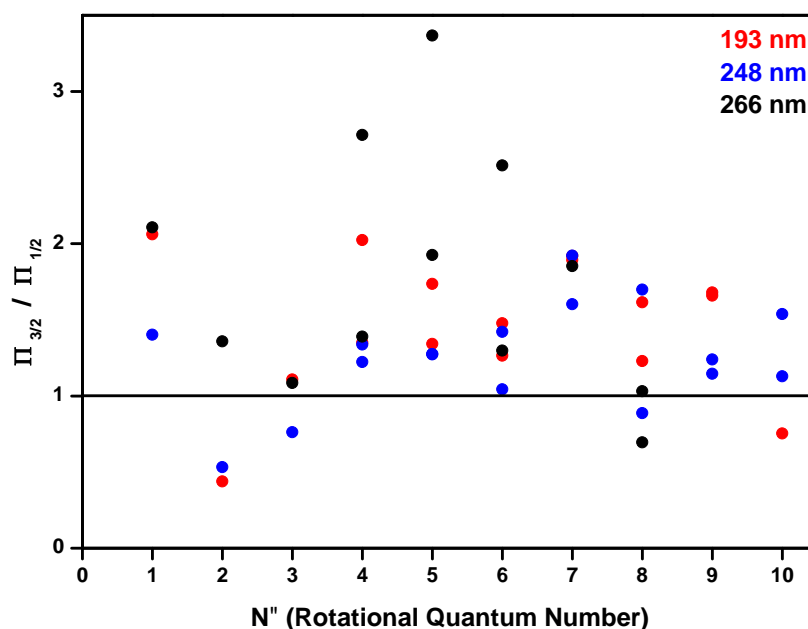
FIG. 5.6: (a) The statistically weighted spin-orbit ratios of nascent OH (v″=0) as a function of the rotational quantum number (N). The black, blue, and red circles denote the ratios at 266, 248 and 193 nm photolysis, respectively for ClNT.
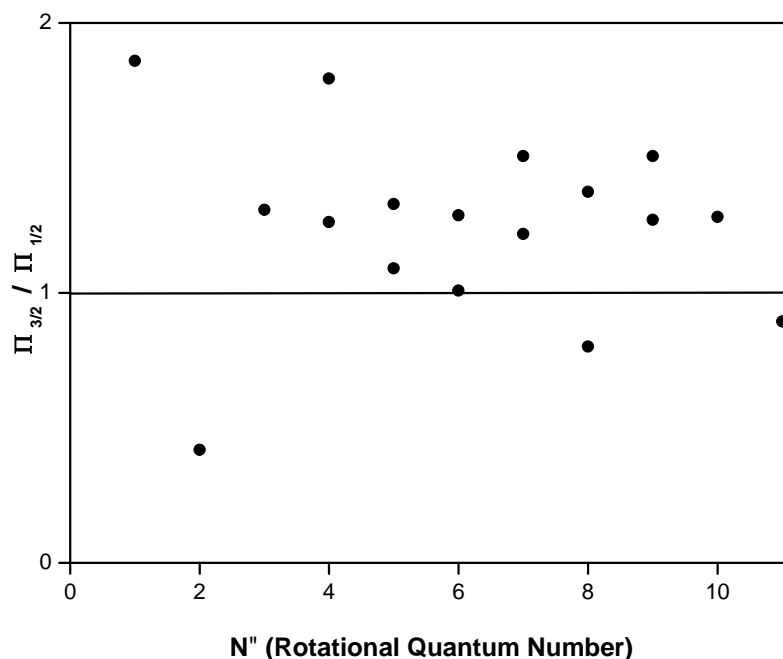
FIG. 5.6: (b) The statistically weighted spin-orbit ratios of nascent OH (v″=0) as a function of the rotational quantum number (N).The black filled circles for NCP.

5.3.4 POPULATION OF THE Λ-DOUBLETS

Each spin-orbit state of OH has two Λ-doublet components, denoted as Π^{+} (or A') and Π^{-} (or A"), depending on the orientation of the π-lobe of the unpaired electron on OH with respect to the plane of rotation. In the high J limit, in Π^{+} (A') state, the π lobe lies in the plane of rotation, while in Π^{-} (A") state, the π-lobe is perpendicular to the plane of rotation. The relative populations of the Λ-doublets provide information about the exit channel dynamics during the breaking of chemical bond. In FIG. 5.6(a) and (b), the Λ-doublet ratio is plotted against the rotational quantum number, N for ClNT and NCP, respectively. From both the figures it can be noticed that there is a clear preference for the Π^{+} (A') state. The Λ-doublet ratios Π^{-} (A")/ Π^{+} (A'), less than unity suggests that the pπ electronic orbital for the unpaired electron generated upon dissociation lies in the plane or it is parallel to the plane of rotation of OH, in the photolysis of both ClNT and NCP.
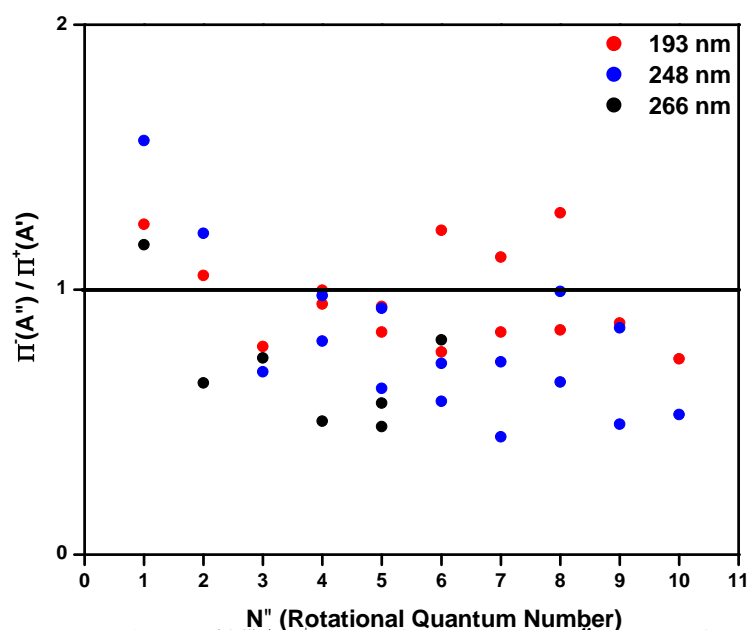
FIG. 5.7: (a) Λ-doublet ratio, Π^- (A")/ Π^+ (A'), of nascent OH(v"=0) as a function of the rotational quantum number (N). The black, blue and red filled circles denote the ratios at 266 248 and 193 nm photolysis, respectively, for ClNT.
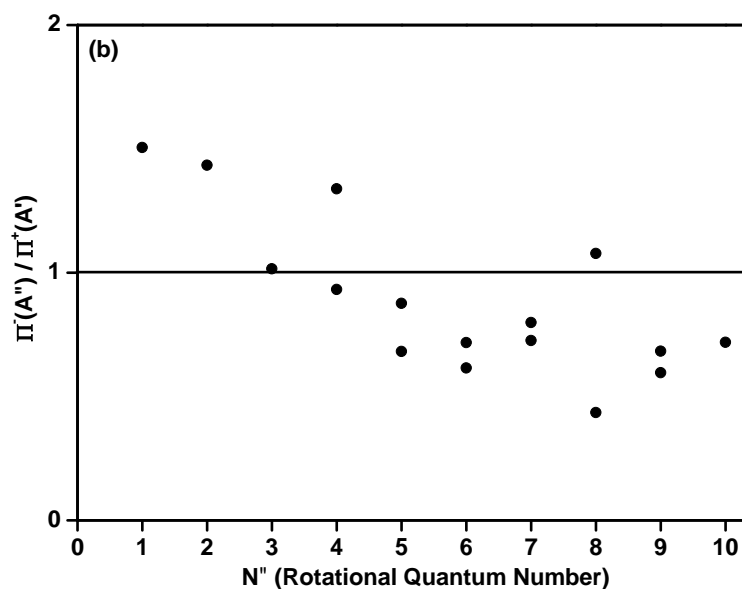
FIG. 5.7: (b) Λ-doublet ratio, Π^- (A")/ Π^+ (A'), of nascent OH(v"=0) as a function of the rotational quantum number (N). The black filled circles for NCP at 193 nm.

5.3.5 EMISSION STUDIES

In nitro-compounds cleavage of the C−N bond on photodissociation results in formation of electronically excited NO_2 as a primary photoproduct, which gives a prompt emission. We have observed a strong UV fluorescence from o-Nitrotoluene[130],

but we were unable to measure any emission from ClNT. Therefore, we can mention that the presence of Cl atom enhances the non-radiative processes in ClNT. However, we could measure an emission from photolysis of NCP at 193 nm, shown in FIG. 5.7(a). The emission spectrum, with maximum around 540 nm is attributed to the excited NO_2 photoproduct. At higher laser intensities, an intense emission band at 310 nm, due to excited OH product, is also observed.
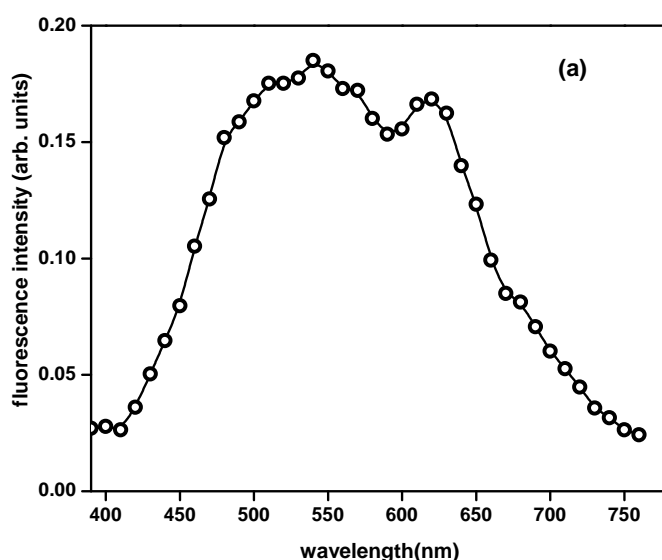
FIG. 5.8: (a) Fluorescence spectra recorded 200 ns after the photolysis of NCP.
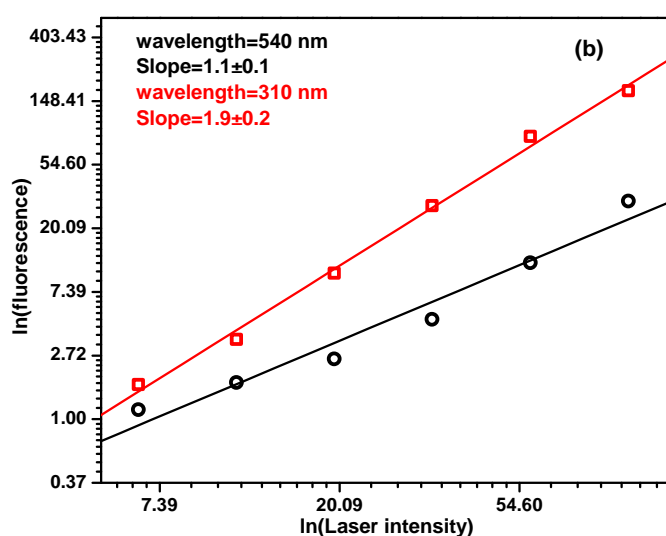
FIG. 5.8: (b) Variation of emission signal at 540 (black) and 310 (red) nm with intensity of the photolyzing laser (193 nm).

A log-log plot of emission signal intensity at 540 and 310 nm with pump laser intensity is shown in FIG. 5.7(b). The slopes of these plots are 1.1±0.1 at 540 nm and

1.9±0.2 at 310 nm, indicating that the origin of the emission at 540 nm is from a monophotonic process, while at 310 nm is due to biphotonic process.

5.3.6 THEORETICAL CALCULATION ON GROUND STATE DISSOCIATION OF ClNT AND NCP

Molecular orbital (MO) calculations were carried out to generate the relative potential energy diagram for the dissociation channels of ClNT and NCP on its ground state. We optimized geometries of various molecules at B3LYP level using 6-31+G* basis set. The relative energy is then calculated at the MP2 level using 6-311++G** basis set, using Gaussian[86] suite of program. All the stationary points were calculated on the ground state, for various dissociation channels. We did not try to locate various transition states involved on the PES. Hence, we report here only the relative energetics for various channels occurring on the ground PES of ClNT and NCP. Vibrational frequencies are calculated with the final optimized geometries.

5.4   DISCUSSION

5.4.1   NATURE OF EXCITED STATES

The gas phase UV absorption spectra of ClNT and NCP are depicted in FIG. 5.7(a) and (b). The UV-vis absorption of ClNT consists of two bands; one strong band with λ_{max} around 195 nm, while the other weak band around 250 nm. Comparing these spectra with the absorption spectra measured for o-nitrotoluene[133] we can assign the strong band to the $\pi \rightarrow \pi^*$ transition and the weaker one to the $n \rightarrow \pi^*$ excitation of a nonbonding electron of O[134]. The detailed study by Abbott et al.[135] and theoretical calculations by Lin et al.[136] attribute the absorption band at 193 nm to a mixture of S_7 and S_8 states and the band around 248 nm to the S_4 state. The UV-vis absorption spectra measured for NCP is similar to that of UV absorption spectra for

nitromethane[137,138] consisting of a strong $\pi \rightarrow \pi^*$ transition with λ_{max} around 200 nm and in agreement with the UV-visible absorption in nitroalkanes, with peaks around 200 nm (strong) and 280 nm (weak) due to $\pi^* \leftarrow \pi$ and $\pi^* \leftarrow n$ transitions, respectively, localized on the NO_2 chromophore[139]. In another work[140], the weaker band at 280 nm was assigned to the $\pi^* \leftarrow \sigma_{C-NO2}$ instead of $\pi^* \leftarrow n$ transition. Also for nitromethane[138] a weak band around 270 nm is also assigned to $\pi \rightarrow \pi^*$ transition.
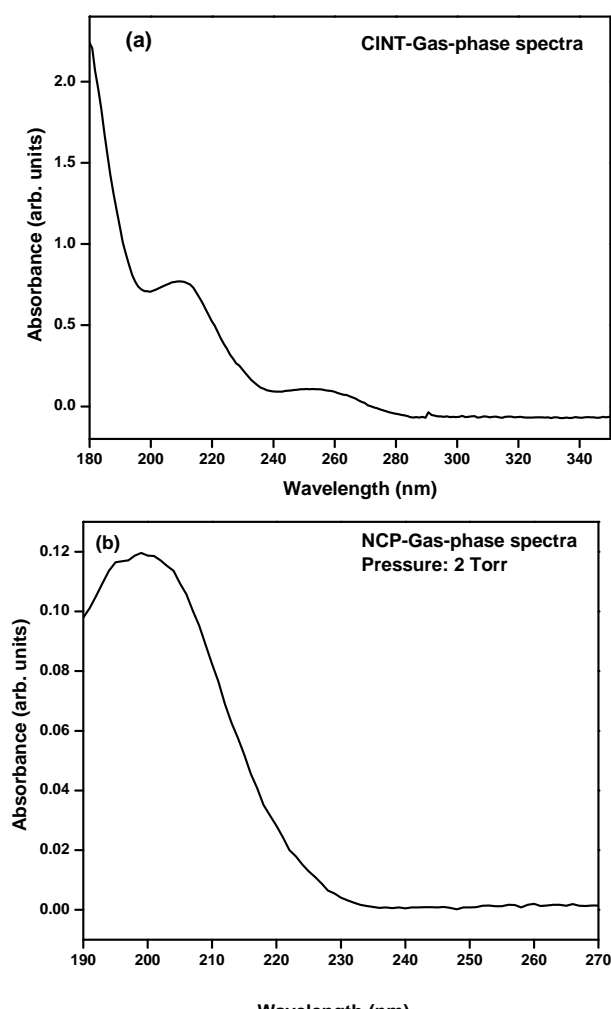
FIG. 5.9: The measured UV absorption spectra for (a) ClNT and (b) NCP in gas phase.

To understand the nature of the transitions involved in ClNT at 266, 248 and 193 nm, and NCP at 193 nm, *ab initio* molecular orbital (MO) calculations were performed, in detail. We optimized the ground state geometries of ClNT and NCP employing density functional theory (DFT) calculation, using cc-pVDZ set of basis

sets. Although the calculated vertical transition energies slightly differ as compared to the experimental results, the nature of transitions and that of the orbitals involved are accurately predicted, using this method. The orbitals participating in the different electronic transitions were visualized, for better understanding of the process. The vertical excitation energies and the respective oscillator strengths of several low-lying singlet states of ClNT and NCP are shown in Table 5.1.

The emission spectra obtained on photoexcitation of NCP at 193 nm is similar to the spectra obtained for previously studied nitroalkanes[131,132], with the maximum at around 540 nm. Similarity of spectra for aliphatic and cyclic nitroalkane indicates that there is not much intramolecular transfer of energy from the excited NO_2 group to the alkyl group in ring during the C−N bond dissociation. Therefore, we can suggest that for cyclic nitroalkane also the NO_2 moiety in the excited state is completely isolated and the molecule dissociates from the ground state after very fast radiationless cross over, through the conical intersections, and fast dissociation of the C−N bond, before randomization of the excitation energy.

Table 5.1: Vertical excitation energies (eV) and oscillator strengths (given in parentheses) of low-lying singlet states of ClNT and NCP with respective designation. The nature of transition and MO's involved in the transitions are also given.

ClNT 2-Chloro-6-nitrotoluene (C_s)				**NCP** Nitrocyclopentane (C_s)			
Excited State	Type of transition	Wavelength (nm)	VEE (eV) and Oscillator strength (in parenthesis)	Excited State	Type of transition	Wavelength (nm)	VEE (eV) and Oscillator strength (in parenthesis)
S_1	$\pi_{ring} \to \pi^*$ $n_O \to \pi^*$ $43 \to 45$	298.53	4.15 (0.0210)	S_1	$n \to \pi^*$ $31 \to 32$	273.75	4.53 (0.0002)
S_2	$\pi \to \pi^*$ $n_{Cl} \to \pi^*$ $44 \to 45$	275.79	4.49 (0.0176)	S_2	$\pi \to \pi^*$ $30 \to 32$	252.78	4.90 (0.0003)
S_3	$\pi_{NO} \to \pi^*$ $41 \to 45$	260.41	4.76 (0.0032)	S_3	$\pi \to \pi^*$ $28 \to 32$	171.48	7.23 (0.0089)
S_4	$\pi_{NO} \to \pi^*$ $42 \to 45$	234.22	5.29 (0.0514)	S_4	$\pi \to \pi^*$ $27 \to 32$ $25 \to 32$	165.96	7.47 (0.0441)
S_5	$\pi \to \pi^*_{ring}$ $43 \to 46$	219.20	5.66 (0.0273)	S_5	$\pi \to \pi^*$ $27 \to 32$	162.47	7.63 (0.0007)
S_6	$n_{Cl} \to \pi^*_{ring}$ $44 \to 46$	206.42	6.01 (0.0860)	S_6	$\pi \to \pi^*$ $26 \to 32$	161.21	7.69 (0.0008)
S_7	$n_{Cl} \to \pi^*$ $39 \to 45$	202.87	6.11 (0.0036)				
S_8	$n \to \pi^*$ $42 \to 47$	196.99	6.29 (0.0509)				
S_9	$n_{NO} \to \pi^*$ $40 \to 45$	192.74	6.43 (0.0902)				
S_{10}	$\pi \to \pi^*$ $n \to \pi^*$ $43 \to 45$	191.77	6.47 (0.1522)				

5.4.2 OH FORMATION CHANNEL

5.4.2.1 FROM ClNT

In the photoexcitation of ClNT at 266, 248, and 193 nm, several dissociation pathways have been proposed for obtaining OH product. However, ClNT does not contain OH moiety, it undergoes either migration of H atom followed by elimination of OH or elimination HONO to obtain OH product. The possible processes on photoexcitation of ClNT are given as follows:

(a) OH elimination after migration of H atom

$$\Delta H = 35.6 \text{ kcal/mol} \quad (5.1)$$

$$\Delta H = 51.6 \text{ kcal/mol} \quad (5.2)$$

$$\Delta H = 31.9 \text{ kcal/mol} \quad (5.3)$$

$$\Delta H = 55.3 \text{ kcal/mol} \quad (5.4)$$

(b) HONO channel

$$\Delta H = 90.9 \text{ kcal/mol} \quad (5.5)$$

$$HONO \longrightarrow OH + NO \quad \Delta H = 39.2 \text{ kcal/mol} \quad (5.6)$$
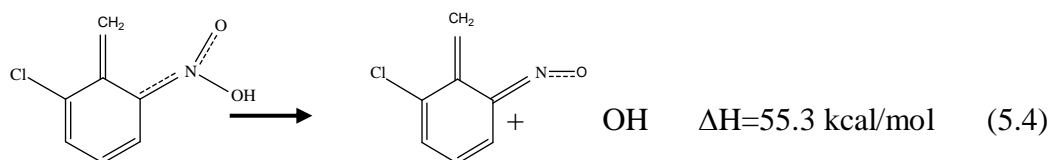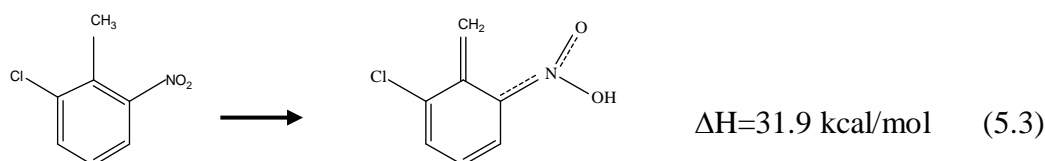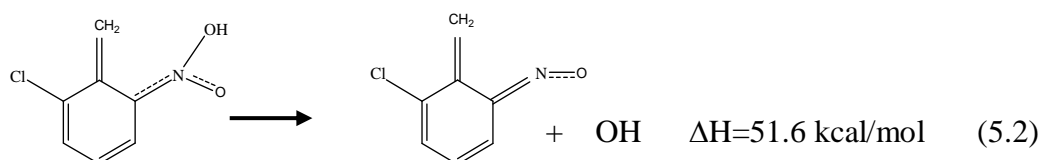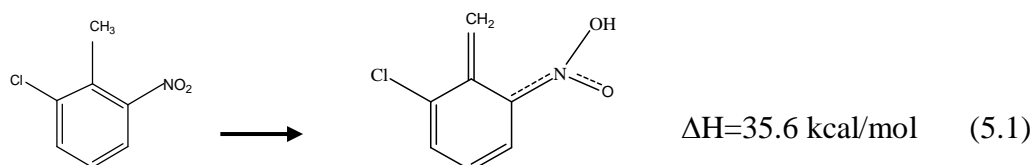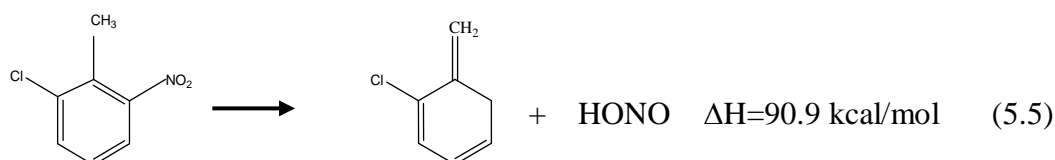
(c) NO_2 elimination channel

$$+ \quad NO_2 \quad \Delta H = 75.7 \text{ kcal/mol} \quad (5.7)$$
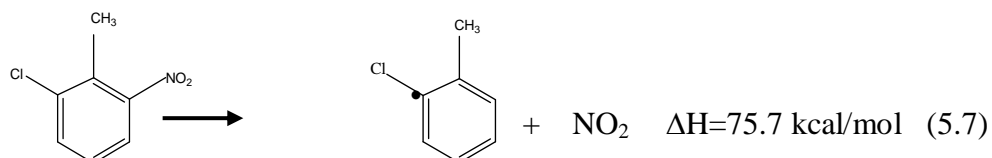
(d) Cl elimination and subsequent OH formation channel

$$+ \quad Cl \quad \Delta H = 100.4 \text{ kcal/mol} \quad (5.8)$$

$$\Delta H = 37.6 \text{ kcal/mol} \quad (5.9)$$

$$+ \quad OH \quad \Delta H = 79.8 \text{ kcal/mol} \quad (5.10)$$

$$\Delta H = 35.2 \text{ kcal/mol} \quad (5.11)$$

$$+ \quad OH \quad \Delta H = 82.2 \text{ kcal/mol} \quad (5.12)$$
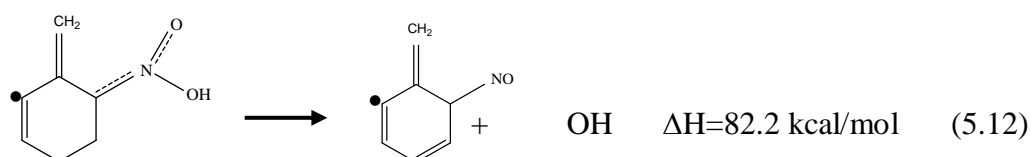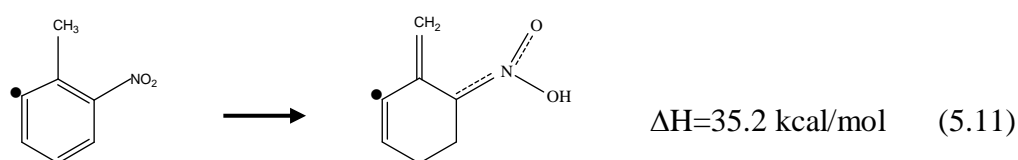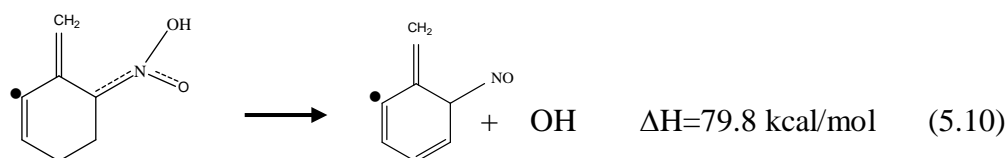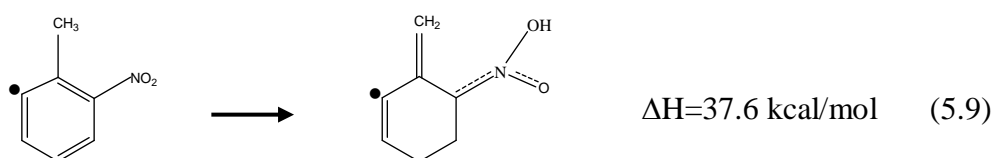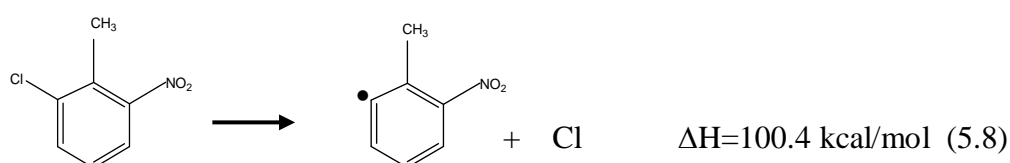
The available energy for ClNT at 266, 248 and 193 nm is 107.48, 115.29 and 148.14 kcal/mol, respectively. On energetic ground, it can be assumed that the most favoured lowest energy path is the sequence of reactions shown in scheme (a), which

is taking place via H atom migration and subsequent elimination of OH moiety. These are the only possible reaction for OH product formation at 248 and 266 nm. At 193 nm the other OH formation channel, by elimination of HONO molecule is also possible. The OH formation channel subsequent to elimination of Cl atom is ruled out based on energy grounds. The NO_2 formation is possible at all excitation wavelengths, but for ClNT we have not observed the any emission from NO_2 moiety.

5.4.2.2 FROM NCP

Although, the NCP molecule also does not contain OH moiety, on photoexcitation at 193 nm it dissociates and forms OH photoproduct. The possible channels for OH formation and NO_2 elimination are given below, along with our calculated energies:

$$+ \quad NO_2 \qquad \Delta H = 56.2 \text{ kcal/mol} \qquad (5.13)$$

$$\Delta H = 11.7 \text{ kcal/mol} \qquad (5.14)$$

$$+ \quad OH \quad \Delta H = 45.6 \text{ kcal/mol} \qquad (5.15)$$

$$+ \quad HONO \quad \Delta H = 65.6 \text{ kcal/mol} \qquad (5.16)$$

$$+ \quad HONO \quad \Delta H = 14.2 \text{ kcal/mol} \qquad (5.17)$$
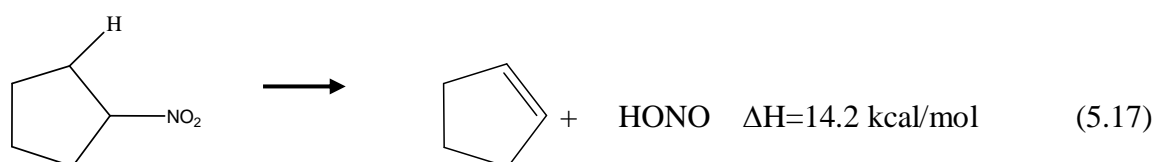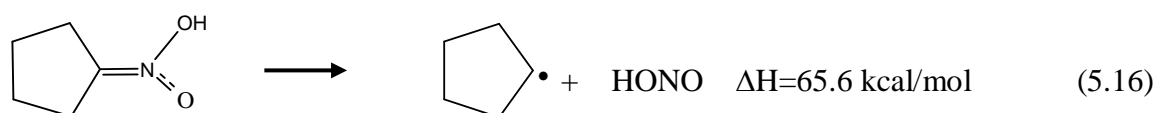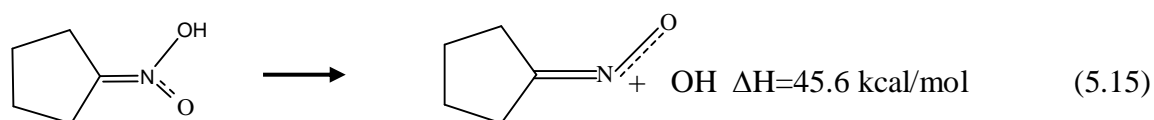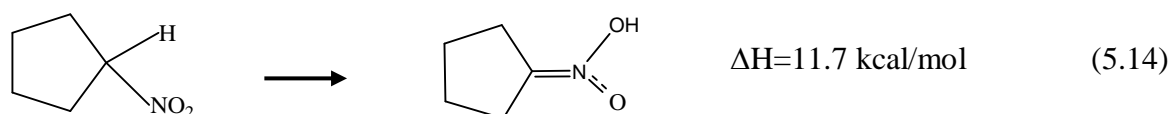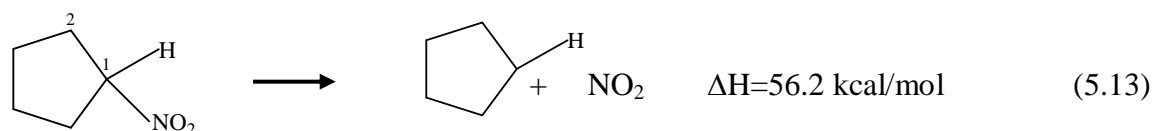
It is evident from the above reaction energetics that the lowest endothermic path for the OH product formation from NCP is through HONO, formed via reaction 5.17. In this reaction, the H-atom from carbon-2 migrates to the NO_2 group and then elimination of HONO takes place. As the H atom on carbon-1 is highly acidic in nature and the carbon-1 carries a negative charge, the migration of H atom from carbon-2 unlikely. This conclusion is supported by theoretical calculations, since we could not optimize the intermediate structure with H-atom migrated from carbon-2 to NO_2 group. The other low energy path for OH elimination is from the intermediate formed by migration of H-atom form carbon-1 to NO_2 group (reaction 5.14 and 5.15). In addition, the formation of HONO with H-atom migration from carbon-1 to NO_2 group and then OH elimination from HONO (reactions 5.16 and 5.6) are comparatively higher energy steps. Though this path is possible with amount of energy available with NCP at 193 nm excitation, it will not preferred after comparing its energy requirements with reactions 5.15 and 5.16.

5.4.3   PARTITIONING OF AVAILABLE ENERGY

The partitioning of the available energy in different degrees of freedom of the products formed upon excitation of ClNT at 266, 248 and 193 nm and NCP at 193 nm was measured by employing LIF. The energy available with molecules at 266, 248 and 193 nm is 107.48, 115.29 and 148.14 kcal/mol, respectively. The available energy, E_{avl}, is the energy remaining after the dissociation, and it is partitioned between photoproducts. This energy is partitioned among various degrees of freedom of the photofragments with

$$E_{avl} = E_{int}(OH) + E_{int}(cofragment) + E_T(OH + cofragment), \quad (5.1)$$

where E_{int} consists of both the rotational and vibrational excitations and E_T is energy partitioned in translational energy of photofragment. For ClNT the energy partitioned in rotational degree of freedom at 266, 248 and 193 nm is ~1.83, ~1.29, and ~1.73 kcal/mol, respectively. Here we did not find any vibrational excitation in the OH photoproduct. However, in previous work on o-nitrotoluene[18], the vibrational excitation was observed at 248 and 193 nm. The translational energy imparted into the OH fragments at 266, 248 and 193 nm is found to be 7.2±1.1, 8.7±1.0 and 11.1±1.1 kcal/mol, respectively. The energy imparted to the relative translation of the OH photoproduct increases with increase in energy pumped in the parent molecule. However, the difference in translational energy of OH produced on photodissociation at 266, 248 and 193 nm is only about 2-3 kcal/mol, though the difference in the photon energies is ~8 kcal/mol between 266 and 248 nm and ~33 kcal/mol between 248 and 193 nm. This could be due to the fact that OH is not formed by a direct dissociation step from one of the excited states of the molecule, and the mechanism of photodissociation involves stable or unstable intermediates. The f_T value calculated from experimental results for direct OH elimination channel for dissociation at 266, 248 and 193 nm is found to be 0.35, 0.31 and 0.18, respectively. The value calculated for this channel using impulsive and statistical model comes to be 0.49 and 0.16. Thus, the experimental value is between impulsive and statistical model estimation. The experimental f_T value for the OH product measured for path (b) involving HONO molecule elimination is estimated to be 0.62, this channel is feasible only at 193 nm excitation.

On photodissociation of NCP at 193 nm, OH is formed in both the vibrationally ground state, $v''=0$, and the excited state, $v''=1$. As discussed in section 5.3.1, the total internal energy of the OH fragment is 8.4±1.9 kcal/mol. The average

translational energy of OH from NCP is estimated from the Doppler profile to be 19.6±3.3kcal/mol. The f_T value calculated from experimental results for direct OH elimination channel is found to be 0.22. The value calculated for this channel using impulsive and statistical model comes to be 0.51 and 0.10.

5.4.4   MECHANISM OF THE DISSOCIATION PROCESS

We shall now present the complete picture of the dissociation process in the light of the above discussion in conjunction with the energy partitioning and the structure calculations performed with the help of *ab initio* method. In both ClNT and NCP there is no OH group present in molecule itself. The OH photofragment is formed either as a primary product from an intermediate isomeric structure or via secondary reaction through the primary, HONO product.

The present results of photodissociation of ClNT at 266, 248 and 193 nm show that the nascent OH fragments do not have an equilibrium distribution in the rotational levels as indicated by the difference in rotational temperatures calculated from Boltzmann's plots for P and Q lines (FIG.5.3 and 5.4). This can be attributed to formation of OH fragments by a single mechanism with non-equilibrium distribution in the rotational states. This is supported by Λ-doublet ratio in which we obtained a clear preference for Π^+ (A′) state, from which the P lines are originating. As orbital-rotational interaction is more pronounced at higher N, the splitting is more pronounced at higher N and this leads to higher temperature of preferred Λ-doublet state. The low internal energy distribution of OH from ClNT photolysis is very similar to that of some carboxylic acids[123] which may indicate the presence of a considerable barrier in the exit channels. The presence of an exit barrier is supported by the fact that the energy partitioned into translational degree of freedom is almost equal,

irrespective of excitation energy. Furthermore, the relative population of the Λ-doublet of OH provides the exit channel dynamics in the bond cleavage process. As the ratio, $\Pi(A'')/\Pi(A')$ is similar at all the three wavelengths studied, the exit channel dynamics of OH formation seems to be similar. In addition, for all the excitations there is a preference in population for the $\Pi_{3/2}$ spin-orbit state. Though the available energy with ClNT is different after dissociation at different wavelengths, the mechanism of OH formation is similar. Therefore, we can conclude that at all the above wavelengths either the same excited state is populated, which is unlikely as the difference in excitation energy is quite large, or all the excited states cross over to either the same excited dissociative state or the ground state and subsequently OH elimination takes place. As the OH formation proceeds via an intermediate, it is most likely to be taking place through the ground state of intermediate. From energy calculation for different OH formation paths, it can be deduced that the elimination of OH via intermediate formation is most probable.

For NCP, a significant amount of energy is partitioned into internal energy of the OH photofragment. Here, the OH fragment is formed in both vibrationally cold and hot states. On photodissociation of nitroalkanes[131] and halogenated nitroalkane[132] (2-bromo-2-nitropropane) studied in our laboratory and nitroalkanes[141] with β-H atom, the OH photofragment formation is favoured via HONO elimination step. However, in case of NCP from energetic calculations performed for different paths producing OH, the lowest endothermic step is elimination of OH from an intermediate. The Greenblatt et al.[142] have proposed a five-membered ring intermediate for direct elimination of the OH photofragment from nitroalkanes. Similarly, Zabarnick et al.[143] has proposed a direct OH elimination from the aci-form for nitromethane (NM). Therefore, we can compare the dissociation dynamics of NCP

with NM. The OH produced from NM[143] at 266 nm photodissociation is rotationally "hotter" similar to that of OH from NCP photodissociation. Thus, we can conclude that on photoexcitation of NCP at 193 nm, OH is formed from an aci-form.

A detailed excited state study for NO_2 elimination channel from NM was carried out by Wade et.al.[138]. They suggested that at 193 nm, nascent NO_2 product is formed in exclusive excited state ($\tilde{A}$ $^2B_2$) from NM, as dissociation does not occur on the ground electronic surface but rather on an excited electronic state that is either purely repulsive or predissociative. Similar analogy we can propose for NO_2 formation from NCP.

5.5 CONCLUSION

In summary, photodissociation of ClNT at 266, 248, and 193 nm and NCP at 193 nm generates OH radical as detected by Laser induced fluorescence spectroscopy. We measured the state distribution of the nascent OH(v', J'') product, and found that it is produced mostly in the vibrational ground state ($v''=0$) in ClNT at all the excitation wavelengths and in both ($v''=0$) and ($v''=1$) states in NCP at 193 nm. The rotational population of ClNT is characterized by rotational energies of ~1.73, ~1.29 and ~1.83 kcal/mol at 193, 248 and 266 nm, respectively. In case of NCP, the population distributions of the OH fragments in ($v''=0$) and ($v''=1$) levels are characterized by rotational temperature of 1570±90 K and 650±180 K, respectively. The spin-orbit components are not in equilibrium for NCP and at all the photolysis wavelengths for ClNT, the average ratio seems to be more than one. Also distribution in Λ-doublets has apprehensible preference for the Π^+ (A') state. The average translational energy partitioned into the OH photofragment for ClNT is found to be 7.2±1.1, 8.7±1.0 and 11.1±1.1 kcal/mol at 266, 248 and 193 nm

excitation, respectively, while for NCP it is found to be 19.6±3.3 kcal/mol. From experimental results for ClNT molecule we have deduced that although photoexcitation energies at 193, 248 and 266 nm are quite different, the mechanism of OH formation is similar. From the theoretical calculations of energetic of different paths of OH formation and feasibility of the reaction, it was concluded that the OH is formed as primary product via an intermediate. Similarly, in photodissociation of NCP at 193 nm, OH formation is attributed to elimination via an aci-form. The energy diagram of dissociation channel is shown in FIG. 5.10.
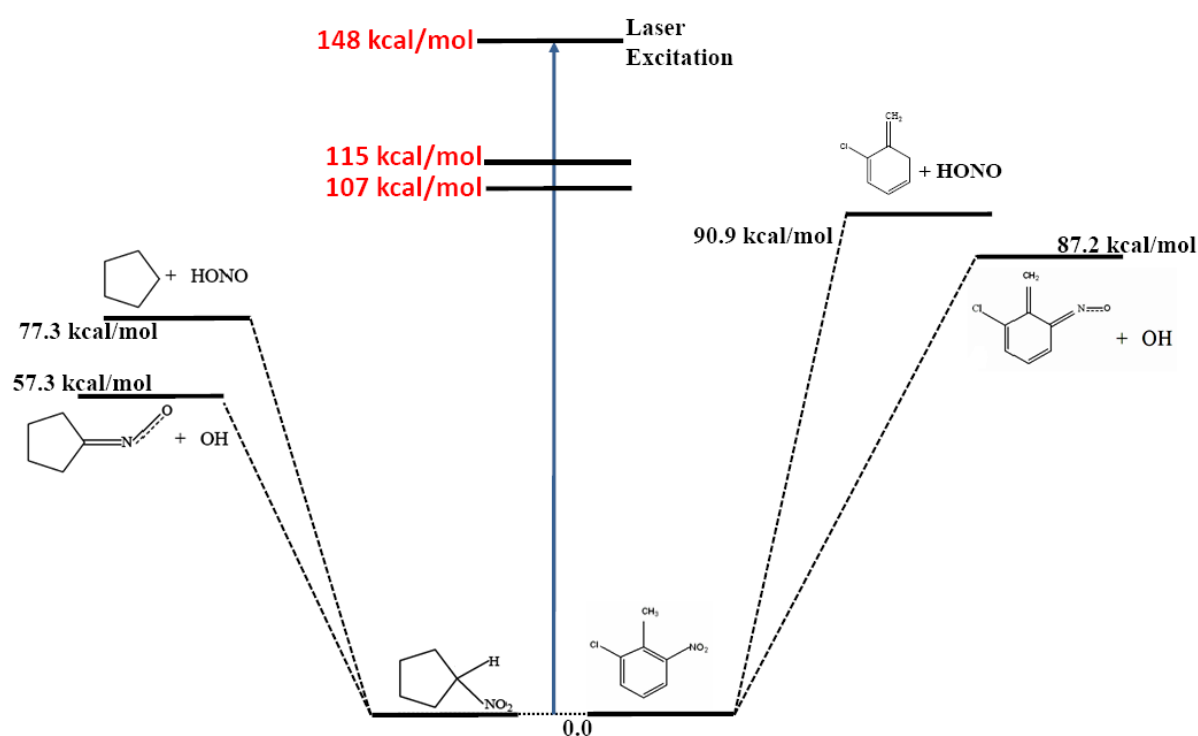
FIG. 5.10: The schematic energy diagram of OH fragment formation pathways on excitation of NCP at 193 nm and ClNT at 193, 248 and 266 nm. For both the molecules the direct OH elimination channel is lower energy channel than the formation of OH fragment via HONO molecule elimination.

CHAPTER 6

DISSOCIATION DYNAMICS OF FUMARYL

CHLORIDE: A REMPI TOF STUDY

6.1 INTRODUCTION

The α,β-unsaturated carbonyl compounds constitute interesting building

blocks for further conceptualizing of various reactions in organic chemistry and have

many important applications in the medical and biological fields[144]. The compounds

with two carbonyl groups (diketones) provide useful information for the study of

intramolecular energy transfer, and interactions involving remote carbonyl groups[145].

It is very interesting to study and identify the mechanism of these types of interactions

between the carbonyl groups. Besides these diketones, there is another class of

compounds, generally termed as α,β-enones, in which the carbon-carbon double bond

(–C=C–)is in conjugation with carbonyl group (–C=O) giving rise to altogether a

different and interesting photochemistry. The extensive research with both

experimental and theoretical approaches has been pursued for the study of

photodissociation dynamics of such type of compounds. The existence of close-lying

excited states and their interactions are mainly responsible for providing fascination to the researchers. These α,β-enones undergo a variety of photochemical rearrangements[115,146], and their photochemistry, in general, has attracted much attention in recent years. In earlier and recently carried out studies by our group, we investigated the dynamics of formation of the OH radical in photodissociation of few enones; such as acrylic acid [$H_2C=CHCOOH$][146], propiolic acid[97], enolic-acetylacetone [$CH_3C(O)CHC(OH)CH_3$][115], pyruvic acid [$CH_3COCOOH$][147] and 1,2-cyclohexanedione[148] (reported in this thesis) using laser photolysis-laser induced fluorescence (LP-LIF) technique. Numerous studies on the photodissociation of carbonyl chlorides are available in the literature; very few of these are focused on the photochemistry of fumaryl chloride ($COClCH=CHCOCl$), an enone with two acid chloride functional group. The UV photodissociation of the most elementary acid chlorides, acetyl chloride (CH_3COCl)[149], and propionyl chloride (CH_3CH_2COCl)[150], have been previously studied in both gas and solid phases. Acetyl chloride, on photodissociation at 236 nm, produces acetyl and chlorine radicals, while propionyl chloride, gives ketene ($H_2C=C=O$) and HCl, in addition to the corresponding radical channel. Photodissociation and isomerization processes of acryloyl chloride ($CH_2=CHCOCl$), an enone similar to fumaryl chloride, have been studied both experimentally[151,152] and theoretically[153]. Apart from the Cl atom formation channel, it photodissociates through two additional channels, one produces ketene and HCl (same as in propionyl chloride[150]), while the other channel involves a 1,3-sigmatropic rearrangement, producing 3-chloro-1,2-propenone ($H_2ClCCH=C=O$). Extensive UV photodissociation studies of oxalyl chloride, $(ClCO)_2$, a lower homologue of fumaryl chloride, have been carried out[154,155]. Suits and co-workers[154] investigated photodissociation dynamics of oxalyl chloride near 235 and at 193 nm, with a

photofragment imaging technique, using REMPI detection of Cl and CO moieties. They suggested that the photodissociation of $(ClCO)_2$ proceeds via an impulsive three-body mechanism yielding translationally hot spin-orbit excited Cl* and ground state Cl, together with translationally hot and rotationally excited CO, and a translationally cold ClCO. The primary product COCl undergoes subsequent dissociation to yield slow CO and Cl. They also measured the translational energy distribution and anisotropies of Cl, Cl*, and CO.

Fumaryl chloride, as shown in FIG. 6.1, is a planar molecule with three stable isomers, out of which two isomers, namely, trans-trans and cis-cis, belong to the C_{2h} point group and the third trans-cis isomer belongs to the C_s point group[156,157]. The relative abundances of these isomers are found to be 30%, 24%, and 46%, respectively, at 480 K[157]. A negligible effect of temperature on the relative abundance indicates only small energy differences among the isomers. The complete IR and Raman studies of liquid and crystal forms have identified two conformers as trans-trans and cis-trans[158]. It has a symmetric structure with both carbonyl groups associated with an identical functionality. The thermal decomposition of fumaryl chloride at 900°C gives rise to various products, such as $C_3O(C=C=C=O)$, HCl, and CO.[159] Besides, fumaryl chloride has many synthetic applications, mainly since it contains unsaturated carbon-carbon double bonds, which can be used for in situ cross-linking. Jabbari et al[160]. have suggested that it can be copolymerized with a poly (ε-caprolactone) for constructing a biocompatible, bioresorbable, injectable, and self-cross-linkable polymer for bone tissue engineering. Poly(ethylene glycol) fumarate, synthesized from fumaryl chloride and polyethylene glycol in the presence of propylene glycol, is used as a rigid coating for the superparamagnetic iron oxide nanoparticles, which are increasingly being evaluated for clinical applications such as

hyperthermia, drug delivery, magnetic resonance imaging, transfection, and cell/ protein separation[161]. Several ultrastructure cross-linked and functional polymer thin films, for potential nonlinear optical (NLO) application, or other applications requiring molecular orientation, are synthesized from fumaryl chloride and maleic anhydride[162].

Trans-Trans   Cis-Trans   Cis-Cis
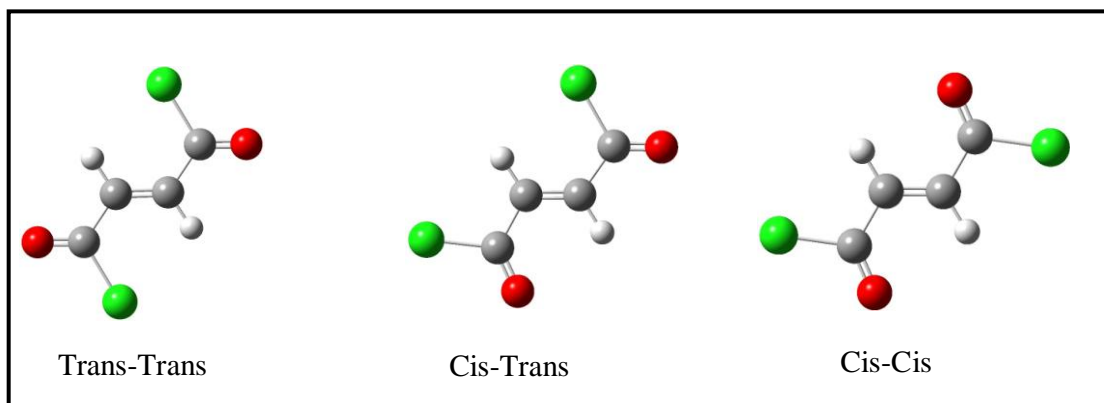
FIG 6.1: Optimized geometries for various isomers of fumaryl chloride.

The present study is undertaken to understand the photodissociation dynamics of fumaryl chloride (ClCO−CH=CH−COCl), a molecule with two C=O groups and a C=C group in conjugation, in a supersonic molecular beam at around 235 nm. The chlorine atom product in both the ground state ($^2P_{3/2}$) and the spin-orbit excited state ($^2P_{1/2}$) has been detected using the REMPI-TOF technique. We have also measured the translational energy distributions for both types of chlorine atoms and relative quantum yield of Cl*. To gain further insights, the anisotropy parameters (β_i) have also been measured.

6.2   EXPERIMENTAL SECTION

The experiment was performed using a molecular beam time-of-flight mass spectrometer system (MB-TOF-MS), as described before in Chapter 2, Section.2.3. Fumaryl chloride on photodissociation forms the Cl and Cl* atoms, which were probed, using 2+1 REMPI transitions in the region of 234-236 nm, as shown in

FIG.6.2 and Table 6.1. A typical REMPI scheme for the chlorine atom detection in two spin-orbit states (separated by 882 cm^{-1}) is shown in FIG. 2.6. The ionization limit for chlorine atom is 104591.0 cm^{-1}. This table gives the position and assignment for the various peaks observed and comparison with the literature values. The peaks at 42492.5 cm^{-1} and 42516.1 cm^{-1}, corresponding to 4p ^{2}D$_{3/2}$ ← 3p ^{2}P$_{3/2}$ and 4p ^{2}P$_{1/2}$ ← 3p ^{2}P$_{1/2}$ transitions, are selected for probing Cl and Cl*, respectively.
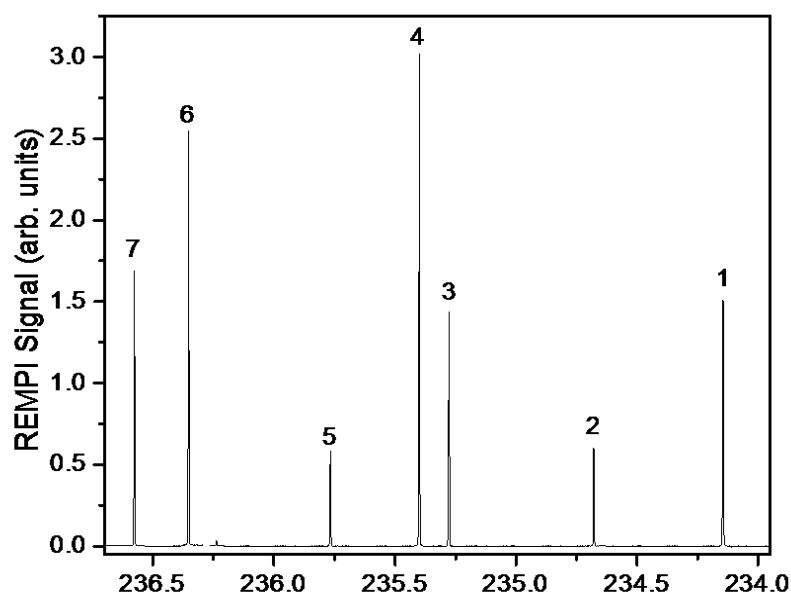
FIG. 6.2: Various REMPI lines for Chlorine atom formed during the photolysis of tetrachloroethylene.

Table 6.1. Comparison of experimental and literature REMPI lines for Cl.

Peak No	Experimental wavelength		Literature wavelength		Two photon Transition From 3p
	(cm^{-1})	Nm	(cm^{-1})	nm	
1	42707.4	234.15	42719.3	234.08	$4p\ ^2P_{3/2} \leftarrow 3p\ ^2P_{3/2}$
2	42610.4	234.68	42618.5	234.63	$4p\ ^2S_{1/2} \leftarrow 3p\ ^2P_{3/2}$
3	42501.8	235.28	42516.1	235.20	$4p\ ^2P_{1/2} \leftarrow 3p\ ^2P_{1/2}$
4	42479.8	235.40	42492.5	235.33	$4p\ ^2D_{3/2} \leftarrow 3p\ ^2P_{3/2}$
5	42412.7	235.77	42427.5	235.69	$4p\ ^4S_{3/2} \leftarrow 3p\ ^2P_{1/2}$
6	42308.6	236.35	42321.9	236.28	$4p\ ^2D_{5/2} \leftarrow 3p\ ^2P_{3/2}$
7	42268.3	236.58	42278.5	236.52	$4p\ ^2P_{3/2} \leftarrow 3p\ ^2P_{1/2}$

The fumaryl chloride sample is a clear to light yellow liquid with boiling point between 160-165°C and density of 1.412 g/dm^3. The sample of 95% purity was supplied by Aldrich and was used without further purification for the experiments. However, the sample was thoroughly degassed by several freeze-pump-thaw cycles.

The power dependence of the one-color REMPI signals for transitions corresponding to the selected Cl ($^2P_{3/2}$) line is shown FIG. 6.3. The signal is linear in a log-log plot over the range of powers used in the present study. For both the types of chlorine atoms, the lines exhibit a slope of $\sim$3.1$\pm$0.2, which is consistent with one-photon dissociation of fumaryl chloride, followed by (2+1) REMPI of the chlorine atoms, assuming that the ionization step is saturated. Apart from the power dependence studies, we also systematically monitored the shape and the width of TOF profiles of Cl atoms at various laser intensities. All the experiments were performed in the intensities, which are much lower than the intensity at which the shape and width of the TOF profiles were invariant. This experimental condition ensures that the

translational energy distributions and the anisotropy parameters are invariant over the

laser fluences used.
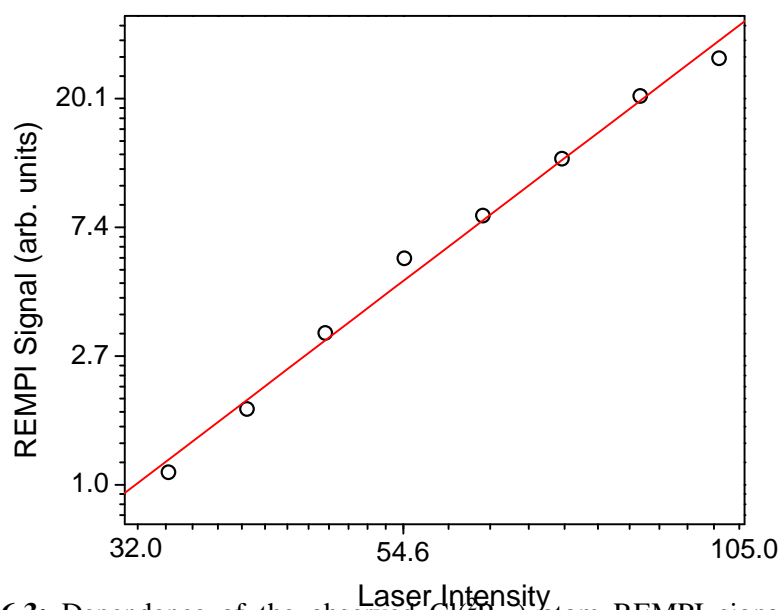
FIG. 6.3: Dependence of the observed $Cl(^2P_{3/2})$ atom REMPI signal from fumaryl chloride photolysis on the laser intensity. The slope of the fitted linear log–log plot is 3.1 ± 0.2.

6.3   RESULTS AND ANALYSIS

6.3.1   ANALYSIS

The TOF profiles of Cl and Cl* are measured at different laser polarizations.

The translational energy distribution and the anisotropy parameter for both Cl and Cl*

are determined from these TOF profiles, using a commonly used forward convolution

(FC) technique, as described in Chapter 2, Section 2.3.2. Using this method, the

parameters are adjusted until a satisfactory agreement with the experimental data is

achieved. Once the photofragment speed distributions have been determined, these

were used to obtain the corresponding translational energy distributions.

6.3.2 SPIN-ORBIT BRANCHING RATIO

The doppler profiles of Cl ($^2P_{3/2}$) and Cl* ($^2P_{1/2}$) atoms, produced in the dissociation of fumaryl chloride on excitation at 235 nm, which are wavelength scans in the region 235.336 and 235.205 nm, respectively, are shown in FIG. 6 4.
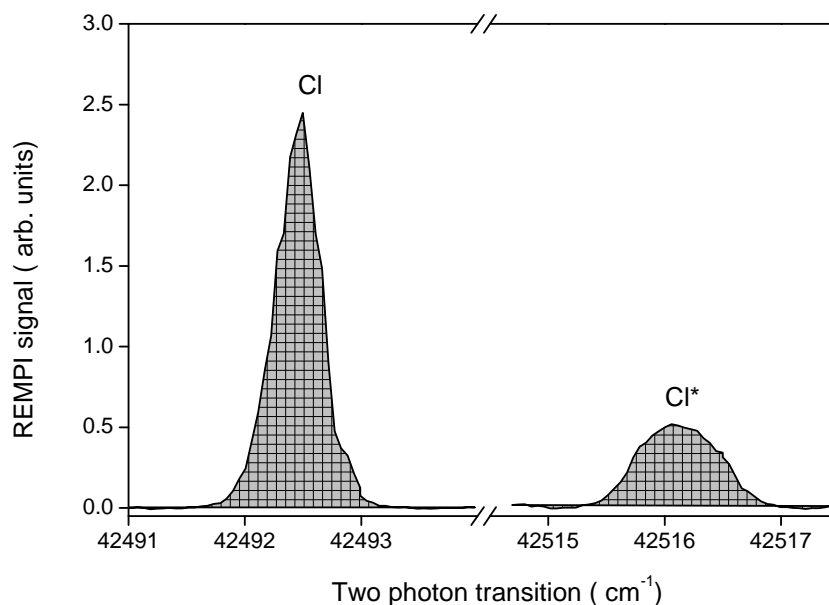
FIG. 6.4: Profiles of Cl and Cl* atoms produced in the 235 nm laser photolysis of fumaryl chloride used for the determination of their relative quantum yields.

The relative quantum yield of chlorine atom fragments in different spin-orbit states was determined by normalizing the integrated intensity, i.e., peak areas, S(Cl) or S(Cl*), of the respective (2+1) REMPI transitions with respect to the laser intensity, and the ratio of the two-photon absorption coefficients. The actual product ratio is proportional to the measured area of (2+1) REMPI lines, with a factor of k, which is the relative ionization probability for Cl and Cl*, f(Cl)/f(Cl*),

$$\frac{N(Cl^*)}{N(Cl)} = k\frac{S(Cl^*)}{S(Cl)} \tag{6.1}$$

where N(Cl) and N(Cl*) designate the number density of Cl and Cl* produced. S(Cl) and S(Cl*) are obtained by integrating the measured ion signal intensity over the proper range containing the Doppler width and the probe laser bandwidth. The measurements were repeated at different laser light intensities, giving similar relative

signal intensities. For fumaryl chloride photodissociation, the average ion integrated signal intensity ratio, S(Cl*)/ S(Cl), has been measured to be 0.39±0.06. From the measured integrated intensity ratio, one can easily obtain the product ratio, using Eqn. (6.1), by taking a value of 0.85±0.10 for k[163]. The relative quantum yields, Φ(Cl) and Φ(Cl*), can be determined from the product ratio, and Φ(Cl*) can be expressed as

$$\Phi(Cl^*) = \frac{N(Cl^*)}{N(Cl^*)+N(Cl)} \tag{6.2}$$

The value of Φ(Cl*) measured for fumaryl chloride dissociation is found to be 0.24±0.03. On statistical grounds one expects a quantum yield, Φ(Cl*) = 0.33. As described in the later section, the low quantum yield for the Cl* can be attributed to the fact that the C-Cl bond fission via the lowest-recoil-kinetic energy mechanism mainly produces Cl atoms in the Cl($^2P_{3/2}$) state; the same is true for the lowest-kinetic-energy C-Cl bond fission channel in photodissociation of many other alkyl chlorides.

6.3.3 TRANSLATIONAL ENERGY DISTRIBUTION AND ANISOTROPY PARAMETER

The TOF profiles of Cl and Cl* were measured using different polarization geometry. The background subtracted TOF spectra, recorded for the laser polarization parallel, at the magic angle ~54.78° and perpendicular to the detection axis, for the Cl and Cl* fragments are shown in FIG. 6.5. The measured Cl atom TOF profiles are analyzed, using a forward convolution procedure, as described in the earlier section, to determine the kinetic energy distribution and the average kinetic energy of the fragments in the fumaryl chloride photodissociation at ~235 nm. The TOF profiles for the Cl and Cl* atoms are converted to the velocity domain. Here, an initial photofragment speed distribution, g(v), and the anisotropy parameter β are assumed. As atomic $v{\cdot}j$ correlations are known to be very weak, we can safely assume the TOF profiles to be independent of the probe polarization.
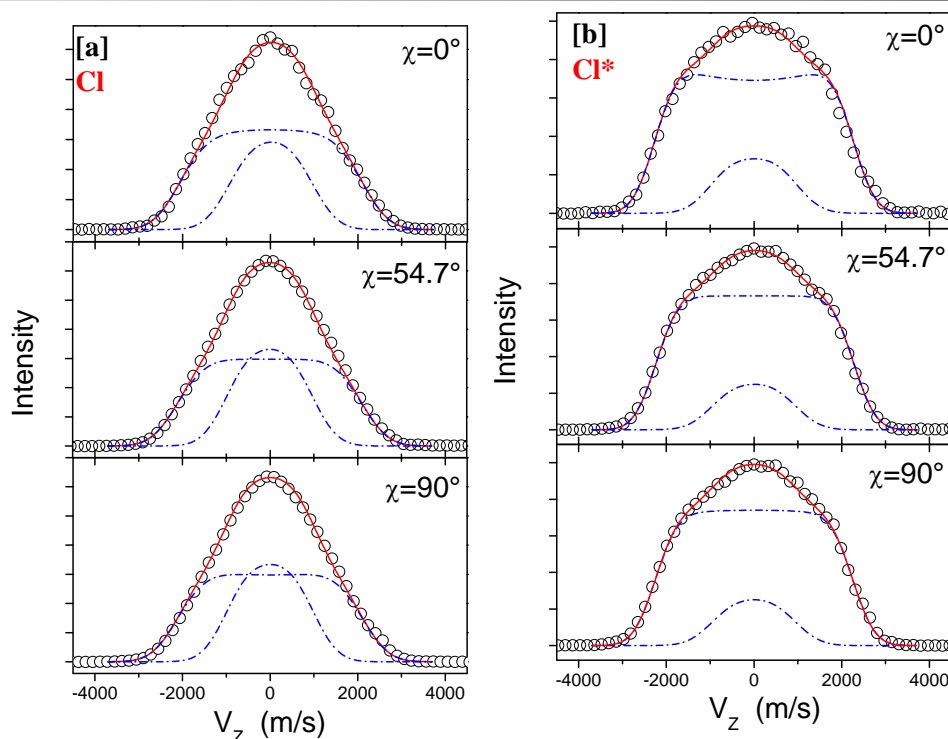
FIG.6.5: REMPI-TOF profiles of [a] Cl($^2P_{3/2}$) and [b] Cl($^2P_{1/2}$) produced from the 235 nm photodissociation of fumaryl chloride. The circles are the experimental data and the solid line is a forward convolution fit. Three panels, namely, upper, middle and lower panels correspond to horizontal, magic angle, vertical, experimental geometries, respectively.

The TOF profiles are calculated for the three experimental configurations, convoluted with the instrumental response function determined, as described in an earlier section, and are compared with the experimental results. The translational energy distributions, $P(E_T)$, determined from the data in FIG. 6.5 for the Cl and Cl*, are depicted in FIG. 6.6. Inspection of FIG. 6.6 reveals that the $P(E_T)$ consists of two components. For the Cl atom, the faster component, centered at ~14.4 kcal/mol, consists of 67±5% of the total fragments, while the slower component, centered at~2.7 kcal/mol, consists of the remaining 33±5%. Similarly, for Cl*, the faster component, centered at ~16.8 kcal/mol, consists of 87±5% of the total fragments while the slower component, centered at~2.4 kcal/mol, consists of the remaining 13±5%.
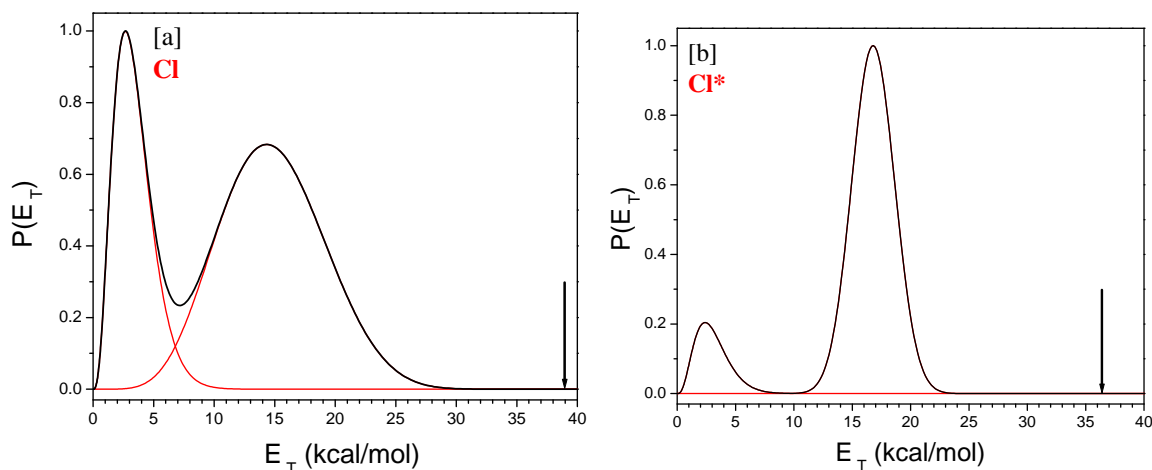
FIG.6.6: Centre-of-mass recoil translational energy distribution derived from FIG. 6.5 for [a] Cl ($^2P_{3/2}$) and [b] Cl*($^2P_{1/2}$) in the photodissociation of fumaryl chloride at 235 nm. The red lines indicate the speed distributions for the fast and slow component for chlorine atom formation channel, respectively; the solid line shows the sum. The vertical arrow indicates the maximum available energy for the respective chlorine, Cl ($^2P_{3/2}$) or Cl*($^2P_{1/2}$), elimination channel.

We have also measured the anisotropy parameter, β for the chlorine atom channel. However, it was not possible to determine independently the anisotropy parameter for the two components, and hence, the anisotropies were assumed to be identical for each channel. The TOF profiles for both Cl and Cl* are independent of laser polarizations, implying the β parameter is well characterized by a value of ~0.0, within the experimental uncertainties. The solid line displays the calculated TOF profiles, with each component shown by a red curve. The difference in the TOF profiles for Cl and Cl* in FIG. 6.6 arises mainly due to the different nature of f_T, their non-statistical branching ratio and the ratio of fast to slow component.

6.3.4 HCl FORMATION CHANNEL

The multiphoton ionization spectrum of fumaryl chloride at 235 nm clearly shows peaks at m/e 36 and 38, corresponding to H^{35}Cl and H^{37}Cl, respectively. To explore the origin of the HCl mass peak, the laser wavelength was scanned over its REMPI region in the range 236-237 nm[164,165]. In our experiments, we did find (2+1)

REMPI lines of HCl in the TOF spectra for the Q(J) branch of the $V^1\Sigma^+(0^+)$ $\leftarrow\leftarrow X^1\Sigma^+(0^+)(12,0)$ band system[164]. Although the signal was weak due to the predissociative nature of this particular transition[164], we were able to carry out the power dependence studies. The predissociative nature of this transition was also established in our experiment, since we observed the corresponding Cl and H atom ion signals at the resonant wavelength corresponding to the REMPI lines of HCl molecules. A linear log-log plot for the power dependence studies shows a slope of 2.9±0.2, which is consistent with one photon dissociation of fumaryl chloride forming HCl followed by its detection with the (2+1) REMPI scheme, similar to the dynamics of Cl atom formation. Laser polarization dependent studies on the HCl, TOF profile to elucidate the translational energy distribution could not be done due to the weak REMPI signal, as discussed earlier. The above set of experiments establishes the formation of HCl in the photodissociation of fumaryl chloride at 235 nm as a primary channel.

6.4   DISCUSSION

6.4.1   NATURE OF EXCITATION AT 235 nm

As discussed earlier, fumaryl chloride contains one C=C and two C=O groups in conjugation, which make it bichromophoric, similar to fumaric acid (HOCO−CH=CH−COOH) and acryloyl chloride (H$_2$C=CHCOCl). Hence, we expect that fumaryl chloride also to have a similar type of absorption spectrum with two bands corresponding to n-π* and π-π* transitions. *Ab initio* molecular orbital (MO) calculations were performed to investigate the nature of the excited electronic states of fumaryl chloride. We optimized ground state geometries of various isomers, as shown in FIG. 6.1, employing time dependent (TD) density function theory (DFT) calculation, using the cc-pVDZ set of basis sets. There are three isomers, namely, cis-

cis, cis-trans, and trans-trans, for fumaryl chloride. The theoretical calculations predict that the relative stabilities of all three isomers differ by less than 0.5 kcal/mol. Thus, these isomers are indistinguishable, given the experimental uncertainty of present study and the accuracy of the theoretical methods employed here. Vertical excitation energies are obtained for various transitions, to understand the nature of excitation at 235 nm. Although the calculated vertical transition energies are red-shifted compared to the experimental results in case of fumaric acid[166], the nature of transition and the orbitals are accurately predicted using this method. Orbitals participating in the different electronic transitions were visualized for better understanding of the process. The vertical excitation of fumaryl chloride is associated with a strong π-π* transition at higher energy and a weaker n-π* at lower energy. The strong transition, with oscillator strengths exceeding 0.4, is the first π-π* transition and is termed as S_2. Topological analyses of the electron density highlight the delocalized nature of the O=C−C=C−C=O chain, wherein the central C=C bond possesses the largest electron density, although less than the pure π-bonds. The C−C bonds consequently possess larger electron populations than the expected σ-bonds. The nature of π and π* orbitals in this transition is having a mixed character involving mainly the C=C and the C=O π electrons. The weaker n-π* transitions at lower energy is termed as S_1 and it mainly involves the transition from the nonbonding orbitals of both Cl and O to the π* orbitals, which have a mixed character as discussed earlier. At 235 nm, we believe that fumaryl chloride is excited to the S_2 state. This S_2 state adiabatically correlates only with highly excited photoproducts, and that is not feasible in a single-photon excitation in the present case. Therefore, it is assumed that fumaryl chloride from the S_2 states crosses over to the nearby states, mostly the n-σ* state, from where the C-Cl bond cleaves forming Cl atoms. In addition, it can undergo rapid internal conversion

to the ground state, from where various other dissociation channels can occur, in addition to the Cl atom elimination.

6.4.2 TRANSLATIONAL ENERGY RELEASE AND ANISOTROPY PARAMETER

Several processes have been proposed as primary dissociation pathways in fumaryl chloride photoexcitation at 235 nm, and these are given as follows:

$$ClOC–CH=CH–COCl \qquad \rightarrow ClOC–CH=\square \: CH–CO + Cl \: \Delta H=83 \: kcal/mol \qquad (6.3)$$

$$\rightarrow \: ClOC–CH=CH + COCl \quad \Delta H=100 \: kcal/mol \quad (6.4)$$

$$\rightarrow \: ClOC–CH=C=CO + HCl \: \Delta H=38 \: kcal/mol \qquad (6.5)$$
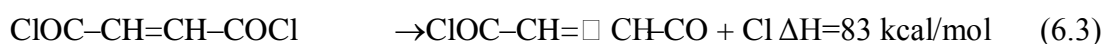
Reactions (6.3) and (6.4) involve the cleavage of single C–Cl and C–C bonds, respectively, while reaction (6.5) is the HCl molecular elimination channel. The Cl atom can be produced directly from reaction (6.3) as a primary product and also from the subsequent dissociation of highly energetic COCl radical [reaction (6.6)] formed in reaction (6.4) as a secondary product. The ΔH values are taken as similar to that of acryloyl chloride from refs 12 and 31.

$$COCl \qquad \rightarrow CO + Cl \quad \Delta H = 8 \: kcal/mol \qquad (6.6)$$
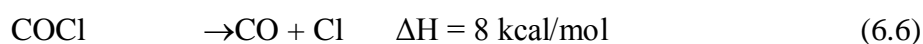
In fumaryl chloride, two types of $P(E_T)$ were observed for the C–Cl bond fission: one producing fragments with high kinetic recoil energies and the other producing fragments with low recoil energies. The $P(E_T)$ for $Cl(^2P_{3/2})$ derived from the forward convolution fit to the high-translational energy C–Cl bond fission channel peaks near 14.4 kcal/mol and extends to 30.0 kcal/mol.

Similarly, the low translational energy C–Cl bond fission channel peaks at 2.7 kcal/mol and extends to 10 kcal/mol. The presence of two types of $P(E_T)$ in C–Cl bond fission is analogous to other systems involving a π-π^* transition, such as acryloyl chloride[151,167], allyl chloride[168], and 2-chloropropene[169]. The high

translational energy chlorine atom channel, most likely, arises from an electronic predissociation via a state repulsive in the C–Cl bond, as observed in the above systems. It is possible that the low translational energy channel results from the C–Cl fission, following internal conversion to the ground electronic state. Another possibility of low energy Cl atom formation may arise from reaction[151]. However, the formation of the COCl radical cannot compete with the Cl formation channel due to its high endothermicity on the ground potential energy surface. Therefore, the only possible route for the formation of COCl, and hence, formation of Cl from it, is from a higher excited state such as, S_1, T_2, and T_1. But this route for the COCl formation is also ruled out in acryloyl chloride[153], a molecule with photochemical behavior similar to that of fumaryl chloride, on the basis of theoretical studies. The nature of $P(E_T)$ of the slow Cl atom obtained in the present studies for fumaryl chloride also rules out this route on the basis of energy consideration. So, the only formation pathway for the slow Cl atom is attributed to the dissociation process from the ground electronic state, after internal conversion. This proposition is further supported by the fact that we did observe the molecular HCl elimination channel, which is conclusively from the ground state of fumaryl chloride. The partitioning of the available energy into various degrees of freedom of the fragments is mainly governed by the nature of the dissociative potential energy surface. Very often, the disposition of the available energy into the fragment translational and the internal degrees of freedom can be predicted, using simple models. These models generally fall into two categories: impulsive and statistical. It is well known that the energy partitioning for a dissociative event on a repulsive surface is well described by an impulsive model. So, an impulsive model[35,170] has been used in this case, to calculate theoretically the translational energy released to the products. In this model, the distribution of energy

among the product states is governed by the dissociative event, i.e., by the repulsive force acting during the breaking of the parent molecule into the products. For example, in the present case, by using only conservation of momentum and energy, and the impulse assumption, one finds that the fraction of the available energy (E_{avl}) released as translational energy is given by

$$E_T = \left(\frac{\mu_{C,\ Cl}}{\mu_{ClCOCHCHCO\ ,\ Cl}} \right) E_{avail} \text{, and } f_T = E_T / E_{avail} \qquad (6.7)$$

where $\mu_{C,\ Cl}$ is the reduced mass of the C and Cl atoms, $\mu_{ClCOCHCHCO,\ Cl}$ is the reduced mass of the ClCOCHCHCO and Cl, E_{avl} is the available energy, and f_T is the fraction of the available energy going into the translational modes of the fragments. In the case of fumaryl chloride, the ratio of reduced masses is 0.32. The available energy is given by

$$E_{avail} = E_{hv} - D_0^0 (ClCOCHCHCO,\ Cl) - E_{SO} \qquad (6.8)$$

where E_{hv} is the photon energy (122.0 kcal/mol), D_0^0(ClCOCHCHCO-Cl) is the C-Cl bond dissociation energy and taken as 83.0 kcal/mol, similar to that for acryloyl chloride [167], and E_{SO} is the spin-orbit energy of chlorine (2.4 kcal/mol). Thus, E_{avl} for the Cl and Cl* channels are 39.0 and 36.6 kcal/mol, respectively. The experimental average translational energy (E_T) for the fast component is found to be 14.9±1.6 and 16.8±1.6 kcal/mol for Cl and Cl* channels, respectively, giving the f_T values of 0.38 and 0.46 for the Cl and Cl*, respectively. The experimental determined f_T so obtained is slightly higher than the value of 0.32 predicted, using the impulsive model. Now, coming to the slow component in the translational energy distribution of the Cl atom, the average energies determined are found to be 3.4±0.8 and 3.1±0.8 kcal/mol for Cl and Cl*, respectively. These values give the same f_T value of 0.08, for both Cl and Cl*, even though the available energies differ by 2.4 kcal/mol (spin-orbit energy) for these channels. A low f_T value suggests that the kinetic energy released for the slow

component can be explained better in light of a statistical model. The statistical model assumes partitioning of the available energy democratically throughout the molecule, and therefore neglects the effects of specific dynamical interactions of the departing fragments. A statistical dissociation process is predominant for a long-lived photoexcited parent molecule, allowing partitioning of the excess energy statistically among the available degrees of freedom of the products. This may be applicable in a process involving a rapid internal conversion to the ground electronic state, followed by the subsequent slow dissociation. Under these circumstances, in a large molecule with many low frequency modes, a relatively small amount of the excess energy is partitioned into translational motion of the products. For this kind of dissociation process, a priori calculations[37,38] were adopted, which give the f_T value of 0.07, matching very well with the experimental value of 0.08. This implies that the slow component in the translational energy distribution is mainly due to the Cl atom, which arises from the ground state potential energy surface, after internal conversion via some curve crossing mechanism. This mechanism is further confirmed by observation of the molecular HCl elimination channel, as described earlier. The higher experimental f_T value as compared to that calculated using the impulsive model obtained in the dissociation of fumaryl chloride for the fast chlorine atom channel prompted us to apply the hybrid model, employed by North et al.[38] for reactions with a barrier. In this model, the E_{avl} for the products is divided into two parts, namely, the excess energy above the exit barrier (E_{stat}) and the exit barrier energy (E_{imp}). The partitioning of E_{stat} and E_{imp} is treated by the statistical and modified impulsive models, respectively. The energy partitioned into each fragment is then obtained by adding contributions from each of these two models. For this type of dissociation with a barrier, E_T does not change much with E_{avl}. Similar results were obtained in our

earlier studies on various saturated and unsaturated carboxylic acids, and also on the enone system[115,146]. Photodissociation studies on acryloyl chloride by Butler and co-workers[151,167] at 193 and 235 nm show similar translational energy release for the Cl atom. At 193 nm dissociation, E_T was obtained to be 27 kcal/mol. Similarly, at 235 nm dissociation, a value of 23 kcal/mol was obtained. Here, it can be clearly seen that the change in the E_{avl} from 65 kcal/mol (for 193 nm) to 39 kcal/mol (for 235 nm) did not change the E_T value considerably for the Cl atom dissociation channel in acryloyl chloride. Also, the theoretical calculation by Cui et al.[153] clearly shows the presence of an exit barrier in the $S_1(^1n\text{-}\pi^*)$ state, for the Cl atom dissociation channel. So, we strongly believe that the dissociation from the S_1 state with an exit barrier cannot be ruled out in the photodissociation of acryloyl chloride in addition to dissociation from the repulsive state with (n-σ^*) nature. With same analogy, we propose that in fumaryl chloride the initially prepared $S_2(^1\pi\text{-}\pi^*)$ state crosses over to various states, namely, $S_1(^1n\text{-}\pi^*)$, (n-σ^*), and the ground state. Finally, the Cl atom can be formed from all these states with different values of E_T. In the analysis of the recoil anisotropy, β, for the Cl fragment, we note that in the limit of an instantaneous dissociation process, $\beta = 2\langle P_2(cos\ \theta_m)\rangle$, where θ_m is the molecular frame angle between the molecular transition dipole moment and the photofragment recoil direction, and $P_2(cos\ \chi)$ is the second-order Legendre polynomial. In a photodissociation process, following excitation via the electric transition dipole moments, namely, parallel or perpendicular, would be expected to give a β value of +2 or −1, respectively. The anisotropy measured in the present work is ~0.0, which indicates an isotropic dissociation process. This value of β does not give any indication of the nature of the transition dipole moment in fumaryl chloride dissociation. Generally, an impulsive dissociation is accompanied with an anisotropic distribution of the photoproducts,

since the dissociation lifetime is much shorter than the rotation period of the molecule. However, the anisotropy in an impulsive dissociation can be reduced[171], or wiped out[172], due to several factors, such as mixed initial transition with both parallel and perpendicular components, longer dissociation lifetime, dissociation not from a single geometry rather from a range of geometries etc. In fumaryl chloride, for C_{2h} geometry, the π-π^* transition, which has B_u symmetry, the transition dipole moment is mainly along the x-axis and y-axis. The same is true for the n-π^* transition. So, in this case even if there is a crossover from the initially prepared π-π^* state to the n-π^* state, the transition dipole moment is not changed. However, during this crossover period the molecule may rotate. The absence of recoil anisotropy in the present studies is expected mainly due to the mixed transition, as discussed, and the relatively longer dissociation lifetime, since the dissociation is not from the initially prepared state rather from the crossover state. In addition, the different geometries of fumaryl chloride also contribute to the β value of $\sim$0.0.

6.5   CONCLUSION

In summary, fumaryl chloride generates a chlorine atom upon excitation at 235 nm, which prepares the molecule initially in its π-π^* state. The nascent distribution of the photofragment chlorine atom is measured by the (2+1) REMPI with the TOF mass spectrometry. We have determined the photofragment speed distribution, the anisotropy parameter β, and the spin-orbit branching ratio for the chlorine atom elimination channels, to gain insight into the dynamics of the chlorine atom formation. Polarization-dependent and state-specific TOF profiles are deconvoluted to get translational energy distributions, using a forward convolution method with least-squares fitting, taking into account the fragment anisotropies. The TOF profiles for Cl and Cl* are independent of the laser polarization; i.e., the

parameter β is well characterized by a value of 0.0, within the experimental uncertainties. Two contributions, namely, the fast and the slow components, are observed in the translational energy distribution, $P(E_T)$, of Cl and Cl* atoms formation channels. The average translational energies for the Cl and Cl* channels for the fast component are 14.9±1.6 and 16.8±1.6 kcal/mol, respectively. Similarly, for the slow component, the average translational energies for the Cl and Cl* channels are 3.4±0.8 and 3.1±0.8 kcal/mol, respectively. The energy partitioning into the translational mode is interpreted with the help of an impulsive model for the fast component, and a statistical model for the slow component. While the experimental f_T value for a slow chlorine atom is nicely described with the statistical model that for the fast Cl atom channel is slightly higher than the predicted value of 0.32, by the impulsive model. Apart from the chlorine atom elimination channel, the molecular HCl elimination is also observed in the photodissociation of fumaryl chloride. The observation of the HCl molecular elimination channel in the dissociation process and the bimodal translational energy distribution of the chlorine atom clearly indicate the existence of a crossover mechanism from the initially prepared state to the ground state. Finally, it is proposed that in fumaryl chloride the initially prepared $S_2(^1\pi\text{-}\pi^*)$ state crosses over to various states, namely, $S_1(^1n\text{-}\pi^*)$, (n-σ*), and the ground state, and the Cl atom can be formed from all these states, with different values of E_T.

CHAPTER 7

PHOTODISSOCIATION DYNAMICS OF

HALOGENATED THIOPHENES AT 235 nm:

A REMPI TOF STUDY

7.1 INTRODUCTION

Recently, many experiments in the ultraviolet (UV) region, accompanied by theoretical studies have been performed, to investigate the photodissociation dynamics of organic halogenated molecules having C−X (X = Cl, Br, and I) bonds. The most of such type of studies have focused particularly on the mechanism of the formation of X atom in its ground, X ($^2P_{3/2}$), and spin-orbit excited, X*($^2P_{1/2}$), states. However, such studies for more complex molecules, especially, cyclic compounds, have been less keenly pursued because of their complex photodissociation mechanism, which also include multiple channels. In this context a detailed study was undertaken, to understand the dynamics of X/X* formation in the photodissociation of halogen-containing thiophenes.

Thiophene (c-C_4H_4S) is a five-membered heterocyclic compound, containing four carbon atoms and one sulfur atom in the ring. The delocalization of electron lone pairs on sulfur, in the conjugated π system, makes thiophene behave like an aromatic

compound[173]. This electron delocalization makes thiophene and thiophene-based materials and polymers an important building block entity for manufacturing various materials, showing unusual electronic and optical properties[174]. The photochemistry of thiophene, especially in the UV region, has been a subject of many investigations, both experimentally and theoretically. To cite a few, the experimental work includes the studies related to its UV absorption spectrum in the gas phase[175,176] and the electron energy loss spectrum[177]. A few experiments were also done, to understand its excited-state dynamics, using femtosecond pump-probe photoelectron spectroscopy[178] and resonance Raman spectroscopy[179]. On the theoretical side, the studies include the electronic structure calculations in the Franck-Condon region, with complete active space self-consistent field and density functional theory[180]. Similarly, ab initio multi-reference configuration interaction calculations were performed to understand its UV spectrum[176,180]. A few other studies were also carried out to investigate its ultrafast internal conversion, and photodissociation dynamics[178,180,181]. Very recently, ultrafast deactivation processes of thiophene were studied theoretically by Cui and Fang[182], and Stenrup[183].

The gas phase UV absorption spectrum of thiophene shows an A-band located at 225 nm (5.5 eV), in the lowest valence state, which has a long vibrational progression, with the lowest absorption at $\sim$240 nm (5.15 eV). This has been attributed to the vibrational origin of the $1^1A_1 \rightarrow 2^1A_1$ or simply a $\pi \rightarrow \pi^*$ transition[184]. Wiebe and Heicklen[185] studied the UV photochemistry of thiophene at 213.9, 228.8, and 253.7 nm, in the gas phase, using end-product analysis. Nayak et al.[186] proposed a mechanism for infrared multiphoton dissociation (IRMPD) that involves breakage of the C−S bond in thiophene, to form an unstable 1,5-diradical, which further decomposes via different channels. Flash photolysis of thiophene showed a transient

absorption spectrum in the region 377-417 nm[187], which was tentatively assigned to the absorption due to the transient C_4H_3 radical. Ng and coworkers[188] studied photodissociation of thiophene at 193 nm using photoionization detection of the hydrocarbon products and (2+1) REMPI detection of the sulfur atom. They observed only two dissociative channels, namely, $C_2H_2S + C_2H_2$ and $C_4H_4 + S$. Later on, similar studies were done at 193 nm by Suits and co-workers[189], using synchrotron radiation as a universal product probe. They observed five primary channels and concluded that all the dissociation processes occur on the ground-state surface, following fast internal conversion.

Among the various substituted thiophenes, the halogen-substituted thiophenes are the most studied thiophenes from the viewpoint of photochemistry and applications thereof. The photoelectron studies on 2-bromothiophene[190] and 2-chlorothiophene[191] suggest that the lone pair electrons on Br and Cl atoms exist in two different orbitals. The orbital lying in the molecular plane does not mix with the ring orbitals, to a significant extent, whereas the other one, which is perpendicular to molecular plane, is delocalized over much of the ring, and significantly involved in bonding and mixing with π electrons of the ring. In the case of 2-bromothiophene, the molecular orbital associated with the in-plane lone pair on bromine atom retains its atomic character, to a great extent than the molecular orbital corresponding to the out-of-plane component. However, in the case of chlorine, the chlorine atomic character is of minor importance. In the UV spectrum of dihalogenated thiophene[175] in solution phase, two $\pi^* \leftarrow \pi$ electronic transitions were observed. Also, in the stretched sheet polarized spectrum of 2,5-dibromothiophene[192], two bands were observed, which were polarized. Very recently, positive and negative photoion spectroscopy studies on monochlorothiophenes were conducted, using synchrotron vacuum ultraviolet

radiation[193]. Wang and co-workers[194] studied the dynamics of Br atom formation in the photodissociation of bromothiophenes at 267 nm, using ion velocity imaging technique. The presence of another chromophore, namely the C−X bond, can alter the photochemistry. Competitive absorption may exist between these two chromophores, when the molecules absorb photons at a particular wavelength.

In this context, the present study is undertaken to understand the photodissociation dynamics of two halogen substituted thiophenes, namely, 2-chlorothiophene and 2-bromo-5-chlorothiophene. Here, we have investigated dynamics of halogen atom (X/X*) formation, around 235 nm, in a supersonic molecular beam, using the REMPI-TOF technique. We have also measured the translational energy distributions for both the types of chlorine and bromine atoms. Besides, we have also measured the relative quantum yields of Cl* and Br*. To gain further insights, the anisotropy parameters (β) are also measured. Further, theoretical calculations have been carried out to understand the dissociation dynamics.

7.2   EXPERIMENTAL SECTION

Studies on photodissociation dynamics of 2-chlorothiophene and 2-bromo-5-chlorothiophene have been carried out in a molecular beam, using REMPI, with time-of-flight (TOF) mass spectrometry, to monitor the chlorine and bromine photoproducts state selectively. The experimental set-up has been discussed in detail in Chapter 2, Section 2.3.1. The halogenated thiophenes samples, 2-chlorothiophene (96% purity, Aldrich) and 2-bromo-5-chlorothiophene (98% purity, Aldrich), were used without further purification. The chlorine and bromine atoms were probed, using (2+1) REMPI transitions in the 234-236 nm region. A typical REMPI scheme for the chlorine atom and for the bromine atom is shown in Chapter 2, FIG. 2.6 and FIG. 2.7, respectively. The two lines for chlorine atom were selected from several lines, shown

in Table 6.1 and FIG. 6.2 of Chapter 6 for quantitative measurements. The bromine atom was probed by (2+1) REMPI transitions in the region of 234-236 nm, shown in FIG. 7.1. The two REMPI lines were chosen from various lines, shown in Table 7.1, and the REMPI spectra are compared with the literature values. The peaks at 233.70 nm (42789.9 cm^{-1}, 6p $^4P_{3/2}$←4p $^2P_{3/2}$) and 234.04 nm (42727.7 cm^{-1}, 6p $^2S_{1/2}$ ← 4p $^2P_{1/2}$) were probed for the present experiment.
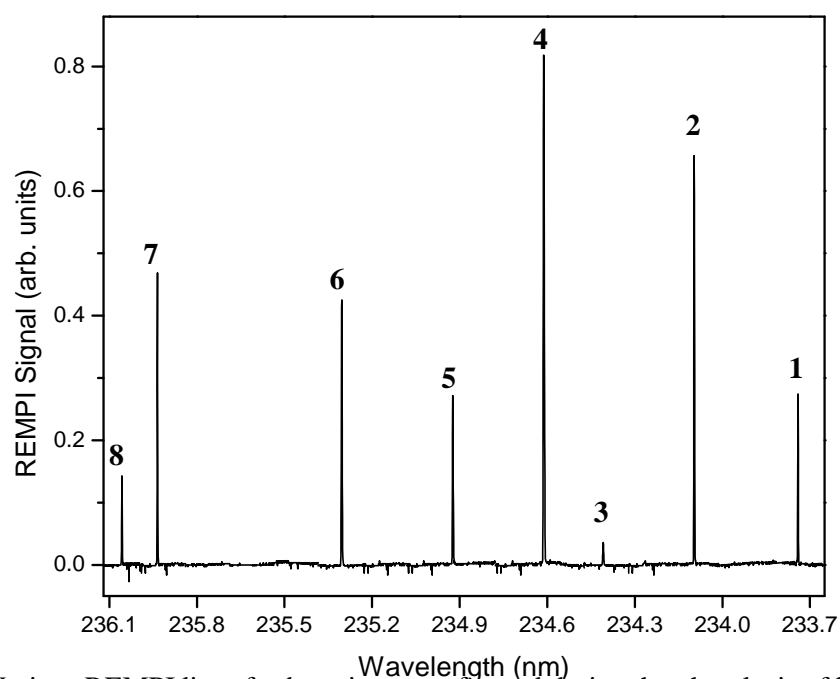
FIG. 7.1: Various REMPI lines for bromine atom formed during the photolysis of bromoform.

Table 7.1. Comparison of experimental and literature REMPI lines for Br.

Peak No	Experimental wavelength		Literature wavelength		Two photon Transition From 4p
	(cm^{-1})	nm	(cm^{-1})	nm	
1	42782.5	233.74	42789.9	233.70	$6p\,^4P_{3/2} \leftarrow 4p\,^2P_{3/2}$
2	42718.6	234.09	42727.7	234.04	$6p\,^2S_{1/2} \leftarrow 4p\,^2P_{1/2}$
3	42660.2	234.41	42671.2	234.35	$6p\,^2D_{5/2} \leftarrow 4p\,^2P_{1/2}$
4	42623.9	234.61	42631.1	234.57	$6p\,^4S_{3/2} \leftarrow 4p\,^2P_{1/2}$
5	42567.6	234.92	42578.5	234.86	$6p\,^2D_{3/2} \leftarrow 4p\,^2P_{1/2}$
6	42498.9	235.30	42495.3	235.32	$5p\,^2F_{5/2} \leftarrow 4p\,^2P_{1/2}$
7	42385.4	235.93	42434.0	235.66	$5p\,^2P_{1/2} \leftarrow 4p\,^2P_{1/2}$
8	42372.8	236.00	42396.2	235.87	$5p\,^2P_{3/2} \leftarrow 4p\,^2P_{1/2}$

The power dependence studies of one-colour REMPI intensities for transitions corresponding to $Cl(^2P_{3/2})$, produced on photolysis of 2-chlorothiophene at ~235 nm, show linear behaviour in the log-log plot with a slope of ~2.9±0.1. This observation is consistent with one-photon dissociation of 2-chlorothiophene, followed by (2+1) REMPI of chlorine. Similar power dependence studies were carried out for one colour REMPI transitions, corresponding to Cl $(^2P_{3/2})$ and Br $(^2P_{3/2})$, produced on photolysis of 2-bromo-5-chlorothiophene. The FIG. 7.2 shows linear behaviour in the log-log plot of REMPI signal against laser intensity for Br $(^2P_{3/2})$, with a slope of 3.3±0.2. Apart from the power dependence studies, we also systematically monitored the shape and the width of TOF profiles of Cl and Br atoms at various laser intensities. The TOF profiles remain invariant at lower laser intensities in the range of 50-75 µJ/pulse. However, for TOF profiles, the energy used was even lower as compared to above mentioned energy. All the experiments were performed at much lower intensity (typically at ~ 300 µJ/pulse) than that at which the shape and the width of the TOF

profiles start varying. This experimental condition ensures that the translational energy distributions and the anisotropy parameters are invariant over the laser fluences used.
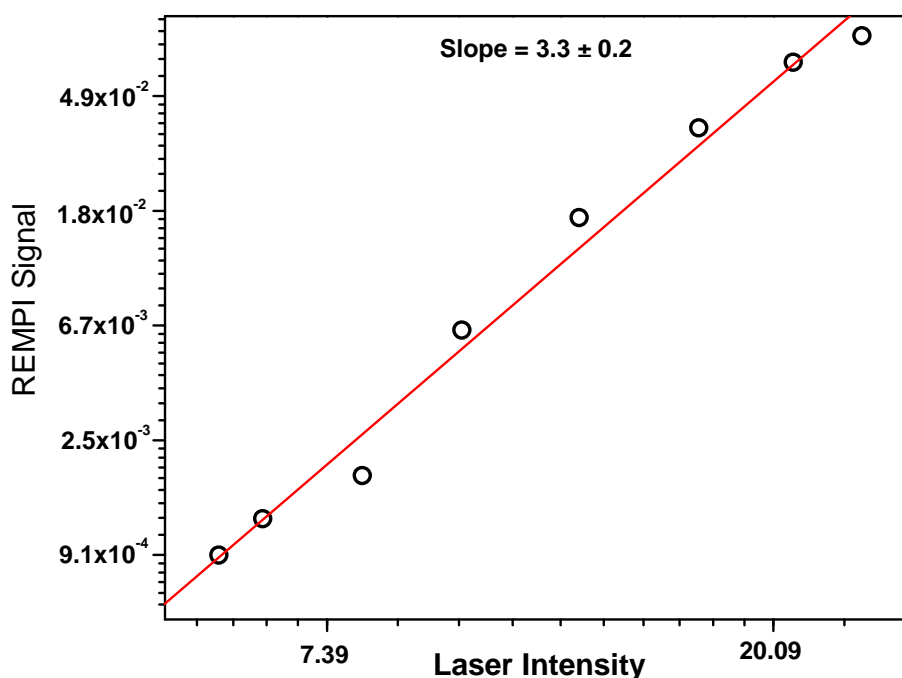
FIG. 7.2: Dependence of the REMPI signal of Br($^2P_{3/2}$) atom from 2-bromo-5-chlorothipohene photolysis on the laser intensity. The slope of the fitted linear log-log plot is 3.3±0.2.

The translational energy distribution (E_T) and the anisotropy parameter (β) for Cl, Cl*, Br and Br* were determined by measuring their TOF profiles at different laser polarizations, using a commonly used forward convolution (FC) technique, as described in Chapter 2, Section 2.3.2. In this method, the knowledge of the instrumental response function is required, and the same was determined by studying the REMPI of aniline[195] beam. These measurements showed the instrumental response function to be well described by a Gaussian function in the time domain, with FWHM of 27 ns at aniline mass. Under space focusing conditions, this leads to a

convolution function in the velocity domain, which is linearly dependent on the extractor voltage V_{ex}.

In the present work, we have used a procedure of non-core sampling data, in which it is assumed that the nature and the shape of the TOF profiles for chlorine/bromine photofragment is independent of the probe polarization. In general, this assumption holds good. However, the presence of atomic **v·j** correlation may make this assumption only approximate. However, these correlations are weak enough to be neglected[196].

7.3   RESULT AND ANALYSIS

7.3.1   SPIN-ORBIT BRANCHING RATIO

The relative quantum yields of the halogen atom (X) fragments, formed in different spin-orbit states (X, X*), were evaluated for both the compounds studied. The relative yields were calculated by normalizing the integrated intensity, i.e., the peak areas S(X), or S(X*), of the respective (2+1) REMPI transitions with respect to the laser intensity, and the ratio of the two-photon absorption coefficients. As discussed earlier, the REMPI spectra of the ground $X(^2P_{3/2})$ and the spin-orbit excited $X*(^2P_{1/2})$ atomic photoproducts were scanned around 42492.5 and 42516.1 cm^{-1} respectively, for the chlorine atom, and around 42789.9 and 42727.7 cm^{-1} respectively, for the bromine atom. The ratio of the measured areas S(X) and S(X*) of (2+1) REMPI lines is proportional to the product ratio, N(X)/N(X*), as given in equation (7.1),

$$\frac{N(X^*)}{N(X)} = k \frac{S(X^*)}{S(X)}$$
(7.1)

where k is the relative ionization probability. The intensities S(X) and S(X*) were obtained by integrating the measured ion signal intensities over the proper range, covering the Doppler width and the probe laser bandwidth. The measurements were

repeated at different laser light intensities, which gave similar relative signal intensities. For photodissociation of 2-chlorothiophene, the integrated ion signal intensity ratio, S(Cl*)/S(Cl), was measured to be 0.23±0.07 (FIG. 7.3). Similarly, for 2-bromo-5-chlorothiophene, the integrated ion signal intensity ratios, S(Cl*)/S(Cl) and S(Br*)/S(Br), were measured to be 0.23±0.07 (FIG. 7.4[a]) and 0.09±0.03(FIG. 7.4[b]), respectively. From the measured integrated intensity ratios, one can easily obtain the product ratios, using equation (7.1), in which the relative ionization probability, k was taken to be 0.85±0.10 for chlorine atom[197] and 0.17±0.05 for bromine atom[198]. The Φ(X*) can be obtained from an expression

$$\Phi(X^*) = \frac{N(X^*)}{N(X^*)+N(X)} \tag{7.2}$$
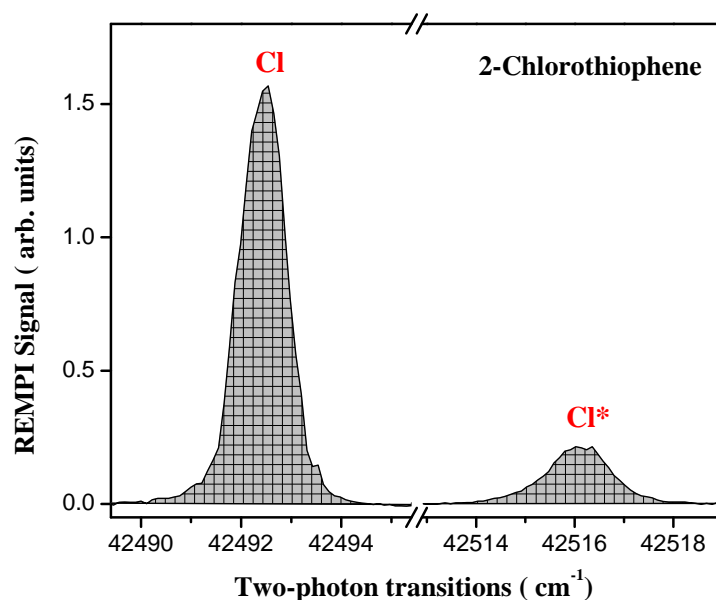
FIG.7.3: REMPI spectral profiles of Cl and Cl* atoms produced in photodissociation of 2-chlorothiophene at 235 nm, used for the determination of their relative quantum yields.

The Φ(Cl*) obtained in the photodissociation of 2-chlorothiophene is found to be 0.19±0.06. Similarly, the Φ(Cl*) and Φ(Br*) in the photodissociation of 2-bromo-5-chlorothiophene are found to be 0.19±0.06 and 0.08±0.03, respectively.
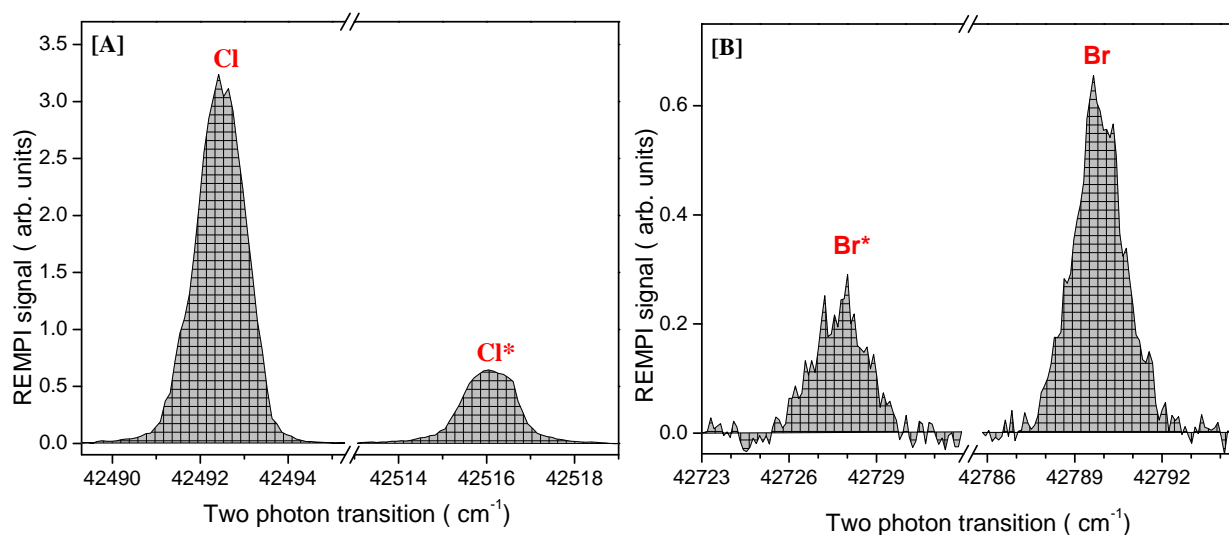
FIG. 7.4: REMPI spectral profiles produced in photodissociation of 2-bromo-5-chlorothiophene at 235 nm; (A) Cl and Cl* and (B) Br and Br*, used for the determination of their ratio.

7.3.2 TRANSLATIONAL ENERGY DISTRIBUTION AND ANISOTROPY PARAMETER

The TOF profiles of the Cl, Cl*, Br and Br* atoms were converted to the velocity domain for both the halogenated thiophenes, as discussed in the Section 2.3.2, Chapter 2. Their TOF profiles have been found to be independent of laser polarization, for both the compounds studied. In FIG. 7.5 we have shown two panels corresponding to the typical TOF profiles recorded for the Cl/Cl*, or Br/Br*, fragments, for the laser polarization at the magic angle ~54.7° to the detection axis.
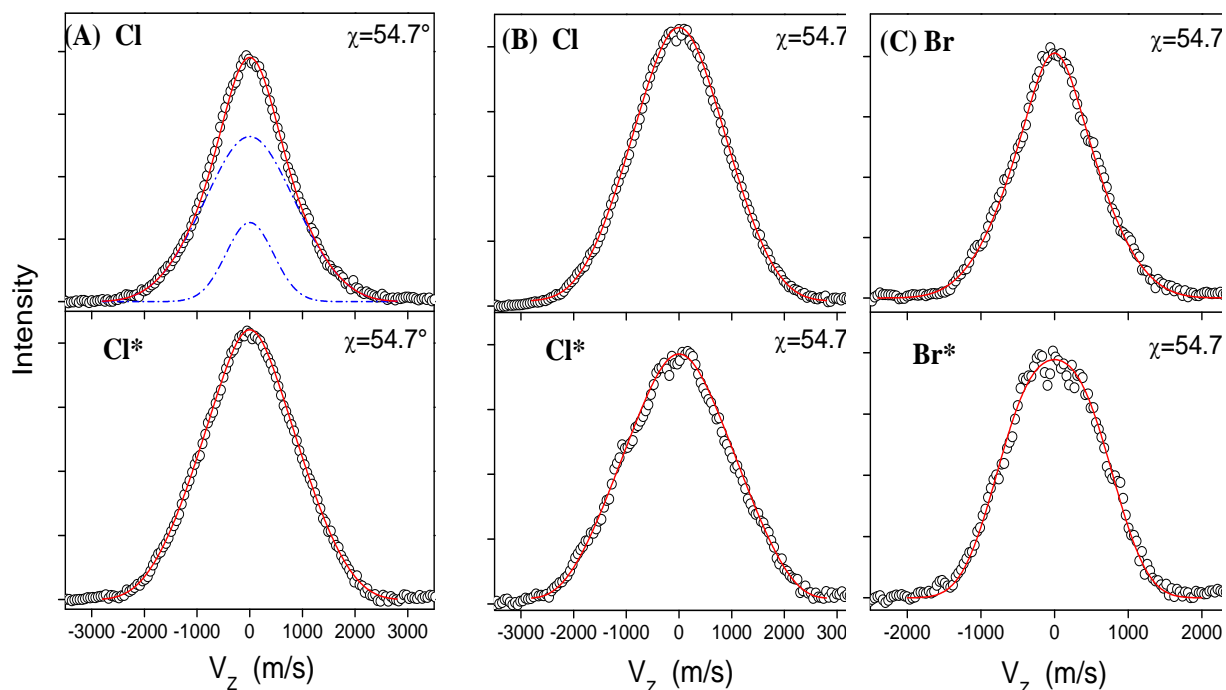
FIG. 7.5: REMPI–TOF profiles; (A) Cl ($^2P_{3/2}$) and Cl* ($^2P_{1/2}$) produced from the photodissociation of 2-chlorothiophene: (B) Cl ($^2P_{3/2}$) and Cl* ($^2P_{1/2}$) and (C) Br ($^2P_{3/2}$) and Br* ($^2P_{1/2}$) produced from the photodissociation of 2-bromo-5-chlorothiophene at 235 nm. The circles are the experimental data and the solid curves are forward convolution fit. Velocity components are depicted as dotted curves. The profiles correspond to the magic angle (χ=54.7°) experimental geometry.

We analyzed the TOF data, using a forward convolution procedure, as described in the Section 2.3.2, Chapter 2. The predicted TOF spectra were calculated, convoluted with the instrumental response function, and compared with the experimental results. The solid curves in FIG. 7.5 display the final calculated TOF profiles. However, we get two components in the profiles of Cl atom produced in photodissociation of 2-chlorothiophene (shown in FIG. 7.5[A]), each component is shown by the dot-dash curves, and the sum by the solid line. The photofragment translational energy distributions, P(E_T), determined from the data in the FIG. 7.5, for the Cl/Cl* and Br/Br*, are depicted in FIG. 7.6 for 2-chlorothiophene and 2-bromo-5-chlorothiophene. Inspection of P(E_T) figures reveals that the translational energy distribution, P(E_T), has two components for Cl atom and only one component for Cl* produced in photodissociation of 2-chlorothiophene. However, both Cl and Br atoms

produced in the case of 2-bromo-5-chlorothiophene have only one component. In the case of 2-chlorothiophene, the average translational energies for the fast and the slow components of the Cl channel are 3.0±1.0 and 1.0±0.5 kcal/mol, respectively. The faster component constitutes of 80±5% of the total fragments, while the slower component constitutes of the remaining 20±5%. For Cl*, which has only one component, the average translational energy is 3.5±1.0 kcal/mol. In the case of 2-bromo-5-chlorothiophene, as mentioned, we have observed only one component for Cl, Cl*, Br and Br* in the translational energy distribution. The average translational energies of the Cl and Cl* channels are 3.5±1.0 and 5.0±1.0 kcal/mol, respectively. Similarly, the average translational energies of the Br and Br* channels are 2.0±1.0 and 3.5±1.0 kcal/mol, respectively. Since the TOF profiles for Cl/Cl* and Br/Br* are independent of laser polarizations, the β parameter is well characterized by a value of 0.0, within the experimental uncertainties.
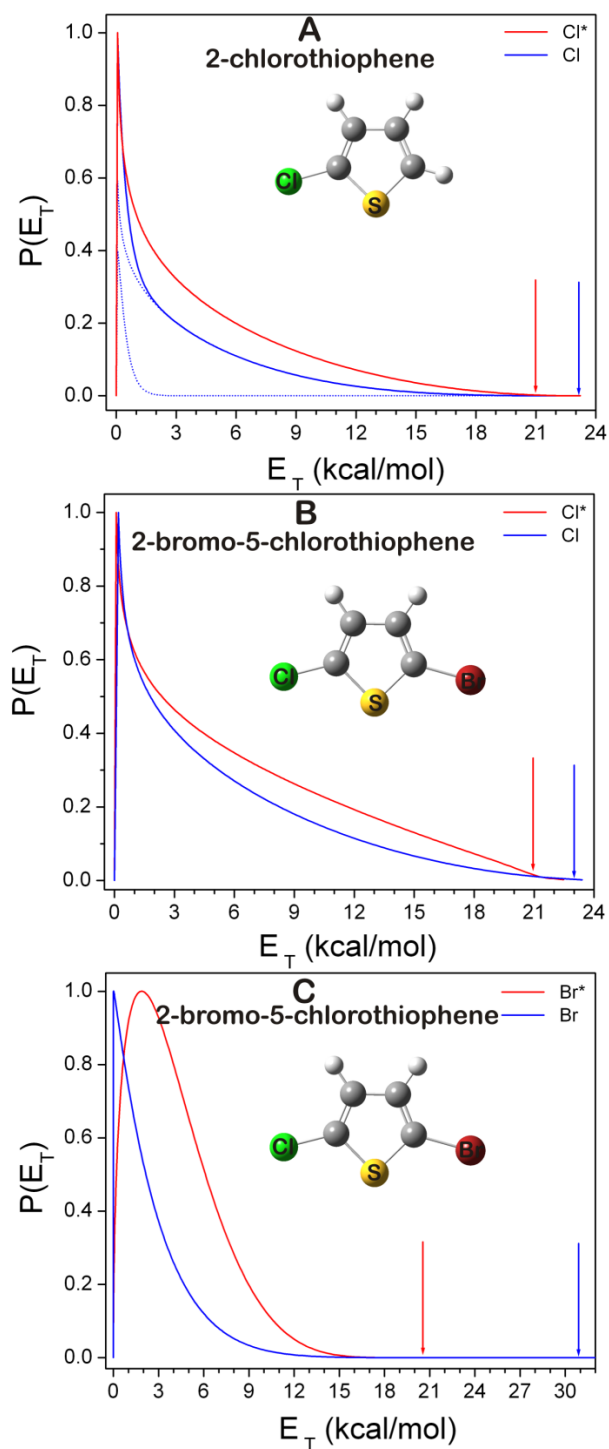
FIG. 7.6: Centre-of-mass recoil translational energy distribution derived from FIG. 7.5: (A) Cl($^2P_{3/2}$) and Cl* ($^2P_{1/2}$), produced in the photodissociation of 2-chlorothiophene, (B) and (C) Cl($^2P_{3/2}$) and Cl* ($^2P_{1/2}$) and Br ($^2P_{3/2}$) and Br* ($^2P_{1/2}$), produced in the photodissociation of 2-bromo-5-chlorothiophene, respectively, at 235 nm. Here, in (A) the dashed lines indicate the translational energy distributions for the fast and slow components for chlorine atom formation channel and the solid line shows the sum. The blue and red vertical arrows indicate the maximum available energy for the Cl ($^2P_{3/2}$) and Cl* ($^2P_{1/2}$) or Br ($^2P_{3/2}$) and Br* ($^2P_{1/2}$) elimination channels, respectively.

7.3.3 MULTIPHOTON IONIZATION OF HALOGENATED THIOPHENES

To understand the fragmentation pattern of the halogenated thiophenes to produce various mass ion peaks, mass spectrum in multiphoton ionization of halogenated thiophenes has been recorded at relatively high laser fluences. Apart from the REMPI lines of halogen atoms, many ion peaks, corresponding to the various fragments of halogenated thiophenes, have been observed in the multiphoton ionization process. In the case of 2-chlorothiophene, the mass spectrum shows various fragments in good agreement with the results by Xu et al.[193], in the positive and negative photoion spectroscopy studies using synchrotron vacuum ultraviolet radiation at 18 eV. In the multiphoton ionization/dissociation process at 235 nm, the parent ion and the various daughter ions are detected, as listed in Table 7.2. The natural isotope abundance ratio for $^{35}Cl/^{37}Cl$ is about 3:1, whereas $^{32}S{:}^{33}S{:}^{34}S{:}^{36}S$ is 95.02:0.75:4.21:0.02. Although we have observed all the isotopes for sulfur and chlorine atoms in the mass spectra, we have listed only the fragments with ^{35}Cl and ^{32}S. Similarly, various ion fragments observed for 2-bromo-5-chlorothiophene have also been listed in Table 7.2.

Table 7.2: Various mass fragments observed in multiphotonic processes of
2-chlorothiophene and 2-bromo-5-chlorothiophene at 235 nm.

2-Chlorothiophene		2-bromo-5-chlorothiophene	
m/z	Fragment	*m/z*	Fragment
32	S	32	S
39	C_3H_3	44	CS
44	CS	56	C_2S
45	CHS	57	C_2HS
57	C_2HS	68	C_3S
58	C_2H_2S	69	C_3HS
69	C_3HS	73	C_3H_2Cl
73	C_3H_2Cl	79	CSCl
79	CSCl	113	CSBr
82	C_4H_2S	116	C_4HSCl
83	C_4H_3S		
92	C_2HSCl		

7.3.5 THEORETICAL CALCULATION ON GROUND STATE DISSOCIATION OF 2-CHLROTHIOPHENE

Molecular orbital (MO) calculations were carried out to generate the relative potential energy diagram for the dissociation channels of 2-chlorothiophene on its ground state. Calculations were done at G3B3 level of theory, using Gaussian[86] suite of program. All the stationary points were calculated on the ground state, for various dissociation channels. Since G3B3 level of theory is not available for Br, the calculation was not done for 2-bromo-5-chlorothiophene, but we expect a similar type of mechanism for the brominated thiophene also. The G3B3 level of theory is very accurate, and is demonstrated by calculating the bond dissociation enthalpies of various heterocycles[199]. In addition, it has the fewest convergence problems. In fact, the G3B3 level of theory calculates ΔH^0_{298}, within an error of ~1 kcal/mol, especially for halogenated heterocyles, such as halo thiophenes. We did not try to locate various transition states involved on the PES. Hence, we report here only the relative energy diagrams for various channels occurring on the ground PES of 2-chlorothiophene. The energy levels are schematically represented in FIG. 7.7, with the energy of each species marked in kcal/mol. The initial step is shown as either the cleavage of the C–Cl bond, forming thiophene radical and Cl atom, or that of the C–S bond. Since the two C–S bonds are not equivalent, their cleavage opens up the ring structure, forming two structures *C–S1* and *C–S2* (shown in FIG. 7.7). The *C–S1* structure is more stable than the *C–S2* by ~ 1 kcal/mol, which indicates that it is harder to break the C–S bond, which involves the C atom attached to Cl atom. Similarly, for thiophene radical, it is harder to break the C–S bond that results in the formation of a radical having an odd electron located on carbon atom. This is reasonable, as the odd electron on the carbon atom overlaps with the lone electron pair of the sulfur atom, forming a stronger C–S

to break. The thiophene radical formed, after the Cl atom elimination, can open up by the C–S bond cleavage, forming structures *C–S3* and *C–S4* (depicted in FIG. 7.7). These structures, *C–S3* and *C–S4*, can also be formed from the primary structures, *C–S1* and *C–S2*, by Cl atom elimination. However, these channels are well above the available photon energy of ~ 122 kcal/mol (FIG. 7.7). The structures *C–S1* and *C–S2* can also form various fragments, after a C–C bond cleavage. The *C–S1* structure can produce acetylene and its co-fragments, whereas the *C–S2* structure can form chloroacetylene and its various co-fragments, as shown in FIG. 7.7. However, no attempts were made to characterize the various transition states involved in the above reaction. From our calculations, it is clear that the formation of chloroacetylene seems to be more favorable than that of acetylene. Similarly, on the ground state of 2-chlorothiophene, the C–S bond cleavage is more favorable than the C–Cl bond cleavage. The C–Cl bond dissociation energy was estimated to be 98.8 kcal/mol in both the halogenated thiophenes. The C–Br bond dissociation energy in bromothiophene is estimated to be 91.2 kcal/mol, which is 7.6 kcal/mol lower than that of the C–Cl bond.[199]
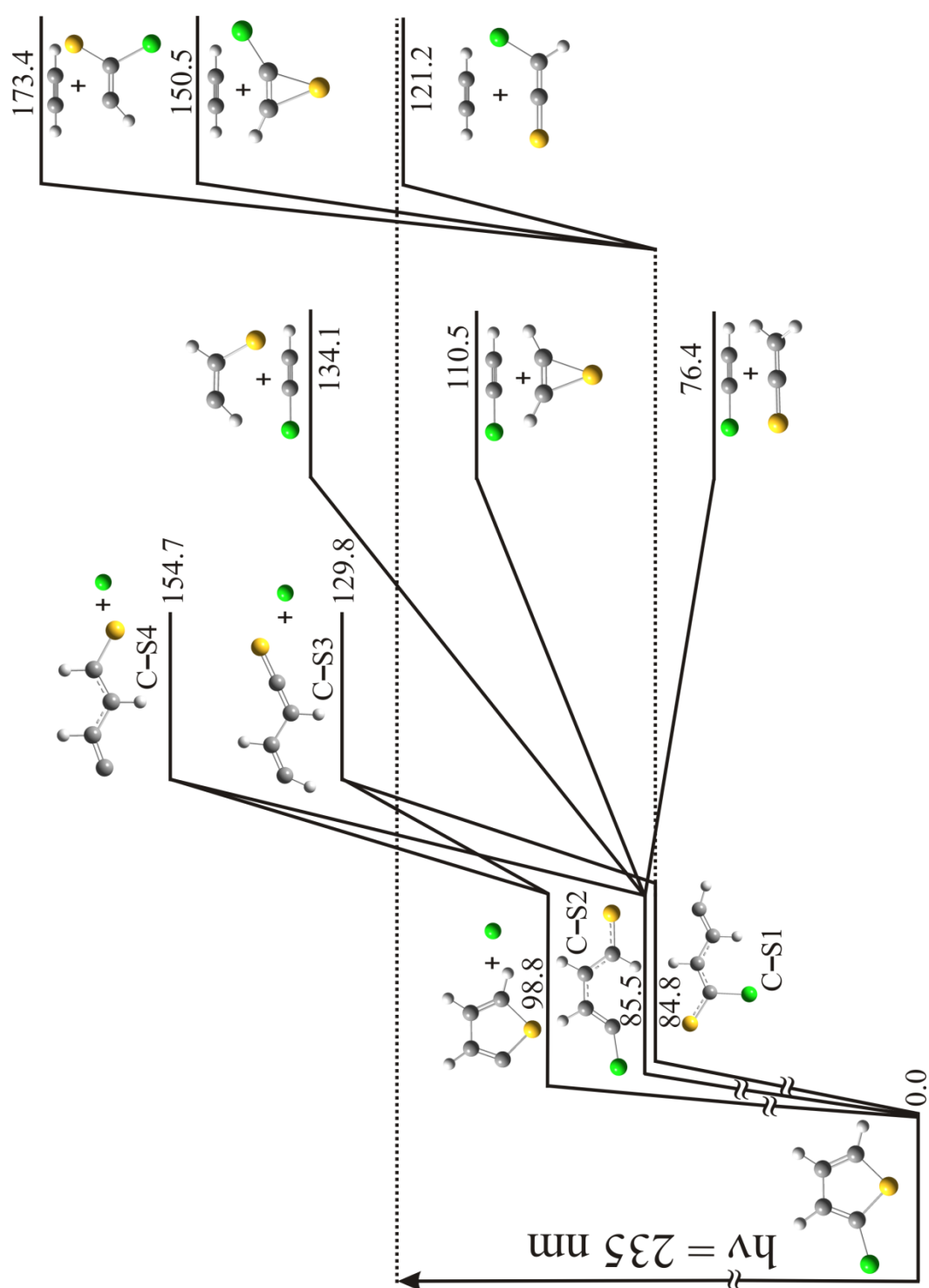
FIG. 7.7: Relative energy diagram in kcal/mol, along with the structures, for various products in the photodissociation of 2-chlorothiophene at 235 nm in its ground state.

7.3.6 ESTIMATION OF ΔH_f^{298} VALUE FOR 2-CHLOROTHIOPHENE

The ΔH_f^{298} value for 2-chlorothiophene was estimated, using the following isodesmic processes.

$$(7.3)$$

$$(7.4)$$
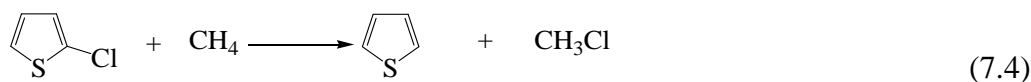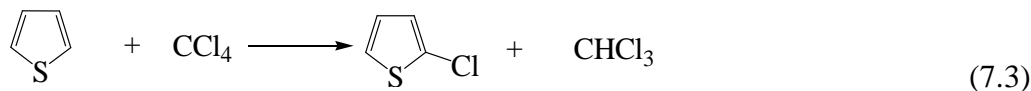
The ΔH_{298}^0 values for the above reactions were calculated at G3B3 level of theory, using Gaussian suite of program. Using the ΔH_f^{298} values for CCl_4, CH_4, $CHCl_3$, CH_3Cl and thiophene, the ΔH_f^{298} value of 2-chlorothiophene was estimated to be 24.1 and 23.0 kcal/mol, using reaction (7.3) and (7.4), respectively. Hence, the average ΔH_f^{298} value for 2-chlorothiophene can be given as 23.5 kcal/mol. The estimated ΔH_f^{298} value for 2-chlorothiophene is about 4.0 kcal/mol lower than that of thiophene. This trend is similar to that observed in benzene (19.8 kcal/mol) and chlorobenzene (13.0 kcal/mol), where the difference in ΔH_f^{298} values is about 6.8 kcal/mol. Considering the higher aromaticity of benzene ring than that of thiophene ring, the difference is reasonable and realistic. In addition, the inter-consistency in the calculation was verified by calculating the ΔH_{298}^0 value for the following isodesmic reaction, involving the above species, and this calculated value matches very well with experimental data.

$$CCl_4 + CH_4 \rightarrow CHCl_3 + CH_3Cl \tag{7.5}$$

Hence, a ΔH_f^{298} value of 23.5 kcal/mole can be taken for 2-chlorothiophene, for further purposes.

7.4 DISCUSSION

7.4.1   NATURE OF EXCITATION AT 235 NM

The onset of optical absorption in thiophene is at about 5 eV (248 nm). Its gas phase UV absorption spectrum with λ_{max} = 225 nm (historically A band), has a long vibrational progression, with the band origin at 240 nm, for the lowest absorption. The nature of this band has been attributed to the vibrational origin of the $1\,^1A_1 \rightarrow 2\,^1A_1$ or the $\pi \rightarrow \pi^*$ transition. The gas phase UV absorption spectrum confirms the valence nature of this strong band at λ_{max}= 225 nm, extending up to 245 nm. On the other hand, UV-vis absorption of 2-chlorothiophene, with $\lambda_{max} \approx 235$ nm, extends up to 260 nm. However, it does not show any vibronic structure, like thiophene. Similarly, 2-bromo-5-chlorothiophene strongly absorbs at ≈ 245 nm, and the absorption extends up to 270 nm. To understand the nature of the transitions involved in these halogenated thiophenes at 235 nm, *ab initio* molecular orbital (MO) calculations were performed, in detail, on these two compounds studied, along with thiophene. We optimized the ground state geometries of thiophene (C_{2v}), 2-chlorothiophene (C_s) and 2-bromo-5-chlorothiophene (C_s), employing density functional theory (DFT) calculation, using cc-pVDZ set of basis sets, maintaining their point group, as mentioned in the parenthesis. The augmented basis set, with diffuse and triple zeta functions, namely, aug-cc-pVTZ, was used for obtaining the vertical excitation energies for various transitions using time-dependent (TD) DFT. Although the calculated vertical transition energies slightly differ as compared to the experimental results, the nature of transitions and that of the orbitals involved are accurately predicted, using this method. The orbitals participating in the different electronic transitions were visualized, for better understanding of the process. The vertical excitation energies and the respective oscillator strengths of several low-lying singlet states of thiophene, 2-chlorothiophene and 2-bromo-5-chlorothiophene are shown in Table 7.3.

Table 7.3: Vertical excitation energies (eV) and oscillator strengths (given in parentheses) of low-lying singlet states of thiophene, 2-chlorothiophene and 2-bromo-5-chlorothiophene with respective designation. The C_{2v}, C_s and C_s symmetry designation of thiophenes, nature of transition and MO's involved in the transitions are also indicated in the heading for thiophene, 2-chlorothiophene and 2-bromo-5-chlorothiophene.

	Thiophene (C_{2v})			2-Chlorothiophene (C_s)			2-bromo-5-chlorothiophene (C_s)	
Excited State	State designation and Type of transition	Vertical excitation energy (eV) and Oscillator strength (in parenthesis)	Excited State	State designation and Type of transition	Vertical excitation energy(eV) and Oscillator strength (in parenthesis)	Excited State	State designation and Type of transition	Vertical excitation energy(eV) and Oscillator strength (in parenthesis)
S_1	$1\,^1B_2$ $\pi \to \pi^*$ $22 \to 23$ $21 \to 29$	5.73 (0.0796)	S_1	$2\,^1A'$ $\pi \to \pi^*$ $30 \to 31$	5.27 (0.1309)	S_1	$1\,^1A''$ $\pi \to \sigma^*_{C\text{-}S,\,C\text{-}Br}$ $47 \to 49$	4.78 (0.0001)
S_2	$2\,^1A_1$ $\pi \to \pi^*$ $21 \to 23$ $22 \to 29$	5.84 (0.0801) ($\lambda_{max} = 5.51$ eV) (Ref.9)	S_2	$1\,^1A''$ $\pi \to \sigma^*_{C\text{-}S,\,C\text{-}Cl}$ $30 \to 33$	5.55 (0.0005)	S_2	$2\,^1A'$ $\pi \to \pi^*$ $47 \to 48$	4.86 (0.2023)
S_3	$1\,^1A_2$ $\pi \to 3s$ $22 \to 24$	5.88 (0.0000)	S_3	$2\,^1A''$ $\pi \to 3s$ $30 \to 32$	5.63 (0.0016)	S_3	$2\,^1A''$ $\pi \to \sigma^*_{C\text{-}S},\,3s$ $47 \to 50, 51$	5.24 (0.0006)
S_4	$1\,^1B_1$ $\pi \to \sigma^*_{C\text{-}S}$ $22 \to 25$	5.98 (0.0111)	S_4	$3\,^1A'$ $\pi \to \pi^*$ $29 \to 31$ $30 \to 37$	5.76 (0.0677)	S_4	$3\,^1A'$ $\pi \to \pi^*$ $46 \to 48$ $47 \to 54$	5.70 (0.0441)
S_5	$2\,^1A_2$ $\pi \to \sigma^*_{C\text{-}S}$ $21 \to 25$	6.23 (0.0000)	S_5	$3\,^1A''$ $\pi \to \sigma^*_{C\text{-}S}$ $30 \to 34$	5.89 (0.0043)	S_5	$3\,^1A''$ $\pi \to \sigma^*_{C\text{-}S}$ $47 \to 50, 51$	5.72 (0.0007)
S_6	$2\,^1B_1$ $\pi \to 3s$ $21 \to 24$	6.27 (0.0005)	S_6	$4\,^1A''$ $\pi \to \sigma^*_{C\text{-}S,\,C\text{-}Cl}$ $29 \to 33$	6.12 (0.0001)	S_6	$4\,^1A''$ $\pi \to \sigma^*_{C\text{-}S,\,C\text{-}Br}$ $46 \to 49$	5.93 (0.0008)

The present computational results for thiophene are found to be in good agreement with the previous results[183]. So, we strongly believe that the present computational method can be well applied, to understand the excited states of 2-chlorothiophene and 2-bromo-5-chlorothiophene as well, and will provide very accurate data. Six excited states are considered, out of which, the four states are valence states and the remaining two are Rydberg states. For understanding the nature of initial excitation, only singlet states are considered because of their non-zero oscillator strengths. However, since the molecules contain heavy atoms like sulfur and bromine, the triplet states can also play a role in the photodissociation process because of efficient singlet-triplet cross-over. The various computed HOMO, LUMO and other MOs involved in the transition of all the above compounds are depicted in FIG. 7.8 and will be now discussed in brief. The valence states are primarily due to excitations from the π orbitals, mostly, HOMO and HOMO-1, to π^* orbitals, mostly, LUMO and LUMO+6, in all the cases. The other valence states are from the π orbitals to σ^*_{C-S} orbitals for thiophene, $\sigma^*_{C-S, C-Cl}$ for 2-chlorothiophene and $\sigma^*_{C-S, C-Cl, C-Br}$ for 2-bromo-5-chlorothiophene. Besides these valence states, Rydberg states involving excitations to a diffuse 3s orbital are also included, for comparison. For 2-chlorothiophene, the S_1 ($2\,^1A'$) state is still a π-π^* transition, with an oscillator strength of ~0.13 at 5.27 eV (235 nm). The second π-π^* transition is S_4 ($3\,^1A'$), at 5.76 eV (215 nm), with an oscillator strength of ~ 0.07. The S_2 ($1\,^1A''$) and S_3 ($2\,^1A''$) are mainly $\pi\rightarrow\sigma^*_{C-S, C-Cl}$ and π-3s transitions, respectively, with very low oscillator strengths (~0.001), as compared to the π-π^* transition. Similarly, for 2-bromo-5-chlorothiophene, the S_1 ($1\,^1A''$) state is a $\pi\rightarrow\sigma^*_{C-Br, C-Cl}$ transition at 4.78 eV (259 nm) with an oscillator strength value of ~0.0001. The S_2 ($2\,^1A'$) and S_4 ($3\,^1A'$) are π-π^* transitions at 4.86 eV (255 nm) and 5.70 eV (217 nm), respectively, with the

corresponding oscillator strengths of ~ 0.22 and ~ 0.046. The S_3 ($2\ ^1A''$), S_5 ($3\ ^1A''$) and S_6 ($4\ ^1A''$) are mainly π-$\sigma^*_{C-S,\ C-Cl}$, π-σ^*_{C-Br}, and π-σ^*_{C-S} transitions, respectively, with an oscillator strength value of almost zero.
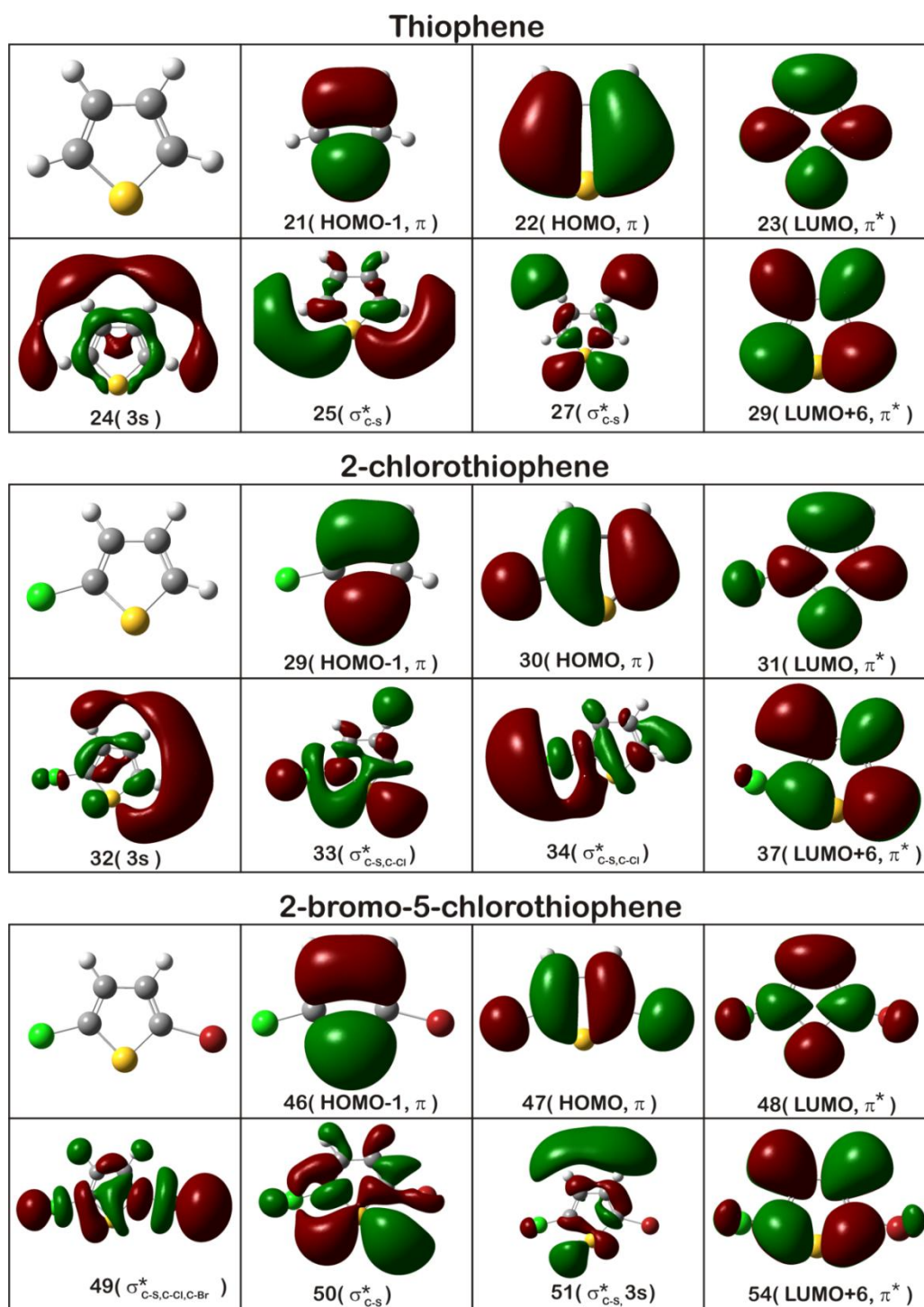
FIG.7.8: Computed HOMO, LUMO, along with other MOs involved in the transition of thiophene, 2-chlorothiophene, and 2-bromo-5-chlorothiophene at 235 nm.

Considering the corresponding wavelengths for vertical excitation energies and the respective oscillator strengths of the various transitions, it is evident that at 235 nm, all the three compounds have a π-π* transition. The excited state, with π-π* transition, adiabatically correlates only with highly excited photoproducts, and it is not feasible in a single-photon excitation in the present case. Therefore, it is assumed that, in the above two compounds, the initially prepared ($\pi\pi$*) states cross over to the nearby states, mostly ($\pi\sigma$*)$_{C-S, C-Cl, C-Br}$ state, from where the C–Cl/C–Br bond cleavages, forming Cl/Br atoms, and the ring opens by scission of the C–S bond. Also, the initially prepared ($\pi\pi$*) or ($\pi\sigma$*)state can undergo rapid internal conversion to the ground state, from where various other dissociation channels can occur, in addition to the above mentioned pathways from the excited state.

7.4.2 TRANSLATIONAL ENERGY RELEASE AND ANISOTROPY PARAMETER

In the photoexcitation of 2-chlorothiophene and 2-bromo-5-chlorothiophene at 235 nm, several processes have been proposed as primary dissociation pathways, and these are given as follows:

i) 2-chlorothiophene

 $\rightarrow$ + Cl $\qquad\qquad$ ΔH = 98.8 kcal/mol $\qquad$ (7.6)

$\qquad\qquad\rightarrow$ S−C(Cl)=CH−CH=CH *(C−S1)* $\quad$ ΔH = 84.8 kcal/mol $\qquad$ (7.7)

$\qquad\qquad\rightarrow$ S−CH=CH−CH=C−Cl *(C−S2)* $\quad$ ΔH = 85.5 kcal/mol $\qquad$ (7.8)
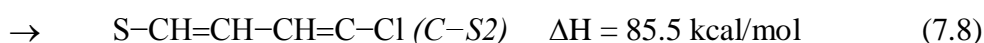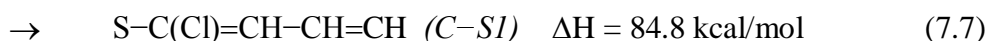
As discussed earlier, ΔH values are calculated at G3B3 level of theory. The reaction (7.6) involves the cleavage of the C–Cl bond, while reactions (7.7) and (7.8) involve ring opening of thiophene structure, by C–S bond cleavage, forming two different

types of biradicals, namely, *C–S1* and *C–S2,* as discussed earlier. The Cl atom can be produced directly as a primary product, as in reaction (7.6), and also from the subsequent dissociation of the biradicals, *C–S1* and *C–S2*, as shown below.

$$S-C(Cl)=CH-CH=CH \ (C-S1) \rightarrow S=C=CH-CH=CH \ + \ Cl \ \ \Delta H = 45.0 \ kcal/mol$$

(7.9)

$$S-CH=CH-CH=C-Cl \ (C-S2) \rightarrow S-CH=CH-CH=C \ + \ Cl \ \ \Delta H = 69.2 \ kcal/mol$$

(7.10)
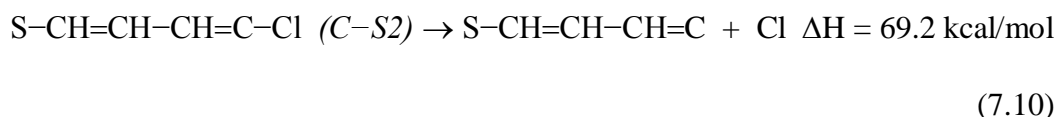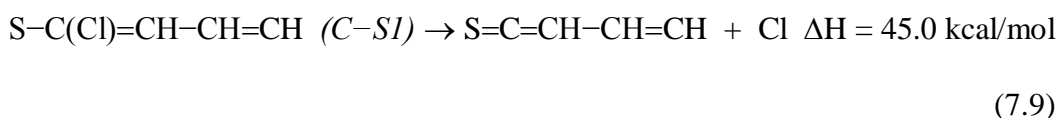
The subsequent formation of Cl atom, after the initial C–S bond cleavage, is ruled out in present experimental condition due to its high endothermicity. Hence, the formation of Cl atom is possible only from the cleavage of the C–Cl bond in the parent molecule itself, as depicted in reaction (7.6). In following paragraphs, the initial C–X bond rupture process on the ground or from an excited potential energy surface is discussed, depending on the dynamics of the processes.

The two types of $P(v)$ or $P(E_T)$ were observed for $Cl(^2P_{3/2})$, in the C–Cl bond fission, one producing fragments with relatively higher recoil energies and the other producing fragments with lower recoil energies. The $P(E_T)$ for the high-translational energy component peaks near 3 kcal/mol, and extends up to ~17 kcal/mol (FIG. 7.6[A]). Similarly, the low translational energy component peaks near 1 kcal/mol, and extends up to ~3 kcal/mol. The presence of two types of $P(E_T)$ in the C–Cl bond fission is analogous to other systems involving a π-π* transition. On the contrary, only one type of $P(v)$ or $P(E_T)$ was observed for $Cl*(^2P_{1/2})$ formation channel, which peaks near 4 kcal/mol, and extends up to ~18 kcal/mol (FIG. 7.5[B]). Although in the case of substituted halo thiophenes, the transitions at 235 nm are purely π-π* in nature, the molecule can predissociate after crossover to the nearby C–Cl repulsive state. It is

also possible that the other translational energy channel having lesser E_T, results from the C–Cl fission, following internal conversion to the ground electronic state.

The partitioning of the available energy into various degrees of freedom of the fragments is mainly governed by the nature of the dissociative potential energy surface, and can be predicted, using simple models, such as impulsive and statistical. It is well known that the energy partitioning in a dissociative event on a repulsive surface is well described by an impulsive model[121]. In this model, the distribution of energy among the product states is governed by the dissociative event, i.e., by the repulsive force acting during the breaking of the parent molecule into the fragments. For example, in the present case, by using only conservation of momentum and energy, and the impulse assumption, one finds that the fraction of the available energy (E_{avl}) released as translational energy is given by

$$E_T = \left(\frac{\mu_{C,Cl}}{\mu_{c-(C_4H_3S),Cl}} \right) E_{avl} \text{, and} \qquad f_T = E_T/E_{avl} \qquad (7.15)$$

where $\mu_{C,Cl}$ is the reduced mass of the C and Cl atoms, $\mu_{c-(C_4H_3S),Cl}$ is the reduced mass of the thiophene radical, c-(C_4H_3S) and Cl, E_{avl} is the available energy and f_T is the fraction of the available energy going into the translational modes of the fragments. For 2-chlorothiophene, the ratio of the reduced masses is 0.36. The available energy is given by,

$$E_{avl} = E_{h\nu} - D_0^0(c - C_4H_3S - Cl) - E_{SO} \qquad (7.16)$$

where $E_{h\nu}$ is the photon energy (122.0 kcal/mol), $D_0^0(c - C_4H_3S - Cl)$ is the C–Cl bond dissociation energy, and E_{SO} is the spin-orbit energy of chlorine (2.4 kcal/mol). The bond dissociation energy is taken as 99.0 kcal/mol. Thus, E_{avl} value for the Cl and Cl* channels are 23.0 and 20.6 kcal/mol, respectively. The experimental average translational energies (E_T) for the fast and slow components are found to be 3.0±1.0

and 1.0 ± 0.5 kcal/mol, respectively, for Cl channels, giving the f_T values of 0.13 and 0.04. Thus, the experimentally determined f_T value is considerably lower than the predicted value of 0.36, using the impulsive model. Similarly, a f_T value of 0.17 is determined for Cl* channel. The much lower experimental f_T value obtained in the dissociation of 2-chlorothiophene, as compared to the predicted value using impulsive model, prompted us to apply the statistical model also, as discussed in following paragraph.

A statistical dissociation process occurs predominantly, if the photo-excited parent molecule is so long-lived that the excess energy is partitioned statistically amongst the available degrees of freedom of the products. This may be applicable in a process wherein a rapid internal conversion to the ground electronic state takes place, followed by the subsequent slow dissociation. Under these circumstances, in a large molecule, with many low frequency modes, a relatively small amount of the excess energy is partitioned into translational motion of the products. For this kind of dissociation process, *a priori* calculations[118,200] were adopted, along with a simple analytical expression established by Klots[120], relating the mean translational energy release, E_T, and the E_{avl}, for a statistical barrier-less dissociation process. These statistical methods predict a f_T value of ~0.06, which matches well with the experimental value of 0.04, for the slow component. This implies that the slow component of Cl is mainly due to the dissociation process, taking place on the ground state potential energy surface, after internal conversion via some curve crossing mechanism. The measured f_T value of 0.13, for the faster component of the Cl atom channel, is higher than the predicted statistical. Similarly, the measured f_T value (0.17) for the Cl* channel, lies in between the values predicted by the impulsive and

statistical models. Thus, the fast component of Cl and Cl* formation channel does not occur on the ground state potential energy surface.

In the present case, the impulsive model does not predict well the experimental results. One of the reasons for such a failure of the impulsive model may be assigned to the scenario, similar to that in CCl_4[201]. In CCl_4, it is proposed that an extensive internal vibrational redistribution takes place, before enough energy is localized in one bond. Consequently, in photodissociation of CCl_4 at 234 nm, the f_T values predicted, using impulsive and statistical models, are 0.33 and 0.13, respectively, whereas the experimental f_T value is 0.10, for both Cl and Cl*. However, a small contribution from the high energy E_T component was observed in the Cl* channel. In halogenated thiophenes, as discussed earlier, the initial excitation is pure π-π* in nature. Hence, to dissociate a C–X bond, an extensive internal vibrational redistribution must take place to localize enough energy in the C–X bond in the crossover process from the (ππ*) state to the nearby (πσ*) state. This process is in complete contrast to the impulsive model assumption.

Another possible reason for deviation of the measured f_T value from the impulsive value can be the error involved in the experimental determination of translational energy. Since the E_{avl} is much lower in all the cases, due to high D_0^0 for the various channels, the width of TOF profile is comparable with the instrumental function width. Due to this reason, the error involved in the determination of E_T is slightly higher, and may change the f_T values considerably. However, the f_T values for Cl* and the fast component of Cl are much higher than the values predicted using statistical model. Therefore, we strongly believe that the dynamics of the fast Cl and Cl* formation takes place on the higher excited states, and not on the ground state. Another valid and strong reason to believe the excited state dissociation dynamics for

the fast Cl and Cl* formation lies in the f_T values for Cl*. A careful examination reveals that the f_T value for Cl* (0.17) is higher than that for the Cl fast channel (0.13), despite its low E_{avl}. If the dissociation occurs on the ground state potential energy surface, then the f_T value is expected to be the same for both Cl and Cl*. Also, the relative quantum yield, $\Phi(Cl^*)$, which is 0.19 for 2-chlorothiophene, deviates significantly from its statistical limit (0.33). Finally, the above discussion concludes that the initially prepared 2-chlorothiophene in the $(\pi\pi^*)$ state crosses over to the nearby $(\pi\sigma^*)_{C-Cl}$ state, and subsequently the C–Cl bond cleavage occurs, resulting in the formation of the fast Cl atom.

ii) 2-bromo-5-chlorothiophene

$$\to \quad Br\text{—}\underset{S}{\bigcirc}\bullet \quad + \quad Cl \qquad\qquad \Delta H = 98.8 \text{ kcal/mol}$$

(7.11)

$$\to \quad \bullet\underset{S}{\bigcirc}\text{—}Cl \quad + \quad Br \qquad\qquad \Delta H = 91.2 \text{ kcal/mol}$$

(7.12)

$$\to \quad S\text{−}C(Br)\text{=}CH\text{−}CH\text{=}C\text{−}Cl \qquad \Delta H= \sim 86.0 \text{ kcal/mol}$$

(7.13)

$$\to \quad S\text{−}C(Cl)\text{=}CH\text{−}CH\text{=}C\text{−}Br \qquad \Delta H= \sim 86.0 \text{ kcal/mol}$$

(7.14)
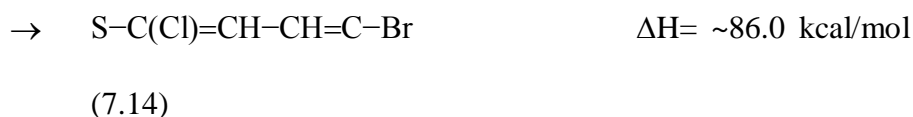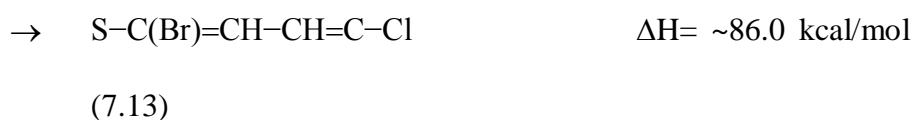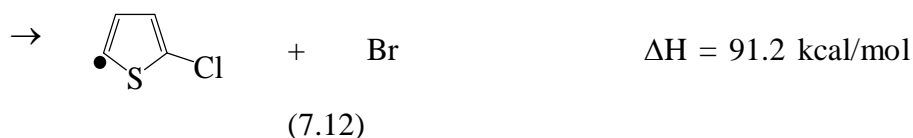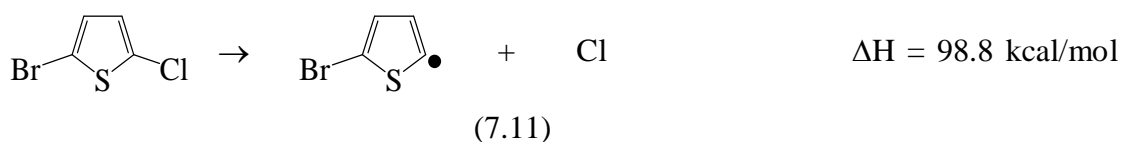
In the case of 2-bromo-5-chlorothiophene, the reaction (7.11) involves cleavage of C–Cl bond, while the reaction (7.12) involves cleavage of the C–Br bond, forming Cl and Br atoms, respectively. The reactions (7.13) and (7.14) are involved in the ring opening of thiophene structure, with the cleavage of the C–S bond, forming two

different types of biradicals. The subsequent formation of Cl/Br atoms from these biradicals is ruled out energetically. Hence, the formation of halogen atom is attributed to the initial cleavage of the C-X bond directly from the parent molecule, similar to that in 2-chlorothiophene.

For 2-bromo-5-chlorothiophene, only one type of P(v) or [P(E$_T$)] was observed for all the halogen atom fragments detected. The P(E$_T$) for Cl(^{2}P$_{3/2}$) derived from the forward convolution fit peaks near 3.5 kcal/mol, and extends up to ~17 kcal/mol. The P(E$_T$) for Cl*(^{2}P$_{1/2}$) channel peaks near 5 kcal/mol, and extends up to ~18 kcal/mol. Similarly, for Br atom elimination channel, the P(E$_T$) peaks near 2 kcal/mol, and extends up to ~14 kcal/mol. For Br* channel, it peaks near 3.6 kcal/mol, and extends up to ~15 kcal/mol. For this halogenated thiophene as well, the f_T values for Cl (0.15) and Cl* (0.24) elimination channel, are much higher than the values predicted using statistical model (0.06), and lower than that predicted, using impulsive model (0.31). In the present case, the measured f_T value (0.24) for Cl* is closer to the value predicted, using the impulsive value (0.31). A similar trend is also observed in the case of Br atom elimination channel. The f_T value (0.17) for Br* matches very well with the value predicted, using impulsive model (0.22), within experimental uncertainties. Although, for Br atom, the f_T value matches very well with the statistical value, the formation of Br atom is believed to be from the excited state only, as discussed earlier for slow component of Cl of 2-chlorothiophene. Also, the P(E$_T$) for Cl(Cl*) and Br(Br*) extend up to the total available energy, with non-Maxwell-Boltzmann type of distribution having a large width. Here also, if the molecule relaxes to the ground state, the most favorable process would be the C−S bond cleavage, which opens up the ring structure. However, the formation of Br on ground state potential energy surface is not totally ruled out. The details of the E$_T$ and

f_T, for all the channels of 2-bromo-5-chlorothiophene, along with that of 2-chlrothiophene, are given in Table 7.4.

Table 7.4: The average translational energy, $\langle E_T \rangle$, available energy (E_{avl}), f_T value, and the relative quantum yield of spin-orbit states (Φ) for photodissociation of 2-chlorothiophene and 2-bromo-5-chlorothiophene at hv=235 nm. The excitation energy is 122 kcal/mol. The D_0^0(C−X) for Cl and Br elimination channel is taken as 99.0 and 91.0 kcal/mol, respectively. All energies are in kcal/mol.

Molecule	Channel		$\langle E_T \rangle$	E_{avl}	$f_{T=}\langle E_T \rangle/E_{avl}$		Relative quantum yield (Φ)
					Experimental	Impulsive (Statistical)	
2-chloro-thiophene	Cl	Fast (0.8)	3.0±1.0	23.0	0.13	0.36(0.06)	0.81±0.08
		Slow (0.2)	1.0±0.5		0.04	0.36(0.06)	
	Cl*		3.5±1.0	20.6	0.17	0.36(0.06)	0.19±0.06
2-bromo-5-chloro-thiophene	Cl		3.5±1.0	23.0	0.15	0.31(0.06)	0.81±0.08
	Cl*		5.0±1.5	20.6	0.24	0.31(0.06)	0.19±0.06
	Br		2.0±1.0	31.0	0.06	0.22(0.06)	0.92±0.10
	Br*		3.6±1.0	20.5	0.17	0.22(0.06)	0.08±0.03

Very recently, Wang and co-workers[194] studied the dynamics of Br atom formation in the photodissociation of bromothiophenes, namely, 2-bromothiophene and 3-bromothiophene, at 267 nm, using ion velocity imaging technique. The Br/Br* channel in these studies showed multiple components in the translational energy distribution, P(E_T). The f_T values were estimated as large as 0.96. In addition, they have shown anisotropy in the products. All these results completely contradict our

findings in photodissociation of 2-bromo-5-chlorothiophene for Br/Br* elimination channel at 235 nm. In their results, the $P(E_T)$ overshoots the available energy, for some of the components, despite a lower value of ~73 kcal/mol was used for the $D_0^0(c - C_4H_3S - Br)$ bond dissociation energy, which is almost 18 kcal/mol less than the value recommended recently, and also used by us[199]. This discrepancy may be due to some contribution from the multiphotonic processes in their studies.

In the limit of an instantaneous dissociation process, the parameter β is given by $\beta = 2\langle P_2(\cos\theta_m)\rangle$, where θ_m is the molecular frame angle between the molecular transition dipole moment and the photofragment recoil direction, and $P_2(\cos\theta_m)$ is the second order Legendre polynomial. Hence, for a parallel or a perpendicular transition, one would expect anisotropy of +2 or −1, respectively. The recoil anisotropy, β, for the all the halogen atom fragments, measured in the present work is ~0.0, which indicates an isotropic dissociation process. This value of β does not give any indication of the nature of the transition dipole moment in dissociation of halogenated thiophenes. As discussed in our previous work[202], the anisotropy in an impulsive dissociation can be reduced, or wiped out, due to several factors, such as mixed initial excitation with both parallel and perpendicular components, longer dissociation lifetime, dissociation not occurring from a single geometry rather from a range of geometries, etc. In halogenated thiophenes, with C_s geometry, for the π-π* transition, with [1]A′ symmetry, the transition dipole moment is mainly along x- and y- direction. However, for the (πσ*) state, with [1]A″ symmetry, the transition dipole moment is mainly along z-direction. Therefore, in the present case, for the formation of Cl and Br atoms, the molecule has to cross over from the initially prepared (ππ*) state to the (πσ*) state. During this crossover period, the molecule may rotate. The absence of recoil anisotropy in the present studies is expected mainly due to the relatively longer

dissociation lifetime, since the dissociation is not from the initially prepared state, rather from the crossover state.

7.5   CONCLUSION

The photodissociation of two halogenated thiophenes, namely, 2-chlorothiophene and 2-bromo-5-chlorothiophene, has been carried out at around 235 nm, and the dynamics of C–X (X=Cl, Br) bond dissociation is investigated, using resonance-enhanced multiphoton ionization, coupled with a time-of-flight mass spectrometer. The excitation at 235 nm prepares the molecules in the $(\pi\pi^*)$ state. We have determined the photofragment speed distribution, the anisotropy parameter β and the spin-orbit branching ratio, for chlorine and bromine atom elimination channels, to gain insights into the dynamics of halogen atom formation. Polarization-dependent and state-specific TOF profiles are utilized, to get translational energy distributions, using a forward convolution method and taking into account the fragment anisotropies. The anisotropy parameters for both Cl(Cl*) and Br(Br*) are the same, and characterized by values of 0.0±0.05. In the translational energy distribution for the chlorine atom elimination channel in the case of 2-chlorothiophene, we have observed two components for Cl, but only one component for the Cl*. The average translational energies for the fast and the slow components of the Cl channel are 3.0±1.0 and 1.0±0.5 kcal/mol, respectively. For Cl*, the average translational energy is 3.5±1.0 kcal/mol. However, for 2-bromo-5-chlorothiophene, we have observed only one component for all the halogen atom channels in translational energy distribution. The average translational energies for the Cl and Cl* channels are 3.5±1.0 and 5.0±1.0 kcal/mol, respectively. Similarly, the average translational energies for the Br and Br* channels are 2.0±1.0 and 3.5±1.0 kcal/mol, respectively. The partitioning of energy into the translational modes is interpreted with the help of various models,

such as impulsive and statistical models. The ΔH_f^{298} value for 2-chlorothiophene is estimated theoretically to be 23.5 kcal/mol.

CHAPTER 8

SUMMARY AND FUTURE DIRECTIONS

This thesis presents work on the photodissociation dynamics of some important organic molecules, which have been studied mainly by employing the Laser Photolysis-Laser Induced Fluorescence (LP-LIF) and Molecular Beam-Resonance Enhanced Multiphoton Ionization-Time of Flight-Mass Spectrometry (MB-REMPI-TOF-MS) techniques. These techniques have been used to probe nascent ro-vibrational state distributions of photofragments. The vibrational and rotational energy distributions in a photofragment are measured by employing LIF technique, whereas the translational energy distribution is obtained from time of flight-mass spectrometer (TOF-MS) and Doppler shift studies. The dynamics involved in photodissociation is deduced by measuring the partitioning of the available energy in different modes of the photoproducts. Angular distributions of photoproducts are estimated by performing the polarization experiments in the REMPI measurements. The mechanism of the photodissociation reactions has been proposed based on experimental and theoretical results. This concluding chapter summarizes all the results obtained from experimental and theoretical work carried

out, and discusses the relevance of these results in addressing the basic aim of the thesis. It also includes a required assistive job that is expected to extend the scope of the research in future direction and also a fruitful marriage between experimental and theoretical work.

An introductory chapter gives a brief account of the general overview of photodissociation dynamics and importance of its study, along with various aspects of this process, which are keys in understanding the dynamics of the event. A description of the instrumentation and analysis of acquired data are the focus of chapter 2. Earlier, the LP-LIF set-up was routinely used for probing photofragments of organic compounds, which are in a liquid state at room temperature. The modification that had been made for flow of the vapour from the solid samples through the reaction chamber is discussed.

The Chapters 3, 4 and 5 in this thesis mainly deals with the study of gas phase photodissociation dynamics of oximes, diketo compound and nitro compounds, respectively, using the LP-LIF technique. The nascent OH photofragment formed on photolysis, is probed state-selectively.

The cyclopentanone oximes (CPO) and cyclohexanone oxime (CHO) are the two oximes studied in this work. Upon excitation at 193 nm, CHO and CPO in the vapour phase produce the OH photofragment. Based on our experimental results and molecular orbital calculations, it is suggested that both CHO and CPO molecules at 193 nm are excited to the S_2 state, which relaxes fast to the T_2 state. The electronically excited CHO and CPO molecules undergo the N–OH bond dissociation from the T_2 state to produce OH. In both CHO and CPO, this dissociation channel has an exit barrier, since the corresponding transition state for OH formation could be located. Except for some differences in the values of energy

partitioned to different degrees of freedom of products in CHO and CPO, overall dissociation dynamics for the OH producing channel remains similar. Thus, the effect of the ring size of CHO and CPO is not pronounced on the dynamics of the N–OH bond dissociation.

The 1,2-cyclohexanedione (CHD) is a diketone, which is expected to have dominant enolic character at room temperature. It is observed that, the enolic form of CHD with hydrogen bonding is lower in energy than the keto form. This molecule generates the OH radical upon excitation at 266, 248, and 193 nm, to ($\pi\pi^*$) and Rydberg states. The nascent state of the OH photofragment is probed with the LIF technique. The detailed *ab initio* quantum calculations suggest that at 266 nm photolysis, the OH produced with higher rotational temperature is formed from an excited state, which is devoid of any effective H-bonding. The OH formed with lower rotational temperature at 266 nm and OH formed at 248 nm are attributed to the structure where the H-bonding is not effective. At 193 nm excitation, the initially prepared Rydberg state can cross over to a nearby σ^* repulsive state along the C–O bond, from where the dissociation can take place. The exit barrier for the OH dissociation channel is estimated to be 14 kcal/mol. The existence of a dynamical constraint due to strong hydrogen bond in the ground state is effectively present in the dissociation process at 266, and somewhat minimized at 248 nm photolysis.

The photodissociation of ClNT at 266, 248, and 193 nm and NCP at 193 nm generates the OH radical, as detected by Laser induced fluorescence spectroscopy. The initial excitation of ClNT at 193 nm absorption can be assigned to the $\pi \rightarrow \pi^*$ transition, while at around 248 nm to the n$\rightarrow\pi^*$ transition. For NCP excitation at 193 nm consists of a strong $\pi \rightarrow \pi^*$ transition. From experimental results for ClNT molecule we have deduce that although photoexcitation energy at 193, 248 and266

nm are quite different, the mechanism of OH formation is similar. From the theoretical calculation of energetic of different paths of OH formation and feasibility of the reaction, it was concluded that the OH is formed as a primary product via an intermediate. Based on the experimental results from photodissociation of NCP at 193 nm and theoretical calculations, we proposed a mechanism involving elimination of OH via an aci-form.

Though, we have proposed the mechanisms for the photodissociation process for above mentioned polyatomic molecules using LP-LIF technique, the better insight of OH formation dynamics can be obtained by performing polarization experiments for the OH fragment. From information obtained on the angular distributions from these studies, the vector quantities associated with the photodissociation process can be estimated.

The Chapters 6 and 7, cover the dissociation dynamics studies on fumaryl chloride and halogenated thiophenes, respectively, at 234 nm. In these investigations, REMPI-TOFMS was employed for probing halogen atom photofragments. The chapter 6 gives the details of the investigation on photodissociation dynamics of fumaryl chloride (ClCO–CH=CH–COCl), a molecule with two C=O groups and a C=C group in conjugation, in a supersonic molecular beam at around 235 nm. At this excitation wavelength, the molecule generates a chlorine atom. From the experimental results for fumaryl chloride it is proposed that on photoexcitation at 235 nm, the initially prepared $S_2(^1\pi\text{-}\pi^*)$ state crosses over to various states, namely, $S_1(^1 n\text{-}\pi^*)$, $(n\text{-}\sigma^*)$, and the ground state, and the Cl atom can be formed from all these states, with different values of E_T. Apart from the chlorine atom elimination channel, the molecular HCl elimination is also observed in the photodissociation of fumaryl chloride. The observation of the HCl molecular elimination channel in the

dissociation process and the bimodal translational energy distribution of the chlorine atom clearly indicate the existence of a crossover mechanism from the initially prepared state to the ground state.

The study reported in chapter 7 is undertaken to understand the photodissociation dynamics of two halogen substituted thiophenes, namely, 2-chlorothiophene and 2-bromo-5-chlorothiophene. The excitation at ~235 nm prepares the molecules in the $(\pi\pi^*)$ state. In photodissociation of 2-chlorothiophene a bimodal distribution of translational energy for Cl is observed with fast & slow components, whereas a single component is observed for Cl*. In photodissociation of 2-bromo-5-chlorothiophene single component is observed for both Cl/Cl* and Br/Br*. The Cl* and fast Cl from 2-chlorothiophene attributed to the dissociation from the excited π-σ^*_{C-Cl} state formed by intramolecular vibrational redistribution, while slow one is from ground state formed via crossover mechanism. The f_T values measured experimentally for Cl* and Br* matches well with f_T^{imp} indicating their formation from the excited state. However, the f_T values of Cl and Br match well with f_T^{stat} indicating their formation from the ground state. The dynamic information suggests that due to the presence of the weak C-Br bond the C-Cl bond cleavage from the ground state is suppressed. Due to strain in the ring, the C-Br bond cleavage is able to compete with the low energy C-S bond cleavage, in the ground state. We have also estimated the ΔH_f^{298} of 2-chlorothiophene theoretically to be 23.5 kcal/mol.

In all the work reported in the thesis employing REMPI technique, the photolysis as well as ionization was carried out by single laser beam (same wavelength, single colour experiments). The better information about excited PESs and their interaction can be deduced by accessing various excited PESs. This will be possible in two colour experiments by employing different frequencies for the pump

and probe lasers. The resolution in translational energy distribution measurement can be improved (better than 1%) by employing the velocity map imaging (VMI) techniques.

Using both LP-LIF and REMPI techniques, the available energy partitioning in various states of OH/Cl and Br was obtained. However, the energy partitioning in the co-fragment was not measured. The measurement of energy distribution in co-fragment of OH/Cl will provide more dynamical information about the system and thus the predicted nature of dissociative PES will be more accurate.

Because of computation resource constraints we have used relatively lower level of theoretical calculations to support the experimental results. This invariably has higher error level, which can be reduced to a greater extent by performing calculations at higher level using Linux system. This, in particular, will be useful in deducing the dynamics of dissociation process occurring on the dissociative surfaces having strong interaction with other nearby PESs. Thus, high level of theoretical calculation is required to obtain more refined results concerning the dynamics of the dissociation process.

References

1   D. C. Neckers, in *Encyclopedia of Chem. Tech.* (Wiley, 2008), pp. 1.

2   J. I. Steinfeld, J. S. Francisco, and W. L. Hase, *Chemical Kinetics and Dynamics*, 2 ed. (Prentice-Hall, Inc., New Jersey, 1999).

3   R. D. Levine and R. B. Bernstein, *Molecular Reaction Dynamics and Chemical Reactivity*. (Oxford University Press, New York, 1987).

4   R. D. Levine, *Molecular reaction Dynamics*. (Cambridge University Press, Cambridge, 2005); Y. T. Lee, Angew. Chem., Int. Ed. Engl. **26**, 939 (1987); D. R. Herschbach, Angew. Chem., Int. Ed. Engl. **26**, 1223 (1987); J. C. Polanyi, Angew. Chem., Int. Ed. Engl. **26**, 925 (1987).

5   M. Kasha, in *Light and Life*, edited by W. D. McElory and B. Glass (John Hopkins University Press, Baltimore, 1960).

6   K. K. Rohatgi-Mukherjee, *Fundamentals of Photochemistry*. (New Age International(P) Ltd., Delhi, 1986).

7   F. F. Crim, J. Phys. Chem. **100**, 12725 (1996).

8   R. Schinke, *Photodissociation Dynamics*. (2006).

9   E. F. v. Dishoeck and R. Visser, *Molecular Photodissociation*. (Springer, 2011).

10   A. Kantrowitz and J. Grey, Rev. Sci. Instrum. **22** (5), 328 (1951).

11   M. D. Morse, *Supersonic Molecular Beams*. (Academic Press, Inc., 1996).

12   L. J. Butler, Annu. Rev. Phys. Chem. **49**, 125 (1998); P. W. Kash, G. C. G. Waschewsky, L. J. Butler, and M. M. Francl, J. Chem. Phys. **99** (6), 4479 (1993).

13   P. L. Houston, J. Phys. Chem. **91**, 5388 (1987); G. E. Hall and P. L. Houston, Annu. Rev. Phys. Chern. **40**, 375 (1989).

14   E. F. Cromwell, D.-J. Liu, M. J. J. Vrakking, and Y. T. Lee, J. Chem. Phys. **95** (1), 297 (1991).

15   A. H. Zewail, J. Phys. Chem. **100**, 12701 (1996).

16   D. G. Imre, J. L. Kinsey, R. W. Field, and D. H. Katayama, J. Phys. Chem. **86**, 2564 (1982); D. G. Imre, J. L. Kinsey, A. Sinha, and J. Krenos, J. Phys. Chem. **88**, 3956 (1984); B. R. Johnson, C. Kittrell, P. B. Kelly, and J. L. Kinsey, J. Phys. Chem. **100**, 7743 (1996).

17   M. Dantus, M. J. Rosker, and A. H. Zewail, J. Chem. Phys. **87**, 2395 (1987); M. Dantus, M. J. Rosker, and A. H. Zewail, J. Chem. Phys. **89**, 6128 (1988); M. Dantus, R. M. Bowman, M. Gruebele, and A. H. Zewail, J. Chem. Phys. **91**, 7437 (1989).

[18] R. N. Zare, Mol. Photochem. **4**, 1 (1972).

[19] L. J. Butler and D. M. Neumark, J. Phys. Chem. **100**, 12801 (1996).

[20] R. N. Zare and P. J. Dagdigian, Science **185**, 739 (1974).

[21] M. Göppert-Mayer, Ann. Phys. **9**, 273 (1931).

[22] W. Kaiser and C. G. Garret, Phys. Rev. Lett. **7** (6), 229 (1961).

[23] G. Radhakrishnan, D. Ng, and R. C. Estler, Chem. Phys. Lett. **84** (2), 260 (1981).

[24] D. W. Chandler and P. L. Houston, J. Chem. Phys. **87**, 1445 (1987).

[25] D. W. Chandler, M. H. M. Janssen, S. Stolte, R. N. Stickland, J. W. J. Thoman, and D. H. Parker, J. Phys. Chem. **94**, 4839 (1990).

[26] J. W. J. Thoman, D. W. Chandler, D. H. Parker, and M. H. M. Janssen, Laser Chem. **9**, 27 (1988).

[27] D. W. Chandler and D. H. Parker, Adv. Photochem. **25**, 59 (1999).

[28] P. L. Houston, J. Phys. Chem. **100**, 12757 (1996).

[29] W. M. Tolles, J. W. Nibler, J. R. McDonald, and A. B. Harvey, Appl. Spect. **31** (4), 253 (1977); A. M. Zhelttikov, J. of Raman Spect. **31**, 653 (2000).

[30] M. D.Wheeler, S. M. Newman., A. J. Orr-Ewing., and M. N. R. Ashfold, Faraday Trans. **94** (3), 337 (1998).

[31] H. Eyring, J. Chem. Phys. **3**, 107 (1935).

[32] M. G. Evans and M. Polanyi, Trans. Faraday Soc. **31**, 875 (1935).

[33] I. W. M. Smith, *The excited state in Chemical physics*. (John-Wiley, New York, 1975); J. M. Farrar and Y. T. Lee, Ann. Rev. Phys. Chem. **25**, 357 (1974).

[34] B. E. Holmes and D. W. Setser, *Physical Chemistry of fast reaction*. (Plenum, 1979); T. Carrington and J. C. Polanyi, presented at the International review of science, Physical chemistry, Butterworth, London, 1972 (unpublished).

[35] A. F. Tuck, J. Chem. Soc. Faraday Trans. 2 **73**, 689 (1977).

[36] D. B. Galloway, T. G. Meyer, J. A. Bartz, L. G. Huey, and F. F. Crim, J. Chem. Phys. **100** (3), 1946 (1994).

[37] J. T. Muckerman, J. Phys. Chem. **93**, 179 (1989).

[38] S. W. North, D. A. Blank, J. D. Gazelter, C. A. Longfellow, and Y. T. Lee, J. Chem. Phys. **102** (11), 4447 (1995).

[39] R. D. Levine and J. L. Kinsey, *Atom-Molecular Collision Theory: A Guide for the Experimentalist*. (Plenum, New York, 1979.).

[40] P. Pechukas and J. C. Light, J. Chem. Phys. **42**, 3281 (1965); P. Pechukas and C. Rankin, J. Chem. Phys. **44**, 794 (1966).

41   C. Wittig, I. Nadler, H. Reisler, M. Noble, J. Catanzarite, and G. Radhakrishnan, J. Chem. Phys. **83**, 5581 (1985).

42   R. D. Levine and R. B. Bernstein, Acc. Chem. Res. **7** (12), 393 (1974).

43   A. H. H. Chang, D. W. Hwang, X.-M. Yang, A. M. Mebel, S. H. Lin, and Y. T. Lee, J. Chem. Phys. **110** (22), 10810 (1999).

44   T. Bayer and D. F. Swinehart, Commun. ACM **16** (6), 379 (1973).

45   I. Nadler, M. Noble, H. Reisler, and C. Wittig, J. Chem. Phys. **82** (6), 2608 (1985).

46   S. K. Kim, Y. S. Choi, C. D. Pibel, Q. Zheng, and C. B. Moore, J. Chem. Phys. **94** (3), 1954 (1991).

47   F. F. Crim, Ann. Rev. Phys. Chem. **44**, 397 (1993).

48   T. M. Ticich, M. D. Likar, H.-R. Dübal, L. J. Butler, and F. F. Crim, J. Chem. Phys. **87**, 5820 (1987); M. D. Likar, A. Sinha, T. M. Ticich, R. L. Vander Wal, and F. F. Crim, Ber. Bunsen-Ges. Phys. Chem. **92**, 289 (1988); M. D. Likar, J. E. Baggott, A. Sinha, T. M. Ticich, R. L. Vander Wal, and F. F. Crim, J. Chem. Soc., Faraday Trans. 2 **84**, 1483 (1988); M. D. Likar, J. E. Baggott, and F. F. Crim, J. Chem. Phys. **90** (11), 6266 (1989).

49   A. Sinha, M. C. Hsiao, and F. F. Crim, J. Chem. Phys. **92** (10), 6333 (1990).

50   G. H. Dieke and H. M. crosswhite, J. Quant.Spectrocc. Radiat. Transfer **2**, 97 (1961).

51   I. L. Chidsey and D. R. Crossley, J. Quant. spectrosc. Radiat.Transfer **23**, 187 (1980).

52   W. C. Wiley and I. H. McLaren, Rev. Sci. Instrum. **26** (12), 1150 (1955).

53   Y. Matsurni, M. Kawasaki, T. Sato, T. Kinugawa, and T. Arikawa, Chern. Phys. Lett. **155**, 486 (1989).

54   K. Bergmann, R. T. Carter, G. E. Hall, and J. R. Huber, J. Chem. Phys. **109** (2), 474 (1998).

55   D. M. Lubman and R. M. Jordan, Rev. Sci. Instrum. **56** (3), 373 (1985); J. H. Brophy and C. T. Rettner, Chem. Phys. Lett. **67** (2,3), 351 (1979).

56   W. S. McGivern, R. Li, P. Zou, and S. W. North, J. Chem. Phys. **111** (13), 5771 (1999); K. Bergmann, R. T. Carter, G. E. Hall, and J. R. Huber, J. Chem. Phys. **109** (2), 474 (1998).

57   R. N. Zare, *Angular Momentum*. (Wiley-Interscience, New York, 1988).

58   R. Vasudev, R. N. Zare, and R. N. Dixon, J. Chem. Phys. **80**, 4863 (1984); M.

Dubs, U. Bruhlmann, and J. R. Huber, J. Chem. Phys. **84**, 3106 (1986).

59 T. Baumert, S. Pedersen, and A. H. Zewail, J. Phys. Chem. **97**, 12447 (1993).

60 R. J. Wilson, J. A. Mueller, and P. L. Houston, J. Phys. Chem. A **101** (41), 7593 (1997); A. S. Bracker, E. R. Wouters, A. G. Suits, Y. T. Lee, and O. S. Vasyutinskii, Phys. Rev. Lett. **80** (8), 1626 (1998).

61 J. A. Syage, J. Chem. Phys. **105** (3), 1007 (1996).

62 S. W. North, A. J. Marr, A. Furlan, and G. E. Hall, J. Phys. Chem. A **101** (49), 9224 (1997); A. S. Bracker, S. W. North, A. G. Suits, and Y. T. Lee, J. Chem. Phys. **109**, 7238 (1998).

63 B. B. Laud, *Laser and Non-Linear Optics*. (Wiley Eastern Limited, Mumbai, 1993).

64 M. Stuke, in *Topics Appl. Phys.* (Springer, Berlin, Heidelberg, 1992), Vol. 70.

65 W. Demtroder, *Laser Spectroscopy*, Third ed. (Springer, Verlag Berlin Heidelberg, 2008).

66 Biltoft, Benapfl, and Swain, *Vacuum Technology*. (Las Positas College, Las Positas, 2002).

67 D. M. Hoffman, J. H. Thomas, and B. Singh, *Handbook of Vacuum Science and Technology*. (Elsevier Science & Technology Books, 1997).

68 in *Photomultiplier Tubes* (Hamamatsu Catalog).

69 D. A. Skoog, F. J. Holler, and S. R. Crouch, *Instrumental Analysis*, Sixth Indian Reprint ed. (Cengage Learning New Delhi, 2007).

70 D. M. Lubman and R. M. Jordan, Rev. Sci. Instrum. **56** (3), 373 (1985).

71 I. C. Choong and J. A. Ellman, J. Org. Chem. **64** (18), 6528 (1999).

72 K. Rose, J. Am. Chem. Soc. **116** (1), 30 (1994).

73 H. Kath, R. Glaser, and J. Weitkamp, Chem. Eng. Technol. **24**, 150 (2001).

74 D. Parmar and L. T. Burka, Drug Metab. Dispos. **19**, 1101 (1991); L. T. Burka, edited by N. Toxicity Report Series (NC 27709, USA., 1996).

75 C. C. Conaway, G. Nie, N. S. Hussain, and E. S. Fiala, Cancer Res. **51**, 3143 (1991).

76 J. F. Marcoccia, K. Yates, and I. G. Csizmadia, J. Mol. Struct.: Theochem. **360**, 1 (1996).

77 Y. Ogata, K. Takagi, and K. Mizuno, J. Org. Chem. **47**, 3694 (1982).

78 T. Mukai, T. Kumagai, H. Saiki, and Y. Kuwamura, J. Photochem. **17**, 365 (1981).

79 M. F. Haley and K. Yates, J. Org. Chem. **52**, 1825 (1987); M. F. Haley and K. Yates, J. Org. Chem. **52**, 1817 (1987).

[80]   H. J. P. d. Lijser, J. S. Kim, S. M. McGrorty, and E. M. Ullao, Can. J. Chem. Phys. **81**, 575 (2003).

[81]   G. Just and L. S. Ng, Can. J. Chem. **46**, 3381 (1968).

[82]   P. J. Dagdigian, W. R. Anderson, R. C. Sausa, and A. W. Miziolek, J. Phys. Chem. **93**, 6059 (1989).

[83]   P. K. Chowdhury, J. Phys. Chem. **106**, 10488 (2002).

[84]   B. Nizamov and P. J. Dagdigian, J. Phys. Chem. A **107**, 2256 (2003).

[85]   S. Dhanya, H. P. Upadhyaya, A. Kumar, P. D. Naik, and R. D. Saini, J. Chem. Phys. **122**, 184322 (2005).

[86]   M. J. Frisch, G. W. Trucks, H. B. Schlegel, G. E. Scuseria, M. A. Robb, J. R. Cheeseman, J. A. Montgomery, T. V. Jr., K. N. Kudin, J. C. Burant, J. M. Millam, S. S. Iyengar, J. Tomasi, V. Barone, B. Mennucci, M. Cossi, G. Scalmani, N. Rega, G. A. Petersson, H. Nakatsuji, M. Hada, M. Ehara, K. Toyota, R. Fukuda, J. Hasegawa, M. Ishida, T. Nakajima, Y. Honda, O. Kitao, H. Nakai, M. Klene, X. Li, J. E. Knox, H. P. Hratchian, J. B. Cross, C. Adamo, J. Jaramillo, R. Gomperts, R. E. Stratmann, O. Yazyev, A. J. Austin, R. Cammi, C. Pomelli, J. W. Ochterski, P. Y. Ayala, K. Morokuma, G. A. Voth, P. Salvador, J. J. Dannenberg, V. G. Zakrzewski, S. Dapprich, A. D. Daniels, M. C. Strain, O. Farkas, D. K. Malick, A. D. Rabuck, K. Raghavachari, J. B. Foresman, J. V. Ortiz, Q. Cui, A. G. Baboul, S. Clifford, J. Cioslowski, B. B. Stefanov, A. L. G. Liu, P. Piskorz, I. Komaromi, R. L. Martin, D. J. Fox, T. Keith, M. A. Al-Laham, C. Y. Peng, A. Nanayakkara, M. Challacombe, P. M. W. Gill, B. Johnson, W. Chen, M. W. Wong, C. Gonzalez, and J. A. Pople, Gaussian 03 (Gaussian, Inc., Pittsburgh, PA, , 2003).

[87]   G. H. Dieke and H. M. Crosswhite, J. Quant. Spectrosc. Radiat. Transfer **2**, 97 (1961).

[88]   I. L. Chidsey and D. R. Crosley, J. Quant. Spectrosc. Radiat. Transfer **23**, 187 (1980).

[89]   J. F. Ogilvie, Can. J. Spectrosc. **19**, 89 (1974).

[90]   S. S. Hunnicutt, L. D. Waits, and J. A. Guest, J. Phys. Chem. **95** (2), 562 (1991).

[91]   D. L. Osborn, H. Choi, D. H. Mordaunt, R. T. Bise, D. M. Neumark, and C. M. Rohlfing, J. Chem. Phys. **106**, 22 (1997); J. L. Miller, L. R. MacCunn, M. J. Krisch, L. J. Butler, and J. Shu, J. Chem. Phys. **121** (4), 1830 (2004).

[92]   S. W. North, D. A. Blank, J. D. Gezelter, C. A. Longfellow, and Y. T. Lee, J. Chem. Phys. **102**, 4447 (1995).

93   S. M. Wu, J. J. Lin, Y.-T. Lee, and X.-M. Yang, J. Phys. Chem. A **104**, 7189 (2000).

94   P. D. Naik, A. Kumar, H. P. Upadhyaya, P. Bajaj, and S. K. Sarkar, *Lasers in Chemistry*. (Wiley New York,, 2008).

95   K. K. Pushpa, H. P. Upadhyaya, A. Kumar, P. D. Naik, P. N. Bajaj, and J. P. Mittal, J. Chem. Phys. **120**, 6964 (2004).

96   A. Kumar and P. D. Naik, Chem. Phys. Lett. **422**, 152 (2006).

97   A. Kumar, H. P. Upadhyaya, P. D. Naik, D. K. Maity, and J. P. Mittal, J. Phys. Chem. A **106**, 11847 (2002).

98   H. P. Upadhyaya, A. Kumar, P. D. Naik, A. V. Sapre, and J. P. Mittal, J. Chem. Phys. **117**, 10097 (2002).

99   P. L. Verheijdt and H. Cerfontain, J. Chem. Soc. Perkin Trans. 2 **11**, 1541 (1982); J. F. Arnett and S. P. McGlynn, J. Phys. Chem. **79**, 626 (1975); D. E. Nicodema, R. S. Silva, D. M. Togashi, M. Fernanda, and V. da Cunha, Journal of Photochemistry and Photobiology A: Chemistry **175**, 154 (2005); R. S. Beckel, L. V. Natarajan, C. Lenoble, and R. G. Harvey, J. Am, Chem. SOC. **110**, 7163 (1988); E. Charney and L. Tsai, J. Am, Chem. SOC. **93** (26), 7123 (1971); M. B. Rubin and R. Gleiter, Chem. Rev. **100**, 1121 (2000).

100   J.-P. Malval, C. Dietlin, X. Allonas, and J.-P. Fouassier, Journal of Photochemistry and Photobiology A: Chemistry **192**, 66 (2007).

101   S. M. Kupchan, R. W. Britton, J. A. Lacadie, M. F. Ziegler, and C. W. Sigel, J. Org. Chem. **40**, 648 (1975); N. Fukamiya, K. Lee, I. Muhammad, C. Murakami, M. O. Harvey, and J. Pelletier, Cancer Lett. **220**, 37 (2005).

102   K. Hoffken, W. Jonat, K. Possinger, M. Kolbel, T. H. Kunz, H. Wagner, R. Becher, R. Callies, P. Friederich, W. Willmanns, H. Maass, and C. G. Schmidt, J. Clin. Oncol. **8**, 875 (1990).

103   M. A. Gianturco, A. S. Giammarino, and R. G. Pitcher, Tetrahedron **19**, 2051 (1963).

104   R. Mondal, A. N. Okhrimenko, B. K. Shah, and D. C. Neckers, J. Phys. Chem. B **112**, 11 (2008).

105   J. T. Francis and A. P. Hitchcock, J. Phys. Chem. **98**, 3650 (1994).

106   A. K. Samanta, P. Pandey, B. Bandyopadhyay, and T. Chakraborty, Journal of Molecular Structure **963**, 234 (2010); A. Mukhopadhyay, A. K. Ghosh, M. Mukherjee, and T. Chakraborty, Int. J. Mass. Spect. **309**, 192 (2012); A. K. Samanta, P. Pandey, B. Bandyopadhyay, and T. Chakraborty, J. Phys. Chem. A

114, 1650 (2010).

[107] Q. Shen, M. Traetteberg, and S. Samdal, Journal of Molecular Structure **923**, 94 (2009).

[108] A. Mukhopadhyay, M. Mukherjee, A. K. Ghosh, and T. Chakraborty, J. Phys. Chem. A **115**, 7494 (2011).

[109] K. N. Walzl, J. I. M. Xavier, and A. Kuppermann, J. Chem. Phys. **86** (12), 6701 (1987).

[110] E. P. Balskus, J. Mendez-Andino, R. M. Arbit, and L. A. Paquette, J. Org. Chem. **66**, 6695 (2001).

[111] M. P. Schwartz, D. E. Barlow, J. John N. Russell, K. P. Weidkamp, J. E. Butler, M. P. D'Evelyn, and R. J. Hamers, J. Am. Chem. Soc. **128**, 11054 (2006).

[112] A. Trivella, T. N. Wassermann, J. M. Mestdagh, C. T. Manca, F. Marinelli, P. Roubin, and S. Coussan, Phy. Chem. Chem. Phys. **12** (29), 8300 (2010); W. M. Horspool, Photochemistry **35**, 17 (2005).

[113] H. P. Upadhyaya, A. Kumar, and P. D. Naik, J. Chem. Phys. **118** (6), 2590 (2003).

[114] R. Vasudev, R. N. Zare, and R. N. Dixon, J. Chem. Phys. **80**, 4863 (1984).

[115] H. P. Upadhyaya, A. Kumar, and P. D. Naik, J. Chem. Phys. **118**, 2590 (2003).

[116] M. F. Arendt, P. W. Browning, and L. J. Butler, J. Chem. Phys. **103**, 5877 (1995).

[117] D. B. Galloway, T. Glenewinkel-Meyer, J. A. Bartz, L. G. Huey, and F. F. Crim, J. Chem. Phys. **100**, 1946 (1994).

[118] R. D. Levine and J. L. Kinsey, edited by R. B. Bernstein (Plenum Press, New York, 1979).

[119] J. T. Muckermann, J. Phys. Chem. **93**, 179 (1989).

[120] C. E. Klots, J. Chem. Phys. **58**, 5364 (1973).

[121] A. F. Tuck, J. Chem. Soc., Faraday T rans. 2 **73**, 689 (1977).

[122] P. D. Naik, H. P. Upadhyaya, A. Kumar, A. Sapre, and J. P. Mittal, Chem. Phys. Letters **340**, 116 (2001).

[123] P. D. Naik, H. P. Upadhyaya, A. Kumar, A. V. Sapre, and J. P. Mittal, Journal of Photochemistry and Photobiology C: Photochemistry Reviews **3**, 165 (2003).

[124] H. P. Upadhyaya, A. Kumar, P. D. Naik, A. V. Sapre, and J. P. Mittal, J. Chem. Phys. **117**, 10097 (2002).

[125] S. Xu, S. T. Park, J. S. Feenstra, R. Srinivasan, and A. H. Zewail, J. Phys. Chem. A **108**, 6650 (2004).

[126] C.-H. Zhou, S.-B. Cheng, J.-L. Sun, H.-M. Yin, K.-L. Han, and G.-Z. He, J. Phys.

Chem. A **113**, 4923 (2009).

[127] X.-F. Yue, J.-L. Sun, H.-M. Yin, Q. Wei, and K.-L. Han, J. Phys. Chem. A **113**, 3303 (2009).

[128] I. Bejan, Y. A. E. Aal, I. Barnes, T. Benter, B. Bohn, P. Wiesen, and J. Kleffmann, Phys. Chem. Chem. Phys. **8**, 2028 (2006).

[129] Q. Wei, H.-M. Yin, J.-L. Sun, X.-F. Yue, and K.-L. Han, Chem. Phys. Lett. **463**, 340 (2008); S.-B. Cheng, C.-H. Zhou, H.-M. Yin, J.-L. Sun, and K.-L. Han, J. Chem. Phys. **130**, 234311 (2009).

[130] S. SenGupta, H. P. Upadhyaya, A. Kumar, S. Dhanya, P. D. Naik, and P. Bajaj, Chem. Phys. Lett. **452**, 239 (2008).

[131] S. Sengupta, Y. Indulkar, A. Kumar, S. Dhanya, P. D. Naik, and P. N. Bajaj, J. Phy. Chem. A **112**, 12572 (2008).

[132] A. Saha, M. Kawade, H. P. Upadhyaya, A. Kumar, and P. D. Naik, J. Chem. Phys. **134**, 044316 (2011).

[133] K. J. Castle, J. E. Abbott, X. Peng, and W. Kong, j. Phy. Chem. *A* **104**, 10419 (2000).

[134] N. S. Bayliss and E. G. McRae, J. Phy. Chem. **58**, 1006 (1954).

[135] J. E. Abbott, X. Peng, and W. Kong, J. Chem. Phys. **117**, 8670 (2002).

[136] M.-F. Lin, Y. T. Lee, C.-K. Ni, S. Xu, and M. C. Lin, J. Chem. Phys. **126**, 064310 (2007).

[137] L. J. Butler, D. Krajnovich, Y. T. Lee, G. Ondrey, and R. Bersohn, J. Chem. Phys. **79**, 1708 (1983).

[138] E. A. Wade, K. E. Reak, S. L. Li, S. M. Clegg, P. Zou, and D. L. Osborn, J. Phy. Chem. A **110**, 4405 (2006).

[139] C. Mijoule, S. Odiot, S. Fliszar, and J. M. Schnur, THEOCHEM **149**, 311 (1987).

[140] J. F. Arenas, J. C. Otero, D. Pelaez, and J. Soto, J. Chem. Phys. **129**, 7814 (2003).

[141] G. Radhakrishnan, T. Parr, and C. Wittig, Chem. Phys. Lett. **111**, 25 (1984).

[142] G. D. Greenblatt, H. Zuckermann, and Y. Haas, Chem. Phys. Lett. **134**, 593 (1987).

[143] S. Zabarnick, J. W. Fleming, and A. P. Baronavski, J. Chem. Phys. **85**, 3395 (1986).

[144] H. M. Wortelboer, M. Usta, Z. J. J., B. P. J., I. M. C. M. Rietjens, and N. H. P. Cnubben, Biochem. Pharmacol. **69**, 1879 (2005); T. Billard, Chem.—Eur. J. **12**, 974 (2006).

[145]   P. H. Schippers and H. P. Dekkers, J. Am. Chem. Soc. **105**, 145 (1983).

[146]   H. P. Upadhyaya, A. Kumar, P. D. Naik, Avinash V. Sapre, and J. P. Mittal, J. Chem. Phys. **117**, 10097 (2002).

[147]   S. Dhanya, D. K. Maity, H. P. Upadhyaya, A. Kumar, P. D. Naik, and R. D. Saini, J. Chem. Phys. **118**, 10093 (2003).

[148]   M. N. Kawade, A. Saha, H. P. Upadhaya, A. Kumar, and P. D. Naik, J. Phy. Chem. (communicated).

[149]   X. Tang, B. J. Ratliff, B. L. Fitzpatrick, and L. J. Butler, J. Phys. Chem. B **112**, 16050 (2008); M. D. Person, P. W. Kash, and L. J. Butler, J. Chem. Phys. **97**, 355 (1992).

[150]   Z.-R. Wei, X.-P. Zhang, W.-B. Lee, B. Zhang, and K.-C. Lin, J. Chem. Phys. **130**, 014307 (2009).

[151]   D. E. Szpunar, J. L. Miller, L. J. Butler, and F. Qi, J. Chem. Phys. **120**, 4223 (2004).

[152]   W. Wu, K. Liu, C. Yang, H. Zhao, H. Wang, Y. Yu, and H. Su, J. Phys. Chem. A **113**, 13892 (2009).

[153]   G.-L. Cui, Q.-S. Li, F. Zhang, W.-H. Fang, and J.-G. Yu, J. Phys. Chem. A **110**, 11839 (2006).

[154]   M. Ahmed, D. Blunt, D. Chen, and A. G. Suits, J. Chem. Phys. **106**, 7617 (1997); N. Hemmi and A. G. Suits, J. Phys. Chem. A **101**, 6633 (1997).

[155]   C.-Y. Wu, Y.-P. Lee, and N. S. Wang, J. Chem. Phys. **120**, 6957 (2004).

[156]   J. E. Katon and J. W. R. Feairheller, J. Chem. Phys. **47**, 1248 (1967); D. F. Koster and T. P. Vasiloff, Spectrochim. Acta **27**, 1633 (1971); N. Pietri, B. Jurca, M. Monnier, M. Hillebrand, and J. P. Aycard, Spectrochimica Acta Part A **56**, 157 (1999).

[157]   K. Hagen, J. Mol. Struct. **128**, 139 (1985).

[158]   J. M. Landry and J. E. Katon, Spectrochim. Acta **40A**, 871 (1984).

[159]   L. Bizzocchi, C. D. Esposti, and L. Dore, Astronomy & Astrophysics **492**, 875 (2008).

[160]   E. Jabbari, J. A. Gruetzmacher, L. Lu, B. L. Currier, and M. J. Yaszemski, presented at the Proc. of the 25th Annu. Inter. Confer. of the IEEE EMBS, Cancun, Mexico., 2003 (unpublished).

[161]   M. Mahmoudi, A. Simchi, M. Imani, and U. O. Hafeli, J. Phys. Chem. C **113**, 8124 (2009).

162   S. Maaref, Z. Roz, S.-S. Sun, K. Seo, K. Winston, and C. E. Bonner, J. Appl. Poly. Science **92**, 317 (2004).

163   R. Liyanage, Y. A. Yang, S. Hashimoto, R. Gordon, and R. W. Field, J. Chem. Phys. **103**, 6811 (1995).

164   D. S. Green, G. A. Bickel, and S. C. Wallace, J. Mol. Spectrosc. **150**, 388 (1991).

165   S. Arepalli, N. Presser, D. Robie, and R. J. Gordon, Chem. Phys. Lett. **118**, 88 (1985); A. Kvaran, A. Logadottir, and H. Wang, J. Chem. Phys. **109**, 5856 (1998).

166   J.-F. Boily and T. M. Seward, J. Sol. Chem. **34**, 1167 (2005).

167   K.-C. Lau, Y. Liu, and L. J. Butler, J. Chem. Phys. **123**, 054322 (2005).

168   M. L. Morton, L. J. Butler, T. A. Stephenson, and F. Qi, J. Chem. Phys. **116** (7), 2763 (2002); Y. Liu and L. J. Butler, J. Chem. Phys. **121** (22), 11016 (2004).

169   J. A. Mueller, B. F. Parsons, L. J. Butler, F. Qi, O. Sorkhabi, and A. G. Suits, J. Chem. Phys. **114** (10), 4505 (2001).

170   H. P. Upadhyaya, A. Saha, A. Kumar, T. Bandyopadhyay, P. D. Naik, and P. N. Bajaj, J. Phys. Chem. A **114**, 5271 (2010); S. J. Riley and K. R. Wilson, J. Chem. Soc., Faraday Discuss. **53**, 132 (1972).

171   R. T. Carter, A. Hallou, and J. R. Huber, Chem. Phys. Lett. **310**, 166 (1999); R. J. Wilson, J. A. Mueller, and P. L. Houston, J. Phys. Chem. A **101** (41), 7593 (1997).

172   E. J. Hintsa, X. Zhao, and Y. T. Lee, J. Chem. Phys. **92** (4), 2280 (1990).

173   S. Gronowitz, *The Chemistry of Heterocyclic Compounds*. (Wiley-Interscience, New York, 1992); F. Bohlmann and C. Zdero, *The Chemistry of Heterocyclic Compounds, Thiophene and its Derivatives*. (Wiley & Sons New York, 1985).

174   C. G. Shuttle, R. Hamilton, B. C. O'Regan, J. Nelson, and J. R. Durrant, Proc. Natl. Acad. Sci. U.S.A. **107** (38), 16448 (2010); A. R. Murphy and J. M. J. Frechet, Chem. Rev. **107** (4), 1066 (2007); Y. Y. Liang and L. P. Yu, Polym. Rev. **50**, 454 (2010); J. B. Kim, K. Allen, S. J. Oh, S. Lee, M. F. Toney, Y. S. Kim, C. R. Kagan, C. Nuckolls, and Y. L. Loo, Chem. Mater. **22** (20), 5762 (2010); J. W. Chen and Y. Cao, Acc. Chem. Res. **42** (11), 1709 (2009).

175   L. Nyulaszi and T. Veszpremi, J. Mol. Struc **140**, 353 (1986).

176   M. H. Palmer, I. C. Walker, and M. F. Guest, Chem. Phys. **241**, 275 (1999).

177   W. M. Flicker, O. A. Mosher, and A. Kuppermann, Chem. Phys. Lett. **38** (3), 489 (1976); W. M. Flicker, O. A. Mosher, and A. Kuppermann, J. Chem. Phys. **64** (4), 1315 (1976).

178   R. Weinkauf, L. Lehr, E. W. Schlag, S. Salzmann, and C. M. Marian, Phys.

Chem. Chem. Phys. **10**, 393 (2008).

[179] X.-F. Wu, X. Zheng, H.-G. Wang, Y.-Y. Zhao, X. Guan, D. L. Phillips, X. Chen, and W. Fang, J. Chem. Phys. **133**, 134507 (2010).

[180] S. Salzmann, M. Kleinschmidt, J. Tatchen, R. Weinkauf, and C. M. Marian, Phys. Chem. Chem. Phys. **10**, 380 (2008).

[181] H. Koppel, E. V. Gromov, and A. B. Trofimov, Chem. Phys. **304**, 35 (2004).

[182] G. Cui and W. Fang, J. Phys. Chem. A **115**, 11544 (2011).

[183] M. Stenrup, Chem. Phys. **397**, 18 (2012).

[184] G. Varsányi, L. Nyulászi, T. Veszprémi, and T. Narisawa, J. Chem. Soc. Perkin Trans. 2 **2**, 761 (1982); G. L. Bendazzoli, F. Bertinelli, and P. Palmieri, J. Chem. Phys. **69** (11), 5077 (1978).

[185] H. A. Wiebe and J. Heicklen, Can. J. Chem. **47**, 2965 (1969).

[186] A. K. Nayak, S. K. Sarkar, R. S. Karve, V. Parthasarathy, K. V. S. Rama Rao, J. P. Mittal, S. L. N. G. Krishnamachari, and T. V. Venkitachalam, Appl. Phys. B **48**, 437 (1989).

[187] S. L. N. G. Krishnamachari and T. V. Venkitachalam, Chem. Phys. Lett. **55** (1), 116 (1978).

[188] C. W. Hsu, C. L. Liao, Z. X. Ma, and C. Y. Ng, J. Phys. Chem. **99** (6), 1760 (1995).

[189] F. Qi, O. Sorkhabi, A. H. Rizvi, and A. G. Suits, J. Phys. Chem. A **103** (42), 8352 (1999).

[190] J. W. Rabalais, L. O. Werme, T. Bergmark, L. Karlsson, and K. Siegbahn, Int. J. Mass Spectrom. Ion Phys. **9**, 185 (1972); A. W. Potts, A. B. Trofimov, J. Schimer, D. M. P. Holland, and L. Karlsson, Chem. Phys. **271**, 337 (2001).

[191] A. B. Trofimov, J. Schirmer, D. M. P. Holland, L. Karlsson, R. Maripuu, K. Siegbahn, and A. W. Potts, Chem. Phys. **263**, 167 (2001).

[192] B. Norden, R. Hakansson, P. B. Pedersen, and E. W. Thulstrup, Chem. Phys. **33**, 355 (1978).

[193] Y.-F. Xu, S. X. Tian, L. Chen, F.-Y. Liu, and L. Sheng, J. Phys. Chem. A **115**, 10920 (2011).

[194] F. Zhang, Z. Cao, X. Qin, Y. Liu, Y. Wang, and B. Zhang, Acta Phys. -Chim. Sin. **24**, 1335 (2008).

[195] D. M. Lubman and R. M. Jordan, Rev. Sci. Instrum. **56** (3), 373 (1985); J. H. Brophy and C. T. Rettner, Chem. Phys. Lett. **67** (2,3), 351 (1979).

[196] R. J. Wilson, J. A. Mueller, and P. L. Houston, J. Phys. Chem. A **101** (41), 7593

(1997); A. S. Bracker, E. R. Wouters, A. G. Suits, Y. T. Lee, and O. S. Vasyutinskii, Phys. Rev. Lett. **80** (8), 1626 (1998).

[197]   R. Liyanage, Y. A. Yang, S. Hashimoto, R. Gordon, and R. W. Field, J. Chem. Phys. **103**, 6811 (1995).

[198]   K. C. Lau, Y. Liu, and L. J. Butler, J. Chem. Phys. **125**, 144312 (2006).

[199]   Y. Garcia, F. Schoenebeck, C. Y. Legault, C. A. Merlic, and K. N. Houk, J. Am. Chem. Soc. **131**, 6632 (2009).

[200]   J. T. Muckermann, J. Phys. Chem. **93**, 179 (1989).

[201]   M. Kawasaki, K. Suto, Y. Sato, Y. Matsumi, and R. Bersohn, J. Phys. Chem. **100** (51), 19853 (1996).

[202]   M. Kawade, A. Saha, H. P. Upadhyaya, A. Kumar, P. D. Naik, and P. N. Bajaj, J. Phys. Chem. A **115**, 1538 (2011).

List of journal publications:

1. Monali N. Kawade, Hari P. Upadhyaya, Awadhesh Kumar, Prakash D. Naik
    Photodissociation dynamics study of nitrocyclopentane at 193 nm and 2-chloro-6-nitrotoluene at 193, 248 and 266 nm. (to be communicated)

2. Ankur Saha, Monali Kawade, Hari P. Upadhyaya, Awadhesh Kumar, Prakash D. Naik
    Photodissociation dynamics of benzyol chloride at 235 nm: Resonance-enhanced multiphoton ionization (REMPI) detection of Cl and HCl. (Communicated)

3. Ankur Saha, Monali N. Kawade, Hari P. Upadhyaya, Awadhesh Kumar, and Prakash D. Naik
    Photoexcitation of 2-bromo-2-chloro-1,1,1-trifluroethane (Halothane) to repulsive surface nσ*(C–Br) at 234 nm: Dynamics of C–Br and C–Cl bond rupture, *Chem. Phys.*, 2013, 416,1-10 (not included in the thesis).

4. Monali N. Kawade, Ankur Saha, Hari P. Upadhyaya, Awadhesh Kumar, and Prakash D. Naik, P. N. Bajaj
    Photodissociation Dynamics of enolic 1,2-cyclohexane dione at 266, 248, and 193 nm: Mechanism and nascent state product distribution of OH study, J. Phys. Chem. A 2013, 117, 2415-2426.

5. Monali N. Kawade, Ankur Saha, Hari P. Upadhyaya, Awadhesh Kumar, Prakash D. Naik, P. N. Bajaj
    Photodissociation Dynamics of Halogenated Thiophenes at 235 nm: A Resonance Enhanced Multiphoton Ionization-Time of Flight (REMPI-TOF) study, J. Phys. Chem. A 2012, 116, 10656-10667.

6. Ankur Saha, Monali N. Kawade, Hari P. Upadhyaya, Awadhesh Kumar, Prakash D. Naik, P. N. Bajaj
    Resonance Enhanced Multiphoton Ionization-Time of Flight (REMPI-TOF) study of phosphorous oxychloride (POCl$_3$) dissociation at 235 nm: dynamics of Cl (^{2}P$_j$) formation, *Chem. Phys.*, 2012, 407,83-91(not included in the thesis).

7. Ankur Saha, Monali Kawade, Hari P. Upadhyaya, Awadhesh Kumar, Prakash D. Naik
    Laser-induced UV photodissociation of 2-bromo-2-nitropropane: Dynamics of OH and Br formation, J. Chem. Phys., 2011, 134, 044316(not included in the thesis).

8. Monali N. Kawade, Ankur Saha, Hari P. Upadhyaya, Awadhesh Kumar, Prakash D. Naik, P. N. Bajaj
    Dynamics of Cl (^{2}P$_j$) Atom Formation in the Photodissociation of Fumaryl Chloride (ClCO - CH = CH - COCl) at 235 nm: A Resonance Enhanced Multiphoton Ionization (REMPI) Time-of-Flight (TOF) Study, J. Phys. Chem. A 2011, 115, 1538-1546.

9. Monali N. Kawade, Ankur Saha, Hari P. Upadhyaya, Awadhesh Kumar, Prakash D. Naik
    Dynamics of N-OH Bond Dissociation in Cyclopentanone and Cyclohexanone Oxime at 193 nm: Laser-Induced Fluorescence Detection of Nascent OH (v'', J''), J. Phys. Chem. A 2010**,** 114, 12369-12377